

國立交通大學

機械工程學系

博士論文

利用射頻反應磁控濺鍍方式來研究
氧化鋅薄膜之材料特性與電漿特性之關係

Investigation of Relationship between the Plasma and
Material Characteristics of Zinc Oxide (ZnO) Thin Film
by Radio Frequency (RF) Reactive Magnetron Sputtering

研究生：許哲維

指導教授：吳宗信 博士

中華民國九十九年一月

利用射頻反應磁控濺鍍方式來研究
氧化鋅薄膜之材料特性與電漿特性之關係

Investigation of Relationship between the Plasma and
Material Characteristics of Zinc Oxide (ZnO) Thin Film
by Radio Frequency (RF) Reactive Magnetron Sputtering

研究生：許哲維

Student : Che-Wei Hsu

指導教授：吳宗信 博士

Advisor : Dr. Jong-Shinn Wu

國立交通大學

機械工程學系

博士論文

A Thesis

Submitted to Department of Mechanical Engineering College of Engineering

National Chiao Tung University

in Partial Fulfillment of the Requirements

for the Degree of Doctor of Philosophy in Mechanical Engineering

January 2010

Hsinchu, Taiwan, Republic of China

中華民國九十九年一月

利用射頻反應磁控濺鍍方式來研究

氧化鋅薄膜之材料特性與電漿特性之關係

研究生：許哲維

指導教授：吳宗信 博士

國立交通大學

機械工程學系(熱流組)

中文摘要

本研究主要利用射頻反應磁控濺鍍系統來沈積氧化鋅(ZnO)薄膜在玻璃基板上。我們分別利用蘭牟爾探針(Langmuir probe)來量測電漿特性、X光繞射儀(XRD)量測材料結構特性、X光光電子能譜儀(XPS)量測材料成份及鍵結特性，可見光-紫外光光譜儀(UV-VIS spectrophotometer)量測光學特性以及接觸角量測儀量測表面親疏水特性。結果顯示，電漿密度、電子溫度、沈積速率以及所計算出之離子轟擊能量均隨著射頻功率(RF power)的增加而遞增。而在薄膜成長的過程中，沈積速率與離子轟擊能量的大小同時會影響氧化鋅薄膜之結構特性。由實驗的結果，我們觀察到三個不同的射頻功率範圍與電漿、材料結構特性有強烈的影響。在低功率的情況下(50-100 瓦)，可以觀察到最大的晶粒(grain size)，這主要是因為沈積速率較慢而產生的結果；在功率次之的情況下(100-200 瓦)，由於沈積速率與離子轟擊能量的效應相互抵銷下，導致最小的晶粒產生；而在高功率的情況下(200-400 瓦)，因為離子轟擊能量增加，間接使基板溫度升高，進而提供能

量使表面不穩定之原子重新排列，所以又可觀察到晶粒尺寸逐漸增大。所以當射頻功率在 400 瓦時，可以得到材料特性最佳的氧化鋅薄膜。此外，在光學特性部分，不管是氧化鋅薄膜或是氧化鋅薄膜沈積在玻璃上，它們在可見光範圍(400-700 奈米)的平均穿透率均可超過 85 %，而且在紫外光範圍(280-400 奈米)也得到較佳的抗紫外光之特性。薄膜厚度的效應在光學特性的影響上比起射頻電源的效應來的更重要。最後，當氧化鋅薄膜沈積在玻璃基板上，它同時也顯示出疏水性特徵。

對於不同氣體比例的影響，沈積速率均隨著氧氣含量的增加而減少，主要是因為氧氣屬於負電漿，進而導致電漿密度降低所致。當氧氣與氫氣之氣體比例為 0.3 時，XRD 的結果指出它屬於多晶系的氧化鋅薄膜，且同時具有較小的半高寬(FWHM)以及最大的晶粒尺寸。另一方面，藉由 X 光光電子能譜儀得知，在此條件下亦同時擁有較多的 O-Zn 鍵結以及較強的鍵結強度。

最後，經由退火處理後，可以同時得到較小的半高寬、較大的晶粒尺寸以及具有較少殘餘應力薄膜。然而，適當的退火溫度是一個相當重要的因素對於有效改善材料的特性上，像是薄膜品質、應力、晶粒大小、穿透率、抗紫外線能力等等。其中，當退火溫度在 300 度以下時則會有較明顯的改善趨勢。反之當溫度超過 400 度時，則對材料的改善效果就趨於和緩。因此，我們推測在玻璃上較佳的退火溫度大約是在 400 度。

綜合目前的結果，我們可以同時得到高穿透率、較佳的抗紫外光能力以及疏水性特徵於氧化鋅薄膜沈積在玻璃基板上，這些特性相當適合用在建築玻璃、車用玻璃等相關

產業上。未來，亦可針對不同的沈積參數做進一步的研究及討論，包括不同的靶材與基板間之距離、操作壓力等參數。

關鍵字: 氧化鋅、濺鍍、蘭牟爾探針、X 光繞射儀、X 光光電子能譜儀、離子轟擊能量、抗紫外線。



Investigation of Relationship between the Plasma and
Material Characteristics of Zinc Oxide (ZnO) Thin Film
by Radio Frequency (RF) Reactive Magnetron Sputtering

Student: Che-Wei Hsu

Advisor: Dr. Jong-Shinn Wu

Department of Mechanical Engineering
National Chiao-Tung University

Abstract

Zinc oxide (ZnO) thin film was deposited on glass substrate by RF reactive magnetron sputtering. The plasma parameters, structural, chemical, optical and hydrophilic/hydrophobic properties of the film were measured using a Langmuir probe, x-ray diffractometry (XRD), X-ray Photoelectron Spectroscopy (XPS), a UV-VIS spectrophotometer, and contact angle measurement, respectively. Results show that plasma density, electron temperature, deposition rate, and estimated ion bombardment energy all increased with increasing applied RF power. The deposition rate and ion bombardment energy were both influenced during ZnO thin film growth. Based on the measurements above, there are three distinct power regimes, which are strongly correlated with plasma properties. In the low power regime (50-100 W), a slow deposition rate produced the largest grain size. The smallest grain size appeared in the medium power regime (100-200 W). This is attributed to insufficient time for the adatoms to migrate on the substrate surface. In the high power regime (200-400 W), a

relatively larger grain size appeared due to very large ion bombardment energy, which heated up the substrate and enhanced the thermal migration of adatoms. The optimal level of RF power for obtaining the optimum material properties of ZnO thin film is RF 400 W. However, the average transmittance is over 85% in the visible region of 400-700 nm for both pure ZnO thin film and ZnO on glass. This thesis also shows that ZnO thin film possessed better UV-shielding characteristics. For all of these optical properties, the thickness effect was more important than the power effect. The ZnO thin film exhibited hydrophobic characteristic when coated on glass substrate.

For the $O_2/(Ar+O_2)$ ratio effect, the results of this study show that the deposition rate decreased with an increasing $O_2/(Ar+O_2)$ ratio. This was caused by a reduction in plasma density due to the addition of electronegative oxygen. At an $O_2/(Ar+O_2)$ ratio of ~ 0.3 , XRD results show that ZnO thin film forms a polycrystalline structure with the lowest FWHM (largest grain size). At the same time, the content fraction of the O^1 peak (O-Zn bond) and the corresponding binding energy reached their highest levels at this $O_2/(Ar+O_2)$ ratio, according to XPS analysis.

The smallest FWHM, largest grain size, and less relaxation stress were simultaneously created by annealing treatment. The moderation annealing temperature is an important factor for improving material properties such as film quality, stress, grain size, transmittance, and UV-shielding characteristics, etc. An annealing treatment below $300^\circ C$ offers significant

improvements, whereas it has no obvious variance when the annealing temperature exceeds 400°C. Finally, we deduced that the best annealing temperature is at 400°C for glass substrate.

In summary, we have obtained the excellent properties of ZnO thin film on glass with the high transparency, good UV-shielding, and hydrophobic characteristics for glass industry applications. The final section of this thesis provides directions for future research on different deposition parameters (distance between target and substrate, working pressure effect, etc.).

Keywords: Zinc Oxide (ZnO), Sputtering, Langmuir probe, x-ray diffractometry (XRD), X-ray Photoelectron Spectroscopy (XPS), Ion bombardment energy, UV-shielding.



誌謝

首先要感謝指導教授吳宗信教授對於學生在博士班期間的指導及協助，使得學生能提昇自己各方面研究相關的能力以及國際視野，最後順利取得博士學位，在此表達最高的敬意與謝意。此外，也要特別感謝魏大欽副教授在相關電漿理論及分析上耐心的教導及指正，使得本研究能更加完整。而鄭宗杰助理教授從碩士班至博士班對於學生在生活及研究上的提攜及建議不遺餘力，亦督促著學生不斷的成長，也致上衷心的謝意。最後，同時也要感謝沈弘俊教授、溫志湧教授、傅武雄教授、陳慶耀教授、周長彬教授、魏大欽副教授、鄭宗杰助理教授、謝健博士等口試委員對於論文中不盡完善的部分給予適當的建議與指教，使本研究益加完備。



另外，也要感謝國家奈米元件實驗室(NDL)在實驗設備上的協助，當然也要特別感謝材料分析組的工程師們的鼎力幫忙，包括楊君惠、沈奕伶、簡依玲、姚潔宜、郭美玲、許瓊姿、周棟煥、林宏旻等。以及張妙如、簡秀芳等人在實驗過程中一般行政事務上的協助，使學生在研究過程中遇到的疑難雜症均能順利解決並完成。其他包含黃文賢、黃仕強、沈志彥、楊忠諺博士、謝健博士、張茂男博士、鄧建龍博士等人均在各種不同領域上給予學生適當的建議及指教，使學生受益良多。還有目前已赴美攻讀博士的鄭明欣學長，謝謝你的傾囊相授，讓我對材料分析開始有進一步的瞭解。最後當然也不能忘記曾經在台南 NDL 內提供學生最多支援的工程師們，包括蔡來福、湯淵富、林育德、薛漢鼎、文祥昇、陳永祥、陽永明等人，在此獻上最深的感謝。

除此之外，在這段研究過程中一起打拼、相互砥礪、陪我度過這段有歡笑淚水過程的謝盛祺、洪政男、蔡尚瑋、張原銘、溫華強等同學。以及無怨無悔被我壓榨的學弟妹們(吳聲堯、毛穎恆、洪嘉良、廖士均、葉帝佑、鍾宛倩)，因為有你們才能呈現如此完整的成果。當然不能忘記還有現在任教於義守大學的簡贖瑞學長，感謝你們的陪伴及支持。希望未來大家還可以一起打拼下去，加油！

然而，最重要的當然還有 APPL 實驗室內所有學長姐、學弟妹們給予課業及生活上的相互支持與砥礪，像是邵雲龍、梁桂雄、許國賢、李允民、周欣芸、鄭凱文、黃柏誠、鍾東霖、陳立軒、梁偉豪、陳百彥、胡孟樺、鄭丞志，以及許多無法一一提及的學弟妹們。其中要特別感謝邵董從碩班開始對我的照顧，除了提點我研究上要注意的所有細節及方法外，對於生活上的瑣事及人際關係也給我許多的協助。當然也不能忘記一群人騎腳踏車挑戰陽明山、東北角的事蹟，多虧這些驚人之舉，也讓求學生涯增添許多不可抹滅的回憶，謝謝你們陪我度過這幾年充實的研究生活。

而家人給予我精神上、經濟上的支持與鼓勵，使得我在研究期間能夠無後顧之憂的專心研究；此外，陪我度過這漫長研究生活的女友林欣儀，謝謝妳當我遇到低潮、不如意時，適時給予我鼓勵並送上溫暖，且不辭辛勞的陪伴我跑遍大大小小的國內、外研討會，讓我能順利地完成學業。至於其他在身邊支持、鼓勵我的所有朋友們，雖然無法

一一提及各位，但也都給你們最深的祝福與感謝。在此將論文獻給你們，沒有你們的支持就沒有現在的我。

許哲維 謹誌

2010.01.31. 于新竹·交通大學



Table of Contents

中文摘要	i
Abstract.....	iv
誌謝	vii
Table of Contents	x
List of Tables	xiii
List of Figures.....	xv
Nomenclature	xxv
Chapter 1. Introduction.....	1
1.1 Background and Motivation	1
1.2 General Properties of Zinc Oxide (ZnO).....	3
1.3 Deposition Techniques of ZnO Thin Films.....	4
1.4 Importance of Plasma Diagnostics	6
1.5 Specific Objectives of the Thesis	10
Chapter 2. Basics Theories	12
2.1. Thin Film Growth Mechanism.....	12
2.2. Fundamentals of Plasma Physics	15
2.3. Principle of Langmuir Probe Diagnostics	17
2.3.1. Introduction to I-V Curve	18
2.3.2. Theory of Langmuir Probe	21
2.3.2.1. Planar Probe with Collisionless Sheath.....	21
2.3.2.2. Cylindrical Probe with Collisionless Sheath.....	27
2.4. Theory of X-Ray Diffraction (XRD)	32
2.5. Theory of Optics	35
Chapter 3. Experimental Methods	38
3.1. Experimental Apparatus	38
3.1.1. RF Reactive Magnetron Sputtering Chamber	38

3.1.1.1. RF Power Subsystem	38
3.1.1.2. The Magnetron Subsystem.....	39
3.1.1.3. The Temperature Control Subsystem	40
3.1.1.4. Mass Flow Control Subsystem	40
3.1.1.5. Pumping Subsystem	41
3.1.1.6. Pressure Control Subsystem and Gauge Meter Components.....	41
3.1.1.7. Target and Gases.....	43
3.2. Experimental Instrumentation	44
3.2.1. Plasma Diagnostics	44
3.2.1.1. Langmuir Probe System	44
3.2.2. Structural Characterization Techniques	46
3.2.2.1. Surface Profilometer (α -step).....	46
3.2.2.2. X-Ray Diffractometry (XRD).....	46
3.2.3. Chemical Characterization Techniques	48
3.2.3.1. X-ray Photoelectron Spectroscopy (XPS)	48
3.2.4. Optical Characterization Techniques.....	49
3.2.4.1. Ultraviolet-Visible Spectrophotometer (UV-VIS Spectrophotometer)	49
3.2.5. Hydrophobic/Hydrophilic Characterization Techniques	50
3.2.5.1. Contact Angle System	50

Chapter 4. Results and Discussion 51

4.1. Summary of Test Conditions.....	51
4.2. Plasma Characteristics	52
4.2.1. Effect of RF Power	52
4.2.2. Effect of Gas Ratio (Ar / O_2).....	57
4.3. Structural Characteristics	59
4.3.1. Effect of RF Power	59
4.3.2. Effect of Gas Ratio (Ar / O_2).....	62
4.4. Chemical Characteristics	64
4.4.1. Effect of RF Power	64
4.4.2. Effect of Gas Ratio (Ar / O_2).....	66
4.5. Optical Characteristics	67
4.5.1. Effect of RF Power	67
4.5.2. Effect of Gas Ratio (Ar / O_2).....	71
4.6. Hydrophobic/Hydrophilic Characteristics	74
4.6.1. Effect of RF Power	74
4.6.2. Effect of Gas Ratio (Ar / O_2).....	74
4.7. Annealing Temperature Effect of ZnO Thin Film.....	75
4.7.1. Structural Characteristics	76

4.7.2. <i>Optical Characteristics</i>	79
Chapter 5. Summary and Recommendation of Future Works....	81
5.1. <i>Summary</i>	81
5.2. <i>Recommendation of Future Works</i>	83
Appendices	86
<i>Appendix A. Langmuir Probe Analysis</i>	86
References.....	89
Publication List of Che-Wei Hsu	221



List of Tables

Table 1.1. Key structural properties of zinc oxide (ZnO)	117
Table 1.2. Key optical properties of zinc oxide (ZnO).....	118
Table 1.3. Key electrical properties of zinc oxide (ZnO).....	119
Table 1.4. Key mechanical properties of zinc oxide (ZnO)	120
Table 2.1. Several inelastic collision types within the plasma [140-141]	121
Table 2.2. Approximation frequencies and vacuum wavelength ranges for various colors [153]	122
Table 4.1. The deposition conditions of ZnO thin films for thickness effect under a constant RF power	123
Table 4.2. The deposition conditions of ZnO thin films for RF power effect under a constant thickness	124
Table 4.3. The deposition conditions of ZnO thin films for thickness effect under a constant.....	125
Table 4.4. The deposition conditions of ZnO thin films for.....	126
Table 4.5. Various thicknesses of ZnO thin films for	127
Table 4.6. Various thicknesses of ZnO thin films for	128
Table 4.7. Various contact angles of ZnO thin films for RF power effect under a constant thickness.	129

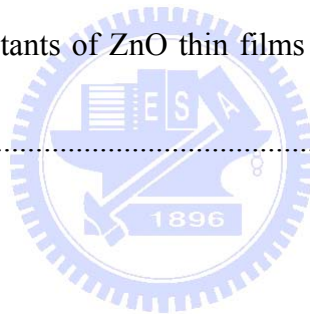
Table 4.8. Various contact angles of ZnO thin films for deposition time (thickness) effect under a constant RF power. 130

Table 4.9. Various contact angles of ZnO thin films for O₂/(Ar+O₂) ratio effect under a constant thickness. 131

Table 4.10. Various contact angles of ZnO thin films for deposition time (thickness) effect under a constant O₂/(Ar+O₂) ratio. 132

Table 4.11. The deposition conditions of ZnO thin films for annealing temperature effect under a constant thickness. 133

Table 4.12. Various lattice constants of ZnO thin films for annealing temperature effect 134



List of Figures

Figure 1.1. Hexagonal wurtzite structure of ZnO (small grey ball is zinc and big red ball is oxygen) [55].	135
Figure 1.2. Hexagonal close-packed (HCP) structure of ZnO.	136
Figure 2.1. Schematic illustration of mechanism of thin film growth [136-137].	137
Figure 2.2. Three different mechanisms for reactive sputter deposition: (a) at the target; (b) in the plasma volume and (c) at the substrate [138].	138
Figure 2.3. Several different electron-atom collisions: (a) ionization collision; (b) excitation collision; (c) relaxation process and (d) dissociation process [140].	139
Figure 2.3. Several different electron-atom collisions: (a) ionization collision; (b) excitation collision; (c) relaxation process and (d) dissociation process [140]. (Continuous)	140
Figure 2.4. Paschen curve for a number of gases. (From A. von Engel, <i>Ionized Gases</i> . Oxford University Press, Oxford, 1965. Reprinted with permission) [143].	141
Figure 2.5. Schematic illustration of plasma diagnostic technique by using a Langmuir probe.	142
Figure 2.6. Typical I - V characteristics for a Langmuir probe.	143

Figure 2.7. Theoretical shape of the saturation current portion of the probe characteristic for various probe shapes (planar, cylindrical and spherical) when the probe current is limited by orbital motions [119].	144
Figure 2.8. Schematic illustration of sheath forms with different geometry of probes.	145
Figure 2.9. The charge particles arrive to the plasma sheath by orbital motion.	146
Figure 2.10. Ion orbital motion within the plasma sheath of a cylindrical Langmuir probe [141].	147
Figure 2.11. Schematic diagram of Bragg diffraction from a set of parallel planes.	148
Figure 2.12. Schematic diagram of x-ray diffraction peak for calculating the grain size (crystallite size) by Scherrer equation.	149
Figure 2.13. Reflection, propagation and transmission of a light beam incident on an optical medium [152].	150
Figure 2.14. The electromagnetic spectrum of radiation; the bandgaps and cutoff frequencies for some optical materials are also shown [154].	151
Figure 2.15. Interaction of photons with a material. In addition to reflection, absorption, and transmission, the beam changes direction, or is refracted. The change in direction is given by the index of refraction n [154].	152
Figure 3.1. The configuration of RF reactive magnetron sputtering system.	153
Figure 3.2. Schematic illustration of RF reactive magnetron sputtering system.	154

Figure 3.3. The configuration of RF power system. (a) Top and (b) front view of RF plasma generator system, respectively; (c) top and (d) side view of automatic matching network system, respectively.....	155
Figure 3.4. The configuration of Magnetron System.	156
Figure 3.5. The configuration of temperature controller system.....	157
Figure 3.6. The configuration of mass flow controller (MFC) system.....	157
Figure 3.7. The configuration of (a) mechanical pump and (b) cryogenic pump.....	158
Figure 3.8. The configuration of MKS self-tuning controller.	158
Figure 3.9. The configuration of ionization & low vacuum gauge controller.....	159
Figure 3.10. The configuration of Baratron capacitance manometer.	159
Figure 3.11. The configuration of thermocouple gauge.....	160
Figure 3.12. The configuration of ion gauge.....	160
Figure 3.13. The configuration of standard ESP analysis system with motorized Z-motion drive (Langmuir probe system).	161
Figure 3.14. Schematic illustrations of standard ESP analysis system with motorized Z-motion drive (Langmuir probe system).	162
Figure 3.15. Schematic illustration of construction of a cylindrical probe. (a) RF-compensated probe outline; (b) compensation electrode and probe tip detail; (c) probe tip assembly.....	163

Figure 3.16. Schematic illustration of a RF-compensated probe for fixed installations and motorised Z-motion drives.	164
Figure 3.17. Schematic illustration of a typical automatic Z-motion driver.	164
Figure 3.18. The configuration of surface profilometer (Sloan Dektak 3030 profilometer).	165
Figure 3.19. The configuration of X'Pert PRO x-ray diffractometry (XRD). (Source by PANalytical).....	166
Figure 3.20. The configuration of goniometer of x-ray diffractometry (XRD). (Source by PANalytical).....	166
Figure 3.21. Schematic diagram of x-ray diffraction measured techniques: (a) Gonio scan and (b) GIXRD scan.	167
Figure 3.22. The configuration of UV-VIS spectrophotometer.	168
Figure 3.23. The configuration of contact angle system.	168
Figure 4.1. Effect of deposition rate as a function of applied RF power at a constant thickness of 60 nm.	169
Figure 4.2. The floating potential (V_f) and plasma potential (V_s) as a function of applied RF power during ZnO thin film deposition.	170
Figure 4.3. The ion flux and ion bombardment energy (V_s-V_f) as a function of applied RF power during ZnO thin film deposition.	171

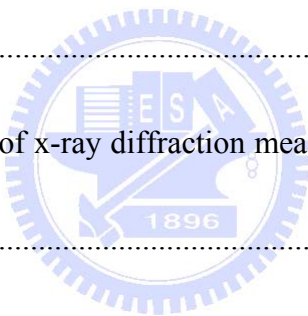


Figure 4.4. The electron temperature (T_e), electron number density (n_e), and ion number density (n_i) as a function of applied RF power during ZnO thin film deposition.	172
Figure 4.5. Relationship between ion flux and deposition rate as a function of applied RF power during ZnO thin film deposition.....	173
Figure 4.6. Effect of deposition rate as a function of $O_2/(Ar+O_2)$ ratio under a constant thickness of 60 nm.....	174
Figure 4.7. XRD patterns of ZnO thin films as a function of deposition time (for thickness effect) under a constant RF power of 100 W.....	175
Figure 4.8. XRD patterns of ZnO thin films as a function of RF power (for power effect) under a constant thickness of 60 nm.....	176
Figure 4.9. Effect of grain size and FWHM as a function of RF power under a constant thickness of 60 nm.....	177
Figure 4.10. SEM image of ZnO thin films for various RF powers - (a) RF 50 W; (b) RF 100 W; (c) RF 200 W; (d) RF 300 W; (e) RF 400 W.	178
Figure 4.11. XRD patterns of ZnO thin films as a function of deposition time under a constant $O_2/(Ar+O_2)$ ratio of 0.25.	179
Figure 4.12. XRD patterns of ZnO thin films as a function of $O_2/(Ar+O_2)$ ratio under a constant thickness of 60 nm.	180

Figure 4.13. Effect of grain size and FWHM of as a function of $O_2/(Ar+O_2)$ ratio at a constant thickness of 60 nm.	181
Figure 4.14. SEM image of ZnO thin films for various $O_2/(Ar+O_2)$ ratios - (a) 0.10; (b) 0.25; (c) 0.30; (d) 0.50; (e) 0.75; (f) 1.00.	182
Figure 4.15. XPS survey spectrum of ZnO thin film.	183
Figure 4.16. The binding energy of (a) Zn 2p peak and (b) O 1s peak of ZnO thin film from the XPS analysis.	184
Figure 4.17. The O 1s spectra (solid line), O ^I peak (dashed line) and O ^{II} peak (dot line) of XPS with various RF powers.	185
Figure 4.18. The O 1s spectra (solid line), O ^I peak (dashed line) and O ^{II} peak (dot line) of XPS with various $O_2/(Ar+O_2)$ ratios.	186
Figure 4.19. The binding energy (●) and the content of O ^I peak (■) with various $O_2/(Ar+O_2)$ ratios.	187
Figure 4.20. Transmittance spectra of pure ZnO thin films as a function of deposition time under a constant RF power of 100 W in (a) overall region and (b) UV region (280-400 nm).	188
Figure 4.21. Absorption spectra of pure ZnO thin films as a function of deposition time under a constant RF power of 100 W in (a) overall region and (b) UV region (280-400 nm).	189

Figure 4.22. Transmittance spectra of pure ZnO thin films as a function of RF power under a constant thickness of 60 nm in (a) overall region and (b) UV region (280-400 nm). 190

Figure 4.23. Absorption spectra of pure ZnO thin films as a function of RF power under a constant thickness of 60 nm in UV region (280-400 nm). 191

Figure 4.24. Transmittance spectra of ZnO/Glass as a function of deposition time under a constant RF power of 100 W in (a) overall region and (b) UV region (280-400 nm). 192

Figure 4.25. Absorption spectra of ZnO/Glass as a function of deposition time under a constant RF power of 100 W in UV region (280-400 nm). 193

Figure 4.26. Transmittance spectra of ZnO/Glass as a function of RF power under a constant thickness of 60 nm in (a) overall region and (b) UV region (280-400 nm). 194

Figure 4.27. Absorption spectra of ZnO/Glass as a function of RF power under a constant thickness of 60 nm in UV region (280-400 nm). 195

Figure 4.28. Transmittance spectra of pure ZnO thin films as a function of deposition time under a constant O₂/(Ar+O₂) ratio of 0.25. 196

Figure 4.29. Absorption spectra of pure ZnO thin films as a function of deposition time under a constant O₂/(Ar+O₂) ratio of 0.25. 197

Figure 4.30. Transmittance spectra of pure ZnO thin films as a function of $O_2/(Ar+O_2)$ ratio under a constant thickness of 60 nm in (a) overall region and (b) UV region (280-400 nm).	198
Figure 4.31. Absorption spectra of pure ZnO thin films as a function of $O_2/(Ar+O_2)$ ratio under a constant thickness of 60 nm.	199
Figure 4.32. Transmittance spectra of ZnO/Glass as a function of deposition time under a constant $O_2/(Ar+O_2)$ ratio of 0.25.	200
Figure 4.33. Absorption spectra of ZnO/Glass as a function of deposition time under a constant $O_2/(Ar+O_2)$ ratio of 0.25.	201
Figure 4.34. Transmittance spectra of ZnO/Glass as a function of $O_2/(Ar+O_2)$ ratio under a constant thickness of 60 nm.	202
Figure 4.35. Absorption spectra of ZnO/Glass as a function of $O_2/(Ar+O_2)$ ratio under a constant thickness of 60 nm in (a) overall region and (b) UV region (280-400 nm).	203
Figure 4.36. Contact angle image of blank glass substrate.	204
Figure 4.37. Contact angle images of ZnO thin Films under a constant thickness for various RF powers - (a) RF 50 W; (b) RF 100 W; (c) RF 200 W; (d) RF 300 W; (e) RF 400 W.	205

Figure 4.38. Contact angle images of ZnO thin Films under a constant RF power for various deposition time - (a) 5 min.; (b) 10 min.; (c) 20 min.; (d) 30 min.; (e) 60 min.....	206
Figure 4.39. Contact angle images of ZnO thin Films under a constant thickness for various O ₂ /(Ar+O ₂) ratio - (a) 0.10; (b) 0.25; (c) 0.50; (d) 0.75; (e) 1.00.....	207
Figure 4.40. Contact angle images of ZnO thin Films under a constant O ₂ /(Ar+O ₂) ratio for various deposition time - (a) 5 min.; (b) 10 min.; (c) 20 min.; (d) 30 min.; (e) 60 min; (f) 90 min.....	208
Figure 4.41. XRD patterns of ZnO (0002) orientations as a function of annealing temperature is shown by (a) separation and (b) overlap way.....	209
Figure 4.42. The ZnO (0002) diffraction peak shifted as a function of annealing temperature.....	210
Figure 4.43. Effect of grain size and FWHM as a function of annealing temperature.	211
Figure 4.44. Transmittance spectra of pure ZnO thin films as a function of annealing temperature in (a) overall region and (b) near UV edge.....	212
Figure A.1. Step 1 – I - V curve raw data by Langmuir Probe.....	213
Figure A.2. Step 2 – (a) I^2 - V curve and (b) a ion current linear regression fit is fitted in the ion saturation.....	214
Figure A.3. Step 3 – the square root of fitted line to I^2 - V curve in ion saturation.....	215

Figure A.4. Step 4 – the electron I - V curve which consists of an electron current component only. 216

Figure A.5. Step 5 – the natural logarithm of electron current ($\ln(I_e)$) versus probe potential from the electron I - V curve..... 217

Figure A.6. Step 6 – the 1st derivative of I_e - V curve..... 218

Figure A.7. Step 7 – the 2nd derivative of I_e - V curve..... 219

Figure A.8. Step 8 – electron energy distribution function (EEDF)..... 220



Nomenclature

a	Probe Radius
Abs	Absorption
Abs_{ave}	Average Absorption
Abs_{ZnO}	Absorption of ZnO
$Abs_{ZnO/Glass}$	Absorption of ZnO on Glass
A_S	Sheath Area
A_P	Probe Area
B	Full Width at Half Maximum (FWHM)
B_m	Bulk Modulus
c_0	The Speed of Light in Vacuum
c	The Speed of Light in Free Space
C_p	Specific Heat
d	Interplanar (Lattice) Spacing
d_p	Probe Length
d_t	The Thickness of Material
e	Elementary Charge; $e = 1.602 \times 10^{-19}$ Coulomb (1 coulomb = 6.24×10^{18})
E	Energy of Light
E_b	Exciton Binding Energy

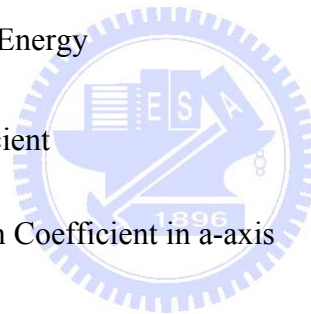


E_{coh}	Cohesive Bandgap
E_g	Energy Bandgap
E_Y	Young's Modulus
F	Potential Function
f_E	Electron Energy Distribution as a Function of Probe Voltage
f_i	Ionicity
h	Planck's Constant; $h = 6.62 \times 10^{-34}$ J·s
H	Hardness
K	Boltzmann Constant; $K = 1.38 \times 10^{-23}$ J/K
k	Constant Dependent on Crystallite Shape
I_0	The Intensity of Incident Light
I_a	The Portion Absorbed of the Incident Light
I_e	Electron Current
$I_{e,Sat}$	Electron Saturation Current
I_i	Ion Current
$I_{i,Sat}$	Ion Saturation Current
I_P	Probe Current
I_r	The Portion Reflected of the Incident Light
I_t	The Finally Transmitted of the Incident Light Through the Materials

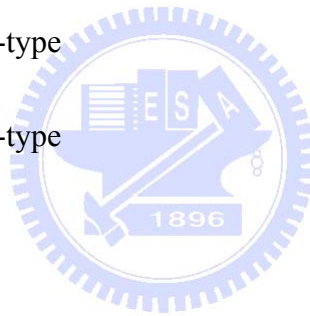
J_r	Particle Current Density
M	Mass
M_e	Electron Mass
M_i	Ion Mass
N	Particle Number Density
n	Refractive Index
n_e	Electron Number Density
n_{es}	Electron Number Density of Sheath
n_i	Ion Number Density
n_{is}	Ion Number Density at Sheath
n_p	Plasma Number Density
n_s	Number Density at Sheath
P	Impact Parameter
R	Reflection
S	Plasma Sheath Radius
S_I	Incident Beam
S_S	Scattered Beam
S_t	Sheath Thickness
$T\%$	Transmittance



T_{ave} %	Average Transmittance
T_e	Electron Temperature
T_{ZnO} %	Transmittance of ZnO
$T_{ZnO/Glass}$ %	Transmittance of ZnO on Glass
u_B	Bohm Velocity
V_f	Floating Potential
V_S	Plasma Potential (Space Potential)
V_P	Probe Potential
$V_S - V_f$	Ion Bombardment Energy
α	Absorption Coefficient
α_a	Thermal Expansion Coefficient in a-axis
α_c	Thermal Expansion Coefficient in c-axis
ϵ_0	Static Dielectric Constant
ϵ_∞	High Frequency Dielectric Constant
κ_c	Thermal Conductivity
ν	The Speed of Light in the Material
ν	The Frequency of Light
v_a	Charge Particle Velocity to Arrive Probe Surface
v_S	Charge Particle Velocity to Arrive Sheath Edge



v_p	Charge Particle Velocity in Plasma
v_r	Radial Velocity
v_ϕ	Azimuthal Velocity
\bar{v}	Mean Speed in Thermal Equilibrium
λ_D	Debye Length
λ_L	Wavelength of Light
λ_M	Mean Free Path
λ_r	Wavelength of Radiation
μ_n	Hall Mobility for n-type
μ_p	Hall Mobility for p-type
θ_B	Bragg's Angle



Chapter 1. Introduction

1.1 Background and Motivation

Nanotechnology has attracted great attention over the past several decades due to the increasing emphasis on convenience, as evidenced in product innovations such as the downscaling of product size, weight reduction, improvement in the operation efficiency of components and decreased costs, etc. In light of this, material science has become more prominent, as it distinguishes the widely varying properties of a material between its macro scale and micro scale. Within this setting, many researchers have investigated the phenomena of various materials in the micro or nano scale and how they apply to various industries [1], such as optoelectronics, mechanical devices, communication, display technology, energy & environment, etc.

Among these research fields, Zinc Oxide (ZnO) is one of the promising candidate materials, and has been extensively investigated for various applications in many fields, including optoelectronics (e.g. light emitting diode (LED) [2-4], laser diodes (LDs) [5], field emission displays (FEDs) [6-7], flat panel displays (FPDs) [7-8], transparent conductive oxides (TCOs) [9-10], solar cells or photovoltaic devices [11-13], photocatalysis [14], and optical waveguides [15]), piezoelectric applications [16-19] (e.g., surface acoustic waves (SAWs) [20], bulk acoustic waves (BAWs) [21], and transducers [22]), sensors [23] (e.g. ultraviolet (UV) detectors [24], photodetector [25],

gas sensor [26]), and glass industry (e.g. heat-reflecting coating [27], architectural windows [28-33]), etc.

Broad applications of ZnO thin film arise from several unique material properties, including a hexagonal wurtzite structure and wide direct band gap at room temperature (RT) which is larger than GaN. In addition, it also exhibits highly efficient UV emission properties resulting from a high exciton binding energy level of 60 meV at RT, which leads to extreme stability of excitons and enables devices to work at a low threshold voltage for optical devices. Furthermore, due to its simultaneously high conductance, high melting point (1975°C), chemical and thermal stability, and high piezoelectric coupling coefficient, ZnO is also an important piezoelectric material for piezoelectric or electronic devices. Additional advantages of ZnO are that [34] (1) it consists of cheap, abundant and non-toxic elements, it can replace tin-doped indium oxide (ITO) elements, (2) it can be coated over a large area; (3) it allows adjusting of the UV absorption or bandgap by doping impurity; (4) it can tolerate reducing chemical environments in a hydrogen plasma [35] because of its high stability; and (5) it can be deposited at a low temperature with different techniques, which allows its growth on flexible substrates for better TCO films. Incidentally, many researchers addresses diverse nanostructures of ZnO [36-37], including one-dimension (such as nanowires [2, 6, 10, 18-19, 38-44], nanotubes [45], nanorods [7, 46-47], nanorings [48], nanocoils [49], nanobelts [50-51],

nanotips [23], nanoneedles [14], etc.), two-dimension (like as thin film [12-14, 52]) and three-dimension (bulk material in general), respectively. It is because of these qualities that ZnO is one of the most interesting semiconductors of II–VI compounds, and maintains broad and significant scientific and technological importance.

1.2 General Properties of Zinc Oxide (ZnO)

ZnO is a hexagonal wurtzite structure with $6mm$ point group symmetry, space group #186 $P6_3mc$ (C_{6v}^4) [53-54] as shown in Fig. 1.1 [55]. According to the Bravais lattice, ZnO is also a hexagonal close-packed (HCP) lattice that is composed of two interpenetrating HCP sublattices of cation (Zn) and anion (O), displayed by the length of the cation-anion bond in the c -direction (see Fig. 1.2). The lattice constants of ZnO structure are $a_1 = a_2 = a_3 = 3.250 \text{ \AA}$ and $c = 5.207 \text{ \AA}$ [35, 55], respectively. ZnO is a compound whose two elements have different ion radii, and the ratio of c -direction to a -direction (c/a) in ZnO is about 1.602. The c/a ratio is slightly smaller than the ideal HCP structure (1.633). The zinc and oxygen crystal surfaces are quite different with regard to their surface energies, deposition rate, etc. The zinc surface has a higher surface energy and faster deposition rate than the oxygen surface. Also, the zinc surface's faster deposition rate causes it to form a steeply inclined pyramidal face [20]. Because of the minimizing surface energy will exhibit on the top surface during the evolution of crystalline morphology. Hence, ZnO tends to grow along the c -axis

orientation normal to substrate, with the crystallographic plane of the lowest free energy parallel to the substrate.

ZnO is also a direct wide bandgap of II-IV semiconductors. Its energy gap is 3.2 eV at RT and 3.44 eV at 4.2 K [56], but its optical bandgap is close to 3.37 eV (300 K; RT) by measuring on the thin film. ZnO films have higher transparency in the visible region because ZnO's optical bandgap is larger than the energy of a visible light wave. The light wavelength of emission of ZnO displays the UV emission (about 370 nm) [57-58]. In addition, it exhibits highly efficient UV emission properties resulting from a large exciton binding energy of 60 meV at RT, which is much larger than other materials such as GaN (28 meV) and ZnSe (19 meV), etc. Based on above advantages, ZnO is also a wonderful piezoelectric material for piezoelectric or electronic devices. For this reason, ZnO remains one of the most interesting semiconductors of II-VI compounds, with many researchers investigating its detail characteristics further. We have organized and summarized several properties of ZnO films list in [Table 1.1](#) to [Table 1.4](#) [4, 35, 37, 59-72].

1.3 Deposition Techniques of ZnO Thin Films

The morphology, structural properties, and physical properties of ZnO thin films depend heavily on deposition conditions and techniques. ZnO thin films have been grown by various deposition methods, such as sputtering [3, 8, 12, 24, 73-89],

metal-organic chemical vapor deposition (MOCVD) [14, 90], molecular beam epitaxy (MBE) [91], plasma enhanced chemical vapor deposition (PECVD) [92], atomic layer deposition (ALD) [93], atomic layer epitaxy (ALE) [94], pulsed laser deposition (PLD) [44, 52, 95-96], chemical bath deposition [97], sol-gel process [43, 98], spray pyrolysis [99], ion beam deposition [100], filtered cathodic vacuum arc technique [32], and vapor phase epitaxy (VPE) [101]. Out of these, the sputtering method is one of the simplest ones that can be used to obtain higher thin film quality (orientation and uniformity) with low growth temperature and even amorphous substrate. Consequently, the mobility of sputtered species on the leading surface is enhanced and the crystallinity is higher at low substrate temperatures. Recently, the radio-frequency (RF) sputtering technique has been developed to insulate oxide films through reactive sputtering and large area deposition. The RF technology exhibits several important advantages of the deposition of oxide films over the conventional DC reactive magnetron sputtering. For instance, it can minimize arcing and improve the properties of films, such as high transparency and conductivity with smooth surface, high deposition rate, high quality, and insulation from oxide material deposition.

In addition, magnetron sputtering offers the important advantage of high density plasma for thin film deposition. Magnetron sputtering produced the magnetic and electric fields to confine the secondary electrons of the plasma in front of the cathode

(target). Because the electrons are significantly influenced by the magnetic field, the high ionization efficiency is achieved. This phenomenon causes the formation of high density plasma when the ionization probability increased. High deposition rate, reduced working pressure, good adhesion of film on the substrate, low substrate temperature, high density of the films and scalability to large areas are additional advantages of magnetron sputtering. Due to the above advantages, RF reactive magnetron sputtering was used in this study.

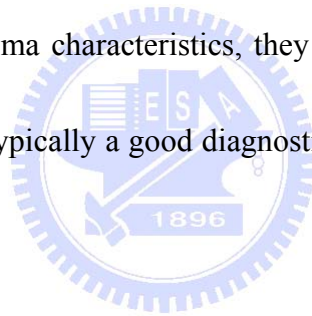
1.4 Importance of Plasma Diagnostics

To interpret the influencing factors of a material, it is imperative to understand the inextricable relationship between deposition conditions and techniques, and the characteristics of microstructures, as described above. Generally speaking, in this study the deposition conditions of sputtering method involve power source (DC, RF), substrate temperature, working pressure, gas flux, gas type (gas ratio), distance between the target and the substrate, substrate rotation, target and substrate types, etc. Unfortunately, all of above deposition conditions affect the plasma characteristics during deposition process. This is because the sputtering technique is based on the plasma. However, the plasma status plays a key role in linking the relationship between the plasma characteristics and the physical properties of the material.

Plasma has taken on increasingly extensive application over the past few decades. In addition to being important in many aspects of our daily lives, plasma is estimated to constitute more than 99 percent of the visible universe [102]. As a result, plasma physics has become one of the major research fields of physics. Understanding the phenomena of plasma permits standard techniques to be applied and interpreted correctly, and also forms the basis of innovation.

Plasma parameters of sputtering process are important conditions to influence both in the deposition processes and investigation of ZnO thin film properties. Therefore, researchers have developed and designed several diagnostics techniques to measure and analyze the plasma during the sputtering. There are various techniques to group diagnostics when studying plasma physics. First, one might divide plasma diagnostics into two possible categories: one is plasma parameter measurements, including the measurement of plasma number density, plasma temperature, plasma potential, and so on; the other one is experimental technique—that which can be learned using several measuring instruments, such as a detector or spectrometer. Therefore, the standard categorization of plasma diagnostics should include classification by magnetic measurement, plasma particle flux measurement, plasma refractive index, electromagnetic emission from free electrons, electromagnetic emission from bound electrons, scattering of electromagnetic wave, natural atom diagnostics, and fast ions

and fusion products [103]. Diagnostic techniques could also be generally divided into *invasive* and *non-invasive* techniques. Microwave diagnostics and optical methods involve non-invasive techniques, like optical emission spectroscopy (OES) [81], laser-induced fluorescence (LIF) [104], laser interferometer [105], or absorption spectroscopy [106], etc. All of these methods generally measure the entire averaged properties of the plasma. On the other hand, the locally plasma diagnostics can be determined by invasive techniques, such as an energy resolved mass spectrometer [107], Langmuir probe [81-85, 104, 107-110] and emissive probe [104]. Although invasive techniques yielded locally plasma characteristics, they also made local perturbation in the plasma. Nonetheless, it is typically a good diagnostics method/tool for investigating plasma phenomena.



Among invasive techniques, the electrostatic probe is the primary technique for measuring the characteristics of plasma. This technique was developed by Langmuir and Mott-Smith [111-117] as early as 1924, and is called Langmuir probe. Based on the electrostatic probe, it consists of a small metallic wire electrode that is immersed into the plasma. The probe is swept a voltage from negative to positive by the external power supply, and is collected the feedback current of inside plasma through the small metallic wire electrode. Based on this characteristic of I - V curve, the detail theory has

been gathered and developed by many scientists [118-124], including F. F. Chen, L. Schott, N. Hershkowitz, etc.

In 1930, Druyvesteyn [125-126] successfully demonstrated that any type of electron energy distribution function (EEDF) could be directly received by the secondary differential of the $I-V$ curve of the probe. Fortunately, the electron energy distribution probability could also be estimated directly by the plasma characteristics. In addition, many scientists [127-128] have demonstrated that the electron velocity distribution does not completely follow the Maxwellian velocity distribution and is not isotropic, especially as demonstrated in low pressure and partial ionization of plasma in 1950s. Johnson and Malter [129-130] developed and designed the double probe in 1949 and Yamamoto [131-132] improved this design to triple probe in 1960. The triple probe measurement coupled the single and double probe measurement to replace the sweeping bias techniques. The development of the above probes led to more selectivity in plasma diagnostics technologies, and more comprehensive applications. To determine plasma characteristics precisely, it is important that the cylindrical and spherical probe be used. For this reason, Laframboise [133] studied the theory of cylindrical and spherical probe. Subsequent scholars frequently quote his results when discussing the investigation and application of the probe. In combination with their contributions, the Langmuir probe and techniques can perform a complete analysis on various modules and theories.

The Langmuir probe has been widely used to understand the plasma physics and phenomena since 1924. Several key plasma characteristics can be acquired based on this technique, including floating potential (V_f), plasma potential (V_s), electron temperature (T_e), electron number density (n_e), and ion number density (n_i), etc. These fundamental plasma characteristics helped us interpret plasma status during sputtering processes and linked the relationship between the plasma characteristics and general physics properties (such as structural, electrical, optical, and chemical, etc.) during thin film growth. At this point, it is an important technology and it helpful to obtain and control the optimal plasma status for enhancing film quality and reproducibility.

1.5 Specific Objectives of the Thesis

Since material properties strongly affect the performance of a device, understanding the influence of deposition conditions with material properties is very important. Many studies have focused on the transmittance of the visible and enhanced hydrophobic characteristics of ZnO film, while almost none have paid attention to simultaneous characteristics of high transmittance in the visible, high absorbance in the UV region, and self-clean capability, which is very important for applications in the glass industry [28]. In this thesis, we have focused on investigating the ZnO thin film effects of RF power, $O_2/(Ar+O_2)$ ratio, annealing temperature, and film thickness on the UV-shielding glasses and films. We also address the relation between deposition rates,

plasma conditions and general physical properties (including structural, optical, and chemical properties) of ZnO thin films. Then we address the construction and diagnosis of the plasma properties of the system, with the objective of simplifying plasma diagnostics in the future.

The organization of the thesis is as follows: it begins by introducing the development and application of II–VI compounds semiconductors of ZnO material; several fundamental principles are then expounded carefully in Chapter 2, including thin film growth mechanism, plasma diagnostics theories, X-ray diffraction and optics principles; the experimental apparatus and measurement methods are described briefly in Chapter 3; the results and discussion are organized and analyzed by theories and experimental data in Chapter 4; Chapter 5 reports the final summary of this thesis and recommendations for future work.

Chapter 2. Basics Theories

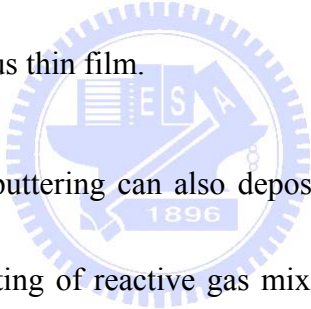
2.1. Thin Film Growth Mechanism

Understanding the thin film growth mechanism is important to interpret the difference between materials by different deposition conditions or techniques. Consequently, brief descriptions of the thin film growth mechanism and deposition processes are contained in the following section. There are three main steps that occur in any thin film growth mechanism: (1) production of the appropriate atomic, molecular, or ionic species; (2) transport of these species to the substrate through a medium; and (3) condensation on the substrate, either directly or via a chemical and/or electrochemical reaction, to form a solid deposit [72, 134]. Figure 2.1 reveals the general scheme of the thin film growth mechanism [72, 135-137], which occurs as follows:

- (a) The species (atomic, molecular, or ionic) lose their velocity component normal to the substrate when they are impacting the substrate. This phenomenon causes them to be physically adsorbed on the substrate surface.
- (b) The adsorbed species migrate to equilibrium position on the substrate surface because of they are in non-thermal equilibrium with substrate at the initial stage. The bigger clusters are forming by their interaction among themselves in this process.

- (c) In general, the clusters are also called the “nuclei”. The nuclei are not thermodynamically stable, and depend on the deposition parameters to desorb from the surface in time. If the cluster collides with other adsorbed species before desorbing, the size of nuclei gradually grows.
- (d) Next, once the cluster reaches a certain critical size, it overcomes the nucleation barrier and becomes thermodynamically stable. The stable chemisorbed and critical-size nuclei are forming in this stage, which is called the nucleation stage.
- (e) The critical nuclei are growing in number and in size until the saturation nucleation density is reached. The number of parameters strongly influences the nucleation density and the average nucleus size, such as the energy of the impinging species, the activation energies of adsorption, thermal diffusion, etc.
- (f) A nucleus can grow both parallel and perpendicular to the substrate by surface diffusion of the adsorbed species and the direct impingement of the incident species, respectively. However, the grown nuclei are called islands.

- (g) The coalescence stage is the stage of thin film formation. The small islands start coalescing with each other to form bigger islands and reducing the surface area, which is a process called agglomeration. Increasing the surface mobility of the adsorbed species can be enhancing the phenomenon of agglomeration.
- (h) The originally thin film structure must undergo the cluster, nucleation, island growth, and coalescence stage. Finally, the thin film structure will reach complete formation in this stage through structural changes from discontinuous islands, porous network type and filling of the channels and holes, resulting in a completely continuous thin film.



Incidentally, the reactive sputtering can also deposit the oxide, nitride and sulfide thin films in a chamber consisting of reactive gas mixed with inert gas. The target of ceramic or metal is able to form these compound thin films. [Figure 2.2](#) illustrates how Holland [138] deduced three possible formation processes in which active gas could combine with metal to form a sputtered gas-metal film. These are (1) at the surface of the target; (2) in the space between the target and the substrate; (3) on the surface of the substrate. Im et al. [139] also found similar phenomena in their work with different oxygen pressures during the PLD process.

2.2. *Fundamentals of Plasma Physics*

Plasma science [112-122, 133, 137-138, 140-147] began in the 1920s with experiments on gas discharges by such noted scientists as Irving Langmuir [118]. Plasma, which is a partially ionized gas consisting of equal numbers of positive and negative charges and a different number of unionized neutral molecules, is also called a “Fourth State of Matter.” More precisely, plasma is a quasi-neutral gas of charged and neutral particles that exhibits collective behavior [137, 140]. In general, laboratory plasma is a weakly ionized plasma discharge, which displays the following qualities: (1) they are driven electrically; (2) they depend on charged particle collisions with neutral gas molecules; (3) there are boundaries at which surface losses are important; (4) ionization of neutrals sustains the plasma in the steady state; and (5) the electrons are not in thermal equilibrium with the ions [141]. An external energy source—such as direct current (DC), alternating current (AC), radio frequency (RF) or microwave (MW) power generator—must supply enough power to ionize and maintain the plasma.

Understanding the phenomenon inside plasma, especially the phenomenon of collisions, is very important to maintaining the plasma. Elastic collisions and inelastic collisions are two kinds of collisions inside plasma. Elastic collisions do not involve energy exchange between the colliding particles, but they are not important to maintain the plasma. Nevertheless, inelastic collisions are significant because there are many

inelastic collisions happening simultaneously in the plasma. This includes collisions between electrons and neutrals, between ions and neutrals, between ions and ions, and between electrons and ions, etc. The following section will describe several critical inelastic collisions, as illustrated in [Table 2.1](#) and [Fig. 2.3](#) [118, 140-141].

In collision ionization, one free electron transfers a portion of its energy to the orbital electron when the free electron collides with an atom or a molecule. When an orbital electron obtains enough energy to leave its orbit and the confinement of the nucleus, it becomes a free electron. This process is called electron-impact ionization by collision. But not every collision generates enough energy for ionization. If the collision provides the orbital electron just enough energy to jump to a higher energy level of orbit, this process is called excitation collision. Nonetheless, this higher energy level of orbit is only stable for a short lifetime. The electron will fall back to the lowest energy level or ground state. This process is called relaxation collision. According to conservation of energy, the excited atom or molecule relaxes to its ground state and releases the extra energy in another form, such as a light emission (photons). When an electron collides with a molecule, the energy is higher than the molecule bonding energy which a molecule breaks the chemical bond causes the free radicals generated. This process is called dissociation collision.

According to Paschen's Law, a plasma discharge can occur only if free electrons accelerated by an electric field gain enough energy between successive collisions with neutral atoms (or molecules) to ionize the atoms. Ionization releases an additional electron which also accelerates, collides with atoms, and causes more ionization. The resulting avalanche leads to a discharge. This behavior is represented by the familiar Paschen curve as shown in Fig. 2.4 [142-143]. The minimum in this curve occurs at the condition where the electronic mean free path is just barely sufficient to allow electrons to gain the ionization energy that the plasma will be generating.

2.3. Principle of Langmuir Probe Diagnostics

A metal probe is one of the earliest and still most useful tools for diagnosing plasma characteristics inside plasma. Metal probes are often used in plasma diagnostics because they are simple and easily constructed. Researchers acquire the electron or ion current, gauging their bias voltage with respect to the plasma potential, while the metal probe is inserted into the plasma. Because these probes are quite small, they produce only minor local perturbations of the plasma. Although probes upset local surroundings of plasma, they can still determine electron temperature (T_e), electron number density (n_e), ion number density (n_i), floating potential (V_f), and plasma potential (V_s) over an extremely wide range of parameters. These metal probes are usually called Langmuir Probe, which were introduced by Langmuir and analyzed in considerable detail by

Mott-Smith and Langmuir (1926) [141]. It is extraordinary that one type of diagnostic, Langmuir probe, has been used to serve the full range of diagnostic roles over such a wide range of plasma densities. Across a broad spectrum of situations, the details of current-voltage (I - V) characteristics can be related to the plasma parameters. The voltage and current of a probe defined in Fig. 2.5 leads to a typical probe I - V characteristic as shown in Fig. 2.6.

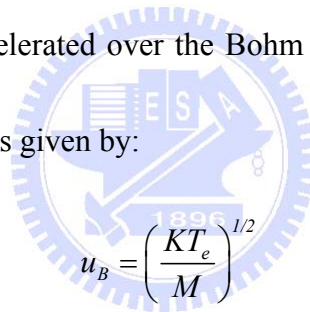
2.3.1. Introduction to I - V Curve

In order to obtain the I - V curve, the probe bias is swept from negative voltage to positive voltage with respect to the ground. Electrons and ions are either attracted or repelled and net current is collected by the probe bias changes. According to this I - V curve, several plasma characteristics are acquired, including plasma number density (n_e , n_i), plasma temperature (T_e), plasma potential (V_f , V_s) and electron energy distribution function (EEDF), respectively. A typical I - V curve can be divided into three regions and two meaningful potential value points [119-122], including: (1) ion saturation region: $V_P < V_f$; (2) transition region: $V_f < V_P < V_s$; (3) electron saturation region: $V_s > V_P$; (4) floating potential: $V_P = V_f$; and (5) plasma potential: $V_P = V_s$, respectively. It should be noted that the measuring current that the probe collects is the summation of the electron current and the ion current, and the magnitude of the ion saturation current is much smaller than the electron current due to its much greater ion mass.

1. Ion saturation Region.

Before measuring the plasma, the probe bias provides a negative voltage to the probe in order to reduce or avoid perturbation of the plasma. The plasma measurement process proceeds until the potential equals the floating potential, which is called the ion saturation region. This is because the main probe bias is negative, causing it to attract most ions or repel most electrons. In the other hands, the number of collective ions is tending saturate state with negative bias increasing. Although many ions can be collected by the Langmuir probe, some cannot. According to the Bohm criterion, the velocity of ions should be accelerated over the Bohm velocity to collect the ion [119,

141, 144]. The Bohm velocity is given by:


$$u_B = \left(\frac{KT_e}{M} \right)^{1/2}$$

(2.1)

2. Transition Region

The $I-V$ curve increases exponentially from the floating potential, then continues until to the plasma potential when none of the electrons are repelled by a negative potential, which is called the transition region. Otherwise, electrons are repelled according to the Boltzmann relation until they reach the floating potential. In this region, the electron temperature can be estimated by the slope of the $(\ln I)-V$ curve. It is a good measure of the electron temperature, and is exactly $1/T_e$ [81-82].

3. Electron Saturation Region

For increasing the probe bias over the plasma potential, the number of collective electrons tends to saturate with positive bias increasing, but almost no ions can be collected in the electron saturation region. The electron sheath forms in the probe surface and the electron current is limited by the thermal motion of electrons arriving to the sheath. The thickness of the sheath would increase with the raising potential in a non-planar probe. The electron saturation current might be a constant in the planar probe, but it is not always a constant, and increases with the raising probe potential in the cylindrical and spherical probes. [Figure 2.7](#) presents the various $I-V$ curve forms in three different probes: planar, cylindrical and spherical probes, respectively [119].

4. Floating Potential (V_f)

When the total collective current of a negative electron and positive ion is equal to zero, $I = 0$, meaning the net current is zero. The point at this moment is called floating potential. The floating potential is sometimes considered to be the ground.

5. Plasma Potential (V_s)

When the probe bias is equal to plasma potential ($V_P = V_s$), the probe and plasma are at the same level. The plasma potential is also called space potential. In this potential, the more mobile electron contributes the main electron because of the positive

current flowing from the probe into the plasma at this moment. If the probe bias is increased over the plasma potential, the saturation of currents will lead electron saturation. This region is called electron saturation region.

2.3.2. Theory of Langmuir Probe

The probe is immersed in the plasma through Langmuir probe. Although its structure is simple, its theory is quite complicated. In order to simplify the probe theory, we must make the following assumptions:

1. The plasma should be uniform and quasi-neutral in the condition without the probe.
2. Electrons and ions must obey Maxwellian velocity distribution.
3. Electron temperature is far higher than ion temperature.
4. The mean free path of electron and ion is far larger than any characteristic length. This means the collisionless is near from the probe.
5. Each charged particle hitting the surface of probe will be neutralized completely and secondary electrons will not occur.

2.3.2.1. Planar Probe with Collisionless Sheath

Based on the basic assumptions above, the probe is immersed in the plasma. The plasma sheath of planar probe is still a plate (one-dimension) due to the geometry of

probe. The plasma sheaths of the cylindrical and spherical probes are two-dimensional and three-dimensional, respectively. [Figure 2.8](#) reveals the different sheath forms with various geometry of probe. Consider a planar probe with the physics probe area $A_P \gg S_t$, where S_t is the sheath thickness, such that the collecting area A_P is essentially independent of S_t . This probe allows the effective collection area of probe A_S to equal the collection area of probe A_P .

In the next two sections, we will discuss electron current and ion current. The first part will focus on electron current. According to the gas dynamics theory, in the thermal equilibrium plasma without perturbation, the particle current density is written by:

$$J_r = \frac{1}{4} N \bar{v} \quad (2.2)$$

where J_r is particle current density, N is particle number density, and \bar{v} is mean speed in thermal equilibrium, also given by:

$$\bar{v} = \left[\frac{8KT}{\pi M} \right]^{1/2} \quad (2.3)$$

Then the electron current I_e can be expressed:

$$I_e = \frac{1}{4} en_e A_S \bar{v}_e \approx \frac{1}{4} en_e A_P \bar{v}_e \quad (2.4)$$

In the electron saturation region, $V_P \geq V_s$, all electrons move into the sheath with thermal equilibrium motion. It causes the electron current to reach saturation state. It can be assumed that the plasma is quasi-natural plasma at the sheath edge, i.e.

$$n_{e\infty} \approx n_{i\infty} \equiv n_{\infty} \quad (2.5)$$

where the number density of electrons, ions and plasma with infinity distance from the probe in the plasma is represented by $n_{e\infty}$, $n_{i\infty}$, and n_{∞} , respectively.

According to Eq. (2.5), the electron saturation current can be rewritten:

$$I_{e,Sat.} = \frac{1}{4} en_{e\infty} A_P \bar{v}_e \approx \frac{1}{4} en_{\infty} A_P \bar{v}_e \quad (2.6)$$

Electrons are repelled by the probe in the ion saturation region and transition region ($V_P < V_S$). Based on previous assumption, electrons and ions must obey the Maxwellian velocity distribution as

$$f(v_e) = n_{e\infty} \left(\frac{2KT_e}{\pi M_e} \right)^{\frac{1}{2}} \exp\left(-\frac{1/2 M_e v_e^2}{KT_e} \right) \quad (2.7)$$

From the Boltzmann relation, the electron number density becomes:

$$n_e = n_{e\infty} \exp\left[\frac{e(V_P - V_S)}{KT_e} \right] \quad (2.8)$$

Therefore, the electron current in the transition region and ion saturation region can be represented as

$$I_e = \frac{1}{4} en_{\infty} \exp\left[\frac{e(V_P - V_S)}{KT_e} \right] A_P \bar{v}_e = I_{e,Sat.} \exp\left[\frac{e(V_P - V_S)}{KT_e} \right] \quad (2.9)$$

Finally, a summary of the electron current derived above is listed as following:

(a). The electron current in electron saturation region: $I_e = I_{e,Sat.}$

(b). The electron current in transition region: $I_e = I_{e,Sat.} \exp\left[\frac{e(V_P - V_S)}{KT_e}\right]$

(c). The electron current in ion saturation region: $I_e = I_{e,Sat.} \exp\left[\frac{e(V_P - V_S)}{KT_e}\right]$

Now we will focus on the ion current. Ions are attracted by the probe during $V_P < V_s$. The analysis of ion current is more complicated than for electron current. This is because ions possess lower temperature, larger mass and far smaller thermal average velocity in thermal equilibrium than electrons. Hence, the Bohm criterion on the ion sheath must be discussed first.

The ion sheath is formed near the probe surface when the probe potential is lower than plasma. The electron number density would decay to shield the electrons from the wall. We deduce that a transition layer or presheath must exist between the neutral plasma and non-neutral sheath in order to maintain the continuity of ion flux, giving rise to an ion velocity at the plasma-sheath edge.

We define the reference electric potential as plasma potential (V_s) and only minor potential difference in the presheath. In addition, the interface between plasma sheath and presheath maintains the assumption of quasi-neutral plasma. Let the ion temperature be zero, based on the cold plasma state. This means the ions are almost stationary with infinity distance from the probe in the plasma.

From the conservation of energy (in collisionless),

$$\frac{1}{2}M_i v_p^2(x) = \frac{1}{2}M_i v_s^2 - eV(x) \quad (2.10)$$

The continuity of ion flux is

$$n_i(x)v_p(x) = n_{is}v_s \quad (2.11)$$

where n_{is} is the ion number density at the sheath edge. The expression of ion number density at sheath can be estimated by the two previous equations (Eq. 2.10 & Eq. 2.11):

$$n_i(x) = n_{is} \left[1 - \frac{2e(V_s - V_p)}{M_i v_s^2} \right]^{\frac{1}{2}} \quad (2.12)$$

From the Boltzmann relation, the electron number density at the sheath is written:

$$n_e(x) = n_{es} \exp \left[\frac{e(V_s - V_p)}{KT_e} \right] \quad (2.13)$$

Setting $n_{es} = n_{is} = n_s$ at the sheath edge and substituting n_i and n_e into Poisson's equation

$$\frac{d^2V}{dx^2} = -\frac{e}{\epsilon_0} [n_i - n_e] \quad (2.14)$$

We obtain

$$\frac{d^2V}{dx^2} = \frac{en_s}{\epsilon_0} \left[\exp \left\{ \frac{e(V_s - V_p)}{KT_e} \right\} - \left\{ 1 - \frac{2e(V_s - V_p)}{M_i v_s^2} \right\}^{\frac{1}{2}} \right] \quad (2.15)$$

Then Eq. (2.15) must be negative due to $n_i > n_e$ at the ion sheath, so

$$\left[1 - \frac{2e(V_s - V_p)}{M_i v_s^2} \right]^{\frac{1}{2}} > \exp \left[\frac{e(V_s - V_p)}{KT_e} \right] \quad (2.16)$$

Eq. (2.16) multiplying by square

$$\exp\left[\frac{2e(V_s - V_p)}{KT_e}\right] > 1 - \frac{2e(V_s - V_p)}{M_i v_s^2} \quad (2.17)$$

and setting $\frac{2e(V_s - V_p)}{KT_e} \ll 1$.

The LHS of Eq. (2.17) can be rewritten by linear expansion

$$LHS(2.17) \approx 1 - \frac{2e(V_s - V_p)}{KT_e} + \dots \quad (2.18)$$

Finally, Eq. (2.17) becomes

$$\begin{aligned} \therefore 1 - \frac{2e(V_s - V_p)}{KT_e} &> 1 - \frac{2e(V_s - V_p)}{M_i v_s^2} \\ \Rightarrow \frac{1}{KT_e} &> \frac{1}{M_i v_s^2} \Rightarrow v_s^2 > \frac{KT_e}{M_i} \Rightarrow v_s > \left(\frac{KT_e}{M_i}\right)^{\frac{1}{2}} \equiv u_B \end{aligned} \quad (2.19)$$

Bohm velocity is a critical velocity and is also a famous criterion called Bohm criterion derived by Langmuir, Bohm, etc. [141, 144-145].

The Bohm criterion, assumes that the probe is biased sufficiently negatively to collect only ion current

$$I_{i,Sat.} = eA_p n_s u_B \quad (2.20)$$

From the Boltzmann relation, the number density at sheath is

$$n_s = n_\infty \exp\left[-\frac{(V_s - V_p)}{T_e}\right] \cong 0.61n_\infty \quad (2.21)$$

Then, the ion current can be obtained [109]

$$I_{i,Sat.} = 0.61eA_p n_\infty \left(\frac{KT_e}{M_i}\right)^{\frac{1}{2}} \quad (2.22)$$

When ion starts to be repelled in the electron saturation region ($V_P > V_s$), the ion current goes to zero rapidly and it can be stated as

$$I_i = I_{i,Sat.} \exp\left[\frac{e(V_s - V_P)}{KT_i}\right] \quad (2.23)$$

Finally, a summary of the ion current derived above can be listed as following:

(d). The electron current in the electron saturation region:

$$I_i = I_{i,Sat.} \exp\left[\frac{e(V_s - V_P)}{KT_i}\right]$$

(e). The electron current in the transition region: $I_i = I_{i,Sat.} = 0.61eA_p n_\infty \left(\frac{KT_e}{M_i}\right)^{1/2}$

(f). The electron current in the ion saturation region: $I_i = I_{i,Sat.} = 0.61eA_p n_\infty \left(\frac{KT_e}{M_i}\right)^{1/2}$

2.3.2.2. Cylindrical Probe with Collisionless Sheath

In the previous section we focused on the planar probe to discuss basic probe theory. However, the planar probe often makes more perturbation in the plasma because of its bigger collection area and worse spatial symmetry. For this reason, the cylindrical [111-117, 120, 133, 141] and spherical probes are usually chosen for plasma diagnostics. The probe tip is made of extremely thin metal wire to decrease perturbation in the plasma. Ideally, we would use the cylindrical probe to most accurately express the characteristics of the plasma.

Under the thick plasma sheath, $(\lambda_D/a) \gg 1$, not all charge particles entering the sheath will directly impact the probe. The charge particles will follow the orbital motion of the attractive central force of the probe into the plasma sheath as shown in Fig. 2.9. This is a theory model of “Orbital Limit-Thick Sheath” and is called “Orbital Motion Limit (OML)” by Langmuir and Mott-Smith (1926). Under the assumption of Orbital Limit-Thick Sheath [119], the collision can be neglected in the plasma sheath by $(\lambda/\lambda_D) \gg 1$. Then setting the probe length d_p far larger than probe radius a as shown in Fig. 2.10. It also assumes only one ion and electron exist in the plasma and only one charge particle is collected in the saturation current region. Consider the orbit of a charge particle in an attractive central forced field. Let its velocity at the sheath edge be v_s , velocity at the probe be v_a , probe radius a , and impact parameter P . Then the conservation of energy

$$\frac{1}{2} M v_s^2 = \frac{1}{2} M v_a^2 + q(V_P - V_s) = \frac{1}{2} M v_a^2 + qV_D \quad (2.24)$$

and conservation of angular momentum,

$$P v_s = a v_a \quad (2.25)$$

Solving for P (if $qV_D < 0$), we have

$$P = a \left(1 + \frac{V_D}{V_0} \right)^{\frac{1}{2}} \quad (2.26)$$

where $-qV_0 = \frac{1}{2} M v_s^2$. When we identify a as the probe radius, any charge particle

with P smaller than that given by Eq. (2.26) will hit the probe and be collected. Hence

the effective collecting radius of the probe is larger than the value of P , and no charge particle can be collected. Therefore, for an isotropic distribution of monoenergetic particles at infinity, the probe current is given by

$$I = 2\pi a d_p j_r \left(1 + \frac{V_D}{V_0} \right)^{\frac{1}{2}} \text{ for Cylindrical Probe} \quad (2.27)$$

$$I = 4\pi a^2 j_r \left(1 + \frac{V_D}{V_0} \right) \text{ for Spherical Probe} \quad (2.28)$$

The electron saturation current increases with the square root of the probe voltage for a cylindrical probe. The current is limited by the impact parameter P and not by the sheath size, which can be infinitely large.

In a more general problem, we must take into account the finite size of the sheath and also the distribution of energies at the sheath edge. First, we use a thin metal wire probe for which the sheath thickness S_t is larger than probe radius a . A given incoming charge particle in the attractive central force of the probe has initial velocity components $-v_r$ and v_ϕ in the radial and azimuthal directions at the edge of the sheath $r=S_t$. At the probe radius $r=a$, the corresponding velocity components are $-v'_r$ and v'_ϕ . For a collisionless sheath we require conservation of energy

$$\frac{1}{2} M (v_{S,r}^2 + v_{S,\phi}^2) = \frac{1}{2} M (v_{a,r}^2 + v_{a,\phi}^2) + qV_D \quad (2.29)$$

and conservation of angular momentum,

$$S_t v_S = a v_a \quad (2.30)$$

Then,

$$v_{a,r}^2 = v_{S,r}^2 + v_{S,\phi}^2 \left(1 - \frac{S_t^2}{a^2}\right) - \frac{2qV_D}{M} \geq 0 \quad (2.31)$$

The charge particle hits the probe when its velocity is $v_{a,r}^2 \geq 0$. Next,

$$v_{S,\phi}^2 \leq \left(v_{S,r}^2 - \frac{2qV_D}{M}\right) \left(1 - \frac{S_t^2}{a^2}\right)^{-1} \equiv v_{S,\phi}^* \quad (2.32)$$

In other words, the charge particle at the sheath edge reaches the probe when its velocity is smaller than $v_{S,\phi}^*$. If the velocity distributions function at sheath edge is $f(v_r, v_\phi)$, therefore

$$j = N \int_0^\infty v_r dv_r \int_{-v_{S,\phi}^*}^{v_{S,\phi}^*} f(v_r, v_\phi) dv_\phi \quad (2.33)$$

Of particular interest is Maxwell's distribution in two dimensions:

$$f(v_r, v_\phi) = \left(\frac{M}{2\pi KT}\right) \exp\left[-\frac{M(v_r^2 + v_\phi^2)}{2KT}\right] \quad (2.34)$$

Substituting Eq. (2.34) into Eq. (2.33) becomes:

$$I = A_a j_r F \quad (2.35)$$

where F is a potential function. Finally,

$$F = \frac{S_t}{a} \operatorname{erf}\left(\Phi^{\frac{1}{2}}\right) + \exp(\eta) \left[1 - \operatorname{erf}\left(\eta + \Phi^{\frac{1}{2}}\right)\right] \text{ for Cylindrical Probe} \quad (2.36)$$

$$F = \frac{S_t^2}{a^2} [1 - \exp(\Phi)] + \exp(-\Phi) \text{ for Spherical Probe} \quad (2.37)$$

where

$$\eta = -\frac{eV_D}{KT} \quad (2.38)$$

$$\Phi = \frac{a^2}{S_t^2 - a^2} \eta \quad (2.39)$$

$$\eta + \Phi = \frac{S_t^2}{S_t^2 - a^2} \eta \quad (2.40)$$

$$\text{erf}(x) = \frac{2}{\sqrt{\pi}} \int_0^x \exp(-t^2) dt \quad (2.41)$$

Now, we will consider two limiting cases: (1) thin sheath limit $\frac{S_t - a}{a} \ll 1$; and (2) thick sheath limit $\frac{S_t - a}{a} \gg 1$. For thin sheath limit, the arguments of the error function are large and we can use the approximation

$$1 - \text{erf}(x) \cong \frac{1}{\sqrt{\pi}} \frac{\exp(-x^2)}{x} \quad (2.42)$$

In addition, for Eq. (2.36), if $\frac{S_t - a}{a} \ll 1$, then $\exp(-\Phi) \rightarrow 0$. Eq. (2.36) and Eq. (2.37) become,

$$F = \frac{S_t}{a} \text{ for Cylindrical Probe} \quad (2.43)$$

$$F = \frac{S_t^2}{a^2} \text{ for Spherical Probe} \quad (2.44)$$

For thick sheath limit, Φ becomes so small that it can be neglected relative to η . The error function for small x is given by $\text{erf}(x) \approx \frac{2}{\sqrt{\pi}} x$ and the exponential by $\exp(-\Phi) \cong 1 - \Phi + \dots$. Thus Eq. (2.36) and Eq. (2.37) become:

$$F \cong \frac{1}{\sqrt{\pi}} \eta^{\frac{1}{2}} + \exp(\eta) \left[1 - \text{erf} \left(\eta^{\frac{1}{2}} \right) \right] \text{ for Cylindrical Probe} \quad (2.45)$$

$$F \cong \eta + 1 \text{ for Spherical Probe} \quad (2.46)$$

In addition, if $\eta \gg 1$. Eq.(2.45) and Eq.(2.42) yield

$$F \cong \frac{2}{\sqrt{\pi}} \left(\eta^{\frac{1}{2}} + \frac{1}{2} \eta^{-\frac{1}{2}} \right) \cong \frac{2}{\sqrt{\pi}} (\eta + 1)^{\frac{1}{2}} \text{ for Cylindrical Probe} \quad (2.47)$$

Thus in large sheath radii, I varies as V for spherical probe, in agreement with Eq. (2.28), while I varies as $V^{\frac{1}{2}}$ for cylindrical probe, in agreement with Eq. (2.27). The latter is true only if $\eta \gg 1$ as well. Note that precise information on the sheath radius is not required in this limit, since Eq. (2.45) and Eq. (2.46) do not depend on sheath thickness.

2.4. Theory of X-Ray Diffraction (XRD)

Over the past several decades, thin films have become an important branch of materials science and technology. Understanding the characterization of structural properties is a very relevant issue in thin film development. Several characterization techniques exist to analyze the thin film properties, such as scanning electron microscopy (SEM), scanning probe microscopy (SPM), auger electron spectroscopy (AES), optical spectroscopy and others. However, many researchers are focus on x-ray diffraction. The suitability of this technique for thin film analysis is based largely on two reasons [148]:

1. The wavelengths of x-rays follow the order of atomic distance in condensed matter, which especially qualifies their use as structural probes.
2. X-ray scattering techniques are non-destructive and leave the investigated sample—or more importantly, the produced device—intact.

In the following section, we will introduce certain basic principles of x-ray diffraction, including Bragg's law and the Scherrer equation.

Bragg's law is one of the most useful and instructive explanations of diffraction from materials. It was proposed by W. H. Bragg and W. L. Bragg in 1913 to describe the position of x-ray scattering peaks in angular space. It relates peak position (the Bragg angle θ), interplanar (lattice) spacing d , and the wavelength of the radiation λ_r . According to Bragg's law, each plane of atoms partially reflects the incident wave much like a mirror. Consider a plane wave incident on rows of period atoms as shown in Fig.

2.11. The vectors S_I and S_S are unit vectors in the direction of the incident beam and the scattered beam, respectively. The first two plane waves of incident beams are scattered, one at point A and the other at point C. These two plane waves are parallel to each other and the angle of incidence of both portions of the incident beam to the atomic planes (hkl) is θ . Likewise, the angle of the scattered beam to the atomic planes is also θ .

According to the Fig. 2.11, two triangles are obtained from the points A, B, C and D. In geometry, the length \overline{AC} is defined as the interplanar spacing d ; the length can then be calculated as $\sin \theta = \overline{BC}/d$. Hence, when the length \overline{BC} is equal to the length \overline{CD} , they are defined as $\overline{BC} = \overline{CD} = d \sin \theta$. Due to constructive interference, the amplitudes of the plane waves will reinforce when the difference in the path lengths of the two interfering waves is equal to a whole number of wavelengths. This path length

difference is equal to $\overline{BC} + \overline{CD} = 2d \sin \theta$. Finally, the overall condition for reinforcement and Bragg's law is written [149-151]:

$$2d \sin \theta = n\lambda \quad (2.48)$$

where n is an integer. Bragg's law is important in wavelength dispersive spectrometry, since by using a crystal of fixed $2d$, each unique wavelength will be diffracted at a unique diffraction angle (Bragg angle) [151].

Next, the Scherrer equation is used frequently in x-ray analysis, particularly for calculating the grain size (crystallite size or particle size) that we are interested in. The breadth of the diffraction peak can be altered by the size of the scattering unit and the variation of interplanar (lattice) spacings. The broadening of the interference function causes a small number of atoms—diffracting as a unit from a particle, grain, or subgrain—to produce grain size broadening. Hence, in Fig. 2.12, the full-width at half-maximum (FWHM) of diffraction peak broadened by this concept is derived approximately by the Scherrer equation [32, 78-80, 85-87, 98, 149-150]:

$$D = \frac{k\lambda_r}{B \cos \theta_B} \quad (2.49)$$

where D is the grain size; λ_r is the wavelength of the x-rays used; θ_B is the Bragg diffraction angle; B is the FWHM; and k is a constant. It is worth noting that the constant k has been determined to change from 0.89 to 1.39 [150]. In this work, the value of k is 0.9.

2.5. Theory of Optics

Optoelectronic or optical materials have played a key role in many technologies related to science, engineering, and industry, just to name a few. The purpose of this section is to review a summary of the fundamental principles that have guided the applications of optical materials. We will review several of the basic and important optical properties in the following section.

Wide-range optical properties have been observed in solid state materials and classified into a small number of general phenomena. A light incident upon the front of a medium causes several general phenomena including reflection, propagation and transmission as shown in Fig. 2.13 [152]. Light is a critical matter in optics in which energy (radiation) is emitted from a material in the form of waves or particles called photons. It corresponds to the electromagnetic radiation in the narrow band of frequencies from 3.84×10^{14} Hz to roughly 7.69×10^{14} Hz (see Table 2.1) [153]. The important characteristics of the photons – their energy E , wavelength λ_L , and frequency ν – are expressed by the equation

$$E = h\nu = \frac{hc}{\lambda_L} \quad (2.50)$$

where c is the speed of light (in a vacuum the speed c_0 is 3×10^{10} cm/s) and h is Planck's constant (6.62×10^{-34} J·s) [154]. Figure 2.14 presents the spectrum of electromagnetic radiation. Gamma and x-rays have a very short wavelength, a high

frequency, and possess very high energies; in contrast, microwaves and radio waves have very low energies. But visible light exhibits a very narrow region of the electromagnetic spectrum. Additionally, several bandgaps (E_g) of semiconductors correspond to wavelengths of light, as Fig. 2.14 shows.

Photons are able to induce a number of optical phenomena when they interact with the electronic or crystal structure of material (see Fig. 2.15). Therefore, we need several quantified parameters to determine the optical phenomena of the material. According to Fig. 2.15, the intensity of incident light I_0 may be partly reflected, partly absorbed, and partly transmitted. The intensity of the incident beam therefore can be expressed as


$$I_0 = I_r + I_a + I_t \quad (2.51)$$

where I_r is the portion of the incident light that is reflected, I_a is the portion that is absorbed, and I_t is the portion finally transmitted through the material.

Reflection occurs when photons contact the surface of a material and identical energy is immediately emitted from the surface of the material. It is defined as the ratio of the reflected power to the power incident on the surface of the material, and is described by the *coefficient of reflection* or *reflectivity* in which it is usually given the symbol R . *Absorption* occurs when a photon releases its energy into the material. The *absorption coefficient* (α) is defined as the fraction of the power absorbed in a unit length of the material by [74, 86, 154]:

$$I = I_0 \exp(-\alpha d_t) \quad (2.52)$$

where I is the intensity of transmitted light when it reaches the back surface, I_0 is the intensity of incident light after reflection at the front surface, and d_t is the thickness of the material. Finally, *transmission* occurs when photons pass through the material without interacting with the electronic or crystal structure. The *coefficient of transmission* or *transmittance* (T) is defined analogous to the ratio of the transmitted power to the incident power. Furthermore, I/I_0 is defined as the transmittance (T), and derives the absorbance coefficient (α) from Eq. (2.3) [74],

$$\alpha = -\frac{\ln(I/I_0)}{d_t} = -\frac{\ln(T)}{d_t} \quad (2.53)$$

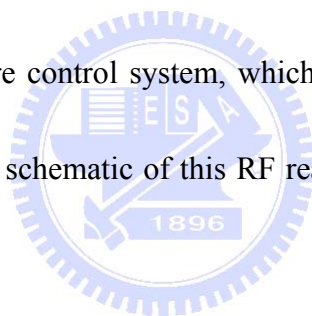
Even in transmission, refraction causes the photons to change velocity less than in free space, leading to the bending of light rays. Hence, the *refractive index* (n) is defined as the ratio of the speed of light in free space (c) to the speed of light in the material (v) according to:

$$n = \frac{c}{v} \quad (2.54)$$

Chapter 3. Experimental Methods

3.1. Experimental Apparatus

Figure 3.1 displays the configuration of the RF magnetron reactive sputtering system. This sputtering chamber facilitates a plasma generator (13.56 MHz RF plasma generator and automatic matching network), a target holder at the bottom under which a set of permanent magnets are installed, a temperature controller system controlled substrate holder with lamp-type heaters in the back, mass flow controller (MFC), pressure gauges (thermocouple gauge and ion gauge), a mechanical roughing pump, a cryogenic pump, and a pressure control system, which is used to control the chamber pressure to a preset value. The schematic of this RF reactive magnetron sputter system is shown in Fig. 3.2.



3.1.1. RF Reactive Magnetron Sputtering Chamber

3.1.1.1. RF Power Subsystem

Figure 3.3 shows the RF power system, which includes the RF plasma generator and automatic matching network, respectively. The RF plasma generator is a Model GHW-12 (ENI. Inc.) and the type of automatic matching network is Model MW-10D (ENI. Inc.). The RF plasma generator is operating at the radio frequency of 13.56 MHz and producing 1250 W of maximum power into a 50 ohm load. The forward RF power and reflected RF power maintain a constant power output within $\pm 2\%$ of the set point

over a dynamic power range of 0 to 1250 W by the DSP-based control module. A new 9-pin digital interface provides remote control, monitoring and diagnostic capability via the RS-233 serial link to a computer or host terminal. In addition, the automatic matching network is an automatic impedance matching network designed to interface with the ENI 13.56 MHz RF plasma generator to obtain plasma. The MW-10D includes two separate assemblies, such as a tuner unit and a controller unit. The tuner unit contains the matching network whose output impedance is varied by two motor-controller capacitors and a fixed inductor. The controller unit drives the tuner motors in response to signals on the remote interface or RF sensors in the tuner unit. In order to improve accuracy and tuning precision, the MW-10D uses a microprocessor-based control circuit. These two instruments can generate and maintain the plasma easier for sputtering processes.

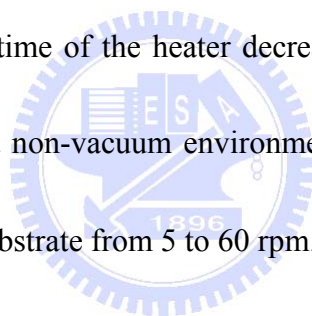
3.1.1.2. The Magnetron Subsystem

The top and side view of the magnetron system is shown in [Fig. 3.4](#). This magnetron system is constructed from a magnet assembly consisting of an iron plate (with a diameter of 8.3 cm) on which is mounted a series of magnets ($1.1 \times 0.6 \times 2.6$ cm) with the entire assembly mounted vertically under the target. It is therefore able to provide the magnetic field for confining the secondary electron motion to enhance the plasma density. The magnetic field strength was measured by the Lakeshore 421

Gaussmeter. This gaussmeter indicated a maximum perpendicular magnetic field of 350 G from the target surface along the center line and a maximum parallel magnetic field of 220 G from the substrate at 2.2 cm along the center line.

3.1.1.3. The Temperature Control Subsystem

The temperature was controlled by a temperature controller system (Model UP150, Yokogawa M&C Corporation) as shown in Fig. 3.5. This temperature controller was a heated substrate holder with lamp-type heaters in the back and a PID temperature controller. The quartz lamp heater is used in a vacuum environment. The maximum temperature is 800°C. The lifetime of the heater decreases when the temperature rises over 800°C or is operated in a non-vacuum environment. The controller panel can be used to adjust the rotation of substrate from 5 to 60 rpm.



3.1.1.4. Mass Flow Control Subsystem

Fig. 3.6 illustrates how mass flow rates of argon or mixture gases are controlled by mass flow controllers (MFC). It consists of a thermal mass flow sensor, a rapidly acting valve, and an electronic control system, such as the Protec PC-540, featuring a multi-channel mass flow control by Sierra Instruments Inc. The purpose of the mass flow controller is to maintain a constant, operator-set flow. The maximum mass flow is 100sccm (standard cubic centimeters per minute). This system provides four channels for the simultaneous mixture of various gases.

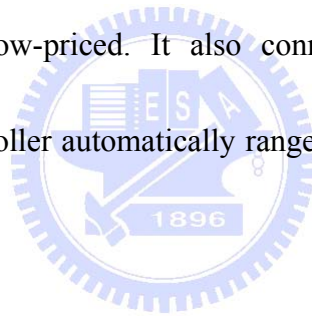
3.1.1.5. Pumping Subsystem

The chamber is facilitated with a mechanical pump for obtaining low vacuum and a cryogenic pump for maintaining high vacuum as shown in Fig. 3.7(a) and Fig. 3.7(b), respectively. The *rotary vane pump* (mechanical pump) is an oil-sealed pump commercially available to pump gas with a pressure range of 760 torr – 10^{-3} torr. A *cryogenic pump* captures molecules on a cooled surface by weak Van der Waals or dispersion forces. It is used in a wide range of applications and in many forms. Liquid nitrogen or liquid helium “cold fingers” are used in the high vacuum chamber. Liquid cryogenics or closed-cycle helium gas refrigerators are used to cool high- and ultra-high-vacuum cryogenic pumps [155]. The cryogenic pump model U-6H (ULVAC Technologies, Inc.) operated at a pressure range from 10^{-3} torr to 10^{-10} torr.

3.1.1.6. Pressure Control Subsystem and Gauge Meter Components

The MKS pressure controller, along with the ionization and low vacuum gauge controller, are the pressure control systems in our laboratory. The MKS Type 651C pressure controller (MKS Instruments, Inc.) is a self-tuning pressure controller for throttle valves as shown in Fig. 3.8. This system takes into account time constants, transfer functions of the valve and plumbing, valve gain, pump speed, and many other important parameters when determining the system characteristics. The default window display on the front panel exhibits the pressure readout and the valve position (% open).

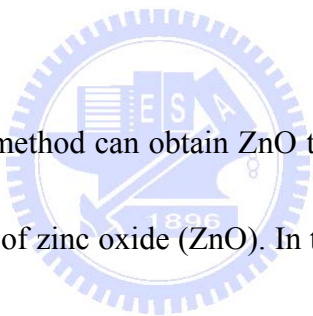
The pressure readout can be displayed in units of Torr, mTorr, mbar, μ bar, Pascal, or kPa. There are five reprogrammable set points provided, each one having the option of being set up for pressure or position control. Valve open, close, and stop functions are also provided on the front panel for use in system setup and diagnostics. The ionization and low vacuum gauge controller (Terranova Model 934) (see [Fig. 3.9](#)) provides pressure measurements across a broad range of vacuum environments. This system has the simultaneous advantageous of easy usability, an intuitive front panel and a large, bright, digital display. And because most of the needed features are built-in, this controller is comparatively low-priced. It also connects with the ion gauge and low-vacuum gauge. This controller automatically ranges throughout its operating range of 1 torr to 10^{-11} torr.



There are three additional pressure gauges in our sputtering system, including a Baratron capacitance manometer, thermocouple gauge and ion gauge. [Figure 3.10](#) exhibits the type 127 Baratron capacitance manometer (MKS Instruments, Inc.). A *capacitance manometer* is simply a diaphragm gauge in which the deflection of the diaphragm is measured by observing the change in capacitance between it and a fixed counterelectrode [155]. This capacitance manometer is able to detect the range of pressure from 10^{-3} torr to 10^{-1} torr. The *thermocouple gauge* measures pressure-dependent heat flow, as shown in [Fig. 3.11](#). It is generally used in a

low-vacuum environmental with an operating range of pressure from 10^{-3} torr to 999 torr. The *ion gauge*, also called the Bayard-Alpert ion gauge, is shown in Fig. 3.12. It generally operates in the high and ultrahigh vacuum region, because extremely small particle density makes it almost impossible to operate. However, in the region below 7.5×10^{-3} torr, pressure is measured by ionization gases. Hence, each ion gauge has its own lower pressure limit at which the ionized particle current is equal to a residual or background current. The ion gauge of our laboratory normally operated in the high vacuum region with a background limit from 10^{-3} torr to 2×10^{-10} torr.

3.1.1.7. Target and Gases

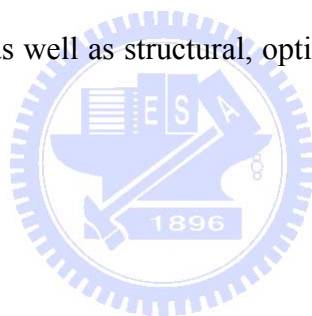


In general, the sputtering method can obtain ZnO thin film by using a metal target of zinc (Zn) and ceramic target of zinc oxide (ZnO). In this study, we introduced the Zn metal target to grow ZnO thin film, because the Zn metal target has several advantages over the ZnO ceramic target. The advantages are: (1) the metal target is much purer than the ceramic target; (2) it has the best cooling efficiency because of its higher thermal conductivity; and (3) the metal target is cheaper than the compound ZnO ceramic target. We determined that the purity of the Zn target is 99.999% (5N) with a 4 inch in diameter and 0.25 inch in thickness (Sinoxp Materials Company). The Zn target has 3 mm thickness of Zn bond, and a 3 mm thickness of copper (Cu) plate on the bottom side. A typical reactive sputtering system is composed of a metallic target with working

(discharge)/reactive gas species. Essentially, the working (discharge) and reactive gas are argon (Ar) and oxygen (O₂), respectively. The atoms of reactive gas will combine with the sputtered atoms from the target to form the compound film of ZnO on the substrate. In this study, the purity of Ar and O₂ are both 99.999%. In order to obtain the ZnO films, these two gases are mixed prior to entering the sputtering chamber with a predetermined ratio in volume flow rate.

3.2. Experimental Instrumentation

There are four main kinds of experimental instrumentation in the following section, including plasma diagnostics, as well as structural, optical, and chemical characteristics and techniques, respectively.



3.2.1. Plasma Diagnostics

In the following section, we will be describing the operating limits, types, and measurement methods of the Langmuir probe system.

3.2.1.1. Langmuir Probe System

The configuration and schematic of a standard ESP analysis system with motorized Z-motion drive (Langmuir probe system) are displayed in [Fig. 3.13](#) and [Fig. 3.14](#), respectively. A complete Langmuir probe system comprises an ESPION Probe Unit (EPIU), a linear motion driver, a gas-cooled RF compensated electrostatic plasma probe, and all the required interconnection cabling. This Langmuir probe system is a

cylindrical type made by Hiden Analytical Inc. (Model: Hiden ESPion). The configuration of a cylindrical probe includes an RF-compensation electrode and probe tip (see Fig. 3.15). All of these components of the cylindrical probe are made from insulator material except for the probe tip. The purpose of the insulator material is to decrease perturbation of the plasma. Figure 3.15(b) shows the connector pin, metal ferrule, ceramic tube and tip wire. The probe tip (whose dimensions appear in Fig. 3.15(c)) also plays a key role in plasma diagnostics by reducing perturbation. It is made of tungsten, and is 10 mm in length and 0.15 mm in diameter, with an estimated effective collection area of about 4.7 mm². The probe tip was placed in the plasma bulk region, 2 cm from the substrate along the center line (see Fig. 3.2). This standard Langmuir probe system has a probe current and tip voltage range of 1 mA to 1 A and of -200 V to 100 V, respectively. It is also suitable to operate with both DC and RF plasmas when using various compensation electrodes. The maximum allowable temperatures at the probe and at the mounting flange are 250°C and 70°C, respectively. If the plasma diagnostics are measured at high temperature, a cooling gas inlet is provided to force the probe compensation components to cool. Hiden Analytical Inc. suggests that the cooling gas (such as air, nitrogen, argon, etc.) may be used at a recommended pressure between 150 torr and 525 torr (3 psi to 10 psi). An automatic motor-driven Z-motion driver is an available option for the Langmuir probe system (see Fig. 3.17). A computer-controlled

stepped motor, with maximum movement of 300mm, powers the automatic Z-motion driver. The stepped motor is controlled by the PC via the EPIU and the Linear Motion Driver as shown in Fig. 3.14. A lead screw drives the probe into the chamber; vacuum sealing is provided by the flexible bellows unit.

3.2.2. Structural Characterization Techniques

In the following section, we will describe the operating limits, types, and measurement methods of surface profile and x-ray diffraction, respectively.

3.2.2.1. Surface Profilometer (α -step)

In Fig. 3.18, film thickness was measured by a surface profilometer (Model 3030, Sloan Dektak Inc.). This is a simple, rapid, and convenient measurement method for obtaining film thickness or surface roughness degree. The measurement range is from 50 Å to 1310 KÅ with a maximum of vertical and horizontal resolution of 1 Å and 0.025 μm (250 Å), respectively. The scan length range is from 50 μm to 50 mm.

3.2.2.2. X-Ray Diffractometry (XRD)

Crystal structure and the degree of preferred orientation of ZnO thin films was determined by X-ray diffraction (XRD) technique (Model: PANalytical X'Pert Pro (MRD), Philips X'Pert Inc.) as shown in Fig. 3.19. Figure 3.20 shows the goniometer, an instrument that consists of an x-ray tube, primary optics, MRD candle, secondary optics, and a detector. The x-ray source used in the X'Pert Pro MRD is a ceramic

filament tube with a copper (Cu) target (anode) using $\text{CuK}\alpha$ radiation ($\lambda=1.5418 \text{ \AA}$).

The detector converts the received x-ray photons into electrical pulses that are individually counted [33]. The unit of counts—counts per second (cps)—is employed for measuring the intensity scattered by the sample. The angular resolution for the instrument is around 0.001° . This instrument was operated at 45 kV and 40 mA. In the present study, two types of XRD scans were performed on different samples: the Gonio scan and GIXRD scan. The Gonio scan is the most commonly used technique for measuring the Bragg reflection of a thin film, and is also called the θ - 2θ scan. The Gonio scan analyzes position, shape, intensity, etc., in order to determine the microstructure information of material. In the GIXRD (grazing incidence x-ray diffraction) scan, the primary beam enters the sample at very small angles of incidence. It is also called the ω - 2θ scan. The angle between the incidence beam and the sample surface is very small and amounts to only a few degrees or even less (in general, $1^\circ\sim 6^\circ$).

The x-ray path travels a small entrance angle is increased the significantly and the structural information. The simple diagram of these two measured techniques is presented in [Fig. 3.21](#).

3.2.3. Chemical Characterization Techniques

In the following section, we will describe the system and operating limits of X-ray Photoelectron Spectroscopy (XPS).

3.2.3.1. X-ray Photoelectron Spectroscopy (XPS)

The composition and chemical state of ZnO thin film was studied with X-ray Photoelectron Spectroscopy (XPS) (Model: VG Scientific Microlab 310F). XPS, also called Electron Spectroscopy for Chemical Analysis (ESCA), is the most widely used surface analysis technique because of its relative simplicity in use and data interpretation. Its element detection range spans from Li to U (atomic number: 3~92). This instrument is based on vacuum systems designed to operate in the ultra-high vacuum (UHV) range of $\sim 10^{-9}$ torr [156]. The UHV environment is necessary because of the surface sensitivity of the techniques themselves and the contamination reduction of sample surfaces by absorbed residual gas molecules [157-158]. The maximum specimen size limit is 1 cm \times 1 cm and the thickness is lower than 0.5 cm. X-rays are generated by bombarding an anode material with high energy electrons from a heated filament [158]. In this instrument, the X-ray source was made by twin anode X-rays, MgK α (1253.6 eV) and AlK α (1486.6 eV). (Aluminum target was used in this study). The electron gun resolution is 15 nm at 25 keV using the Schottky Field Emission Source. In addition, the electron energy analyser measures the energy distribution of

electrons emitted from the specimen. Here it uses a Concentric Hemispherical Analyzer (CHA) mode and its resolution is 0.02% ~2%. However, XPS is suitable for analysis of surface chemical characteristics because it can simultaneously identify the chemical state of various elements. Eventually, we employed this instrument to detect the composition and chemical state of ZnO thin film.

3.2.4. Optical Characterization Techniques

In the following section, we will describe the operating limits, types, and measurement methods of ultraviolet-visible (UV-VIS) spectroscopy.

3.2.4.1. Ultraviolet-Visible Spectrophotometer (UV-VIS Spectrophotometer)

[Figure 3.22](#) presents a measurement of transmittance and absorption of the ZnO thin film, carried out using a UV-VIS spectrophotometer (Shimadzu Inc., Model UV-2501PC). The system consists of an intelligent photometer unit, IBM PC/AT compatible series of personal computers, and the UVPC Personal Spectroscopy Software package. Data are acquired through three basic modes: wavelength scanning, quantitative (Single Wavelength), and time scanning, with the software controlling all acquisition parameters and storage formats. In the light source compartment, a halogen lamp is built in for visible region, and a deuterium lamp for UV region. The scanning region of UV-VIS spectrophotometer is from 190 nm to 1100 nm, but the effective scanning region is from 190 nm to 900 nm. The light source switching wavelength is

selectable from 282~393 nm. However, the spectra of transmittance and absorption are obtained by the UV-VIS spectrophotometer.

3.2.5. Hydrophobic/Hydrophilic Characterization Techniques

In the following section, we will describe the operating limits, types, and measurement methods of the contact angle system.

3.2.5.1. Contact Angle System

In Fig. 3.23, the surface characteristics of the contact angle were recorded by a contact angle system with a universal surface tester (Model GH-100, KRÜSS Inc.), which can measure contact angle and surface energy. The system consists of an automatic sample positioning system for process control, PC-controlled motor-driven zoom and focus, 2/3" CCD camera, illumination unit and process measuring head. Four kinds of liquids can be used for analyzing the surface energy of materials. Water (H₂O), Diiodo Methane, and Ethylene Glycol are always provided in the first three needles and the last one is a standby for special cases. The system has three different measurement modes, including static mode, advance mode, and recede mode. The measuring range of the contact angle system is from 2° to 175° and the resolution is 0.1°. However, we are solely interested in the surface characteristic of contact angle degree in present study.

Chapter 4. Results and Discussion

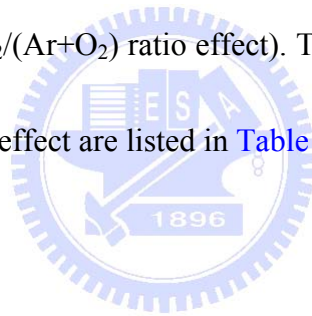
4.1. Summary of Test Conditions

In this study, we try to clarify the critical influence for the multi-function ZnO thin film by examining relationship between deposition (plasma) parameters and material properties during the ZnO thin film growth on glass substrate by RF reactive magnetron sputtering. A 4-inch diameter Zn target (99.999%) is used. Argon (99.999%) and oxygen (99.999%) are employed as the working (discharge) and reactive gas, respectively. These two gases are mixed prior to entering the sputtering chamber with a predetermined ratio in mass flow rate. Distance between the target and substrate is kept as 8 cm unless otherwise specified. The normal procedures of operating the sputtering system include: 1) Evacuate the chamber to a base pressure below 1.0×10^{-4} Pa (8.0×10^{-7} torr) through roughing and cryo pumps; 2) Send the mixed argon-oxygen gas through the chamber for 10 minutes while maintaining the chamber pressure at 2 Pa (15 mtorr); 3) Pre-sputter the chamber for 20 minutes, which removes any possible contamination or oxides from the Zn target surface.

Firstly, for influence of various RF power (a constant $O_2/(Ar+O_2)$ ratio of 0.5), two major test conditions for preparing ZnO thin film include: 1) Deposition time ranges from 5 to 60 min. with a constant RF power of 100 W (for thickness effect at fixed RF power); 2) RF power ranges from 50 to 400 W with a constant film thickness of 60 nm

(for power effect). The detail test conditions of these two cases for RF power effect are listed in [Table 4.1](#) and [Table 4.2](#), respectively. At the same time, we also used the Langmuir probe to acquire plasma characteristics at the substrate center during the deposition process.

Secondly, to measure the influence of various $O_2/(Ar+O_2)$ ratio (a constant RF power of 100 W), two major test conditions for preparing ZnO thin film include: (1) Deposition time ranges from 5 to 60 min. with a constant $O_2/(Ar+O_2)$ ratio at 0.25 (for thickness effect at fixed gas ratio); (2) Gas ratio ranges from 0.1 to 1.0 with a constant film thickness of 60 nm (for $O_2/(Ar+O_2)$ ratio effect). The detail test conditions of these two cases for $O_2/(Ar+O_2)$ ratio effect are listed in [Table 4.3](#) and [Table 4.4](#), respectively.



4.2. Plasma Characteristics

4.2.1. Effect of RF Power

[Figure 4.1](#) illustrates the deposition rate of ZnO thin film as a function of applied RF power. In general, the deposition rate increases nearly linearly with increasing RF power [80-81, 85-87, 159-160]. Increasing RF power increases the plasma number density in the bulk and ion bombardment energy onto the Zn target by increasing the ionization probability and the ion impact target surface probability, which sputters more Zn or ZnO particles into the plasma. More ZnO particles are thus formed by reacting with atomic oxygen in the discharge, and in turn, the deposition rate becomes larger.

To explain the argument, we must note that in this study the typical I - V curve was measured by the Langmuir probe. The detail analysis process is reported in Appendix A. The floating potential (V_f) and plasma potential (V_s) were determined from the I - V curve as shown in Fig. 4.2. The ion bombardment energy ($V_s - V_f$) of sputtered particles bombarding the substrate is estimated by the difference between plasma potential and floating potential [81-82, 108], as a function of applied RF power, as shown in Fig. 4.3. Due to RF power increasing, the input voltage and current were increased. Hence, the particles were able to obtain higher energy for the ionization process by absorbing the input voltage and current. For this reason, it was possible to observe that the floating potential has only slight increases with increasing RF power, but plasma potential and ion bombardment energy have more obvious increases.

Therefore, the moderation ion bombardment energy is likely to increase the surface mobility of adatoms and lead to the formation of dense layers during the deposition process [81]. Furthermore, the RF power increased with process temperature during deposition process. Then the higher process temperature induced the worse vacuum (high pressure). In order to maintain the constant working pressure, the pumping speed of the cryogenic pump was increased. Compared with low process temperature, particle concentration was decreased, but the mean free path (MFP) was increased. Meanwhile, particle energy dispersion was reduced with less collision probability and the

probability of impact substrate was increased. However, $(V_s - V_f)$ generally increases with increasing applied RF power, except in the case with the applied power of 50W. Influence of increasing $(V_s - V_f)$ has three stages. First, more Zn atoms or ZnO particles are sputtered into the plasma bulk, and thus more ZnO particles are formed, because the ions bombard the target with higher impact energy. This causes the increase of deposition rate, as presented earlier. Second, it is highly likely that the energetic ions which bombard the substrate cause the substrate temperature to rise substantially at where they bombard. This in turn enhances the local surface mobility of adatoms and thus produces larger-grain ZnO layers during the deposition process [84]. Third, electrons obtain higher energy through the acceleration in the sheath with increasing $(V_s - V_f)$. These higher-temperature electrons will enhance the ionization in the plasma bulk, which further increases the plasma number density, as shown in Fig. 4.4.

For this reason, electron temperature increases from 2.8 eV (at 50 W) to 4.2 eV (at 400 W), which is normal in highly vacuum sputtering plasmas. It should be noted that the increase of electron temperature from applied power of 50 W to 100 W becomes minimal due to the slightly decrease of $(V_s - V_f)$.

Incidentally, Fig. 4.4 also indicated that electron number density (n_e) and ion number density (n_i) increase with RF power. Ion number density increases from $3.03 \times 10^{17} \text{ \#/m}^3$ (at 50 W) to $6.15 \times 10^{17} \text{ \#/m}^3$ (at 400 W), while electron number

density increases from $9.28 \times 10^{16} \text{ \#/m}^3$ at 50W to $3.25 \times 10^{17} \text{ \#/m}^3$ at 400 W.

Otherwise, ion flux could be calculated by following simple plasma theory:

$$Ion\ Flux = n_i \sqrt{\frac{KT_e}{m_i}} \quad (4.1)$$

Therefore, the calculation of ion flux is approximate to our analysis data because ion flux is proportional to ion number density. This is because greater ion number density will generate more atoms from the target, which then makes ion flux increase. In addition, the deposition rate increases about 11 times from 50 W to 400 W by this study (see Fig. 4.1). However, ion flux and ion number density only added about 2 times at the same condition, meaning that the amount of atoms deposited onto substrate increases when RF power increases. Therefore, we deduced that the sputtering yield (γ_{sput}) might increase 5.5 times because it is defined as the number of target atoms ejected per incident ion [137]. Furthermore, we also drew a relation figure between ion flux and deposition rate as shown in Fig. 4.5. Results reveal that ion flux and deposition rate present a linear relationship when RF power increases. Actually, we believed that the sputtering yield multiplication of the ion flux should be equal to the deposition rate [141]. Likewise, note that

$$\frac{D.R.}{Ion\ Flux} \propto \gamma_{sput} \quad (4.2)$$

In other words, we conjectured that the sputtering yield increases 5.5 times while the RF power changed from 50 W to 400 W.

In order to explain this phenomenon, we used a simple plasma hypothesis. In general, ion number density and potential (DC bias of target) increase $\sqrt{2}$ times when the power becomes 2 times for capacitively coupled plasma (CCP) type. Here, ion number density and potential (DC bias of target) could be assumed to be current (I) and voltage (V), respectively. Electrical power is calculated using Joule's law:

$$P = I \cdot V \quad (4.3)$$

In this study, power and current (meaning ion number density) are equal to 8 (from 50 W to 400 W) and 2 (see Fig. 4.4), respectively. According to Joule's law, we knew that the voltage increases 4 times. This means that the bombardment energy near sheath also increases. These results indicated the power increases not only increase ion number density, but also the potential of the bombardment target. Owing to the potential means of the capability of the bombardment target, the voltage increases accompany with sputtering yield increasing. Consequently, we thought that the sputtering yield increase of 5.5 times was reasonable, although ion number density only promoted to 2 times.

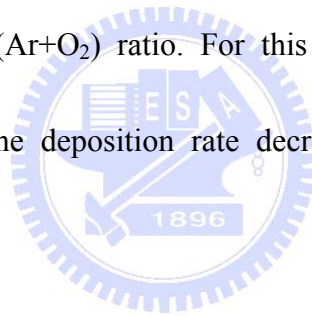
Due to this result, there is enough evidence to show that the RF power might enhance the number of particles that arrives at the substrate, so the deposition rate also increases during the sputtering process (see Fig. 4.1). Additionally, oxygen might produce negative charge particles (O^- , O_2^-) in the plasma environment, called negative plasma; hence the electron number density is not equal to ion number density. For pure

argon plasma, electron number density should be nearly equal to ion number density. This is because the electron number density is defined by electron saturation in the I - V curve region of the Langmuir probe. When positive voltage was applied to the probe tip, it collected the negative charge and repelled the positive charge. The negative charge can be classified into electron and oxygen (O^- , O_2^-). These two charges of molecule weight had very large difference. Strictly speaking, the probe collected charge particles when the number of light charge particles (electron; e^-) was higher than heavy charge particle (O^- , O_2^-). Finally, the difference between these two particles represents approximately the total number density of negative charge species (O^- , O_2^- , etc.) in this electronegative (Ar/ O_2) plasma. In the present case, total number density of negative charged species amounts to approximately 3×10^{17} #/m³ at all power levels, except at 50 W ($\sim 2 \times 10^{17}$ #/m³), in which the electric field is not strong enough to generate more negative charged species.

4.2.2. Effect of Gas Ratio (Ar / O_2)

Figure 4.6 illustrates the deposition rate of the ZnO thin film as a function of $O_2/(Ar+O_2)$ ratio. In general, the deposition rate decreases monotonically with an increasing $O_2/(Ar+O_2)$ ratio; this is correlated with the ionization energies of argon and oxygen [161-162]. We concluded that there were two possible causes of the $O_2/(Ar+O_2)$ ratio effect.

One of the most crucial factors is the amount of oxygen concentration. Oxygen is an electronegative gas containing a very high affinity of electrons in the discharge, in addition to higher ionization threshold energy as compared to argon [161-163]. Nevertheless, the plasma depends mainly on electrons to produce positive ions. Thus, electrons generate negative ions more easily when oxygen is added into the plasma. The results of the study show that the reduction of plasma number density results in insufficient electrons to bombard argon for producing positive argon ion (Ar^+). Regardless of the ion number density or electron number density, they both decrease along with an increasing $\text{O}_2/(\text{Ar}+\text{O}_2)$ ratio. For this reason, more oxygen leads to weaker plasma. Eventually, the deposition rate decreases according to the oxygen concentration increasing.



Target poisoning is another possible issue that can decrease the deposition rate. This can occur through contact with air; or when oxygen gas added to the sputtering chamber. Both of these ways will create a very thin oxide layer on the surface of metal target. Therefore, the target surface maybe changed from metal to similar ceramic ($\text{Zn} \rightarrow \text{ZnO}_x$). As we know, the ion bombardment of metal (Zn) surface is easier than on a ceramic (ZnO_x) surface because metal has better ductility. For this reason, the deposition rate decreases after target poisoning.

In summary, our results indicated a reduction in plasma number density and thus the reduction of ion flux in bombarding the target [82, 164-165]. Accordingly, this also reduced the sputtering yield, which resulted in a lower deposition rate at a higher $O_2/(Ar+O_2)$ ratio [164, 166].

4.3. Structural Characteristics

4.3.1. Effect of RF Power

Figure 4.7 and Fig. 4.8 display the XRD pattern of ZnO thin film for various RF powers. All these XRD patterns observed several peaks located at 31.6° , 34.3° , 36.1° , and 47.3° , corresponding to ZnO ($10\bar{1}0$), ZnO (0002), ZnO ($10\bar{1}1$), and ZnO ($10\bar{1}2$), respectively. But only the intensity of (0002) diffraction peak in the ZnO thin film was fairly strong, while the other intensities of diffraction peaks were weaker. Hence, all of these ZnO thin films are in the poly-crystalline phase with a hexagonal structure and the major orientation is (0002). It is also indicated that these ZnO thin films belong to the c-axis orientation of the film (the powder-diffraction file No.79-0208). Figure 4.7 exhibits the thickness effect of ZnO thin films. The detail film thickness for different deposition times with a constant RF power is shown in Table 4.5. Results clearly show that the ZnO thin films grown less than 10 min. (smaller than 50nm in thickness) are almost in the amorphous phase [88]. It is quite likely that the ZnO film began to accumulate and form on the substrate because ZnO particles were still able to move to a

suitable site in this stage. Consequently, there were not enough period arrangement/diffraction patterns to reveal the crystalline structure of the XRD pattern. As the ZnO thin film grows over 20 min. (larger than 60 nm in thickness), a crystalline structure of (0002) diffraction peak begins to appear and become dominant in the film structure with further increasing of deposition time [81, 85, 87].

In addition, Fig. 4.8 presents the power effect on grown ZnO thin films with approximately 60 nm in thickness. Results show that ZnO thin films with enough film thickness are dominated by the (0002) orientation no matter what the RF power is, although the intensity of the diffraction peak increases significantly by increasing RF power. At the same time, the relative intensities of diffraction peak $(10\bar{1}0)$ and $(10\bar{1}1)$ reduce gradually with increasing RF power. According to Gang et al. [167], when the leading edge of steep crystal touches the lateral of vertical crystal it thereafter stops growing, whereas the vertical crystal keeps growing. This corresponds to the phenomenon of “evolutionary selection” [167] or “survival of the faster” [86], which was first proposed by Van der Drift [168] to explain the preferred orientation of a vapor-deposited PbO layer. As mentioned above, it seems possible to elucidate why the intensity of diffraction peak $(10\bar{1}0)$ and $(10\bar{1}1)$ gradually decreased. On the other hand, the RF power also enhanced the substrate temperature during the deposition process by the ion bombardment energy. So the surface mobility increased with enough

temperature (thermal energy). For this reason, the quality of the ZnO thin film was increased when the grain size increased and the amount of defect decreased. Detailed descriptions of quality and defect with grain size will be examined later again. In conclusion, the thickness and power effect were found to enhance crystalline when the deposition time (thickness) and RF power increased.

Figure 4.9 shows the FWHM and the calculating average grain size (crystalline size) as a function of applied RF power. The deposition rate increases with increasing RF power, which is strongly correlated with incident ion flux towards the substrate as shown in Fig. 4.3. Based on the Scherrer equation (see Eq. (2.49)), the grain size is calculated using the FWHM data by XRD pattern. Grain size decreases from 34 nm at 50 W down to 26.4 nm at 100 W and 200 W, and then increases gradually up to 29.6 nm at 400 W. In addition, Fig. 4.10 presents the SEM images to confirm the calculating average grain size scale by the Scherrer equation for RF power effect. The results show that the average grain size is very close to the grain size of SEM images. However, we could not observe the slight difference from the SEM images. In contrast with the almost monotonously increasing deposition rate, ion bombardment energy, and grain size with increasing RF power, we attribute the observed unusual trend of grain size to the three distinct power regimes as detailed next.

In the low-power regime (50 W), the largest grain size appears corresponding to the slowest deposition rate because of the lowest ion flux (see Fig. 4.1, Fig. 4.3 and Fig. 4.9). Thus, crystal growth is mostly deposition rate controlled, in which the ion bombardment energy and plasma density are both small. The medium-power regime (100-200 W), presents higher ion flux (and higher plasma density) along with still low ion bombardment energy (8.7-10.2 eV) and thus higher ZnO particle flux towards the substrate causes adverse effects in crystal growth since there is insufficient time for adatom migration on the substrate. Hence, the lowest grain size is observed in this regime. Finally, in the high-power regime (300-400 W), very high ZnO particle flux migrates towards the substrate, but with very high ion bombardment energy (12.9-15.8 eV), which can heat up the substrate and enhance thermal diffusion of the adatoms on the substrate, and thus favors the crystal growth of the ZnO thin film [87]. Therefore, grain size increases with increasing RF power in this regime, and is mainly ion bombardment energy controlled.

4.3.2. Effect of Gas Ratio (Ar / O_2)

Figure 4.11 and Fig. 4.12 show the XRD data of ZnO thin film for all combinations of $O_2/(Ar+O_2)$ ratios, while Fig. 4.13 shows that the FWHM of (0002) as well as estimated grain size [162] as a function of the $O_2/(Ar+O_2)$ ratio. Drawing from

the XRD pattern, all of these results are similar to the various RF power cases, whatever the thickness effect or the $O_2/(Ar+O_2)$ ratio effect.

According to our observation, the thickness effect of RF power and $O_2/(Ar+O_2)$ ratio demonstrated an identical trend, as shown in Fig. 4.7 and Fig. 4.11. The detail film thickness shown in Table 4.6 reports different deposition times with a constant $O_2/(Ar+O_2)$ ratio. Consequently, the amount of atomic layers (film thickness) is an important factor in the strength of ZnO (0002) peak intensity under a constant deposition condition. Next, for the $O_2/(Ar+O_2)$ ratio effect, results indicated that XRD patterns are very similar to each other as shown in Fig. 4.12. However, the peak intensity has slight variations with different $O_2/(Ar+O_2)$ ratios. Therefore, the FWHM and grain size help to understand and explain the various $O_2/(Ar+O_2)$ ratio change in ZnO thin film structural. A minimal value of FWHM was obtained at ~ 0.3 of the $O_2/(Ar+O_2)$ ratio where the corresponding grain size was the largest (35.68 nm), as shown in Fig. 4.13. Bachari *et al* [169] argued that in the film structure, less oxygen will cause an increase in crystallographic defects, while more oxygen will destroy the stoichiometry due to the lower surface mobility of the deposited atoms and lower kinetic energy for surface diffusion. In addition, adding more oxygen into the discharge might produce more neutral oxygen atoms which diffuse into films without enough energy [161-162, 164], thus creating additional unexpected defects. Furthermore, grain

size increases from 29.28 nm at 0.1 of $O_2/(Ar+O_2)$ ratio up to 35.68 nm at 0.3 of $O_2/(Ar+O_2)$ ratio, and then decreases gradually until it eventually gets down to 30.86 nm at 1.0 of $O_2/(Ar+O_2)$ ratio. At the same time, we also observed similar results from SEM images as shown in Fig. 4.14. In other words, the maximum grain size also occurs at 0.3 of $O_2/(Ar+O_2)$ ratio that is consistent with the lowest FWHM of ZnO thin film observed in this study.

4.4. Chemical Characteristics

4.4.1. Effect of RF Power

Figure 4.15 illustrates the XPS survey spectrum of ZnO thin film. In all of these specimens, the result was very similar. In order to effectively analyze the variation of chemical shift, all obtained spectra were calibrated to a C 1s electron peak at 284.6 eV [170] before we started analysis. The results show that the compositions of ZnO thin film contain not only Zn and O elements, but also carbon elements. Essentially, the C 1s peak is observed in the survey spectrum due to the hydrocarbon from the instrument itself. In addition, Fig. 4.16 exhibited the Zn 2p peak and O 1s peak that we were interested in. First, the main binding energy of the Zn 2p_{3/2} was about 1021.8 eV [171] for all specimens as shown in Fig. 4.16(a). Thus, the Zn 2p_{3/2} peak was not seen to exhibit obvious change in its chemical state over the course of this study. Therefore, the following section will focus on the O 1s peak. Next, Fig. 4.16(b) reveals how the

binding energy of the O 1s peaks were divided into two components, O^I (the binding energy at 529.8 eV) and O^{II} (the binding energy at 531.6 eV), respectively. The O^I peak was attributed the presence of O²⁻ ions in the wurtzite ZnO thin films (O-Zn bond), while the O^{II} peak may have been caused by the loosely bound oxygen created by absorbed H₂O (due to the O-H group) or by the O²⁻ ions in the oxygen deficiency produced on the surface during the ZnO thin film growth (O-H bond or O-O bond) [172-173]. However, Jo *et al.* state that the hydrogen forms a strong bond with oxygen and is very difficult to remove from the crystal growth environment [172]. The defect of the O-H bond is that it possesses the ability to influence the film surface and decreases the formation probability of O-Zn bond. Nevertheless, the chemical state of the O 1s peak showed appreciable shift as illustrated in Fig.4.17.

According to Fig. 4.17, both the O^I peak and O^{II} peak shifted to higher binding energy from RF power 50 W to 100 W due to the bombardment energy reduction. Next, these two peaks gradually moved toward lower binding energy when the RF power rose over 200 W. These phenomena indicated that the bonding strength seems consistent with the degree of bombardment energy (see Fig. 4.3). The strongest bonding strength was obtained at RF power 100 W due to the weak bombardment energy. Hence, we conjectured that the higher bombardment energy might influence the bonding strength between molecules.

4.4.2. Effect of Gas Ratio (Ar / O_2)

As shown in Fig. 4.18, both O^I and O^{II} peaks shifted to a higher binding energy with an increasing ratio of $O_2/(Ar+O_2)$ in the range of 0.1-0.3, which had the effect of decreasing the number of defect sites. In contrast, as more oxygen was added to the discharge (the $O_2/(Ar+O_2)$ ratio is from 0.5 to 1.0), more low energy neutral oxygen might diffuse into the growing film, destroying its stoichiometry. These findings are summarized in Fig. 4.19, which shows the binding energy and content fraction of O^I peak as a function of the $O_2/(Ar+O_2)$ ratio, in which the trend of these two properties correlate very well with each other. In addition, clear maximal values were found at the $O_2/(Ar+O_2)$ ratio of 0.3, coinciding with the minimal value observation of FWHM observed in the XRD analysis (Fig. 4.13). In fact, these findings reveal that the magnitudes of both the binding energy and content fraction of the O^I peak (O-Zn bond) play a key role in the stoichiometry of ZnO film. Therefore, the strongest binding energy with the highest content of O-Zn bond will enhance the O-Zn bond strength and eliminate other defects or impurities bound with ZnO structure to damage its quality or stoichiometry. The above observations suggest that suitable oxygen content can produce ZnO film that is close to stoichiometric. Therefore, we deduce that the optimum stoichiometric and quality of ZnO thin film may be obtained at the $O_2/(Ar+O_2)$ ratio of 0.3 under the current experimental configuration.

4.5. Optical Characteristics

In this section, we will discuss the optical characteristics of transmittance (T%) and absorption (abs.) under the following topics:

- (A) The thickness effect for a constant RF power;
- (B) The power effect for a constant thickness at 60 nm;
- (C) The thickness effect of ZnO/glass (ZnO thin film coated on glass substrate) for a constant RF power;
- (D) The power effect of ZnO/glass for a constant thickness at 60 nm;
- (E) The thickness effect for a constant $O_2/(Ar+O_2)$ ratio;
- (F) The $O_2/(Ar+O_2)$ ratio effect for a constant thickness at 60 nm;
- (G) The thickness effect of ZnO/glass for a constant $O_2/(Ar+O_2)$ ratio;
- (H) The $O_2/(Ar+O_2)$ ratio effect of ZnO/glass for a constant thickness at 60 nm.

4.5.1. Effect of RF Power

Topic (A) used the thickness effect of pure ZnO thin film to investigate the transmittance and absorption spectra in the visible (400-700 nm) and UV (280-400 nm) region as shown in Fig. 4.20 and Fig. 4.21, respectively. Figure 4.20(a), shows that the average transmittance of ZnO thin film ($T_{ZnO,ave}\%$) decreases from 98% to 86% with increasing the deposition time from 5 min. to 60 min. The relative thicknesses were from 31.5 nm to 171.7 nm in the visible region [73-75, 80]. These results indicate that

the method proposed in this study achieved excellent optical transparency. It is an important property for optical device applications, especially in transparent conductive oxide (TCO) and glass industries. Correspondingly, Fig. 4.20(b) clearly shows that the $T_{\text{ZnO,ave}}$ decreases from 80% down to 5% by increasing the deposited time in the UV region. This phenomenon means that thicker ZnO film was accompanied with better UV-shielding characteristics. In addition, for absorption spectra, all of the specimens demonstrated lower absorption in the visible region as illustrated in Fig. 4.21(a). But the most significant absorption phenomenon appeared in the UV region due to ZnO characteristics. Therefore, the following figures of absorption are only present in the UV region. According to Fig. 4.21(b), the degree of absorption increases when the ZnO film thickness becomes increases. Therefore, the film thickness plays a key factor in UV sunlight absorption. Based on the observations of this study, the optimal UV-shielding level of ZnO thin film thickness is about 170 nm. In conclusion, we deduce that the complete UV-shielding characteristics of ZnO thin film may be obtained when the thickness is over 200 nm.

The aim of topic (B) was to investigate the transmittance and absorption spectra in the visible and UV region for the power effect of pure ZnO thin film as shown in Fig. 4.22 and Fig. 4.23, respectively. To understand the power effect, we maintained a constant ZnO thin film thickness of 60 nm, with various RF powers. All of the

transmittance spectra trends were nearly identical due to the constant thicknesses. Furthermore, the results indicate that the $T_{\text{ZnO,ave}}\%$ decreases from 90% down to 86% in the visible region and from 50% down to 41% in the UV region (see Fig. 4.22(b)) with increasing RF power, respectively. However, both transmittance and absorption spectra (see Fig. 4.23) exhibit exponential decreases when the RF power increases, but the decay trends gradually diminish until reaching RF 400 W. Thus, the RF power still influences the optical properties of ZnO thin film. Kim et al. [76] also observed the similar result. Appropriate RF power seems to effectively create better UV-shielding characteristics. In this study, the best transparency with good UV-shielding characteristics was ultimately obtained at RF 400 W. From what has been discussed above, we can conclude that the main influencing factor of UV-shielding characteristics is thickness regardless of RF power. However, RF power is also able to affect the UV-shielding characteristics if all the ZnO thin films are fixed at the same thickness. The difference between this result and the thickness effect is a matter that remains to be discussed further.

Next, it is important to present the overall sample of degree of transparency and absorption, and to explain why it is critical for practical applications. For this reason, it is necessary to focus on the influence of ZnO thin film coated on glass substrate by following topics (C) and (D). To understand the difference between pure ZnO thin film

and ZnO thin film coated on glass substrate, we aimed at the blank glass to measure the transmittance and absorption, respectively. The results show that the UV-shielding characteristics of blank glass are only good below a certain UV wavelength (~280 nm). It indicates that blank glass has the highest transparency and well UV-shielding characteristics, as shown in Fig. 4.24 to Fig. 4.27. By combining ZnO thin film with blank glass, we have demonstrated that high transmittance (80-91%) in the visible region can still be obtained, and better UV-shielding characteristics are found with increasing deposition time as shown in Fig. 4.24(a). For example, less than 10% of optical transmittance can be obtained for the wavelength below 350 nm.

The following section will be addressing the glass substrate effect. In Fig. 4.24(a) and Fig. 4.26(a), it was observed that the transmittance spectra seem combined with blank glass spectra and pure ZnO thin film spectra by thickness effect and power effect, respectively. Nevertheless, the absorption spectra also obtain a similar tendency (please refer to Fig. 4.21 to Fig. 4.27). Compared with absorption of pure ZnO and ZnO thin film coated on glass substrate, there is enough evidence to show that the absorption of ZnO thin film coated on glass substrate is higher than the absorption of pure ZnO thin film in the same conditions. Regardless of thickness effect or power effect, the average optical transmittance still keeps high transparency over 86% in the visible region with

ZnO thin film coated on glass substrate; however, the average optical absorption of UV region is clearly better than pure ZnO thin film.

To summarize briefly, effect of varying the RF power with a constant ZnO thickness on the optical transmittance from UV to visible is relatively minor [76] as compared to that of varying the film thickness, especially in the UV region. However, for transparency, the pure ZnO and ZnO thin film coated on glass substrate were exhibiting high transmittance (over 85%) in visible region regardless of the thickness effect or power effect. The best transparency and UV-shielding characteristics were obtained at RF 100 W with 170 nm thickness for thickness effect and RF 400 W with 60 nm thickness for power effect, respectively.

4.5.2. Effect of Gas Ratio (Ar / O_2)

Figure 4.28 and Fig. 4.29 illustrate the transmittance and absorption of pure ZnO thin film at a constant $O_2/(Ar+O_2)$ ratio with different film thicknesses (for topic (E)), respectively. According to Fig. 4.28, it was also determined that the $T_{ZnO,ave}\%$ (transparent) decreases from 98.3% to 87.7% with increasing deposition time from 5 min. to 90min. in the visible region [73, 80]. Correspondingly, the $T_{ZnO,ave}\%$ (UV-shielding characteristics) decreases from 78.3% down to 13.1% with increasing deposition time in the UV region [174]. Likewise, the absorption of ZnO thin film in the UV region increases when the thickness increases, as shown in Fig. 4.29. Regardless of

transmittance or absorption, both results present the identical tendency under a constant condition for thickness effect.

Next, we explored the $O_2/(Ar+O_2)$ ratio effect with the thickness fixed at 60 nm as displayed in Fig. 4.30. Figure 4.30(a) shows that all of the $T_{ZnO,ave}\%$ in the visible region exhibit higher transparency (over 86.5%) and the $T_{ZnO,ave}\%$ in the UV region display UV-shielding characteristics (from 50% to 30%) with the fixed film thickness at 60nm using different $O_2/(Ar+O_2)$ ratios. Results clearly revealed that the transmittance spectra have no obvious variation with the $O_2/(Ar+O_2)$ ratio variance, although there was still a slight difference in the UV region as illustrated in Fig. 4.30(b). The similar phenomena were discovered in the absorption spectra as shown in Fig. 4.31. We do not have enough evidence to explain non-regular tendency at this point. According to several reports, the oxygen-rich condition improves optical transmittance, but the oxygen-deficient condition will induce the lower transmittance [73]. This is due to an improvement of the stoichiometry of ZnO thin film which decreases loss in light scattering [164, 167, 175]. Nonetheless, we imagine that a slight variance will influence the optical characteristics, such as film thickness, grain size, crystalline, composition, etc.

Topic (G) and topic (H) both point out overall transparency (combined with glass substrate) for practical applications. Moreover, we have demonstrated that high

transparency (80-90%) can still be acquired, and better UV-shielding characteristics are found with increasing deposition time (film thickness) when the ZnO thin film coated on glass substrate ($T_{\text{ZnO/Glass}}\%$) as presented in Fig. 4.32. Figure 4.33 also points out the high absorption in the UV region when the film thickness gradually increases. Likewise, Fig. 4.34 and Fig. 4.35 demonstrate the same consequences. These results reveal that very good UV-shielding characteristics with excellent high transparency can be easily obtained on glass, if the ZnO thin film thickness is large enough.

In summary, when dealing with either pure ZnO thin film or ZnO thin film on glass, results show that the film thickness plays a more important role both in transparency and UV-shielding characteristics than RF power effect or $\text{O}_2/(\text{Ar}+\text{O}_2)$ ratio effect. We expect that the optimum thick film thickness will produce complete UV-shielding with highly transparent ZnO thin film in some applications. Therefore, ZnO thin film is an excellent candidate material for high transparency and UV-shielding applications in optoelectronics and the glass industry, etc. Incidentally, color characteristics can be observed by these transmittance spectra [176]. For instance, according to Fig. 4.22(a), the strong absorption that appears near the edge between blue and violet and leads to couple with red and green exhibits slightly yellow characteristics in all approximately 60 nm ZnO thin films.

4.6. Hydrophobic/Hydrophilic Characteristics

4.6.1. Effect of RF Power

Self-cleaning capability is another important factor for the future, especially in glass fields (such as building glass, windshields, etc.). In Fig. 4.36, the blank glass substrate exhibits obvious hydrophilic characteristics with a contact angle of 52.5° , while in Fig. 4.37 the glass substrate coated with ZnO thin film shows a very large contact angle—up to 96° . Figure 4.37 displays the contact angle image of ZnO thin films under a constant thickness for various RF powers. This study indicated that RF 400 W is an optimum condition, and also displays the best contact angle at 82° , as shown in Fig. 4.37(e). On the other hand, better hydrophobic characteristics were also observed for different thickness effects under a constant RF power, as shown in Fig. 4.38. (It should be noted that for all the tested specimens, all contact angles are at least 20° larger than the specimen of blank glass substrate.)

4.6.2. Effect of Gas Ratio (Ar / O_2)

In addition to the $O_2/(Ar+O_2)$ ratio effect, similar evidence is also present in Fig. 4.39 and Fig. 4.40, respectively. The optimum condition of $O_2/(Ar+O_2)$ ratio of 0.25 demonstrates a larger contact angle at 92.7° , while the maximum value of contact angle is about 111.3° , which was discovered at the constant $O_2/(Ar+O_2)$ ratio of 0.25 for 5 min. of deposition time (see Fig. 4.40(a)). (Note that for all the tested specimens, all

contact angles are at least 30° larger than the specimen of blank glass substrate. The details of contact angle values are listed in [Table 4.7](#) to [Table 4.10](#).)

In brief, the present results clearly show that the ZnO thin film is able to modify the surface of blank glass substrate from hydrophilic to hydrophobic. This demonstrates that glass substrate coated with ZnO film exhibits excellent self-cleaning capability in some applications.

4.7. Annealing Temperature Effect of ZnO Thin Film

In recent years, low temperature techniques have attracted a great deal of attention because of flexible substrate [177] and several other materials developing practical optical devices for the huge future market needs. Deposition and annealing temperatures are both affected by TCO thin film characteristics, depending upon their applications [178-179]. For instance, liquid crystal display (LCD) applications should be lower than 140°C or 250°C, because the substrate is plastic or glass. Meanwhile, the deposition temperature should be lower than 400°C for plasma display panels (PDP) applications. There are more and more researchers interested in chemical solution techniques because it is cheaper, easier, requires low temperature processes, etc. For this reason, annealing (thermal) treatment is necessary to achieve high-performance devices after the fabrication processes of several kinds of optoelectronic devices [180].

Annealing treatment is an important and easy way to improve the material properties [181-182]. The annealing time, temperature and ambient are both critical conditions for annealing treatment. In fact, the annealing temperature is one of the most sensitive factors for effectively qualifying the crystal quality, defect and local structure of semiconductor material during the annealing process [183]. Consequently, we investigated annealing effect by adjusting the annealing temperature range up to 500°C to better understand the thermal energy effect on the structural and optical characteristics of ZnO thin films in this study.

For testing the annealing effect, we chose the best condition of sputtering, as mentioned above, to prepare ZnO thin film. The details of this condition are: RF 400 W, 15 mtorr, O₂/(Ar+O₂) ratio of 0.30 and 10 minutes for deposition time, respectively. To comprehend the difference of various annealing temperature effects, the film thickness is fixed at 200 nm ± 5% for approximation in practical applications. The specimens are subsequently annealed in a high-temperature oven for 1 hour at 200-500°C with 3°C/min. of heating rate and allowed to return to RT slowly. The detail of the test conditions for annealing temperature effect is listed in [Table 4.11](#).

4.7.1. Structural Characteristics

[Figure 4.41](#) exhibits the XRD pattern of the ZnO thin films taken at different annealing temperatures. All of these specimens are poly-crystalline, with its c-axis

normal to the substrate surface as shown in Fig. 4.41(a). Results demonstrated that the (0002) diffraction peak possesses a remarkable improvement at the intensity and the angle of diffraction peak, respectively. In addition, we zoomed in on the (0002) diffraction peak to clearly indicate this point, as illustrated in Fig. 4.41(b). There are two main phenomena that we observed. For one thing, the intensity of the diffraction peak increases with increasing the annealing temperature [182, 184]. This is because the thermal energy promotes the surface mobility of adatoms and reduces surface energy to occupy the correct site or re-grow in the crystal structure by higher annealing temperature [185]. Therefore, the structure's internal atoms rearrange its lattice constant, causing it to produce the period arrangement/diffraction patterns to enhance the intensity of the diffraction peak. But the raise rate of intensity gradually slows as the annealing temperature increases. This means that higher annealing temperature can be effectively improved to high crystalline quality, but the temperature is not without limits.

Figure 4.42 displays the ZnO (0002) diffraction peak shift as a function of annealing temperature. The (0002) diffraction peaks obviously shift to higher 2θ angles below 300°C of annealing temperature, and then maintain a constant 2θ angle however much the annealing temperature increased. Based on this information, we imagined that a moderate annealing temperature is necessary for obtaining the optimum material

properties. Liu et al. [183] argues that ZnO films experience compressive in-plane strain attributed to lattice misfit [59] when the thickness is below 200 nm, which is consistent with this study. Hong et al. argue that the residual stress in c-axis direction is partly relaxed due to the gradual increase of the 2θ angles with increasing annealing temperature [186]. Likewise, the lattice constant (interplanar spacing) decreases with increasing annealing temperature, also consistent with the stress relaxation as shown in Table 4.12 [185]. Incidentally, the lattice constant is calculated by Bragg's law and is closed to the bulk ZnO lattice constant (about 5.2069 Å) [70] after annealing treatment.

However, the as-grown ZnO thin film was transitioned from the compressive to tensile one to raise the 2θ angle and reduce the lattice constant by using annealing treatment.

The influence of grain size and FWHM of ZnO thin films as a function of annealing temperature is illustrated in Fig. 4.43. The film quality evaluated from the FWHM of (0002) diffraction peak is enhanced by annealing treatment [182, 184-185, 187]. The minimum value of FWHM was observed above 300°C of annealing temperature. All of these specimens indicated that the value of FWHM is very close when the annealing temperature over 300°C. It is consistent with the result of (0002) diffraction peak shift, as mentioned above. Additionally, the annealing temperature provides thermal energy to obtain the larger grain size by the re-grow mechanism better

than as-grown ZnO thin film. However, the largest grain size appeared at 400°C of annealing temperature.

In conclusion, the smallest value of FWHM, largest grain size and best relaxation stress were simultaneously found by annealing treatment. But the moderation annealing temperature is an important key to improve the film quality, defects, surface roughness, etc. It shows significant improvement below 300°C, whereas it has no obvious variance over 400°C [179]. Finally, we deduced that the best annealing temperature is 400°C.

4.7.2. Optical Characteristics

Figure 4.44 shows transmittance of pure ZnO thin film as a function of annealing temperature. Regardless of as-grown or annealed specimens, the highly transparent (~90%) and UV-shielding characteristics (below 16%) can be observed in Fig. 4.44(a).

Actually, the average transmittance of ZnO thin film slightly increases by increasing the annealing temperature. This improvement of transmittance may be attributed to the crystalline and surface roughness [179]. Defects and surface roughness induced various non-radiative centers and reduced light emission from the ZnO thin films. In addition to H. Li et al. report [185], the grain growth and the reduction of grain boundary density induced decreasing optical scattering. In Fig. 4.44(b), a blueshift phenomenon occurred near the UV edge when the annealing temperature increased. It is believed to originate from the residual stress along the c-axis due to lattice distortion [186]. Moreover, the

UV-shielding characteristics seem to improve at higher annealing temperatures. But these variances of optical characteristics make only a little difference for annealing treatment.

Ultimately, the annealing treatment is a critical method for improving the material properties of thin film structures, such as film quality, stress, grain size, transmittance and UV-shielding characteristics. Consequently, we determined that the best annealing temperature is about 400°C for the glass substrate.



Chapter 5. Summary and Recommendation of Future Works

5.1. Summary

In this study, ZnO thin film was deposited on a glass substrate at room temperature by a RF reactive magnetron sputtering method. To begin with, results showed that plasma density, electron temperature, deposition rate and estimated ion bombardment energy increases with increasing RF power. There exist three distinct power regimes, in which the controlling mechanism for the ZnO thin film quality differs, including: 1) The low-power regime, in which the highest grain size is observed due to slow deposition rate; 2) The medium-power regime, in which the lowest grain size is found; 3) The high-power regime, in which both high ion bombardment energy and high plasma density contribute to the higher grain size. Diverse results were obtained for $O_2/(Ar+O_2)$ ratio effect. The deposition rate decreases with an increasing $O_2/(Ar+O_2)$ ratio, caused by a reduction in plasma density due to the addition of electronegative oxygen. This is because the ionization energy of oxygen is larger than argon.

Secondly, all of these ZnO thin films are in the poly-crystalline phase with a hexagonal structure and the major orientation is (0002). The (0002) diffraction peak increases and other diffraction peaks decrease by increasing applied RF power at the same time. This corresponds to the phenomenon of “evolutionary selection” or “survival of the faster.” Similar XRD pattern events were observed in all different

$O_2/(Ar+O_2)$ ratios. Moreover, both less and more oxygen will cause crystallographic defects due lower surface mobility or neutral oxygen atoms, respectively. So, the lowest FWHM and largest grain size can be obtained at an $O_2/(Ar+O_2)$ ratio of ~ 0.3 . Regardless of the RF power effect or $O_2/(Ar+O_2)$ ratio effect, the film thickness plays a very important factor in the strength of ZnO(0002) diffraction peaks.

According to XPS spectra, both O^I peak (O-Zn bond) and O^{II} peak were shifted to higher binding energy (RF power 50-100 W) and then moved to lower binding energy (RF power 200-400 W). Therefore, we deduced that the bonding strength of intermolecules depends on the bombardment energy. In addition, we simultaneously observed that the content fraction of O-Zn bond and the corresponding binding energy also reach the highest levels at an $O_2/(Ar+O_2)$ ratio of ~ 0.3 , consistent with the best film quality by XRD. Eventually, these findings indicate that the magnitude of both the binding energy and content fraction of the O-Zn bond play a key role in the ZnO stoichiometry.

Next, higher transparency (over 86%) with enough UV-shielding characteristics (below 50%) were both acquired at 60nm of film thickness regardless of the RF power effect or $O_2/(Ar+O_2)$ ratio effect. In addition, the film thickness plays a more prominent role in controlling optical properties, especially in the UV-shielding characteristics, than the RF power or $O_2/(Ar+O_2)$ ratio. So, very good UV-shielding characteristics with high

transparency can be easily obtained with and without glass substrate, if the ZnO thin film thickness is large enough.

Lastly, for the annealing treatment, the smallest value of FWHM, largest grain size and best relaxation stress were found simultaneously. But the moderation annealing temperature is an important factor for improving the material properties such as film quality, stress, grain size, transmittance, UV-shielding characteristics, etc. It yields significant improvement below 300°C of annealing temperature, whereas it has no obvious difference when the annealing temperature is over 400°C. Consequently, we thought that the best annealing temperature for the glass substrate is about 400°C.

In summary, with properly coated ZnO thin film, we can obtain a glass substrate which is highly transparent, has good UV-shielding characteristics, and possesses highly hydrophobic characteristics, which is highly suitable for applications in the glass industry.

5.2. Recommendation of Future Works

Our study indicates that deposition parameters might influence the plasma characteristics during sputtering process and general physical properties in ZnO thin films. Moreover, investigation and discussion with different deposition parameters are an important for understanding the relationship between the plasma and physical properties. We suspect that there several critical deposition parameters influence the

above phenomena, including various working pressure, substrate temperature, distance between target and substrate, gas flow rate (gas flux), substrate rotation, etc. Based on the above parameters, we posit that the effect of various distances between target and substrate is the most important factor for the plasma situation.

The current measurement methods of material properties are not enough to interpret all of phenomena of material properties. For instance, although we obtained the hydrophobic characteristics of the ZnO thin film coating on the glass substrate, we still do not understand what mechanism causes it to produce high hydrophobic characteristics. However, we should acquire several measuring instruments to help us understand and interpret the phenomena of material properties and their relationship. In the future work, we will need to use several measuring instruments, as following:

- (1) scanning electron microscopy (SEM) or transmission electron microscopy (TEM), to photograph the morphology of the microstructure of ZnO thin film;
- (2) atomic force microscopy (AFM), to record the surface roughness of ZnO thin film;
- (3) fourier transform infra-red spectroscopy (FTIR), to determine the surface bonding of the ZnO thin film;
- (4) photoluminescence (PL) measurement, to confirm the luminescence characteristics of ZnO thin film;

- (5) stress measurement, to obtain the stress of ZnO thin film;
- (6) nanoindenter, to observe the hardness of ZnO thin film;
- (7) 4-point probe and Hall measurement, to measure the electrical properties;
- (8) other mechanical apparatus, to take the mechanical properties.



Appendices

Appendix A. Langmuir Probe Analysis

The Langmuir probe is a powerful plasma diagnostic tool which is capable of determining the fundamental characteristics of plasma, such as the ion number density, electron number density, electron temperature, floating potential, plasma potential and electron energy distribution function (EEDF). The simplified schematic of a plasma diagnostic technique and a typical $I-V$ curve are shown in [Fig. 2.5](#) and [Fig. 2.6](#), respectively. The complete process of measuring the $I-V$ curve, analysing and displaying the results were described in following section.

For measuring the $I-V$ curve, we inserted a small cylindrical probe into the plasma and applied a sweep voltage to the probe while measuring the resulting current drawn from the plasma. For example, the raw $I-V$ curve was measured as illustrated in [Fig. A.1](#). According to this data, we could analyze and understand the variance of the plasma during the sputtering process. In the next section, we will describe the step-by-step analysis of the $I-V$ curve by ESPsoft software (Hidden analytical software).

First, the floating potential is the easiest parameter to determine after we obtained the $I-V$ curve. It is defined as the voltage at which the probe collects no current, specifically, when the net current is equal to zero, as shown in [Fig. A.1](#). Then, we stated the square to the $I-V$ curve and plotted the I^2-V curve, as in [Fig. A.2\(a\)](#). We zoomed out

the ion saturation region to analyze the ion number density. The Orbital Motion Limited (OML) technique is considered briefly here. In short, a regression line is fitted to the I^2-V curve in the ion saturation region, as present in Fig. A.2(b). According to the slope of this line, the ion number density could be calculated by following equation:

$$n_i = \frac{1.42 \times 10^{15} M(\text{amu})^{1/2} \cdot (-\text{slope})^{1/2}}{A_p(\text{m}^2)} \quad (\text{A.1})$$

Next, the ion current function was observed by the square root of the fitted line (see Fig. A.3). Consequently, we could draw the electron $I-V$ curve when the square root of the fitted line was added to the original $I-V$ curve. This means that Fig. A.1 plus Fig. A.3 equals Fig. A.4. This I_e-V curve neglects the ion current component and shifts the current in the ion saturation region to zero.

Finally, the natural logarithm of the I_e-V curve is plotted from the above electron current characteristic, as revealed in Fig. A.5. The electron temperature, plasma (space) potential and electron number density were determined in this stage. The electron temperature is found when we choose a fitted line in the transition region, and is calculated by following equation:

$$T_e = -\frac{1}{\text{Slope}} \quad (\text{A.2})$$

Then, another fitted line was plotted in the electron saturation region. Therefore, the intersection of the fitted electron saturation and transition lines is called plasma

potential. After we knew the electron temperature and plasma potential, the electron number density was acquired by following a simplification equation:

$$n_e = 3.73 \times 10^{13} \frac{I_{e,Sat} (amps)}{A_p (m^2) \sqrt{T_e (eV)}} \quad (A.3)$$

The EEDF is also analyzed by ESPsoft software. However, the main method is the Druyvestyn method, which is calculated by the second derivative of the I_e-V curve. [Figure A.6](#) and [Fig. A.7](#) exhibit the first and second derivative of the I_e-V curve, respectively. The plasma potential was found at the maximum value of the 1st derivative or the zero of 2nd derivative, respectively. By observing the plasma potential, the EEDF is determined as following:

$$f_E(V) = \frac{-4}{A_p e^2} \left(\frac{m_e (V_s - V_p)}{2e} \right) \frac{d^2 I_e(V)}{dV^2} \quad (A.4)$$

Eventually, the EEDF is plotted as shown in [Fig. A.8](#).

References

- [1] Arthur P. Ramirez, “Applied Physics: Oxide Electronics Emerge”, Science 315 (2007) 1377.
- [2] Athavan Nadaraah, Robert C. Word, Jan Meiss and Rolf Könekamp, “Flexible Inorganic Nanowire Light-Emitting Diode”, Nano Lett. 8 (2008) 534.
- [3] Jae-Kong Lim, Chang-Ku Kang, Kyoung-Kook Kim, Il-Kyu Park, Dae-Kue Hwang and Seong-Ju Park, “UV Electroluminescence Emission from ZnO Light-Emitting Diodes Grown by High-Temperature Radiofrequency Sputtering”, Adv. Mater. 18 (2006) 2720.
- [4] S. Tüzemen and Emre Gür, “Principal Issues in Producing New Ultraviolet Light Emitters Based on Transparent Semiconductor Zinc Oxide”, Opt. Mater. 30 (2007) 292.
- [5] Eunice S. P. Leong, S. F. Yu and S. P. Lau, “Directional Edge-Emitting UV Random Laser Diodes”, Appl. Phys. Lett. 89 (2006) 221109.
- [6] Debasish Banerjee, Sung Ho Jo and Zhi Feng Ren, “Enhanced Field Emission of ZnO Nanowires”, Adv. Mater. 16 (2004) 2028.
- [7] Chen HongSheng, Qi JunJie, Zhang Yue, Liao QingLiang, Zhang XiaoMei and Huang YunHua, “Field Emission Characteristics of ZnO Nanotetrapods and the Effect of Thermal Annealing in Hydrogen”, Chinese Science Bulletin

59 (2007) 1287.

- [8] M. Chen, Z. L. Pei, C. Sun, J. Gong, R. F. Huang and L. S. Wen, “ZAO: An Attractive Potential Substitute for ITO in Flat Display Panels”, Mater. Sci. Engineering B 85 (2001) 212.
- [9] John F. Wager, “Applied Physics: Transparent Electronics”, Science 300 (2003) 1245.
- [10] Sanghyun Ju, Antonio Facchetti, Yi Xuan, Jun Liu, Fumiaki Ishikawa, Peide Ye, Chongwu Zhou, Tobin J. Marks and David B. Janes, “Fabrication of Fully Transparent Nanowire Transistors for Transparent and Flexible Electronics”, Nature Nanotechnol. 2 (2007) 378.
- [11] A. Shah, P. Torres, R. Tscharnner, N. Wyrsh and H. Keppner, “Photovoltaic Technology: The Case for Thin-Film Solar Cells”, Science 285 (1999) 692.
- [12] Jinsu Yoo, Jeonghul Lee, Seokki Kim, Kyunghoon, I. Jun Park, S. K. Dhungel, B. Karunakaran, D. Mangalaraj and Junsin Yi, “The Properties of Surface Textured ZnO:Al Films for Thin Film Solar Cells”, Phys. Stat. Sol. (c) 2 (2005) 1228.
- [13] V. Tvarozek, I. Novotny, P. Sutta, S. Flickyngerova, K. Schtereve and E. Vavrinsky, “Influence of Sputtering Parameters on Crystalline Structure of ZnO Thin Films”, Thin Solid Films 515 (2007) 8756.

- [14] Jia Long Yang, sung Jin An, Won Il Park, Gyu-Chul Yi and Wonyong Choi, “Photocatalysis Using ZnO Thin Films and Nanoneedles Grown by Metal-Organic Chemical Vapor Deposition”, Adv. Mater. 16 (2004) 1661.
- [15] Matt Law, Donald J. Sirbuly, Justin C. Johnson, Josh Goldberger, Richard J. Saykally and Peidong Yang, “Nanoribbon Waveguides for Subwavelength Photonics Integration”, Science 305 (2004) 1269.
- [16] Brian A. Korgel, “Nanosprings Take Shape”, Science 309 (2005) 1683.
- [17] Zhong Lin Wang and Jinhui Song, “Piezoelectric Nanogenerators Based on Zinc Oxide Nanowire Arrays”, Science 312 (2006) 242.
- [18] Yong Qin, Xudong Wang and Zhong Lin Wang, “Microfibre-Nanowire Hybrid Structure for Energy Scavenging”, Nature 451 (2008) 809.
- [19] Thomas Thundat, “Energetic Materials: Flexible Approach Pays Off”, Nature Nanotechnol. 3 (2008) 133.
- [20] F. S. Hickernell, “Zinc Oxide Films for Acoustoelectric Device Applications”, IEEE Trans. On Sonics and Ultrasonics SU-32 (1985) 621.
- [21] G. Ferblantier, F. Maily, R. Al Asmar, A. Foucaran and F. Pascal-Delannoy, “Deposition of Zinc Oxide Thin Films for Application in Bulk Acoustic Wave Resonator”, Sensors and Actuators A 122 (2005) 184.
- [22] Q. F. Zhou, C. Sharp, J. M. Cannata, K. K. Shung, G. H. Feng and E. S. Kim,

- “Self-focused High Frequency Ultrasonic Transducers Based on ZnO Piezoelectric Films”, Appl. Phys. Lett. 90 (2007) 113502.
- [23] Choonsup Lee, Sam Y. Bae, sohrab Mobasser and Harish Manohara, “A Novel Silicon Nanotips Antireflection Surface for the Micro Sun Sensor”, Nano Lett. 5 (2005) 2438.
- [24] Tae-Hyoung Moon, Min-Chang Jeong, Woong Lee and Jae-Min Myoung, “The Fabrication and Characterization of ZnO UV Detector”, Appl. Sur. Sci. 240 (2005) 280.
- [25] S. J. Young, L. W. Ji, S. J. Chang, S. H. Liang, K. T. Lam, T. H. Fang, K. J. Chen, X. L. Du and Q. K. Xue, “ZnO-Based MIS Photodetectors”, Sensors and Actuators A 141 (2008) 225.
- [26] Sebastian Polarz, Abhijit Roy, Michael Lehmann, Matthias Driess, frank Einar Kruis, Andreas Hoffmann and Patrick Zimmer, “Structure-Property-Function Relationships in Nanoscale Oxide Sensors: A Case Study Based on Zinc Oxide”, Adv. Funct. Mater. 17 (2007) 1385.
- [27] Quan-Bao Ma, Zhi-Zhen Ye, Hai-Ping He, Li-Ping Zhu, Jing-Yun Huang, Yin-Zhu Zhang and Bing-Hui Zhao, “Influence of Annealing Temperature on the Properties of Transparent Conductive and Near-Infrared Reflective ZnO-Ga Films”, Scr. Mater. 58 (2008) 21.

- [28] Y. U. Feng, "Research of Environment-Friendly Low Emissivity Glass", Journal of Wuhan University of Technology-Mater. Sci. Ed. 22 (2007) 385.
- [29] Danny H. W. Li, Joseph C. Lam, Chris C. S. Lau and T. W. Huan, "Lighting and Energy Performance of Solar Film Coating in Air-Conditioned Cellular Offices", Renew. Energy 29 (2004) 921.
- [30] E. Ando and M. Miyazaki, "Moisture Degradation Mechanism of Silver-Based Low-Emissivity Coatings", Thin Solid Films 351 (1999) 308.
- [31] E. Ando and M. Miyazaki, "Moisture Resistance of the Low-Emissivity Coatings with a Layer Structure of Al-doped ZnO/Ag/Al-doped ZnO", Thin Solid Films 392 (2001) 289.
- [32] T. David, S. Goldsmith and R. L. Boxman, "Electro-Optical and Structural Properties of Thin ZnO Films, Prepared by Filtered Vacuum Arc Deposition", Thin Solid Films 447-448 (2004) 61.
- [33] E. Ando and M. Miyazaki, "Durability of Doped Zinc Oxide-Silver-Doped Zinc Oxide Low Emissivity Coatings in Humid Environment", Thin Solid Films 516 (2008) 4574.
- [34] A Vaseashta, D. Dimova-Malinovska and J. M. Marshall, "Nanostructured and Advanced Materials for Application in Sensor, Optoelectronic and Photovoltaic Technology: Proceedings of the NATO Advanced Study

Institute ... II: Mathematics, Physics and Chemistry”, Springer, Chapter 9, 2005.

- [35] D. P. Norton, Y. W. Heo, M. P. Ivill, K. Ip, S. J. Pearton, M. F. Chisholm and T. Steiner, “ZnO: Growth, Doping & Processing”, Mater. Today 7 (2004) 34.
- [36] Zhong Lin Wang, “Nanostructures of Zinc Oxide”, Mater. Today 7 (2004) 26.
- [37] Zhong Lin Wang, “Zinc Oxide Nanostructures: Growth, Properties and Applications”, J. Phys.:Condens. 16 (2004) R829.
- [38] Micheal H. Huang, Samuel Mao, Henning Feick, Haoquan Yan, Yiying Wu, Hannes Kind, eicke Weber, Richard Russo and Peidong Yang, “Room-Temperature Ultraviolet Nanowire Nanolasers”, Science 292 (2001) 1897.
- [39] Hou T. Ng, Jun Li, Michael K. Smith, Pho Nguyen, Alan Caesll, Jie Han and M. Meyyappan, “Growth of Epitaxial Nanowires at the Junctions of Nanowalls”, Science 300 (2003) 1249.
- [40] Woong-Ki Hong, Jung Inn Sohn, Dae-Kue Hwang, Soon-Shin Kwon, Gunfo Jo, sunghoon Song, Seong-Min Kim, Hang-Ju Ko, Seong-Ju Park, Mark E. Welland and Takhee Lee, “Tunable Electronic Transport Characteristics of Surface-Architecture-Controlled ZnO Nanowire Field Effect Transistors”, Nano Lett. 8 (2008) 950.

- [41] Yung-Kuan Tseng, Chorng-Jye Huang, Hsin-Min Cheng, I-Nan Lin, Kuo-Shung Liu and I-cherng Chen, "Characterization and Field-Emission Properties of Needle-like Zinc Oxide Nanowires Grown Vertically on Conductive Zinc Oxide Films", Adv. Funct. Mater. 13 (2003) 811.
- [42] J. W. Park, J. K. Kim and K. Y. Suh, "Fabrication of Zinc Oxide Nanostructures Using Solvent-Assisted Capillary Lithography", Nanotechnology 17 (2006) 2631.
- [43] Apurba Dev and Subhadra, "Uniform Large-Scale Growth of Micropatterned Arrays of ZnO Nanowires Synthesized by a Surfactant Assisted Approach", Nanotechnology 18 (2007) 175607.
- [44] J. Zúñiga-Pérez, A. Rahm, C. Czekalla, J. Lenzner, M Lorenz and M. Grundmann, "Ordered Growth of Tilted ZnO Nanowires: Morphological, Structural and Optical Characterization", Nanotechnology 18 (2007) 195303.
- [45] Ye Sun, Gareth M. Fuge, Neil A. Fox, D. Jason Riley and Michael N. R. Ashfold, "Synthesis of Aligned Arrays of Ultrathin ZnO Nanotubes on a Si Wafer Coated with a Thin ZnO Film", Adv. Mater. 17 (2005) 2477.
- [46] Xudong Wang, Christopher J. Summers and Zhong Lin Wang, "Large-Scale Hexagonal-Patterned Growth of Aligned ZnO Nanorods for Nano-Optoelectronics and Nanosensor Arrays", Nano Lett. 4 (2004) 423.

- [47] J. X. Wang, X. W. Sun, Y. Yang, H. Huang, Y. C. Lee, O. K. Tan and L. Vayssieres, “Hydrothermally Growth Oriented ZnO Nanorod Arrays for Gas Sensing Applications”, Nanotechnology 17 (2006) 4995.
- [48] Xiang Yang Kong, Yong Ding, Rusen Yang and Zhong Lin Wang, “Single-Crystal Nanorings Formed by Epitaxial Self-Coiling of Polar Nanobelts”, Science 303 (2004) 1348.
- [49] Brian A. Korgel, “Self-Assembled Nanocoils”, Science 303 (2004) 1308.
- [50] Zheng Wei Pan, Zu Rong Dai and Zhong Lin Wang, “Nanobelts of Semiconducting Oxides”, Science 291 (2001) 1947.
- [51] Pu Xian Gao, Yong Ding, Wenjie Mai, William L. Hughes, Changshi Lao and Zhong Lin Wang, “Conversion of Zinc Oxide Nanobelts into Superlattice-Structured Nanohelices”, Science 309 (2005) 1700.
- [52] J. Fryar, E. McGlynn, M. O. Henry and J.-P. Mosnier, “Study of Exciton-Polariton Modes in Nanocrystalline Thin Films of ZnO Using Reflectance Spectroscopy”, Nanotechnology 16 (2005) 2625.
- [53] Theo Hahn, “International Tables for Crystallography: Volume A: Space-Group Symmetry, Second, Revised Edition”, Springer, pp. 574-575, 1989.
- [54] H. Wondratschek and U. Müller, “International Tables for Crystallography,

Volume A1: Symmetry relations between space groups (International Tables for Crystallography), First Edition”, Springer, pp. 335, 2004.

- [55] http://www.webelements.com/compounds/zinc/zinc_oxide.html
- [56] Rameshwar Bhargava, “Properties of Wide Bandgap II-IV Semiconductors”, Institution of Electrical Engineers, 1997.
- [57] http://www.mtmi.vu.lt/pfk/funkc_dariniai/diod/led.htm
- [58] Brian S. Mitchell, “An Introduction to Materials Engineering and Science: For Chemical and Materials Engineers, First Edition”, Wiley-Interscience, John Wiley & Sons, Inc., Chapter 6, 2003.
- [59] Ü. Özgür, Ya. I. Alivov, A Teke, M. A. Reshchikov, S. Doğan, V. Avrutin, S.-J. Cho and H. Morkoç, “A Comprehensive Review of ZnO Materials and Devices”, J. Appl. Phys. 98 (2005) 041301.
- [60] S. J. Pearton, D. P. Norton, K. Ip, Y. W. Heo and T. Steiner, “Recent Progress in Processing and Properties of ZnO”, Prog. Mater. Sci. 50 (2005) 293.
- [61] N. Izyumskaya, V. Avrutin, Ü. Özgür, Y. I. Alivov and H. Morkoç, “Preparation and Properties of ZnO and Devices”, Phys. Stat. Sol. (b) 244 (2007) 1439.
- [62] C. Klingshirn, “ZnO: From Basics Towards Applications”, Phys. Stat. Sol. (b) 244 (2007) 3027.

- [63] S. J. Pearton, D. P. Norton, K. Ip, Y. W. Heo and T. Steiner, “Recent Advances in Processing of ZnO”, J. Vac. Sci. Technol. B 22 (2004) 932.
- [64] C. Klingshirn, “ZnO: Material, Physics and Applications”, Chem. Phys. Chem. 8 (2007) 782.
- [65] Kiyoshi Takahashi, Akihiko Yoshikawa and Adarsh Sandhu, “Wide Bandgap Semiconductors: Fundamental Properties and Modern Photonic and Electronic Devices, First Edition”, Springer, 2007.
- [66] Otfried Madelung, “Semiconductors: Data Handbook, Third Edition”, Springer, pp. 194-200, 2004.
- [67] Kenneth A. Jackson and Wolfgang Schröter, “Handbook of Semiconductor Technology: Electronic Structure and Properties of Semiconductors, Volume 1, First Edition”, Wiley-VCH, 2000.
- [68] S. J. Pearton, C. R. Abernathy, M. E. Overberg, G. T. Thaler, D. P. Norton, N. Theodoropoulou, A. F. Hebard, Y. D. Park, F. Ren, J. Kim and L. A. Boatner, “Wide Band Gap ferromagnetic Semiconductors and Oxides: Applied Physics Reviews – Focused Review”, J. Appl. Phys. 93 (2003) 1.
- [69] Lev I. Berger, “Semiconductor Materials (Physical Sciences References), First Edition”, CRC Press, 1996.
- [70] Chennupati Jagadish and Stephen J. Pearton, “Zinc Oxide Bulk, Thin Films

and Nanostructures: Processing, Properties and Applications”, Elsevier Ltd., 2006.

- [71] Maria C Tamargo, “II-VI Semiconductor Materials and Their Applications (Optoelectronic Properties of Semiconductors and Superlattices, Volume 12), First Edition”, Taylor & Francis, 2002.
- [72] Kiyotaka Wasa and Shigeru Hayakawa, “Handbook of Sputter Deposition Technology: Principles, Technology and Applications (Materials Science and Process Technology Series)”, Noyes Publications, 1992.
- [73] Sang-Hun Jeong, Bong-Soo Kim and Byung-Teak Lee, “Photoluminescence Dependence of ZnO Films Grown on Si (100) by Radio-Frequency Magnetron Sputtering on the Growth Ambient”, Appl. Phys. Lett. 82 (2003) 2625.
- [74] Z. Q. Li, D. X. Zangl and J. J. Lin, “Optical and Electrical Transport Properties of Facing-target Sputtered Al Doped ZnO Transparent Film”, J. Appl. Phys. 99 (2006) 124906.
- [75] K. S. Kim, H. W. Kim and N. H. Kim, “Growth of ZnO Thin Film on SiO₂ Substrates by the RF Magnetron Sputtering Method”, J. Mater. Sci. Lett. 22 (2003) 1155.
- [76] Kyoung-Kook Kim, Jae-Hoon Song, Hyung-Jin Jung and Won-Kook Choi, Jong-Han Song, and Jong-Han Song, “The Grain Size Effects on the

Photoluminescence of ZnO/ α -Al₂O₃ Grown by Radio-Frequency Magnetron Sputtering”, J. Appl. Phys. 87 (2000) 3573.

[77] R. J. Hong, X. Jiang, B. Szyszka, V. Sittinger and A. Pflug, “Studies on ZnO:Al Thin Films Deposited by In-line Reactive Mid-Frequency Magnetron Sputtering”, Appl. Sur. Sci. 207 (2003) 341.

[78] J.J. Chen, Y. Gao, F. Zeng, D.M. Li and F. Pan, “Effect of Sputtering Oxygen Partial Pressures on Structure and Physical Properties of High Resistivity ZnO Films”, Appl. Sur. Sci. 223 (2004) 318.

[79] Z. B. Fang, Z. J. Yan, Y. S. Tan, X. Q. Liu and Y. Y. Wang, “Influence of Post-annealing Treatment on the Structure Properties of ZnO Films”, Appl. Sur. Sci. 241 (2005) 303.

[80] I. Sayago, M. Aleixandre, L. Arés, M. J. Fernández, J. P. Santos, J. Gutiérrez and M. C. Horrillo, “The Effect of the Oxygen Concentration and the RF Power on the Zinc Oxide Films Properties Deposited by Magnetron Sputtering”, Appl. Sur. Sci. 245 (2005) 273.

[81] M. Nisha, K. J. Saji, R. S. Ajimsha, N. V. Joshy and M. K. Jayaraj, “Characterization of Radio Frequency Plasma Using Langmuir Probe and Optical Emission Spectroscopy”, J. Appl. Phys. 99 (2006) 033304.

[82] T. Nagata, A. Ashida, N. Fujimura and T. Ito, “The Effects of Xe on an RF

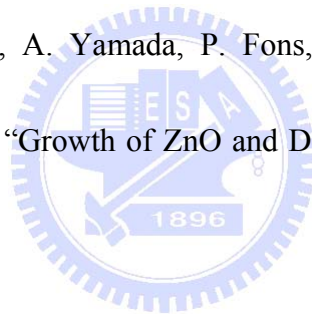
- Plasma and Growth of ZnO Film by RF Sputtering”, J. Appl. Phys. 95 (2004) 3923.
- [83] S. Z. Wu, “Dependence of Plasma Characteristics on DC Magnetron Sputter Parameters”, J. Appl. Phys. 98 (2005) 083301.
- [84] Jung W. Lee, Jerome J. Cuomo and Mohamed Bourham, “Plasma Characteristics in Pulsed Direct Current Reactive Magnetron Sputtering of Aluminum Nitride Thin Film”, J. Vac. Sci. Technol. A 22 (2004) 260.
- [85] R. Cebulla, R. Wendt and K. Ellmer, “Al-doped Zinc Oxide Films Deposited by Simultaneous RF and DC Excitation of a Magnetron Plasma: Relationships between Plasma Parameters and Structural and Electrical Film Properties”, J. Appl. Phys. 83 (1998) 1087.
- [86] Kun Ho Kim, Ki Cheol Park and Dae Young Ma, “Structural, Electrical and Optical Properties of Aluminum Doped Zinc Oxide Films Prepared by Radio Frequency Magnetron Sputtering”, J. Appl. Phys. 81 (1997) 7764.
- [87] Yuantao Zhang, Guotong Du, Dali Liu, Xinqiang Wang, Yan Ma, Jinzhong Wang, Jingzhi Yin, Xiaotian Yang, Xiaoke Hou and Shuren Yang, “Crystal Growth of Undoped ZnO Films on Si Substrates Under Different Sputtering Conditions”, J. Cryst. Growth 243 (2002) 439.
- [88] Y. Yoshino, K. Inoue, M. Takeuchi and K. Ohwada, “Effect of Interface

Micro Structure in crystallization of ZnO Thin Films Prepared by Radio Frequency Sputtering”, Vacuum 51 (1998) 601.

[89] Wataru Shindo and Tadahiro Ohmi, “Ion Energy, Ion Flux, and Ion Mass Effects on Low-Temperature Silicon Epitaxy Using Low-Energy Ion Bombardment Process”, Thin Solid Films 79 (1996) 2347.

[90] Hyong Woo Kim, Kwang Sik Kim and Chongmu Lee, “Low Temperature Growth of ZnO Thin Film on Si (100) Substrates by Metal Organic Chemical Vapor Deposition”, J. Mater. Sci. Lett. 22 (2003) 1117.

[91] K. Iwata, H. Tampo, A. Yamada, P. Fons, K. Matsubara, K. Sakurai, S. Ishizuka and S. Niki, “Growth of ZnO and Device Applications”, Appl. Surf. Sci. 244 (2005) 504.



[92] J. J. Robbins, J. Harvey, J. Leaf, C. Fry and C. A. Wolden, “Transport Phenomena in High Performance Nanocrystalline ZnO:Ga Films Deposited by Plasma-Enhanced Chemical Vapor Deposition”, Thin Solid Films 473 (2005) 35.

[93] S. J. Lim, Soonju Kwon and H. Kim, “ZnO Thin Films Prepared by Atomic Layer Deposition and RF Sputtering as an Active Layer for Thin Film Transistor”, Thin Solid Films 516 (2008) 1523.

[94] Jongmin Lim, Kyoungchul Shin, Hyounwoo Kim and Chongmu Lee,

“Enhancement of ZnO Nucleation in ZnO Epitaxy by Atomic Layer Epitaxy”,
Thin Solid Films 475 (2005) 256.

- [95] F. K. Shan and Y. S. Yu, “Band Gap Energy of Pure and Al-doped ZnO Thin Films”, J. Eur. Ceram. Soc. 24 (2004) 1869.
- [96] R. D. Vispute, V. Talyansky, Z. Trajanovic, S. Choopun, M. Downes, R. P. Sharma, T. Venkatesan, M. C. Woods, R. T. Lareau, K. A. Jones and A. A. Iliadis, “High Quality Crystalline ZnO Buffer Layers on Sapphire (001) by Pulsed Laser Deposition for III–V Nitrides”, Appl. Phys. Lett. 70 (1997) 2735.
- [97] V. R. Shinde, C. D. Lokhande, R. S. Mane and Sung-Hwan Han, “Hydrophobic and Textured ZnO Films Deposited by Chemical Bath Deposition: Annealing Effect”, Appl. Sur. Sci. 245 (2005) 407.
- [98] Young-Sung Kim and Weon-Pil Tai, “Electrical and Optical Properties of Al-doped ZnO Thin Films by Sol–Gel Process”, Appl. Surf. Sci. 253 (2007) 4911.
- [99] Ren-De Sun, Akira Nakajima, Akira Fujishima, Toshiya Watanabe and Kazuhito Hashimoto, “Photoinduced Surface Wettability Conversion of ZnO and TiO₂ Thin Film”, J. Phys. Chem. B 105 (2001) 1984.
- [100] Zhi Yan, Zhi Tang Song, Wei Li Liu, Qing Wan, Fu Min Zhang and Song Lin Feng, “Optical and Electrical Properties of P-Type Zinc Oxide Thin Films

Synthesized by Ion Beam Assisted Deposition”, Thin Solid Films 492 (2005) 203.

[101] Y. Ma, G. T. Du, S. R. Yang, Z. T. Li, B. J. Zhao, X. T. Yang, T. P. Yang, Y. T. Zhang and D. L. Liu, “Control of Conductivity Type in Undoped ZnO Thin Films Grown by Metalorganic Vapor Phase Epitaxy”, J. Appl. Phys. 95 (2004) 6268.

[102] <http://www.plasmacoalition.org/what.htm>

[103] I. H. Hutchinson, “Principles of Plasma Diagnostics, Second Edition”, Cambridge University Press, 2002.

[104] Dongsoo Lee, Greg Severn, Lutfi Oksuz and Noah Hershkowitz, “Laser-Induced Fluorescence Measurements of Argon Ion Velocities Near the Sheath Boundary of an Argon–Xenon Plasma”, J. Phys. D: Appl. Phys. 39 (2006) 5230.

[105] Lawrence J Overzet and Jennifer Kleber, “Effect of Metastable Atom Reactions on the Electron Energy Probability Functions in Afterglows”, Plasma Sources Sci. Technol. 7 (1998) 512.

[106] Takeshi Kitajima, Toshiki Nakano, Seiji Samukawa and Toshiaki Makabe, “Diagnostics of N₂ Dissociation in RF Plasmas by Vacuum Ultraviolet Emission and Absorption Spectroscopy”, Plasma Sources Sci. Technol. 17

(2008) 5230.

- [107] A. Palmero, E. D. van Hattum, H. Rudolph and F. H. P. M. Habraken, “Characterization of an Ar/O₂ Magnetron Sputtering Plasma Using a Langmuir Probe and an Energy Resolved Mass Spectrometer”, Thin Solid Films 494 (2006) 18.
- [108] F. Delmotte, M. C. Hugon, B. Agius, A. M. Pointu and S. Teodoru, “Langmuir Probe Analysis of Distributed Electron Cyclotron Resonance Silicon Nitride Deposition Plasma”, Appl. Phys. Lett. 72 (1998) 1448.
- [109] Nathan W. Schmidt, Thomas S. Totushek, William A. Kimes, David R. Callender and James R. Doyle, “Effects of Substrate Temperature and Near-Substrate Plasma Density on the Properties of DC Magnetron Sputtered Aluminum Doped Zinc Oxide”, J. Appl. Phys. 94 (2003) 5514.
- [110] Seong-Young Kim and Jai-Sung Lee, “Characterization of an Argon Magnetron Plasma by Cylindrical Langmuir Probe”, J. Mater. Sci. Lett. 16 (1997) 547.
- [111] I. Langmuir and H. M. Mott-Smith, “The Theory of Collectors in Gaseous Discharges”, Phys. Rev. 28 (1926) 727.
- [112] I. Langmuir and H. M. Mott-Smith, Gen. Elec. Rev. 26 (1923) 731.
- [113] I. Langmuir and H. M. Mott-Smith, “Studies of Electric Discharges in Gases

at Low Pressure: Part I ”, Gen. Elec. Rev. 27 (1924) 449.

[114] I. Langmuir and H. M. Mott-Smith, “Studies of Electric Discharges in Gases at Low Pressure: Part II – Typical Experimental Data Illustrating the Use of Plane Collectors”, Gen. Elec. Rev. 27 (1924) 538.

[115] I. Langmuir and H. M. Mott-Smith, “Studies of Electric Discharges in Gases at Low Pressure: Part III – Typical Experimental Data Illustrating the Use of Cylindrical Collectors”, Gen. Elec. Rev. 27 (1924) 616.

[116] I. Langmuir and H. M. Mott-Smith, “Studies of Electric Discharges in Gases at Low Pressure: Part IV – Data on Discharges in Mercury Vapor Obtained with Cylindrical Electrodes”, Gen. Elec. Rev. 27 (1924) 762.

[117] I. Langmuir and H. M. Mott-Smith, “Studies of Electric Discharges in Gases at Low Pressure: Part V – The Use of Spherical Collectors and the Effects of Magnetic Fields”, Gen. Elec. Rev. 27 (1924) 810.

[118] Francis F. Chen and Jane P. Chang, “Lecture Notes on Principles of Plasma Processing”, Kluwer Academic / Plenum Publishers, New York, 2003.

[119] Richard H. Huddlestone and Stanley L. Leonard, “Plasma Diagnostic Techniques”, Academic Press, New York, Chapter 4, 1965.

[120] Paul M. Chung, Lawrence Talbot and Kenell J. Touryan, “Electric Probes in Stationary and Flowing Plasmas: Theory and Application”, Springer Verlag,

New York, 1975.

- [121] Orlando Auciello and Daniel L. Flamm, "Plasma Diagnostics Volume 1: Discharge Parameters and Chemistry", Academic Press, Inc., New York, Chapter 3, 1989.
- [122] W. Lochte-Holtgreven, "Plasma Diagnostics (American Vacuum Society Classics)", AIP Press, New York, Chapter 11, 1995.
- [123] Francis F. Chen, "Langmuir Probe Analysis for High Density Plasmas", Mini-Course on Plasma Diagnostics, Low Temperature Plasma Technology Laboratory, UCLA, Los Angeles, California 90095-1594, June, 2000.
- [124] Francis F. Chen, "Lecture Notes on Langmuir Probe Diagnostics", Mini-Course on Plasma Diagnostics, IEEE-ICOPS meeting, Jeju, Koera, June 5, 2003.
- [125] M. J. Druyvesteyn, "Der Niedervoltbogen", Z. Phys. 64 (1930) 781.
- [126] M. J. Druyvesteyn and N. Warmoltz, Phil. Mag. 17 (1935) 1.
- [127] W. H. Schneider, Acta. Phys. Austriaca 10 (1956) 54.
- [128] R. L. F. Boyd and N. D. Twiddy, "Electron Energy Distributions in Plasmas", Proc. Roy. Soc. A 205 (1959) 53.
- [129] E. O. Johnson and L. Malter, "Double-Probe Method for Determination of Electron Temperatures in Steady and Time-Varying Gas Discharges", Phys.

Rev. 76 (1949) 1411.

- [130] E. O. Johnson and L. Malter, “A Floating Double Probe Method for Measurements in Gas Discharges”, Phys. Rev. 80 (1950) 58.
- [131] K. Yamamoto and T. Okuda, “On the Floating Probe Method for the Measurement of Ionized Gas”, J. Phys. Soc. 11 (1956) 57.
- [132] T. Okuda and K. Yamamoto, “Asymmetrical Triple Probe Method for Determining Energy Distribution of Electron in Plasma”, J. Appl. Phys. 31 (1960) 158.
- [133] J. G. Laframboise, “Institute for Aerospace Studies Report No. 100”, University of Toronto, 1966.
- [134] Rointan F. Bunshah, “Deposition Technologies for Films and Coatings: Developments and Applications”, Noyes Publications, 1982.
- [135] Alfred Wagendristel and Yuming Wang, “An Introduction to Physics and Technology of Thin Films”, World Scientific Publishing Company, Chapter 2, 1994.
- [136] K. D. Leaver and B. N. Chapman, “Thin Films”, Wykeham Publications, London, 1971.
- [137] B. N. Chapman, “Glow Discharge Processes: Sputtering and Plasma Etching”, Wiley-Interscience Publication, John Wiley & Sons, Inc., 1980.

- [138] R. Behrisch and K. Wittmaack, "Sputtering by Particle Bombardment III: Characteristics of Sputtered Particles, Technical Applications (Topics in Applied Physics)", Springer Verlag, New York, 1991.
- [139] S. Im, B. J. Jin and S. Yi, "Ultraviolet Emission and Microstructural Evolution in Pulsed-Laser-Deposited ZnO Films", J. Appl. Phys. 87 (2000) 4558.
- [140] Hong Xiao, "Introduction to Semiconductor Manufacturing Technology", Prentice-Hall Inc., Chapter 7, 2001.
- [141] Michael A. Lieberman and Allan J. Lichtenberg, "Principles of Plasma Discharges and Materials Processing, Second Edition", Wiley-Interscience, John Wiley & Sons, Inc., 2005.
- [142] Yuri P. Raizer, "Gas Discharge Physics, First Edition", Springer-Verlag, 1991.
- [143] Milton Ohring, "Materials Science of Thin Films: Deposition & Structure, Second Edition", Academic Press, 2002.
- [144] R. K. Walkerling and A. Guthrie, "The Characteristics of Electrical Discharges in Magnetic Fields", McGraw-Hill Book Company, New York, Chapter 3, 1949.
- [145] C. Guy Suits, "Collected Worked of Irving Langmuir, Volume 4: Electrical Discharge", Pergamon Press, Inc., New York, 1961.
- [146] S. Lee and P. H. Sakanaka, "Small Plasma Physics Experiments II:

Proceedings of Symposium on Small Scale Laboratory Plasma Experiments, Spring College on Plasma Physics”, World Scientific Publishing Co. Inc., 1990.

[147] Alexander Fridman and Lawrence A. Kennedy, “Plasma Physics and Engineering, First Edition”, Taylor & Francis Books, Inc., 2004.

[148] Mario Birkholz, “Thin Film Analysis by X-Ray Scattering”, Wiley-VCH, Weinheim, 2006.

[149] Aaron D. Krawitz, “Introduction to Diffraction in Materials Science and Engineering, First Edition”, Wiley-Interscience Publication, John Wiley & Sons, Inc., 2001.

[150] C. Suryanarayana and M. Grant Norton, “X-Ray Diffraction: A Practical Approach”, Plenum Press, New York, 1998.

[151] Eric Lifshin, “X-Ray Characterization of Materials”, Wiley-VCH, Weinheim, 1999.

[152] Mark Fox, “Optical Properties of Solids, First Edition”, Oxford University Press Inc., New York, Chapter 1, 2002.

[153] Eugene Hecht, “Optics, Fourth Edition”, Addison Wesley, Chapter 3, 2003.

[154] Donald R. Askeland and Pradeep P. Phulé, “The Science and Engineering of Materials, Fifth Edition”, Cengage-Engineering, Chapter 21, 2005.

- [155] John F. O'Hanlon, "A User's Guide to Vacuum Technology, Third Edition", John Wiley & Sons, Inc., 2003.
- [156] http://www.ndl.org.tw/web/department/nmlab/device_aes.php
- [157] John F. Watts, John Wolstenholme, "An Introduction to Surface Analysis by XPS and AES", John Wiley and Sons Ltd., Chapter 2, 2003.
- [158] D. Briggs, "Surface Analysis of Polymers by XPS and Static SIMS", Cambridge University Press, Chapter 2, 1998.
- [159] Jhy-Ming Ting and Chia-Kang Lin, "Characteristics of Transparent Conducting Nano-Scaled Thin Films Based on ZnO", J. Am. Ceram. Soc. 89 (2006) 3676.
- [160] Jaehyeong Lee, Dongjin Lee, Donggun Lim and Keajoon Yang, "Structural, Electrical and Optical Properties of ZnO:Al Films Deposited on Flexible Organic Substrates for Solar Cell Applications", Thin Solid Films 515 (2007) 6094.
- [161] I-Tseng Tang, Y. C. Wang, W. C. Hwang, C. C. Hwang, N. C. Wu, Mau-Phon Houg and Yeong-Her Wang, "Investigation of Piezoelectric ZnO Film Deposited on Diamond Like Carbon Coated onto Si Substrate Under Different Sputtering Conditions", J. Cryst. Growth 252 (2003) 190.
- [162] Ren-Chuan Chang, Sheng-Yuan Chu, Cheng-Shong Hong and Yu-Ting

Chuang, “An investigation of Preferred Orientation of Doped ZnO Films on the LiTaO₃ Substrates and Fabrications of Love-Mode Devices”, Surf. Coat. Technol. 200 (2006) 3235.

[163] Charles Kittel, “Introduction to Solid State Physics, Eighth Edition”, John Wiley & Sons, Inc., New York, p. 54, 2005.

[164] Yee-shin Chang and Jyh-Ming Ting, “Growth of ZnO Thin Films and Whiskers”, Thin Solid Films 398-399 (2001) 29.

[165] M Noguchi, T Hirao, M Shindo, K Sakurauchi, Y Yamagata, K Uchino, Y Kawai and K Muraoka, “Comparative Studies of the Laser Thomson Scattering and Langmuir Probe Methods for Measurements of Negative Ion Density”, Plasma Source Sci. Technol. 12 (2003) 403.

[166] Rashmi Menon, K. Sreenivas and Vinay Gupta, “Influence of Stress on the Structural and Dielectric Properties of RF Magnetron Sputtered Zinc Oxide Thin Film”, J. Appl. Phys. 103 (2008) 094903.

[167] Li Gang, Lin Rui-Sen, Kikuchi Eiichi and Matsukata Masahiko, “Growth Mechanism of a Preferentially Oriented Mordenite Membrane”, J. Zhejiang Unvi. Sci. 6B (2005) 369.

[168] A. van der Drift, “Evolutionary Selection, a Principle Governing Growth Orientation in Vapor-Deposited Layers”, Philips Res. Repts. 22 (1967) 267.

- [169] E. M. Bachari, G. Baud, S. Ben Amor and M. Jacquet, “Structural and Optical Properties of Sputtered ZnO Films”, Thin Solid Films 348 (1999) 165.
- [170] P. T. Hsieh, Y. C. Chen, K. S. Kao and C. M. Wang, “Luminescence Mechanism of ZnO Thin Film Investigated by XPS Measurement”, Appl. Phys. A 90 (2008) 317.
- [171] Li-Wen Lai and Ching-Ting Lee, “Investigation of Optical and Electrical Properties of ZnO Thin Films”, Mater. Chem. Phys. 110 (2008) 393.
- [172] Jae Hyung JO, Tae-Bong HUR, Jin Sung KWAK, Dae Young KWON, Yoon-Hwae HWANG and Hyung Kook KIM, “Effect of Oxygen on the Crystalline of ZnO Films Grown on Sapphire by PLD Method”, J. Korean Phys. Soc. 47 (2005) S300.
- [173] Jianguo Lu, Zhizhen Ye, Jingyun Huang, Lei Wang and Binghui Zhao, “Synthesis and Properties of ZnO Films with (100) Orientation by SS-CVD”, Appl. Sur. Sci. 207 (2003) 295.
- [174] Bai Lin ZHU, Xiao Hua SUN, Shi Shang GUO, Xing Zhong ZHAO, Juan WU and Jing LIU, “Effect of Thickness on the Structure and Properties of ZnO Thin Films Prepared by Pulsed Laser Deposition”, Jan. J. Appl. Phys. 45 (2006) 7860.
- [175] Li-Jian Meng and M P dos Santos, “Characterization of ZnO Films Prepared

by DC Reactive Magnetron Sputtering at Different Oxygen Partial Pressures”,
Vacuum 46 (1995) 1001.

[176] W. W. Wang, X. G. Diao, Z. Wang, M. Yang, T. M. Wang and Z. Wu,
“Preparation and Characterization of High-Performance Direct Current
Magnetron Sputtered ZnO:Al Films”, Thin Solid Films 491 (2005) 54.

[177] Xiao-jing Wang, Qing-song Lei, Wei Xu, Wei-li Zhou and Jun Yu,
“Preparation of ZnO:Al Thin Film on Transparent TPT Substrate at Room
Temperature by RF Magnetron Sputtering Technique”, Mater. Lett. 63 (2009)
1371.

[178] Sookjoo Kim, Wan In Lee, El-Hang Lee, S. K. hwang and Chongmu Lee,
“Dependence of the Resistivity and the Transmittance of Sputter-Deposited
Ga-doped ZnO Films on Oxygen Partial Pressure and Sputtering Temperature”,
J. Mater. Sci. 42 (2007) 4845.

[179] Keunbin Yim and Chongmu Lee, “Dependence of the Electrical and Optical
Properties of Sputter-deposited ZnO:Ga Films on the Annealing Temperature,
Time, and Atmosphere”, J. Mater Sci.: Mater. Electron 18 (2007) 385.

[180] J. M. Yuk, J. Y. Lee, T. W. Kim, D. I. Son and W. K. Choi, “Effects of
Thermal Annealing on the Microstructural Properties of the Lower Region in
ZnO Thin Films Grown on n-Si (001) Substrate”, J. Mater. Res. 23 (2008)

1082.

- [181] K. Laurent, D. P. Yu, S. Tusseau-Nenez and Y. Leprince-Wang, “Thermal Annealing Effect on Optical Properties of Electrodeposited ZnO Thin Films”, J. Phys. D: Appl. Phys. 41 (2008) 195410.
- [182] Y. Z. WANG and J. XU, “Annealing Effects of Sapphire Substrate on Properties of ZnO Films Grown by Magnetron Sputtering”, Appl. Phys. A 88 (2007) 727.
- [183] Weiwei Liu, Bin Yao, Yongfeng Li, Binghui Li, Changji Zheng, Bingye Zhang, Chongxin Shan, Zhenzhong Zhang, Jiying Zhang and Dezhen Shen, “Annealing Temperature Dependent Electrical and Optical Properties of ZnO and MnZnO Films in Hydrogen Ambient”, Appl. Surf. Sci. 255 (2009) 6745.
- [184] Deyi Wang and Shuxia Gao, “Influence of Annealing Condition on The Structure and Optical Properties of Na-doped ZnO Thin Films Prepared by Sol-Gel Method”, J. Alloys Comp. 476 (2009) 925.
- [185] Hongxia Li, Hong Liu, Jiyang Wang, Shushan Yao, Xiufeng Cheng and R. I. Boughton, “Influence of Annealing on ZnO Films Grown by Metal–Organic Chemical Vapor Deposition”, Mater. Lett. 58 (2004) 3630.
- [186] Ruijin Jong, Jianbing Huang, Hongbo He, Zhengxiu Fan and Jianda Shao, “Influence of Different Post-treatments on the Structure and Optical Properties

of Zinc Oxide Thin Films”, Appl. Surf. Sci. 242 (2005) 346.

[187] M. Bouderbala, S. Hamzaoui, M. Adnane, T. Sahraoui and M. Zerdali,
“Annealing Effect on Properties of Transparent and Conducting ZnO Thin
Films”, Thin Solid Films 517 (2009) 1572.

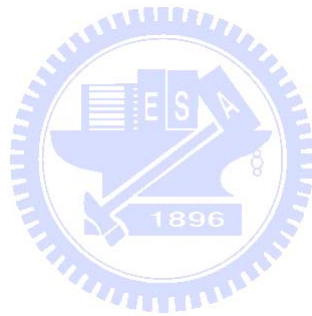


Table 1.1. Key structural properties of zinc oxide (ZnO).

Characteristics	Value
Mineral name	zincite
Crystal structure	Hexagonal (Wurtzite) [60, 64-65, 67-68]
Space group	$P6_3mc$ (C_{6v}^4) [53-54, 61, 64, 66]
Point group	$6mm$ [64]
Molecular weight	81.37 [67, 69]
Average atomic weight	40.69 [69]
Average atomic number	19 [69]
Lattice constant (Å)	a: 3.2475~3.2501 [59-61, 70]
	c: 5.2042~5.2075 [59-61, 70]
	c/a: 1.593~1.6035 [59-61, 70]
Lattice spacing, d (Å)	1.980 [65, 71]
Density (g/cm ³)	5.605 [60, 70, 72]
Melting point (°C)	1975 [60]
Ionicity, f_i	0.616 [59]

Table 1.2. Key optical properties of zinc oxide (ZnO).

Characteristics	Value	
Bandgap, E_g (eV)	RT: 3.37 ^[37, 59, 61, 65, 71]	
	1.6 K: 3.4376 ^[59, 67, 71]	
Cohesive energy, E_{coh} (eV)	1.89 ^[71]	
Optical transparency (nm)	400~2500 ^[72]	
Refractive index (at 632.8 nm)	n_o : 1.9985 ^[72]	
	n_e : 2.0147 ^[72]	
Dielectric constant	<i>Film</i>	<i>Bulk</i>
	$\perp c$: 7.46 ^[59, 70]	$\perp c$: 7.77 ^[59, 70]
Static, ϵ_0	$\parallel c$: 8.59 ^[59-60, 70]	$\parallel c$: 8.91 ^[59, 70]
	$\perp c$: 3.61 ^[59]	$\perp c$: 3.70 ^[59, 66]
High frequency, ϵ_∞	$\parallel c$: 3.76 ^[59]	$\parallel c$: 3.78 ^[59, 66]

Table 1.3. Key electrical properties of zinc oxide (ZnO).

Characteristics	Value	
Exciton binding energy at RT*, E_b (meV)	60 [37, 59-60, 65, 70-71]	
Exciton binding energy at 6K, E_b (meV)	63.1 [66]	
Biexciton binding energy (meV)	15 [65]	
Bohr radius (nm)	1.4 [65]	
Electron effective mass	0.24 m_0 [60, 65]	
Hole effective mass	0.59 m_0 [60]	
	<i>n-type</i>	<i>p-type</i>
Carrier concentration (cm ⁻³)	10 ⁶ ~10 ²⁰ [60-61, 70]	~10 ¹⁹ [70]
Hall mobility at RT* (cm ² /V·s)	μ_n : 200 [60-61, 63, 68, 70]	μ_p : 5~50 [60, 70]

* $RT \approx 300K$

Table 1.4. Key mechanical properties of zinc oxide (ZnO).

Characteristics	Value	
Thermal expansion coefficient ($10^{-6}/\text{K}$)	$\alpha_a : 2.9\sim 3.2495$ ^[59, 66, 70] $\alpha_c : 4.75\sim 5.2069$ ^[59, 66, 70]	
Thermal conductivity at RT* (W/cm·K)	$\kappa_c : 0.46\sim 1.35$ ^[59-60, 66, 71]	
Specific heat with constant pressure at RT* (J/mol·K)	$C_p : 40.3$ ^[70]	
	<i>Bulk</i>	<i>Epitaxial</i>
Young's modulus, E_Y (Gpa)	111.2 ± 4.7 ^[59, 70]	310 ± 40 ^[70]
Hardness, H (Gpa)	5.0 ± 0.1 ^[59, 70]	5.75 ± 0.8 ^[70]
Bulk modulus, B_m (Gpa)	142.4 ^[70]	

* $RT \approx 300\text{K}$

Table 2.1. Several inelastic collision types within the plasma [140-141].

Collisions Types	Expression
Ionization	$e + O_2 \rightarrow O_2^+ + 2e$
Excitation	$e + O_2 \rightarrow O_2^* + e$
Recombination	$O_2^+ + O^- \rightarrow O_2 + O$
Dissociation	$e + O_2 \rightarrow O^- + O$
Radiation	$O_2^* \rightarrow O_2 + h\nu$
Charge Transfer	$O_2^+ + O_2 \rightarrow O_2 + O_2^+$
Elastic Scattering	$O_2^+ + O_2 \rightarrow O_2^+ + O_2$
Elastic Scattering	$O_2^- + O_2 \rightarrow O_2^- + O_2$

O_2^* means excited state of O_2 ; O_2 is oxygen.

Table 2.2. Approximation frequencies and vacuum wavelength ranges for various colors [153].

Color	λ_0 (nm)	ν (THz)*
Red	780-622	384-482
Orange	622-597	482-503
Yellow	597-577	503-520
Green	577-492	520-610
Blue	492-455	610-659
Violet	455-390	659-769

* 1 terahertz (THz) = 10^{12} Hz.

Table 4.1. The deposition conditions of ZnO thin films for thickness effect under a constant RF power.

Deposition Conditions	
<i>Fixed Condition</i>	
Base Pressure	7.5×10^{-7} torr
Working Pressure	15 mtorr
O ₂ /(Ar+O ₂) Ratio	0.5
Gas Flux	10 sccm
Distance (Target and Substrate)	80 mm
Substrate Temperature	RT
<i>Controlled Condition</i>	
RF Power	100 W
<i>Test Condition</i>	
Deposition Time	5 ~ 60 min.

Table 4.2. The deposition conditions of ZnO thin films for RF power effect under a constant thickness.

Deposition Conditions	
<i>Fixed Condition</i>	
Base Pressure	7.5×10^{-7} torr
Working Pressure	15 mtorr
O ₂ /(Ar+O ₂) Ratio	0.5
Gas Flux	10 sccm
Distance (Target and Substrate)	80 mm
Substrate Temperature	RT
<i>Controlled Condition</i>	
Thickness	60 nm ± 5%
<i>Test Condition</i>	
RF Power	50 ~ 400 W

Table 4.3. The deposition conditions of ZnO thin films for thickness effect under a constant O₂/(Ar+O₂) Ratio.

Deposition Conditions	
<i>Fixed Condition</i>	
Base Pressure	7.5×10 ⁻⁷ torr
Working Pressure	15 mtorr
RF Power	100 W
Gas Flux	10 sccm
Distance (Target and Substrate)	80 mm
Substrate Temperature	RT
<i>Controlled Condition</i>	
O₂/(Ar+O₂) Ratio	0.25
<i>Test Condition</i>	
Deposition Time	5 ~ 90 min.

Table 4.4. The deposition conditions of ZnO thin films for O₂/(Ar+O₂) Ratio effect under a constant thickness.

Deposition Conditions	
<i>Fixed Condition</i>	
Base Pressure	7.5×10^{-7} torr
Working Pressure	15 mtorr
RF Power	100 W
Gas Flux	10 sccm
Distance (Target and Substrate)	80 mm
Substrate Temperature	RT
<i>Controlled Condition</i>	
Thickness	60 nm \pm 5%
<i>Test Condition</i>	
O₂/(Ar+O₂) Ratio	0.1 ~ 1.0

Table 4.5. Various thicknesses of ZnO thin films for RF power effect.

Deposition Time (min.)	Thickness (nm)
5	~ 31.5
10	~ 46.0
20	~ 60.0
30	~ 90.1
60	~ 171.7

Table 4.6. Various thicknesses of ZnO thin films for O₂/(Ar+O₂) ratio effect.

Deposition Time (min.)	Thickness (nm)
5	~ 43.4
10	~ 51.4
20	~ 73.4
30	~ 129.6
60	~ 235.6
90	~ 369.9

Table 4.7. Various contact angles of ZnO thin films for RF power effect under a constant thickness.

Specimens	Contact Angle (°)
Blank Glass Substrate	52.5
<i>RF Power Effect</i>	
RF 50 W	68.9
RF 100 W	71.7
RF 200 W	72.2
RF 300 W	72.7
RF400 W	82

Table 4.8. Various contact angles of ZnO thin films for deposition time (thickness) effect under a constant RF power.

Specimens	Contact Angle (°)
Blank Glass Substrate	52.5
<i>Deposition Time (Thickness) Effect</i>	
5 min.	95.0
10 min.	81.8
20 min.	71.8
30 min.	83.9
60 min.	96.0

Table 4.9. Various contact angles of ZnO thin films for $O_2/(Ar+O_2)$ ratio effect under a constant thickness.

Specimens	Contact Angle (°)
Blank Glass Substrate	52.5
<i>$O_2/(Ar+O_2)$ Ratio Effect</i>	
0.10	93.6
0.25	92.7
0.50	86.0
0.75	90.1
1.00	96.5

Table 4.10. Various contact angles of ZnO thin films for deposition time (thickness) effect under a constant O₂/(Ar+O₂) ratio.

Specimens	Contact Angle (°)
Blank Glass Substrate	52.5
<i>Deposition Time (Thickness) Effect</i>	
5 min.	111.3
10 min.	81.4
20 min.	90.9
30 min.	94.7
60 min.	107.9
90 min.	109.7

Table 4.11. The deposition conditions of ZnO thin films for annealing temperature effect under a constant thickness.

Deposition Conditions	
<i>Fixed Condition</i>	
Base Pressure	7.5×10^{-7} torr
Working Pressure	15 mtorr
RF Power	400 W
O ₂ /(Ar+O ₂) Ratio	0.5
Gas Flux	10 sccm
Distance (Target and Substrate)	80 mm
Deposition Time	10 min.
<i>Controlled Condition</i>	
Thickness	200 nm ± 5%
Annealing Time	1 hour
Heating Rate	3 °C/sec.
<i>Test Condition</i>	
Annealing Temperature	200 ~ 500 °C

Table 4.12. Various lattice constants of ZnO thin films for annealing temperature effect.

Annealing Temperature (° C)	Lattice Constant (Å)
as-grown	5.24648
200	5.23548
300	5.20527
400	5.20468
500	5.20366

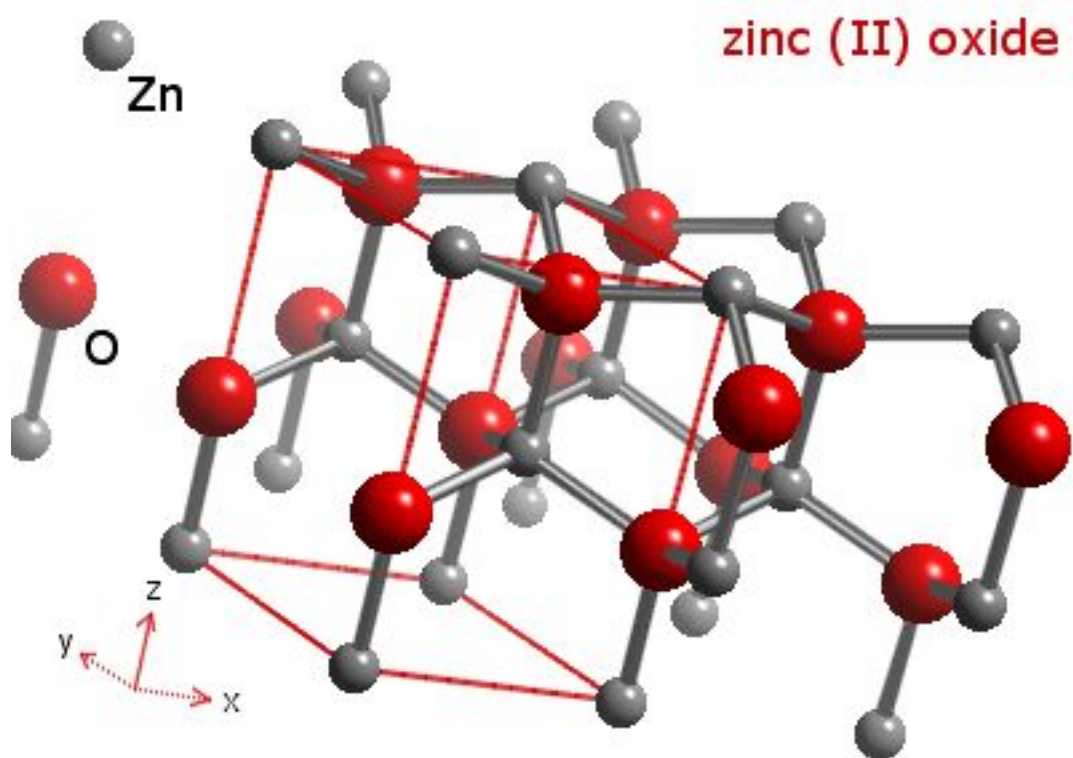


Figure 1.1. Hexagonal wurtzite structure of ZnO (small grey ball is zinc and big red ball is oxygen) [55].

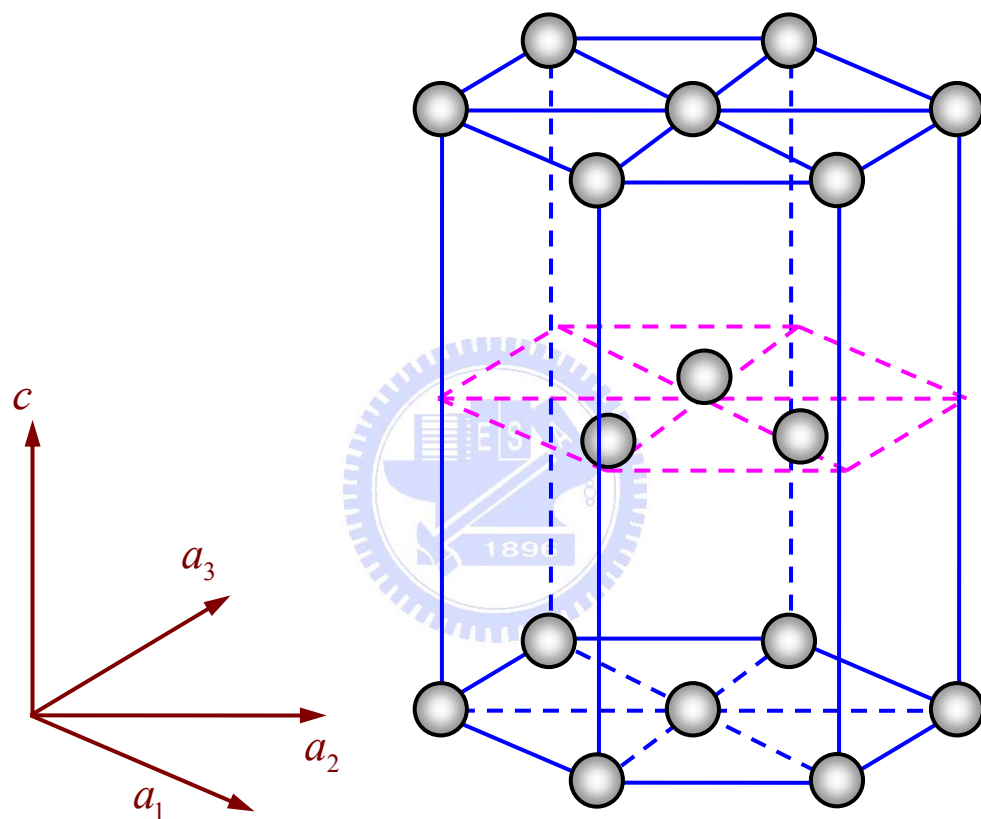


Figure 1.2. Hexagonal close-packed (HCP) structure of ZnO.

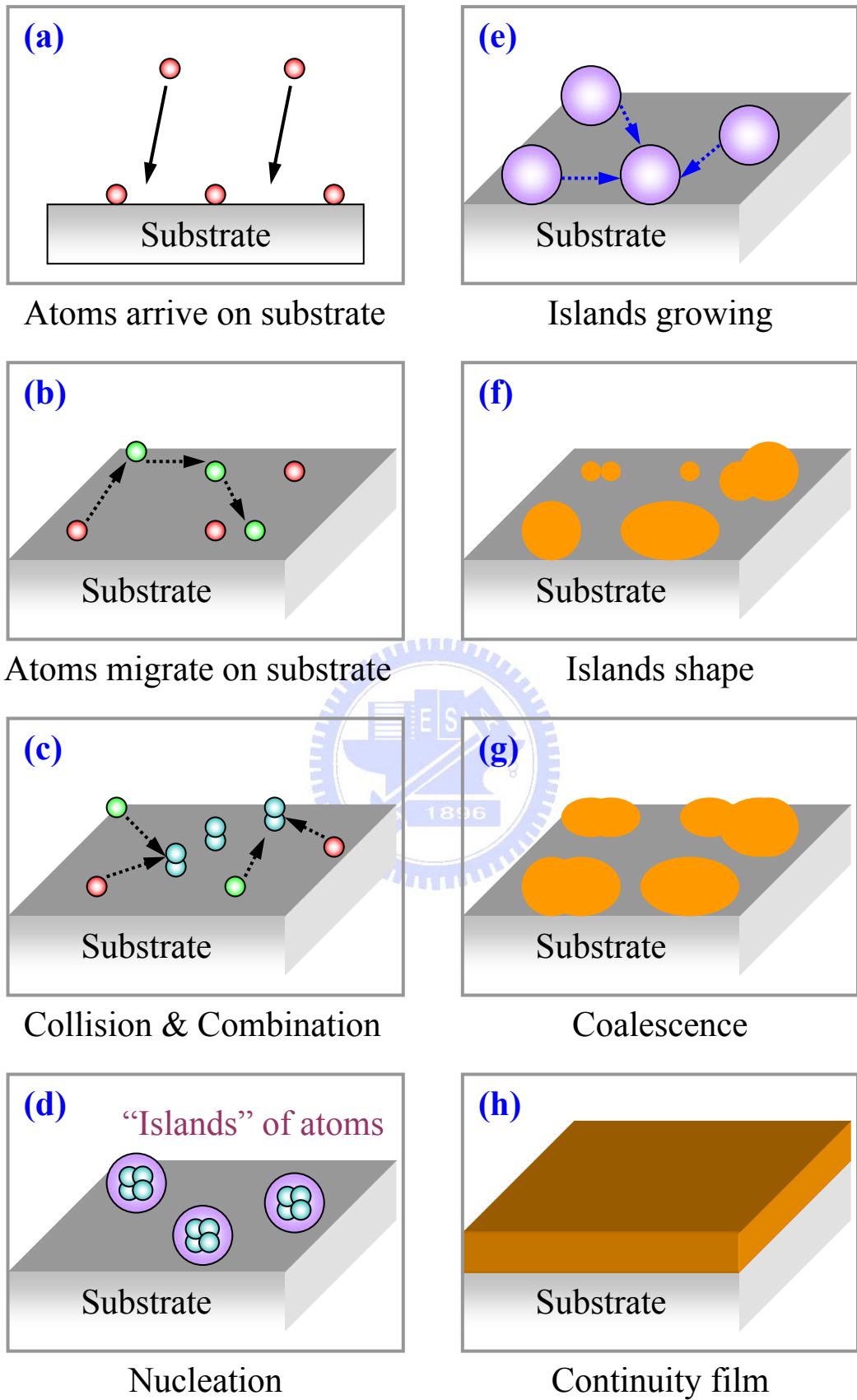


Figure 2.1. Schematic illustration of mechanism of thin film growth [136-137].

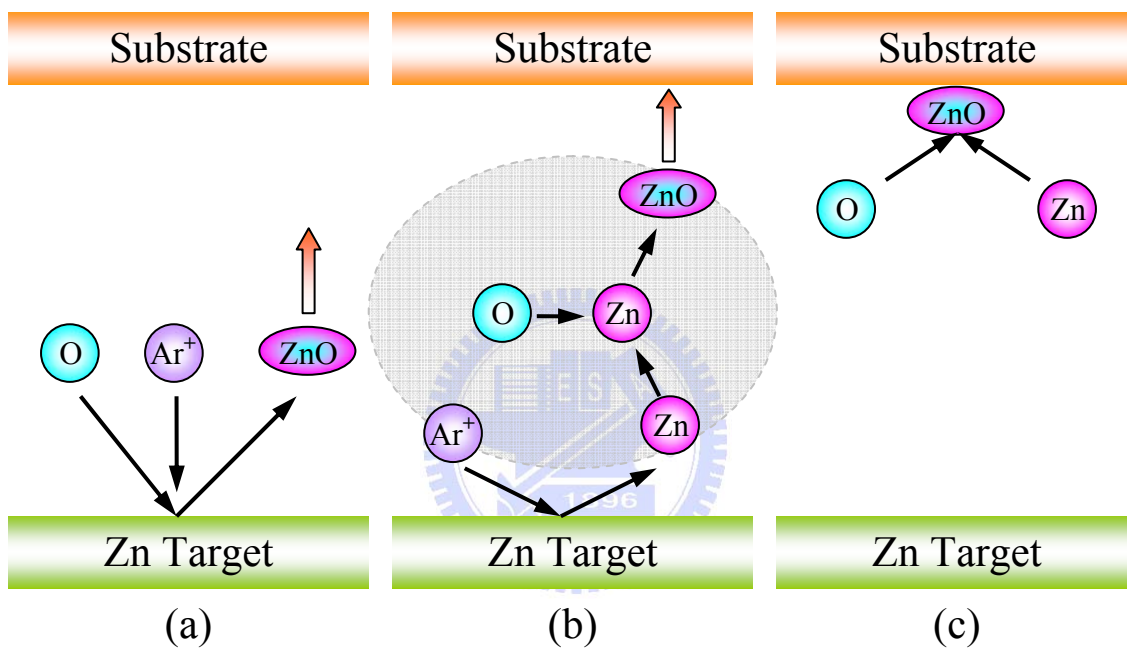


Figure 2.2. Three different mechanisms for reactive sputter deposition: (a) at the target; (b) in the plasma volume and (c) at the substrate [138].

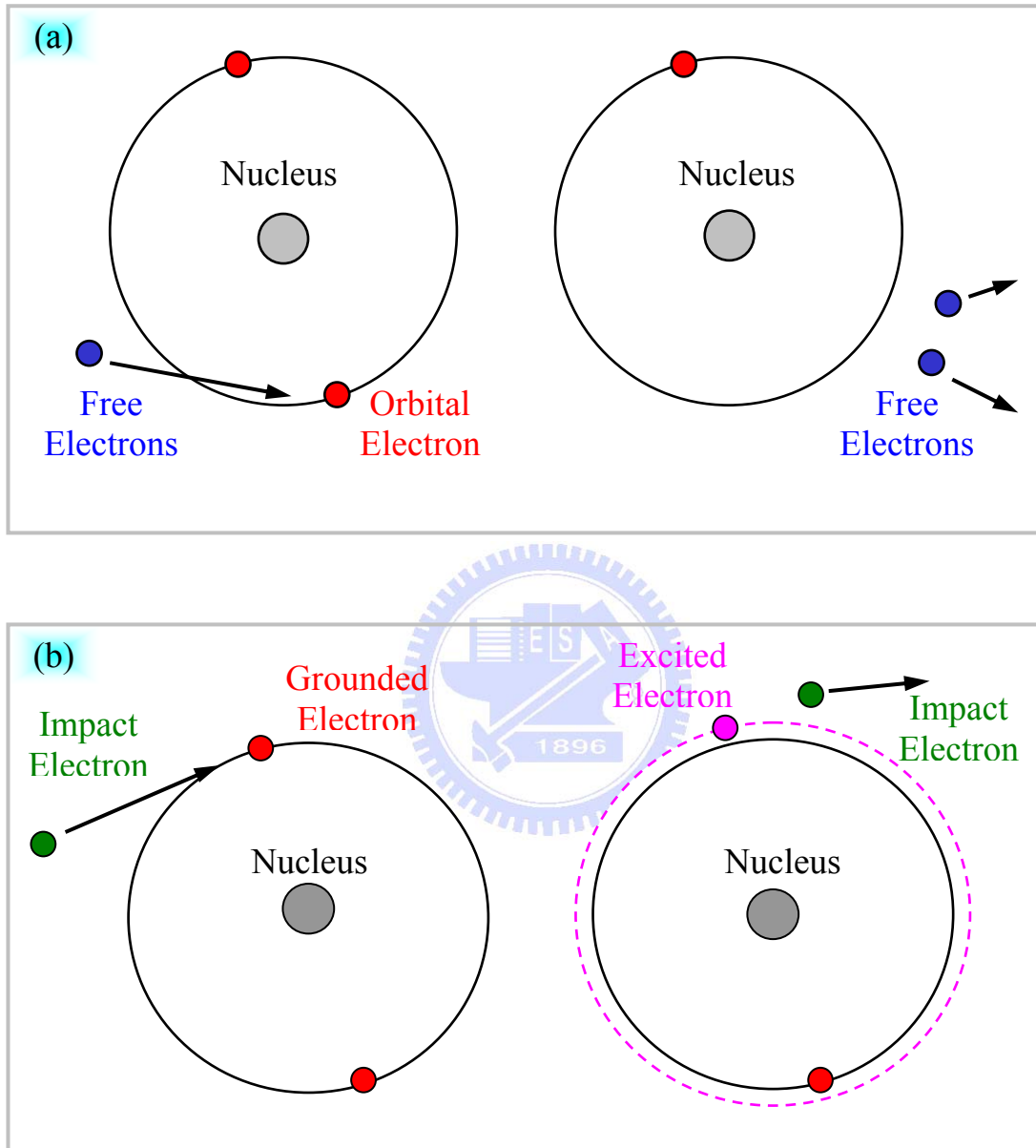


Figure 2.3. Several different electron-atom collisions: (a) ionization collision; (b)

excitation collision; (c) relaxation process and (d) dissociation process

[140].

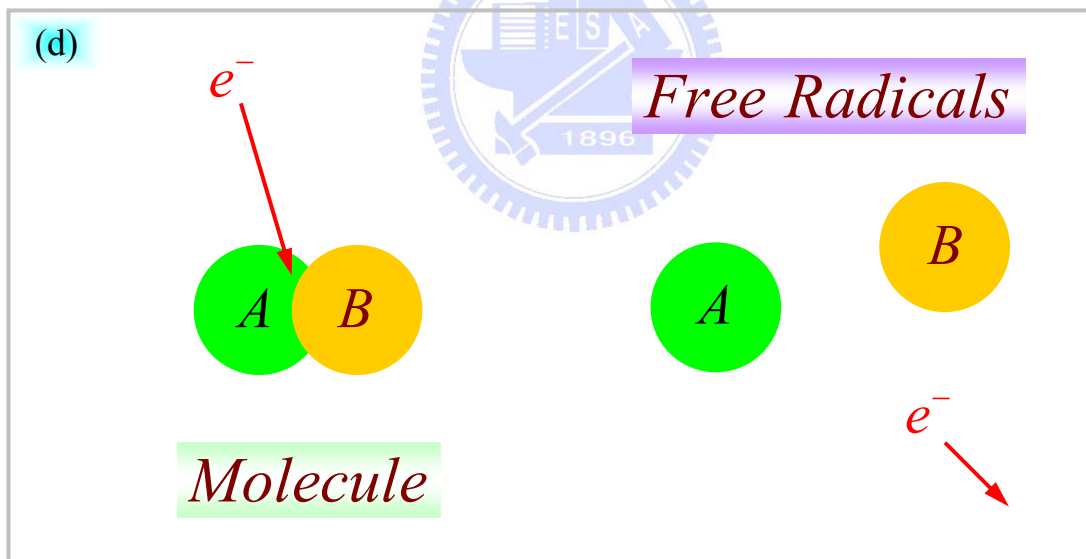
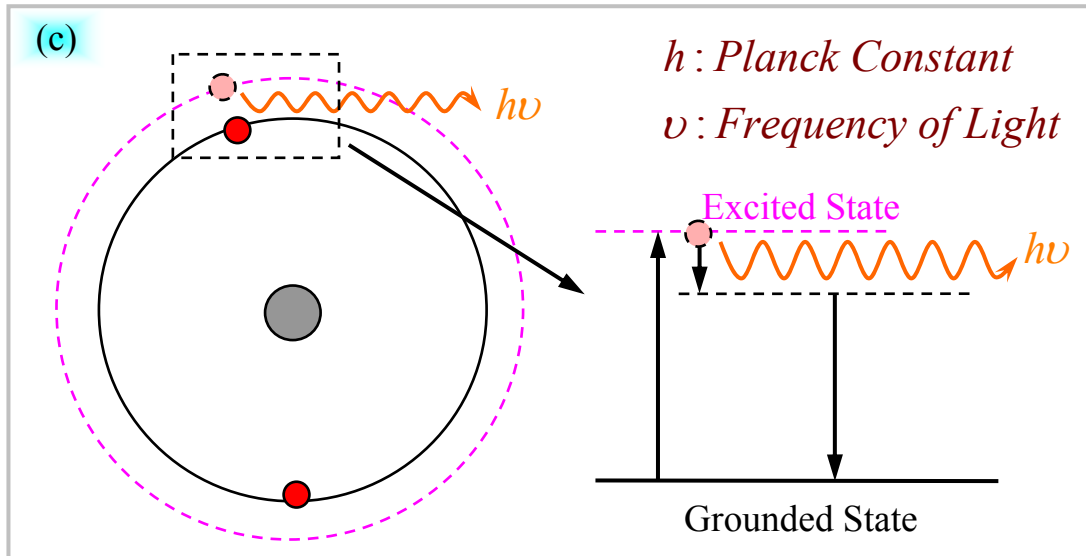


Figure 2.3. Several different electron-atom collisions: (a) ionization collision; (b)

excitation collision; (c) relaxation process and (d) dissociation process

[140]. (Continuous)

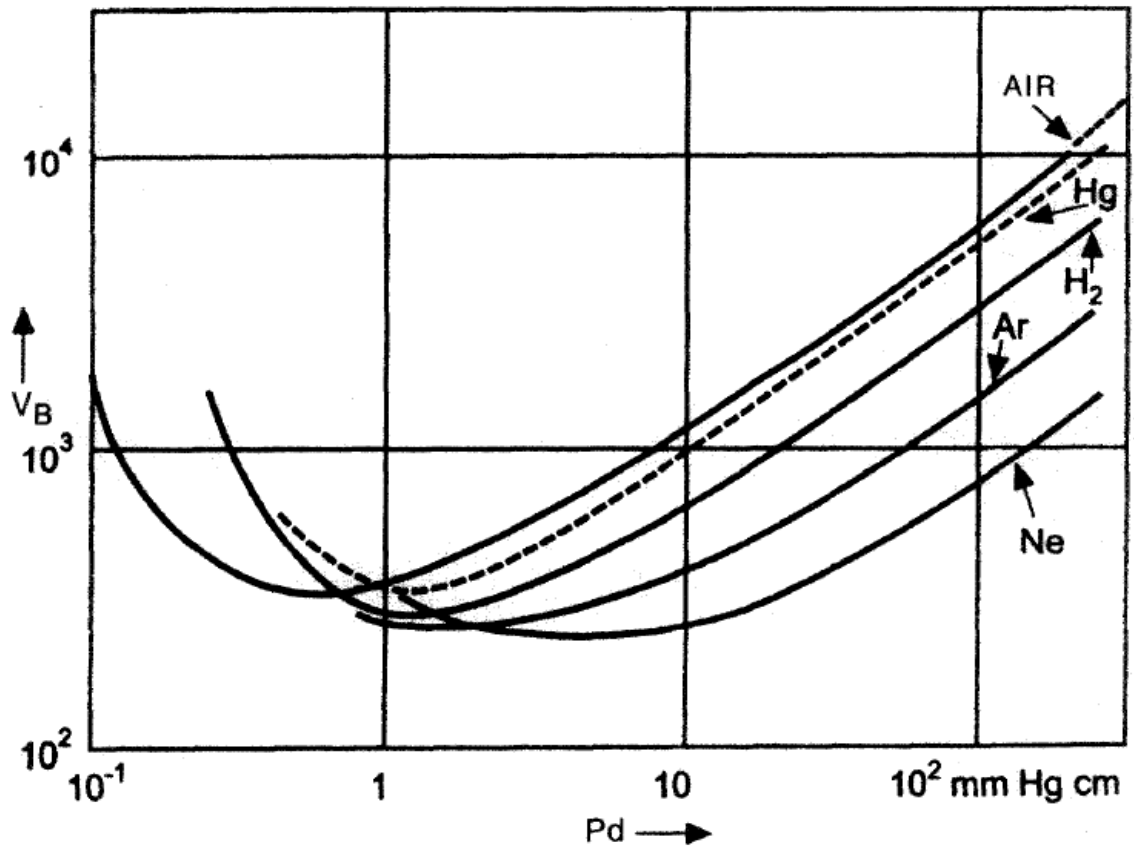


Figure 2.4. Paschen curve for a number of gases. (From A. von Engel, *Ionized Gases*. Oxford University Press, Oxford, 1965. Reprinted with permission) [143]

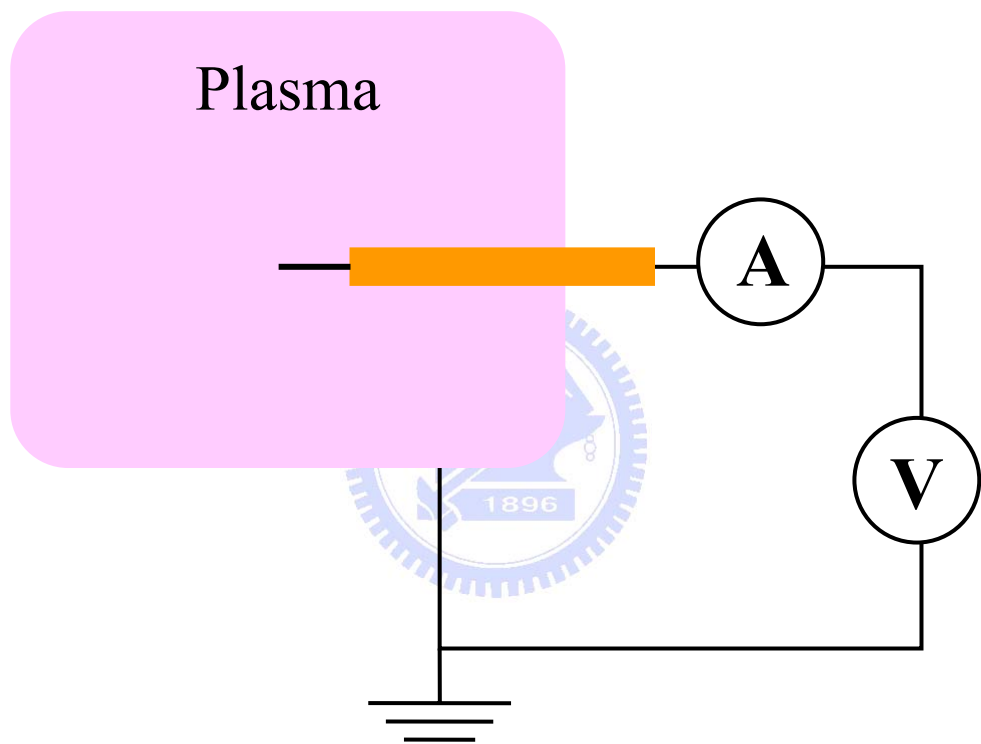


Figure 2.5. Schematic illustration of plasma diagnostic technique by using a Langmuir probe.

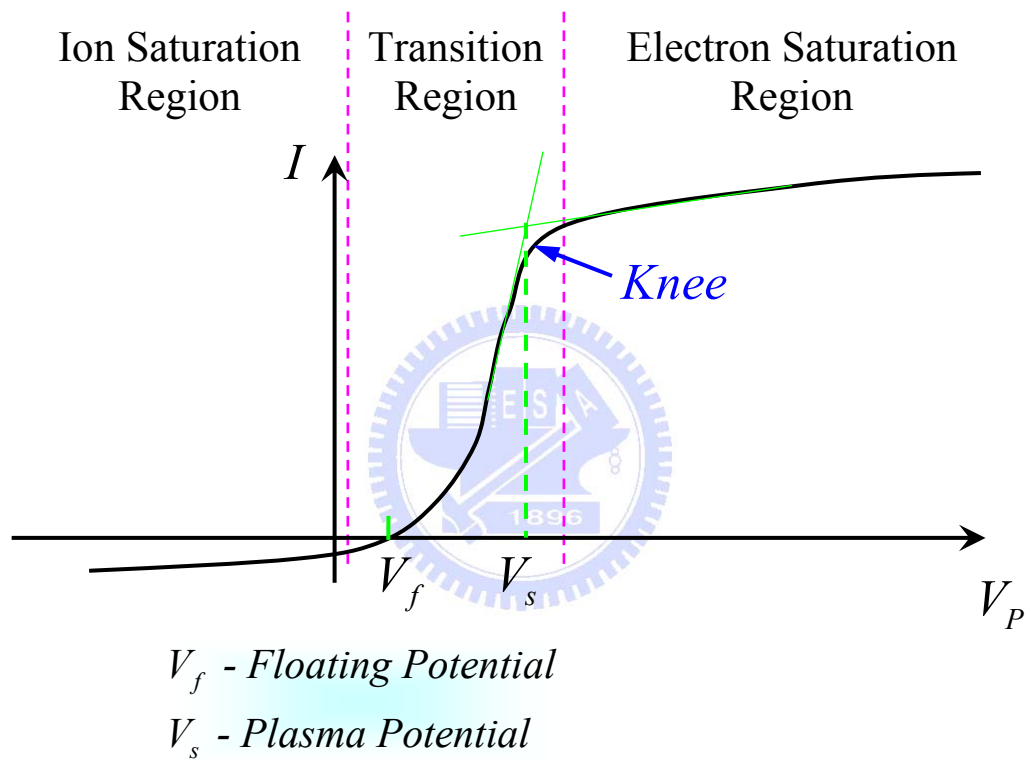


Figure 2.6. Typical I - V characteristics for a Langmuir probe.

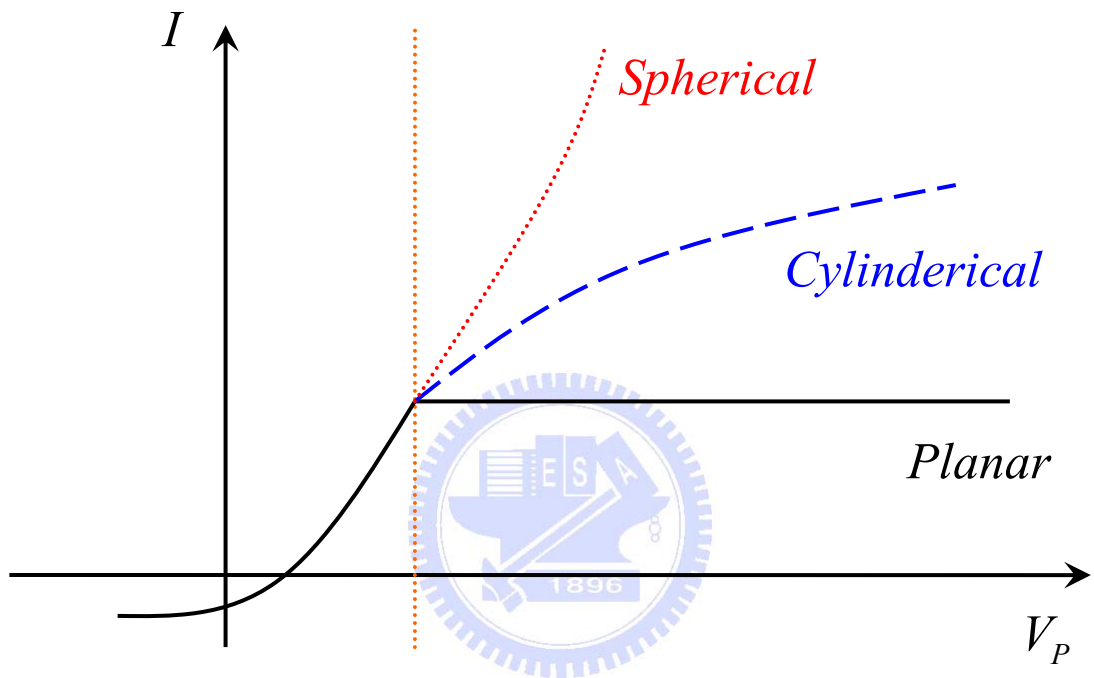


Figure 2.7. Theoretical shape of the saturation current portion of the probe characteristic for various probe shapes (planar, cylindrical and spherical) when the probe current is limited by orbital motions [119].

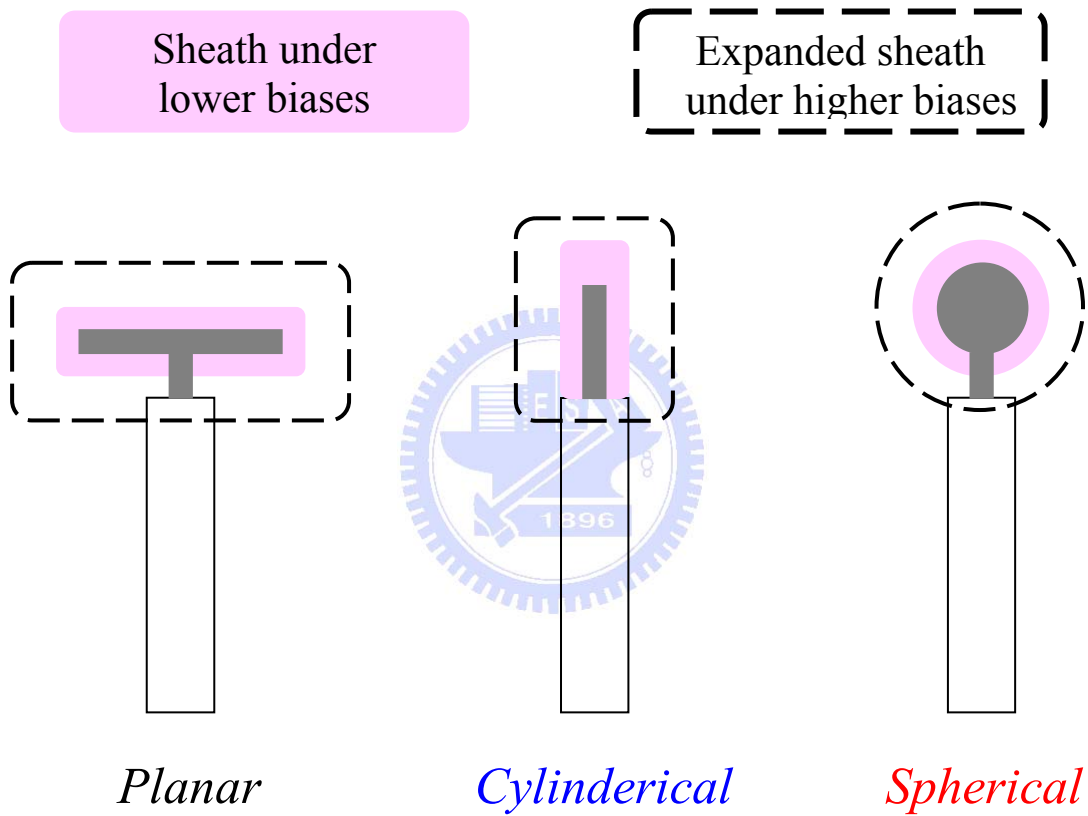


Figure 2.8. Schematic illustration of sheath forms with different geometry of probes.

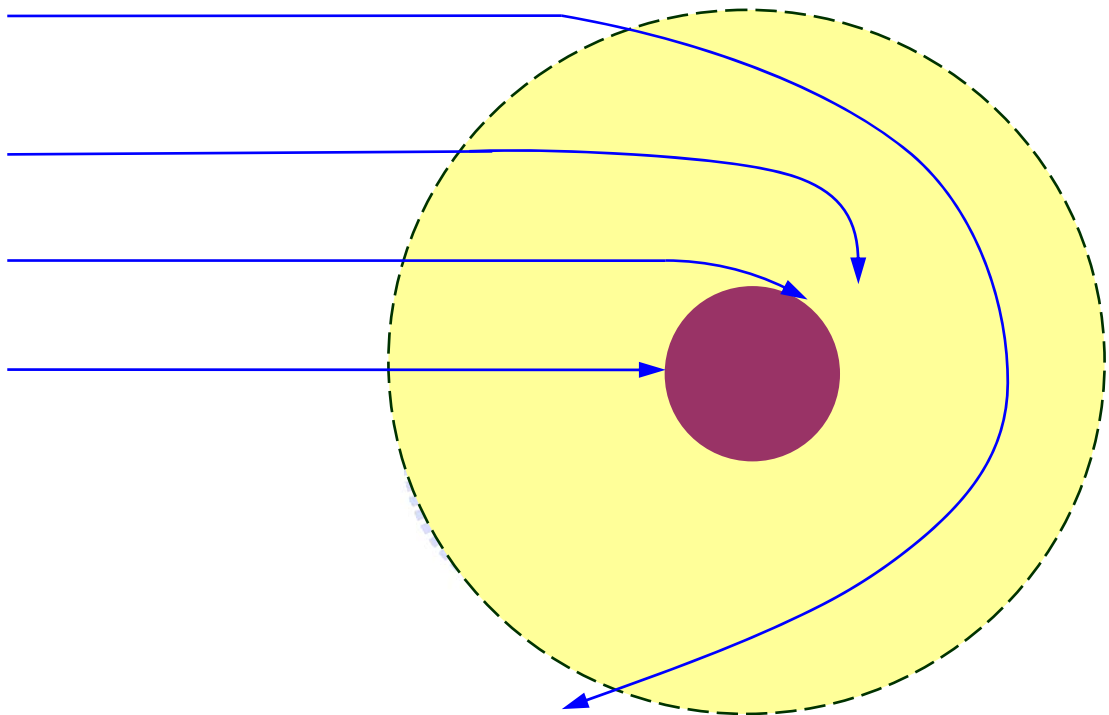


Figure 2.9. The charge particles arrive to the plasma sheath by orbital motion.

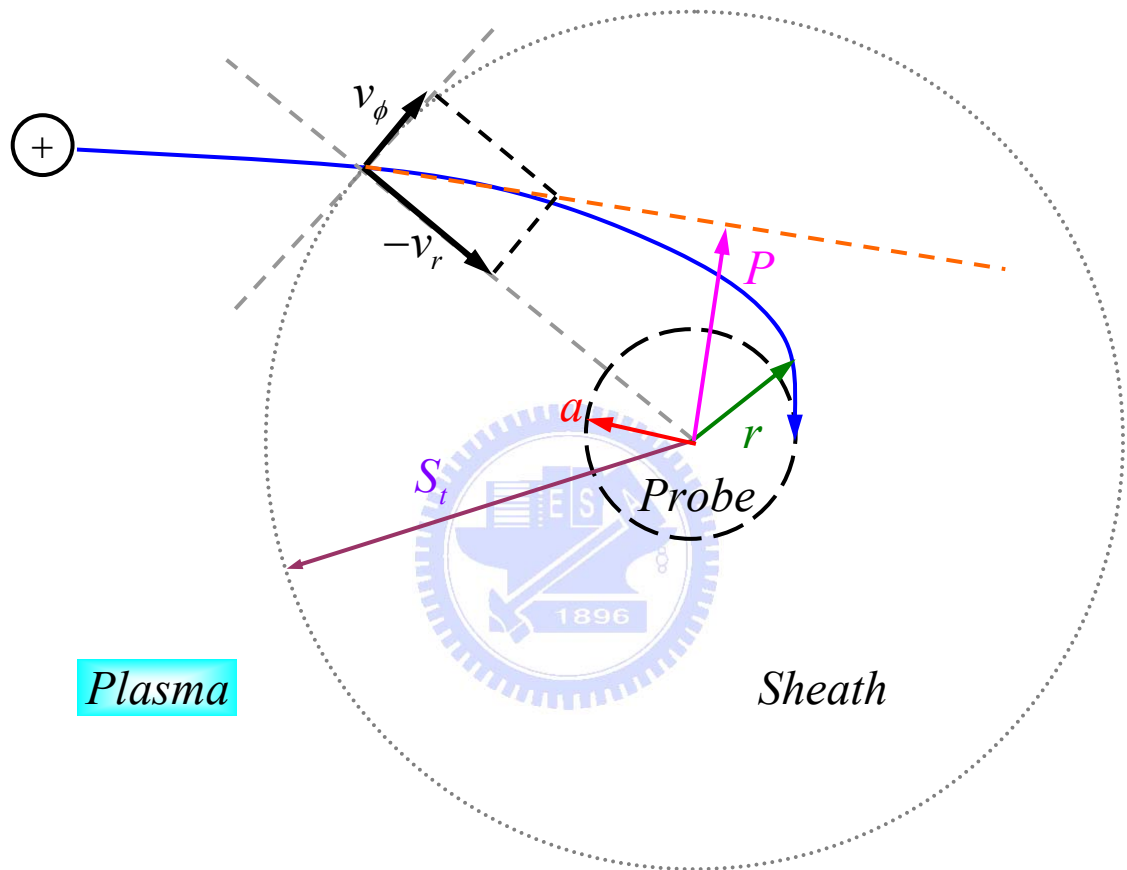


Figure 2.10. Ion orbital motion within the plasma sheath of a cylindrical Langmuir probe [141].

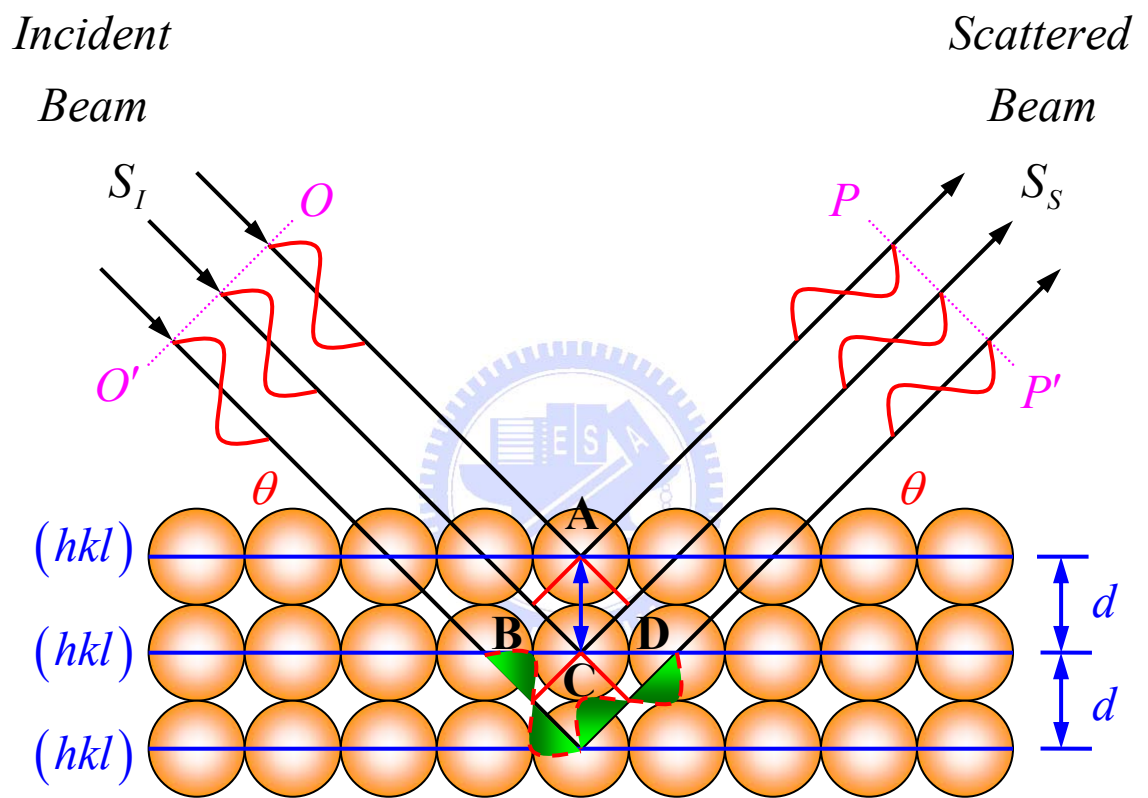


Figure 2.11. Schematic diagram of Bragg diffraction from a set of parallel planes.

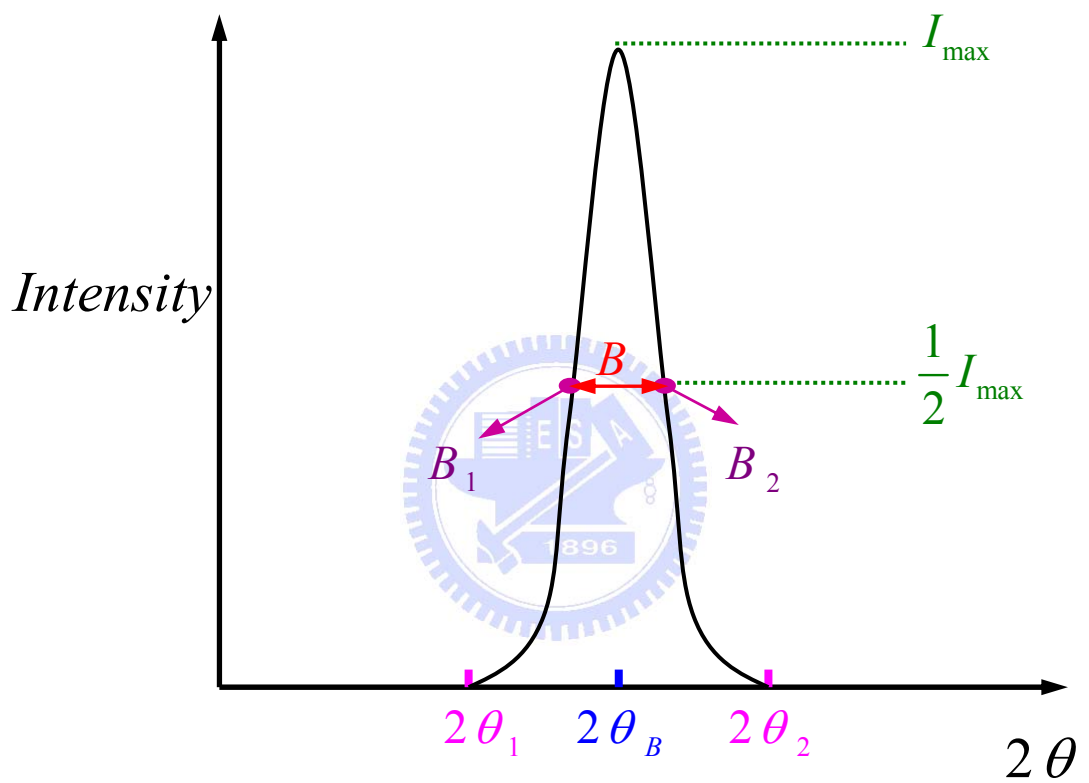


Figure 2.12. Schematic diagram of x-ray diffraction peak for calculating the grain size (crystallite size) by Scherrer equation.

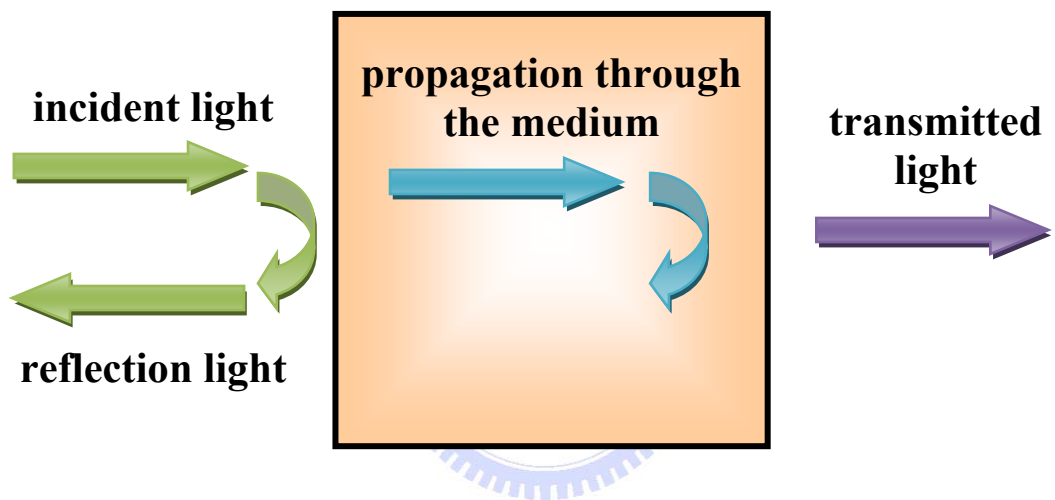


Figure 2.13. Reflection, propagation and transmission of a light beam incident on an optical medium [152].

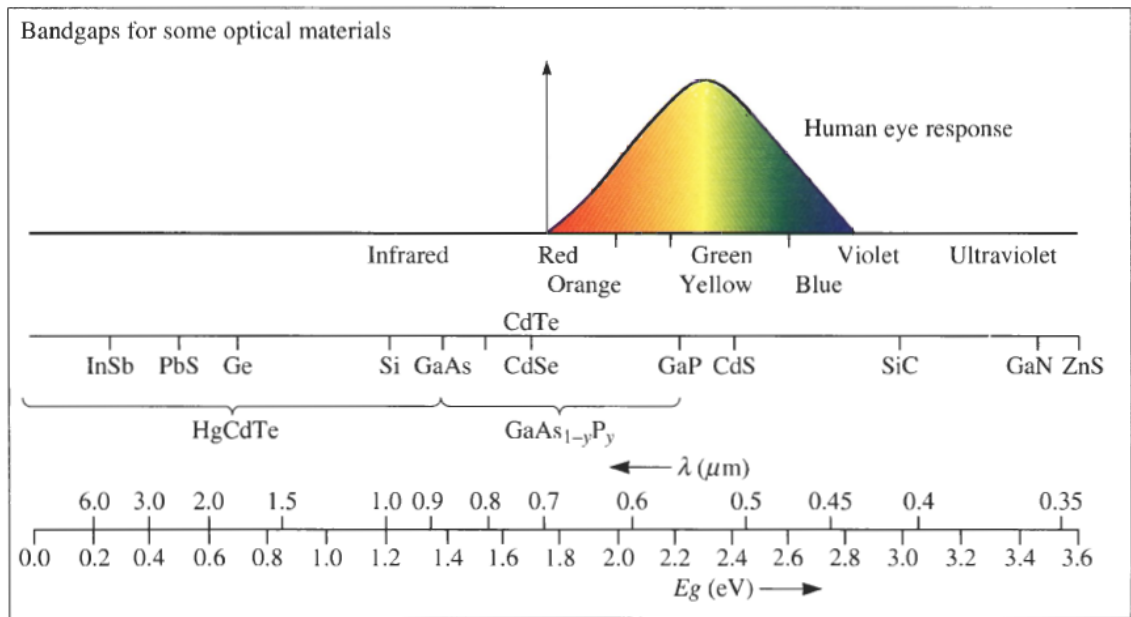
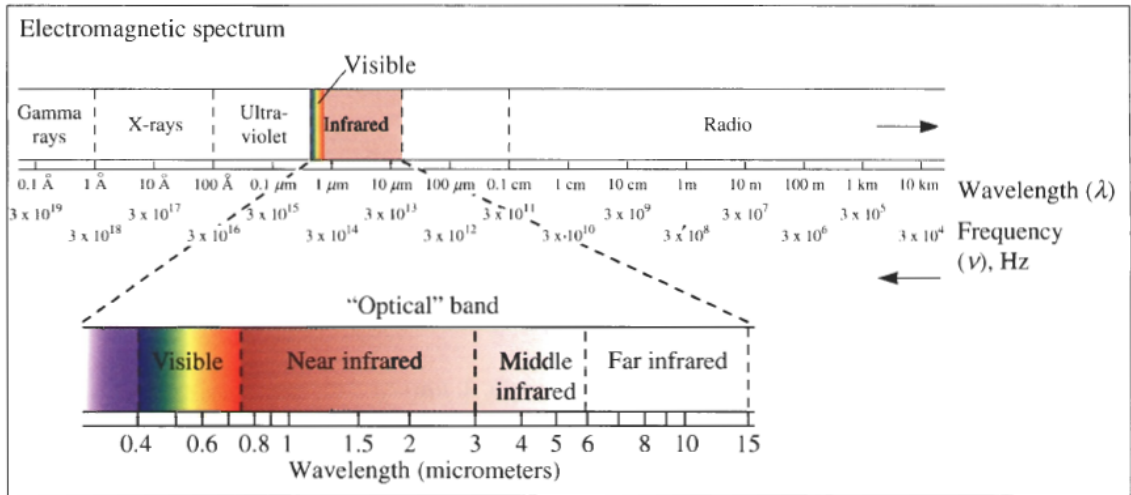


Figure 2.14. The electromagnetic spectrum of radiation; the bandgaps and cutoff

frequencies for some optical materials are also shown [154].

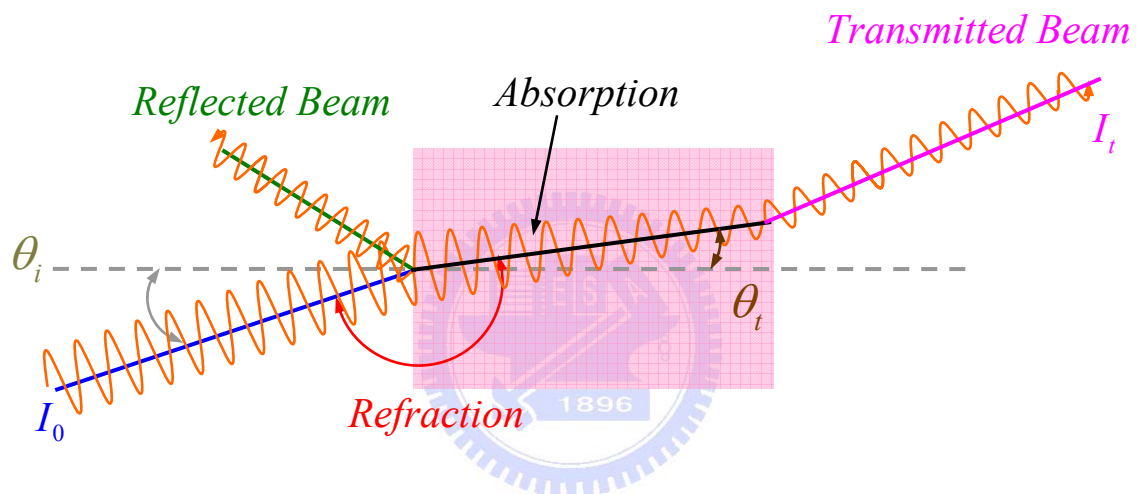


Figure 2.15. Interaction of photons with a material. In addition to reflection, absorption, and transmission, the beam changes direction, or is refracted.

The change in direction is given by the index of refraction n [154].

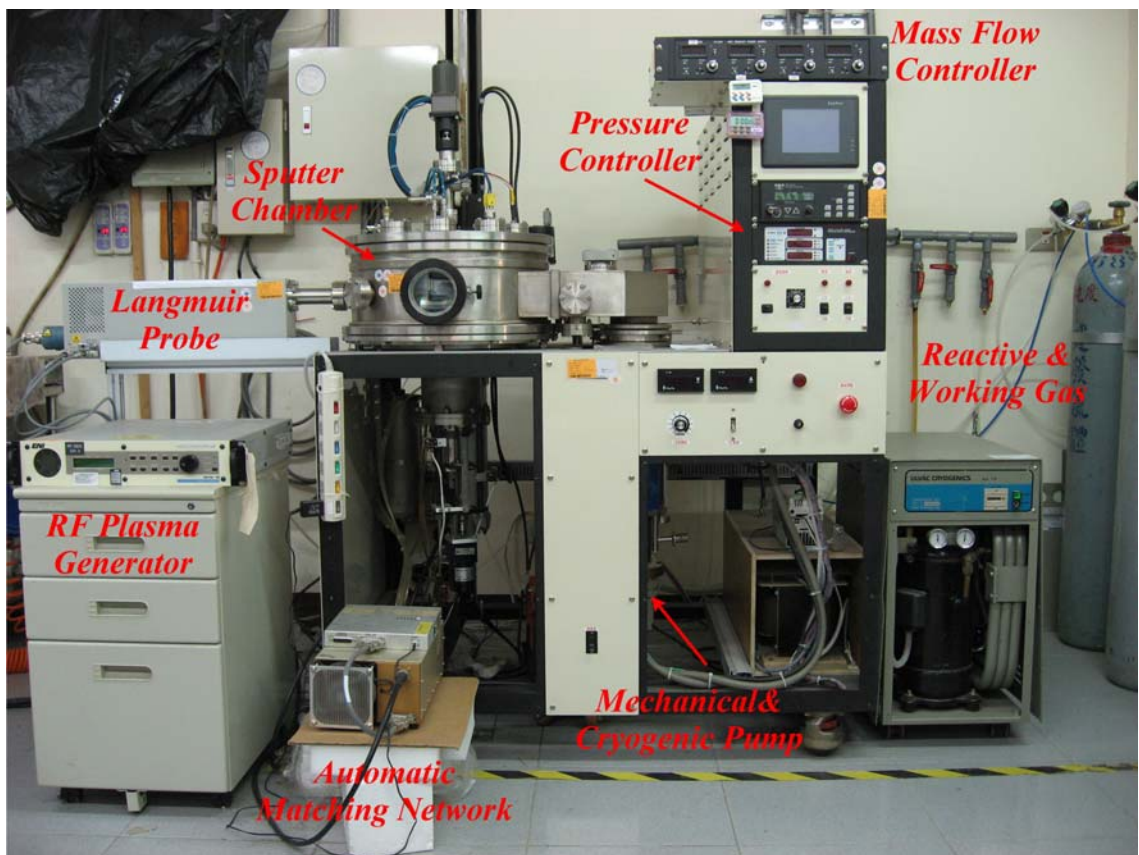


Figure 3.1. The configuration of RF reactive magnetron sputtering system.

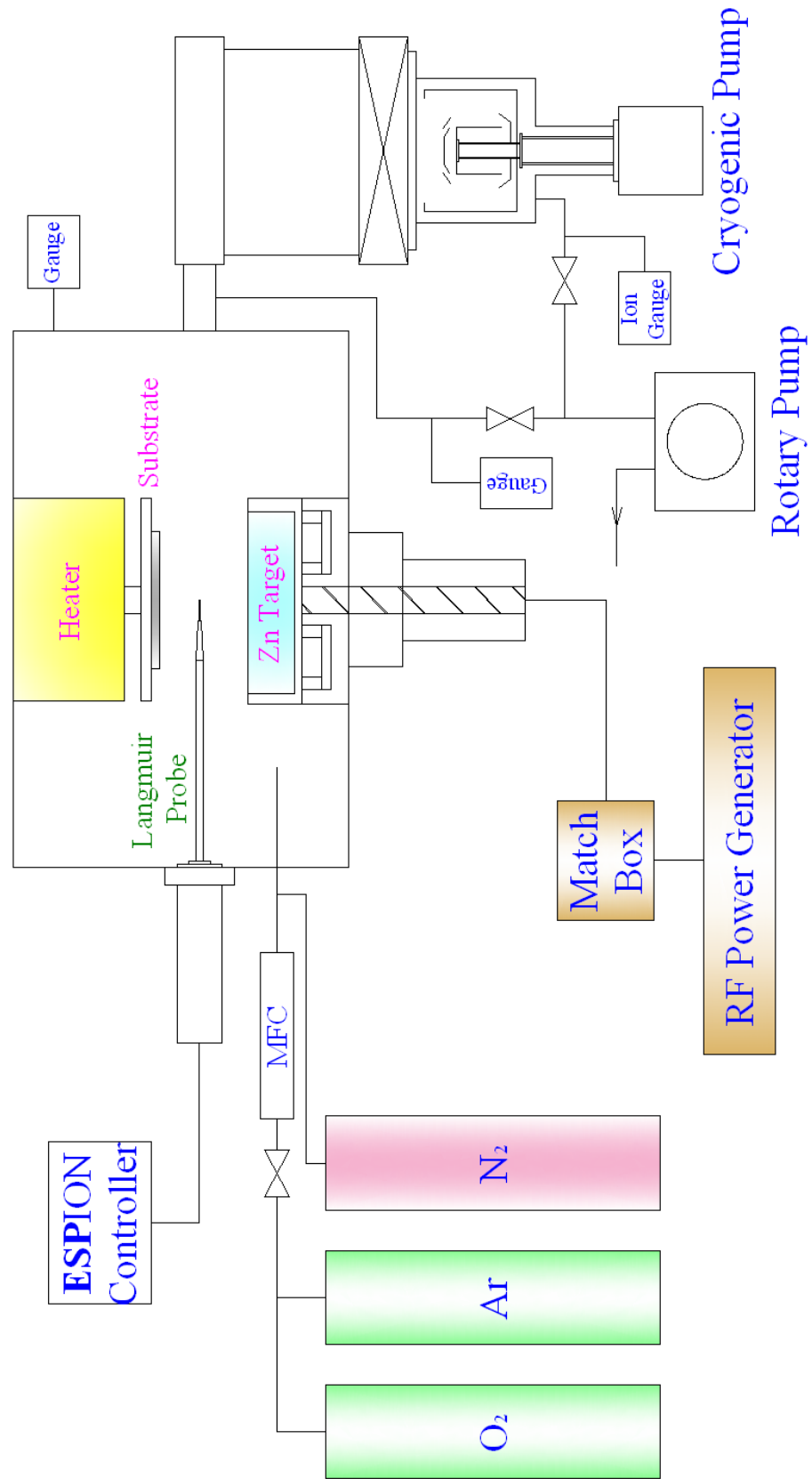
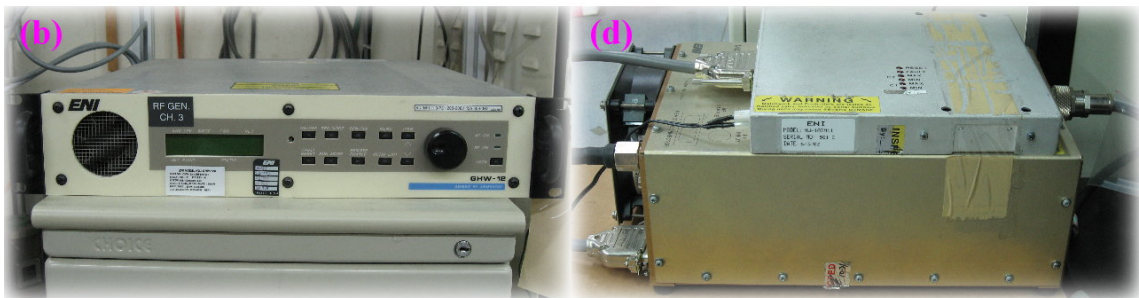


Figure 3.2. Schematic illustration of RF reactive magnetron sputtering system.



Top View



Front View

Side View

Figure 3.3. The configuration of RF power system. (a) Top and (b) front view of RF plasma generator system, respectively; (c) top and (d) side view of automatic matching network system, respectively.

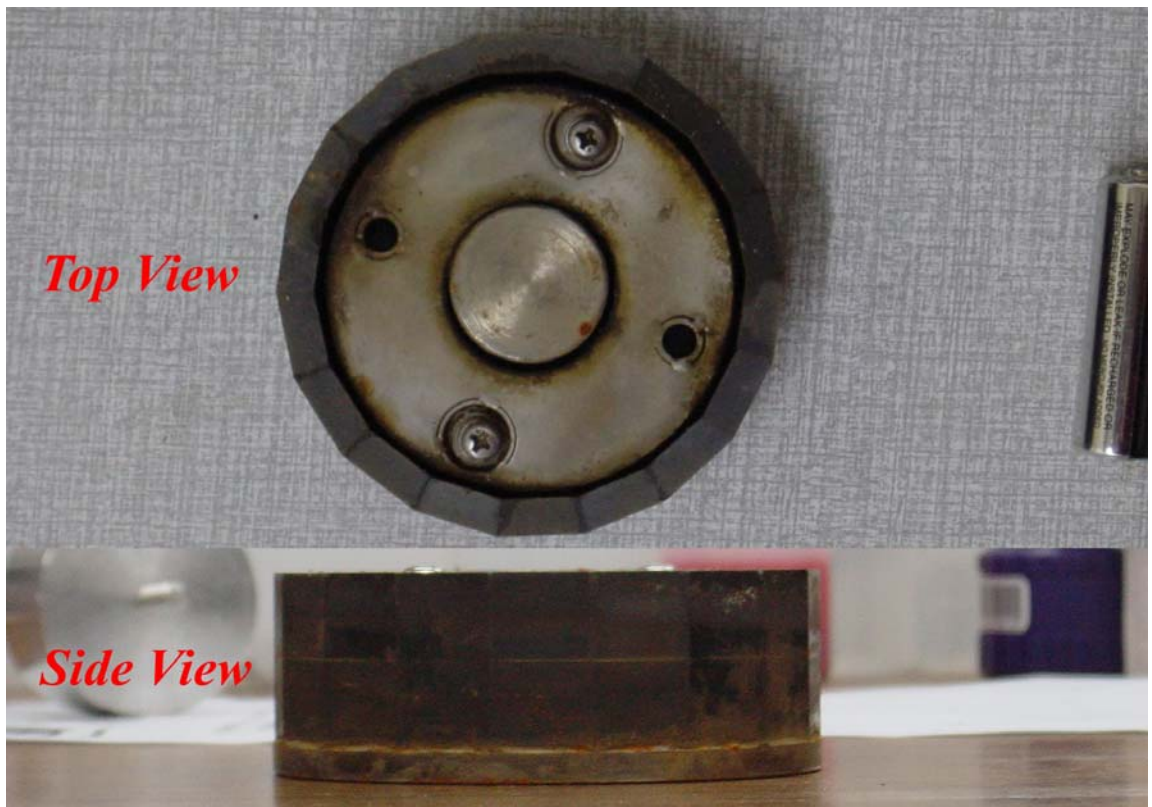


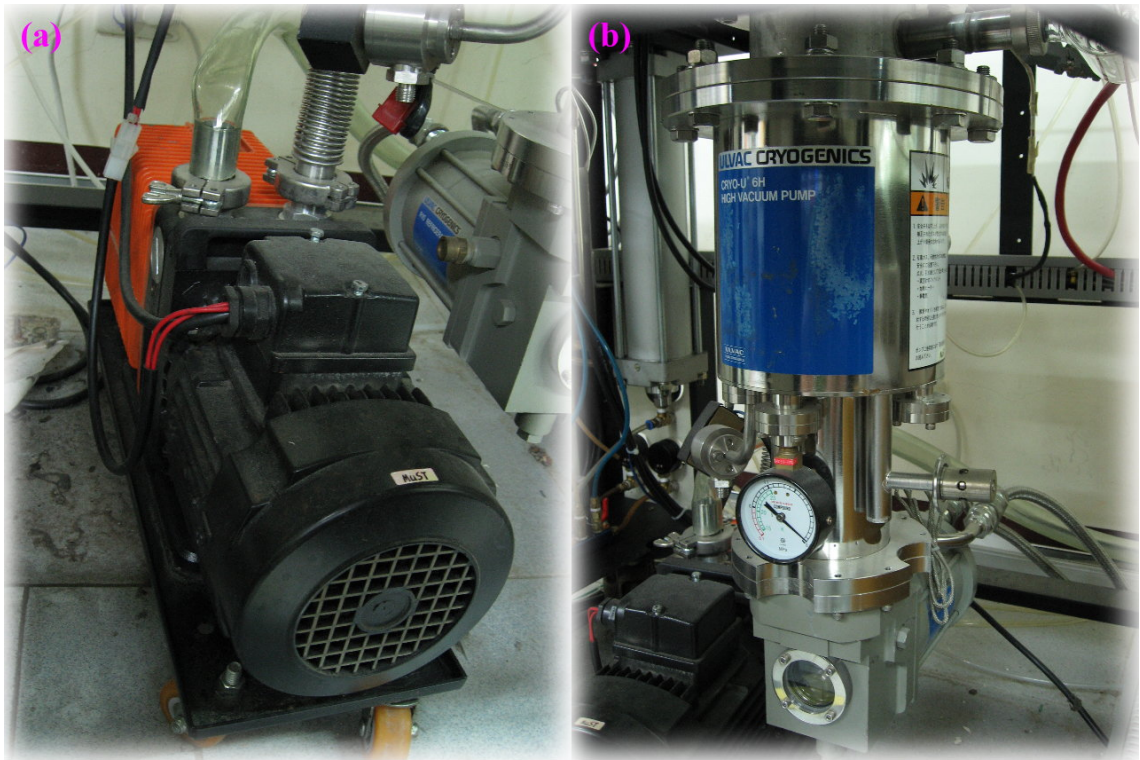
Figure 3.4. The configuration of Magnetron System.



Figure 3.5. The configuration of temperature controller system.



Figure 3.6. The configuration of mass flow controller (MFC) system.



Mechanical Pump

Cryogenic Pump

Figure 3.7. The configuration of (a) mechanical pump and (b) cryogenic pump.



Figure 3.8. The configuration of MKS self-tuning controller.

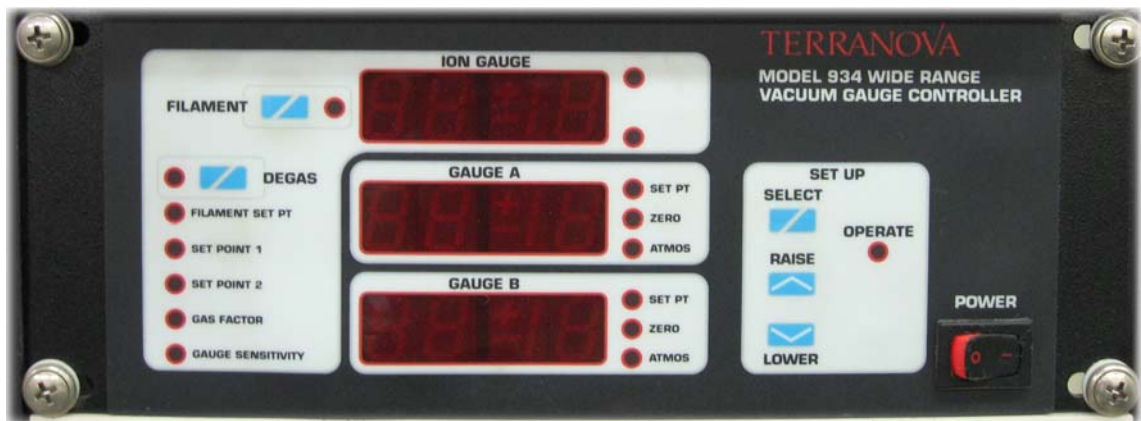


Figure 3.9. The configuration of ionization & low vacuum gauge controller.



Figure 3.10. The configuration of Baratron capacitance manometer.



Figure 3.11. The configuration of thermocouple gauge.

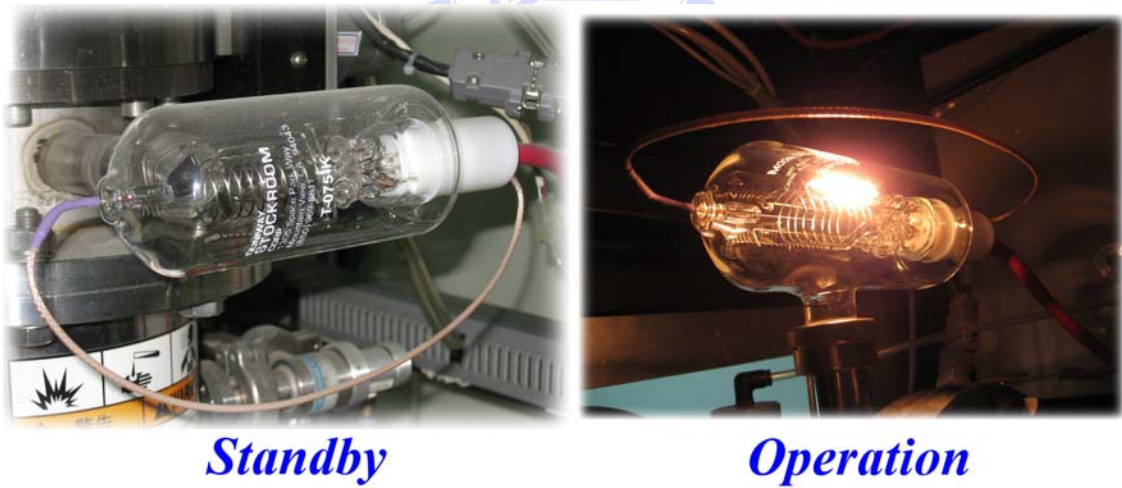


Figure 3.12. The configuration of ion gauge.



Langmuir Probe



Standard ESP Analysis System

Figure 3.13. The configuration of standard ESP analysis system with motorized Z-motion drive (Langmuir probe system).

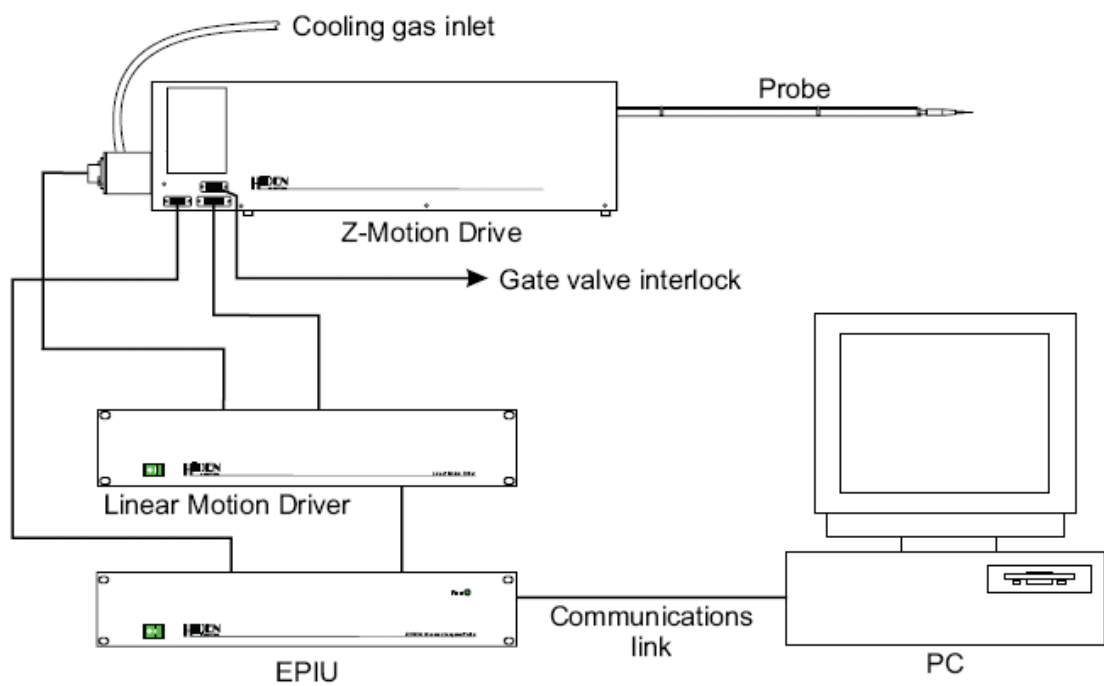


Figure 3.14. Schematic illustrations of standard ESP analysis system with motorized Z-motion drive (Langmuir probe system).

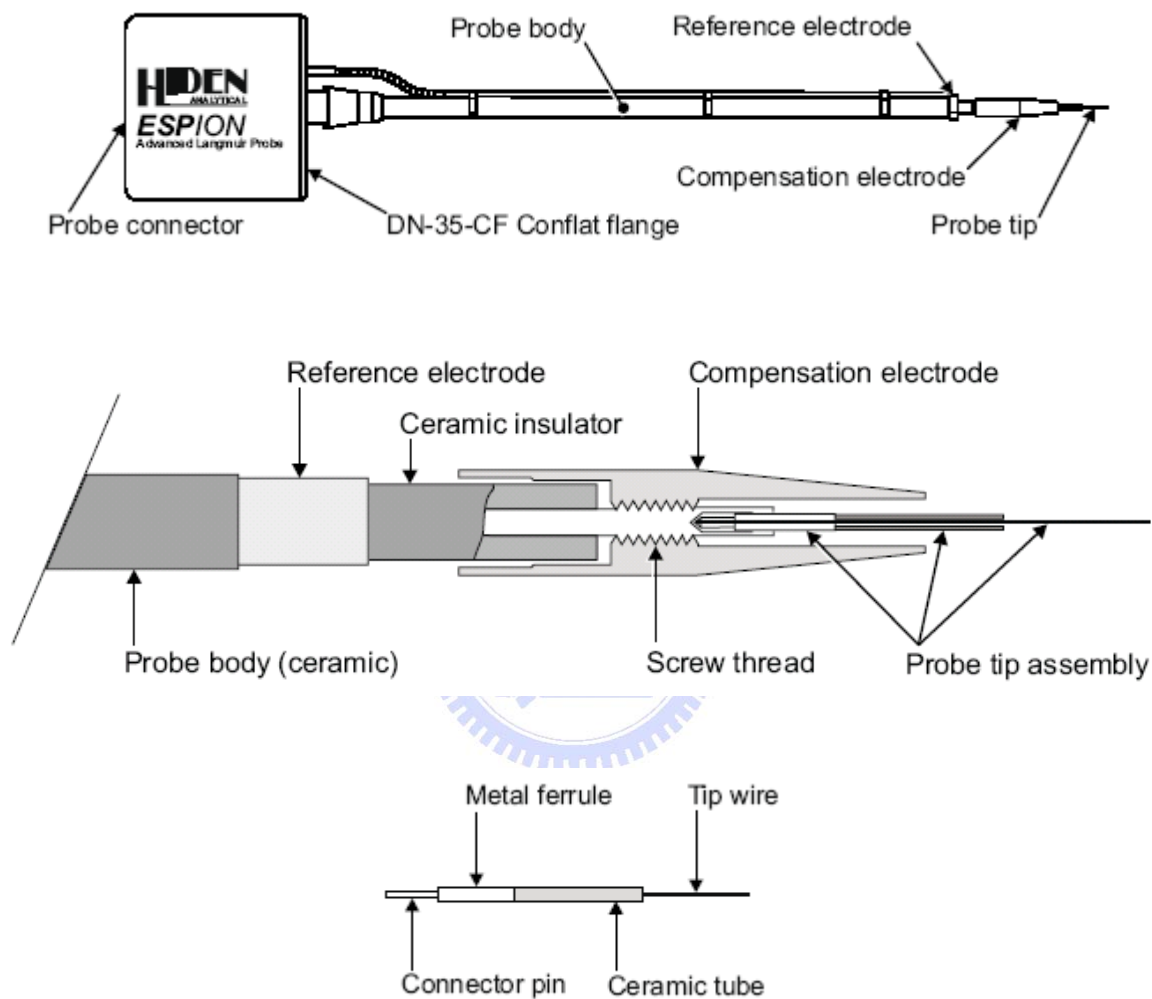


Figure 3.15. Schematic illustration of construction of a cylindrical probe. (a)

RF-compensated probe outline; (b) compensation electrode and probe

tip detail; (c) probe tip assembly.

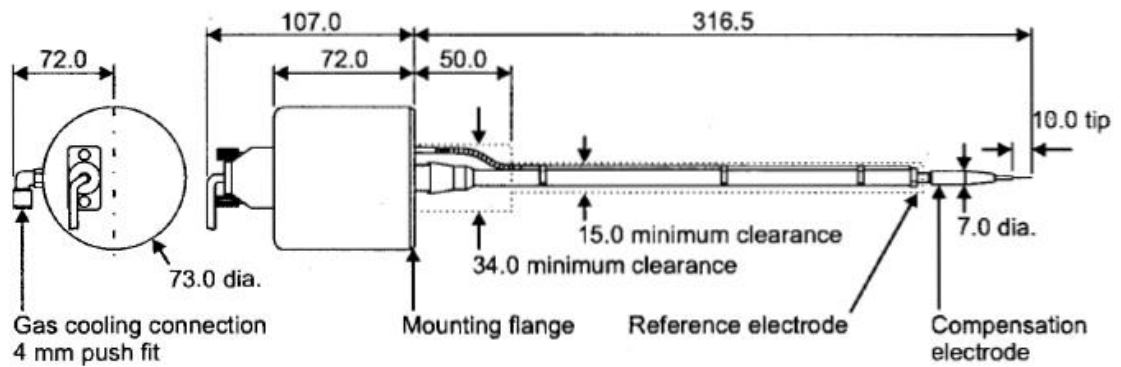


Figure 3.16. Schematic illustration of a RF-compensated probe for fixed installations and motorised Z-motion drives.

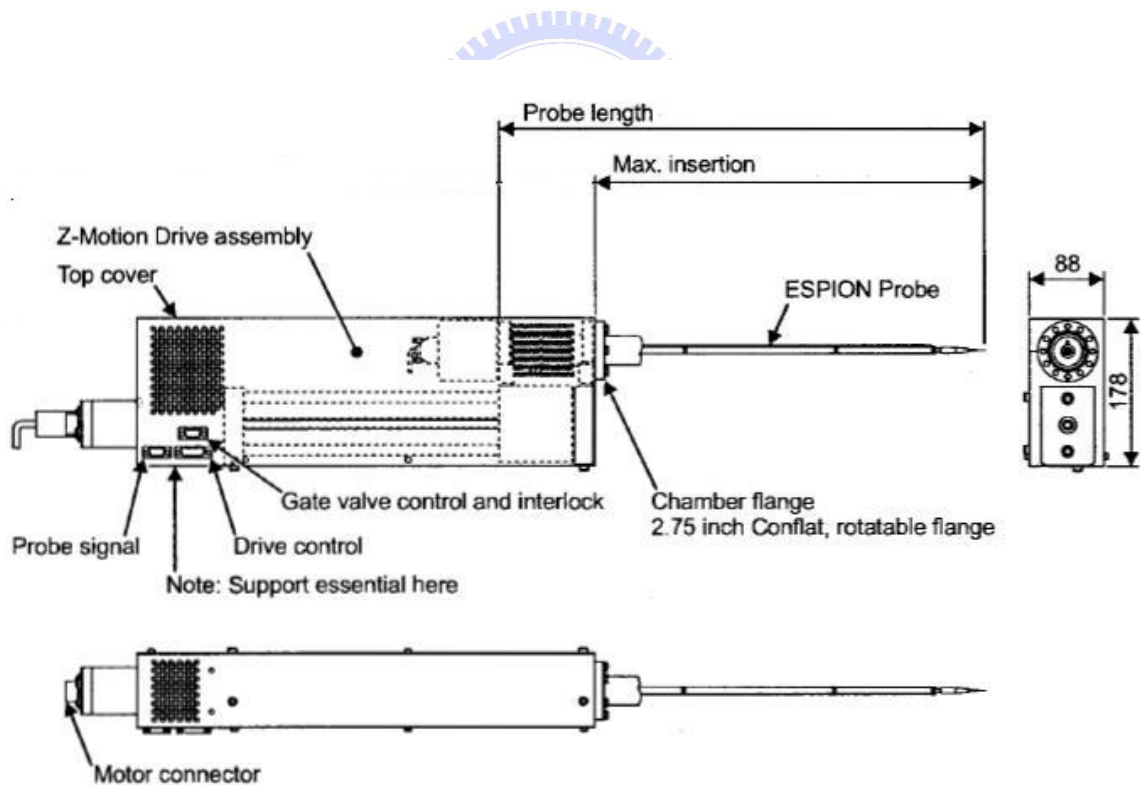


Figure 3.17. Schematic illustration of a typical automatic Z-motion driver.



Figure 3.18. The configuration of surface profilometer (Sloan Dektak 3030 profilometer).



Figure 3.19. The configuration of X'Pert PRO x-ray diffractometry (XRD). (Source by PANalytical)

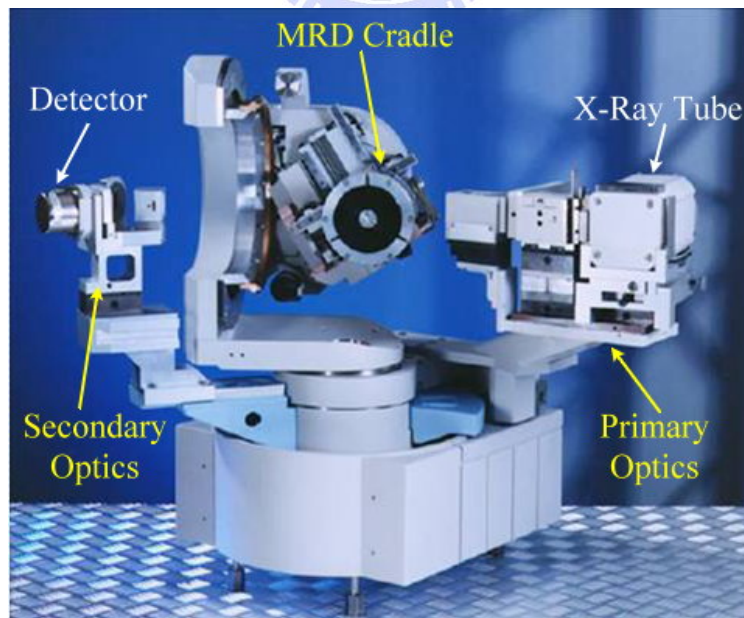
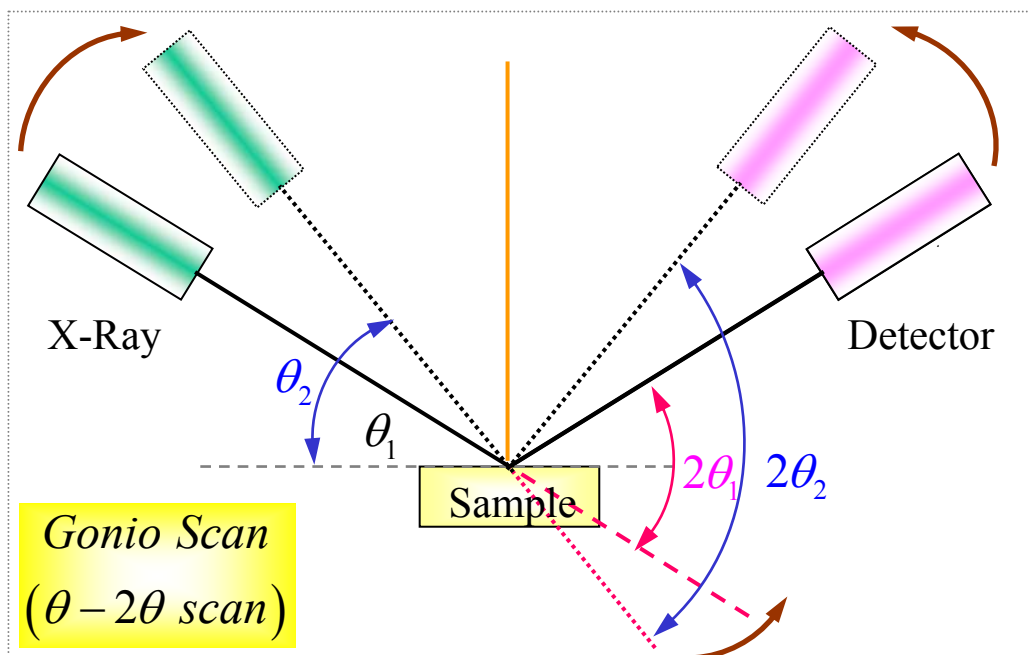
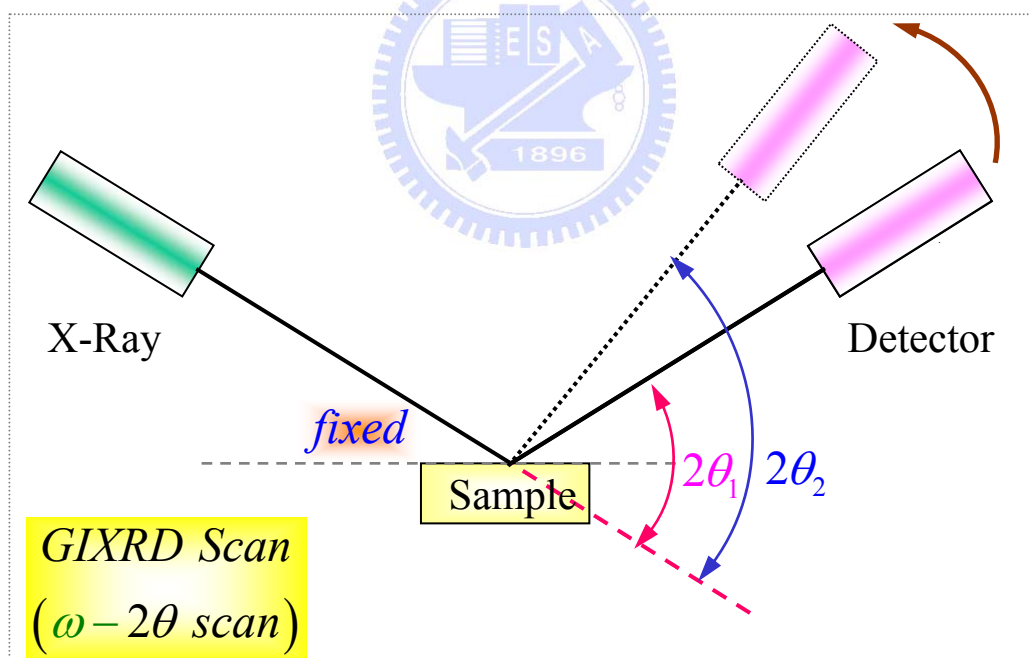


Figure 3.20. The configuration of goniometer of x-ray diffractometry (XRD). (Source by PANalytical)



(a)



(b)

Figure 3.21. Schematic diagram of x-ray diffraction measured techniques: (a)

Gonio scan and (b) GIXRD scan.



Figure 3.22. The configuration of UV-VIS spectrophotometer.



Figure 3.23. The configuration of contact angle system.

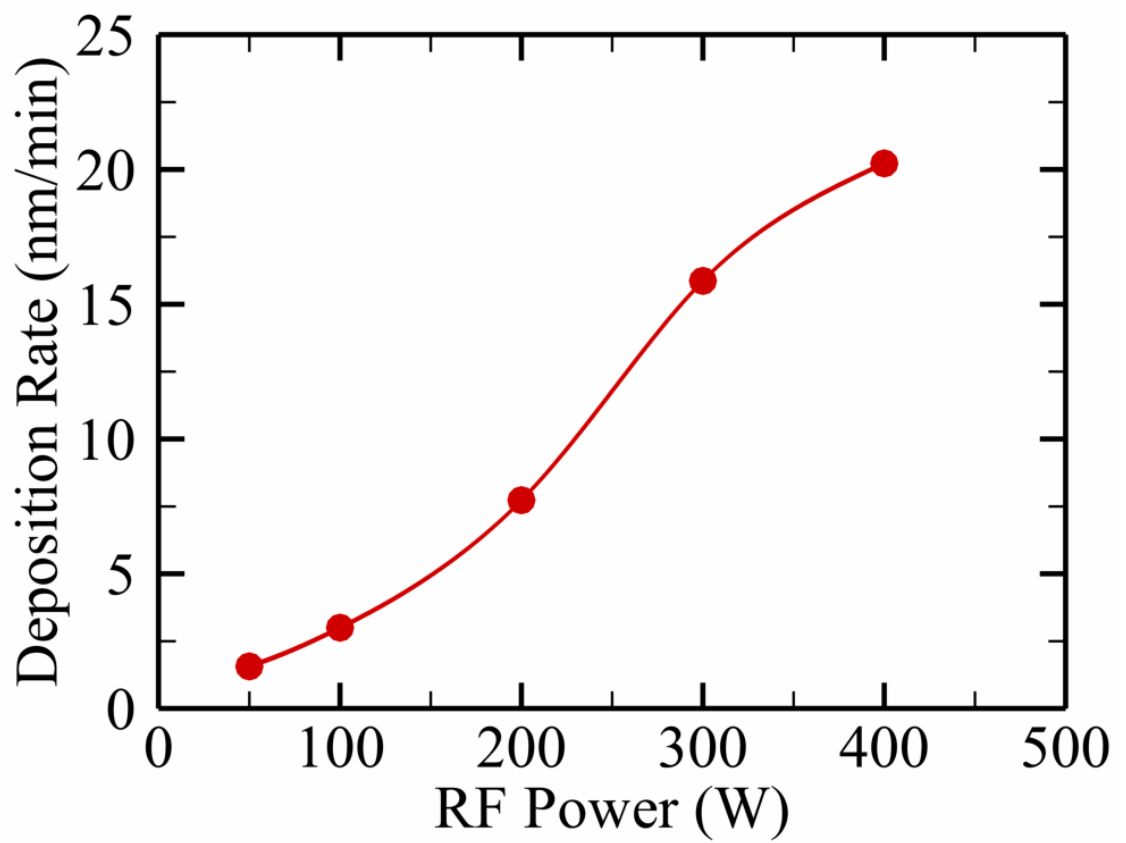


Figure 4.1. Effect of deposition rate as a function of applied RF power at a constant thickness of 60 nm.

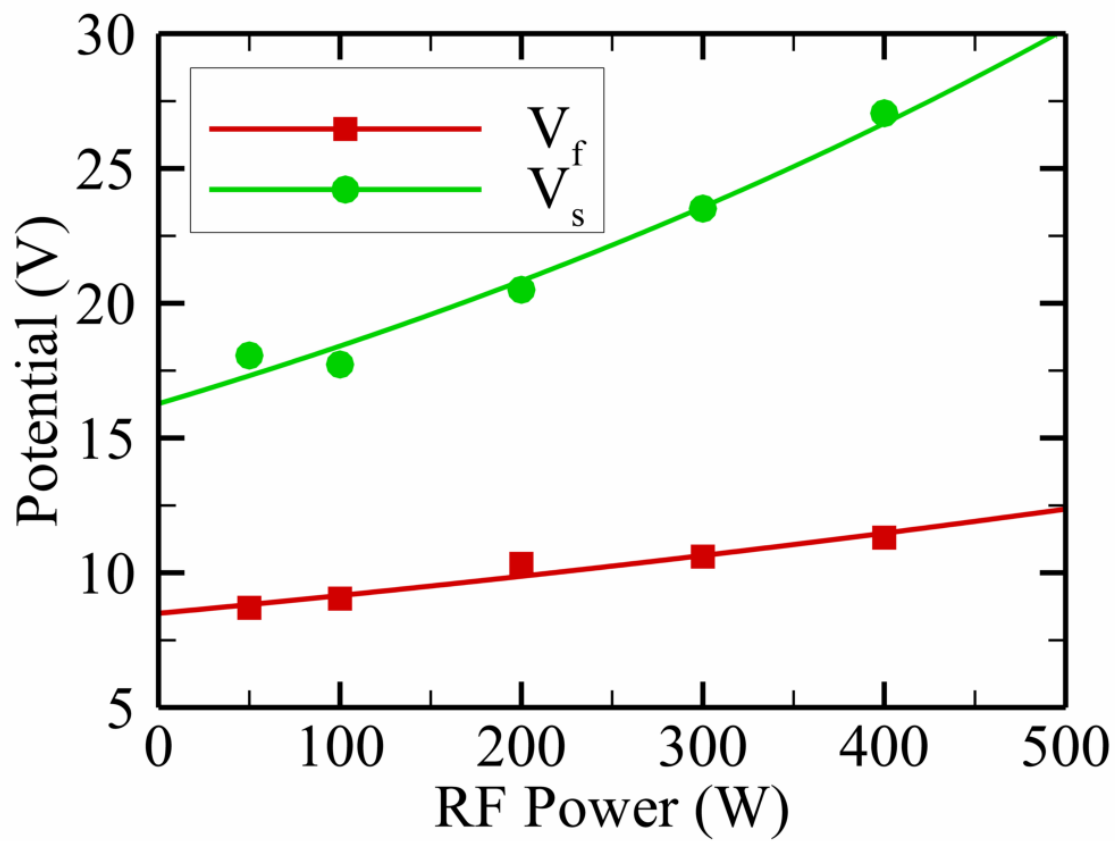


Figure 4.2. The floating potential (V_f) and plasma potential (V_s) as a function of applied RF power during ZnO thin film deposition.

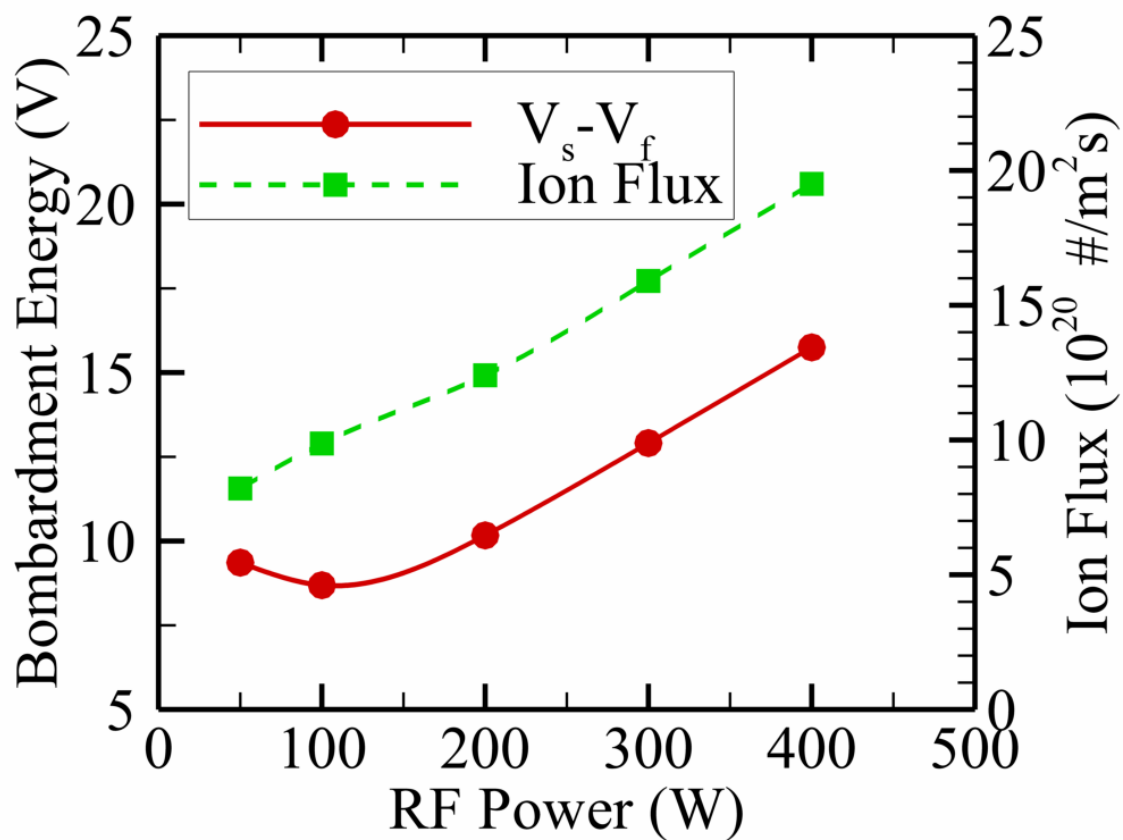


Figure 4.3. The ion flux and ion bombardment energy ($V_s - V_f$) as a function of applied RF power during ZnO thin film deposition.

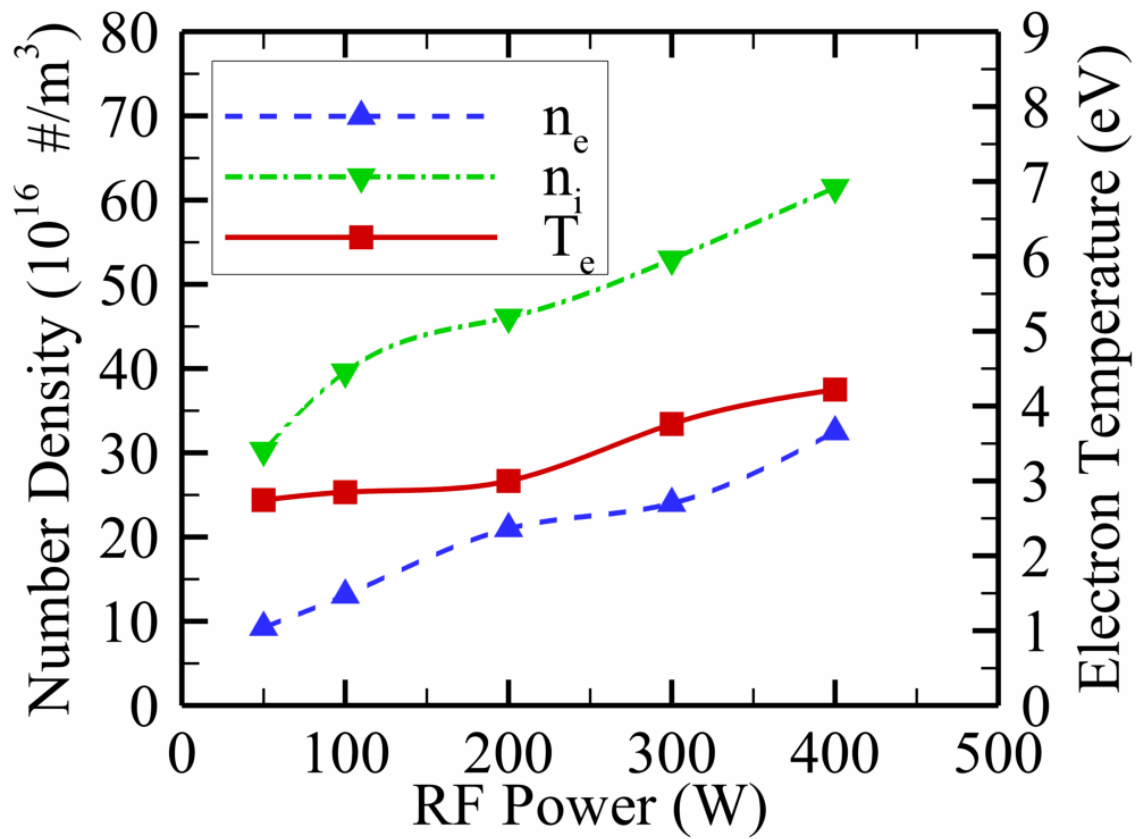


Figure 4.4. The electron temperature (T_e), electron number density (n_e), and ion number density (n_i) as a function of applied RF power during ZnO thin film deposition.

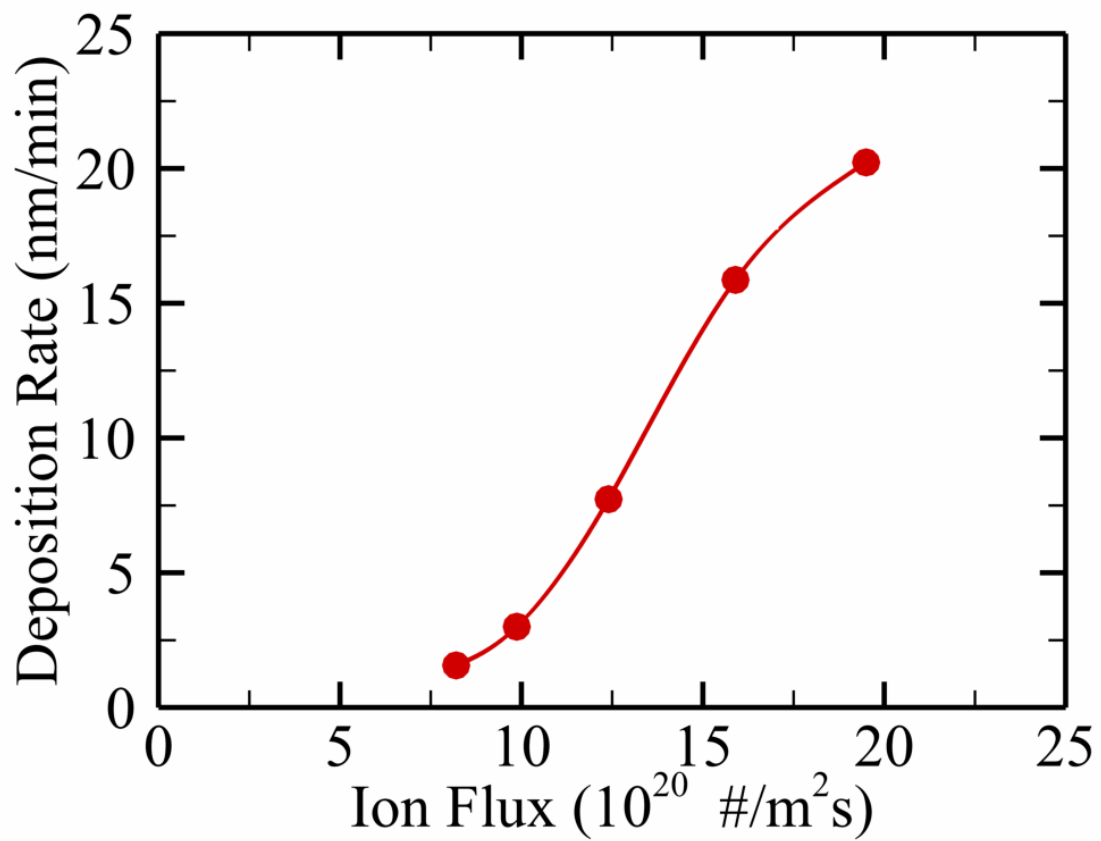


Figure 4.5. Relationship between ion flux and deposition rate as a function of applied RF power during ZnO thin film deposition.

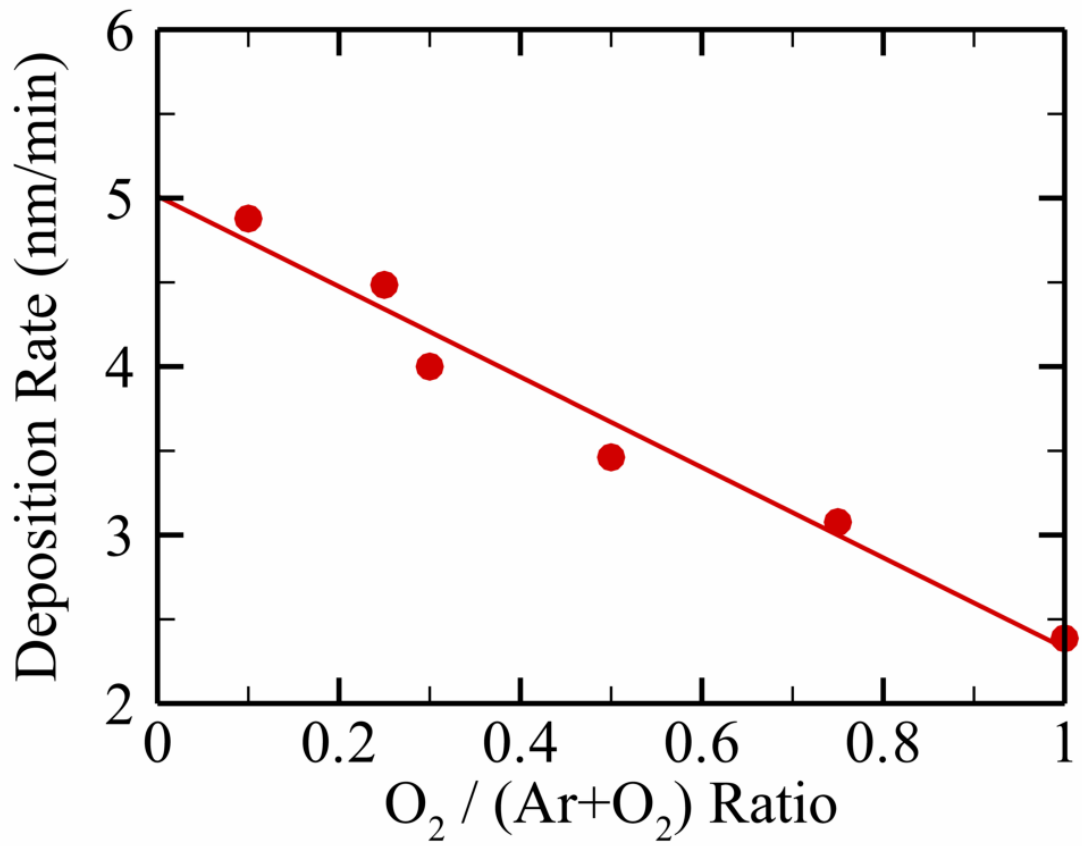


Figure 4.6. Effect of deposition rate as a function of $O_2/(Ar+O_2)$ ratio under a constant thickness of 60 nm.

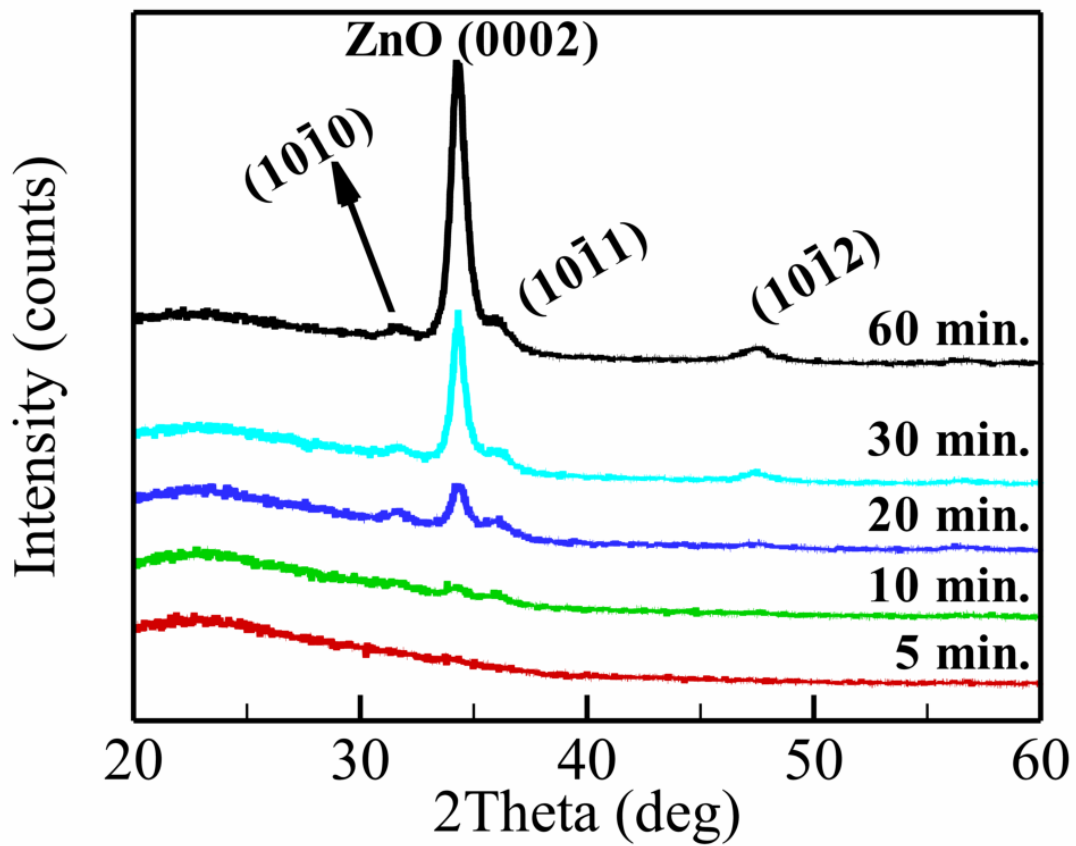


Figure 4.7. XRD patterns of ZnO thin films as a function of deposition time (for thickness effect) under a constant RF power of 100 W.

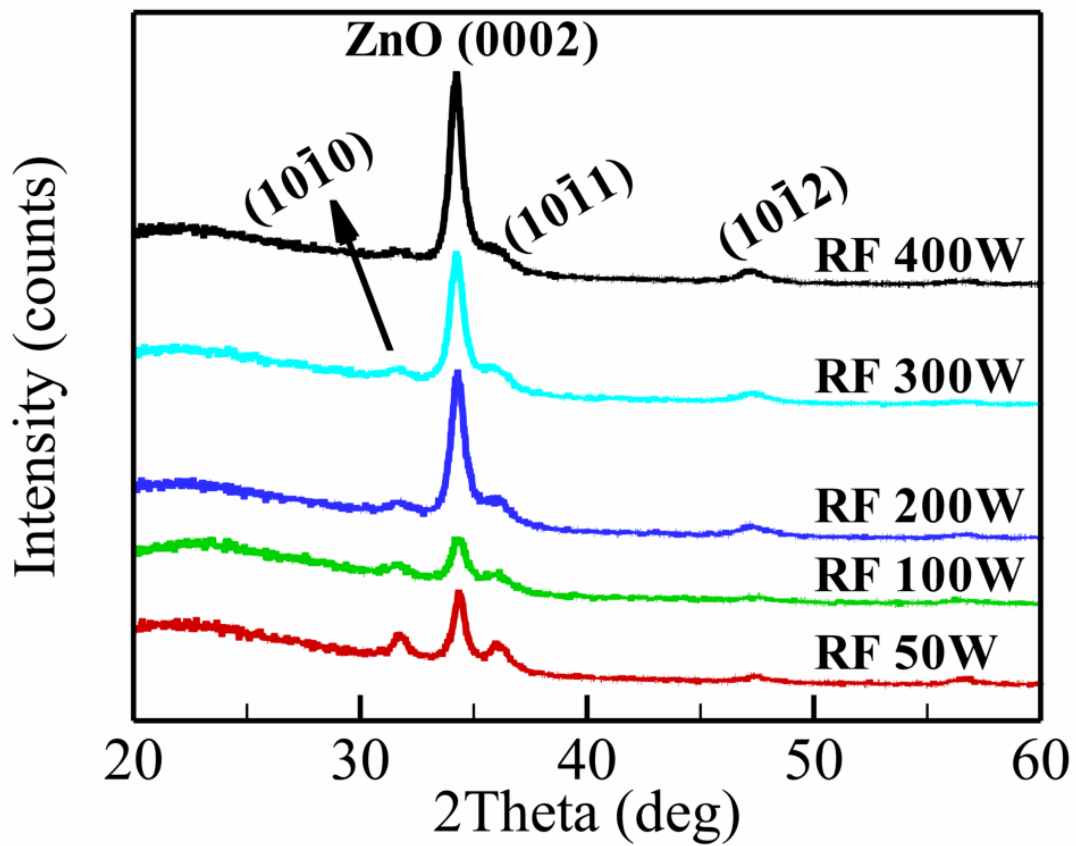


Figure 4.8. XRD patterns of ZnO thin films as a function of RF power (for power effect) under a constant thickness of 60 nm.

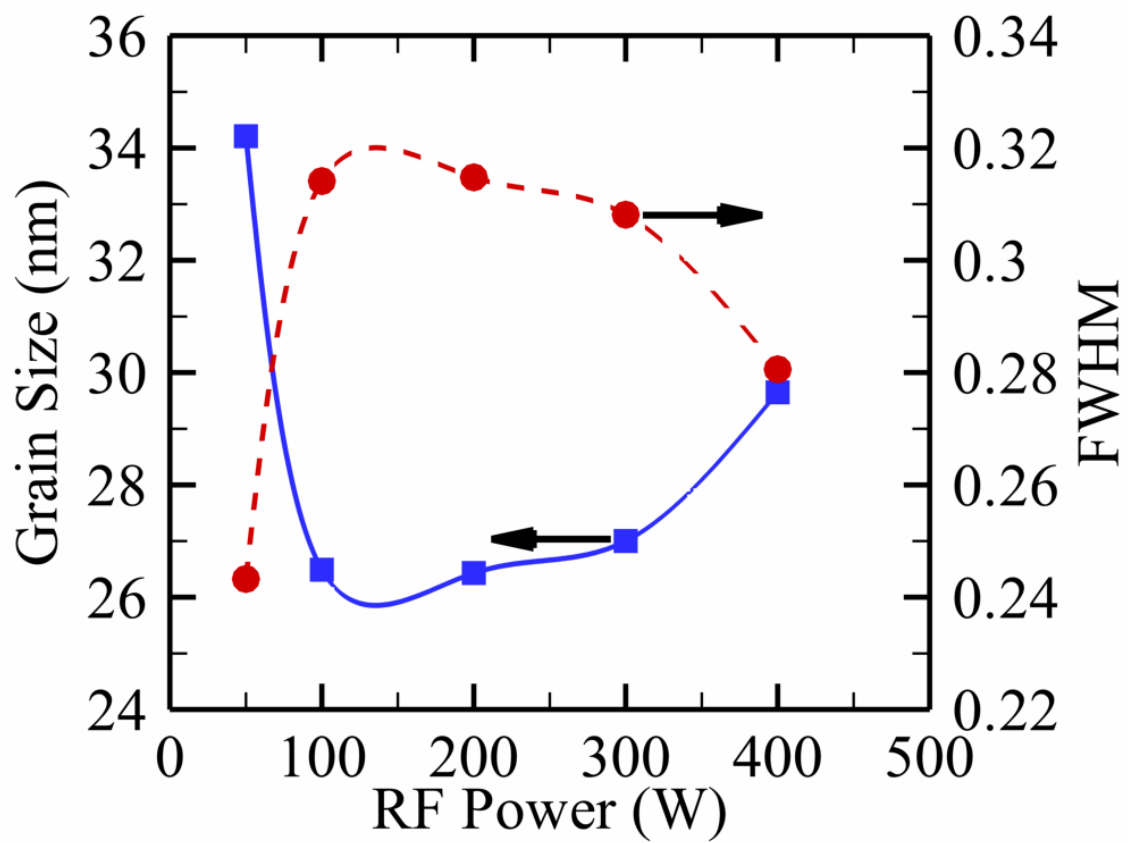


Figure 4.9. Effect of grain size and FWHM as a function of RF power under a constant thickness of 60 nm.

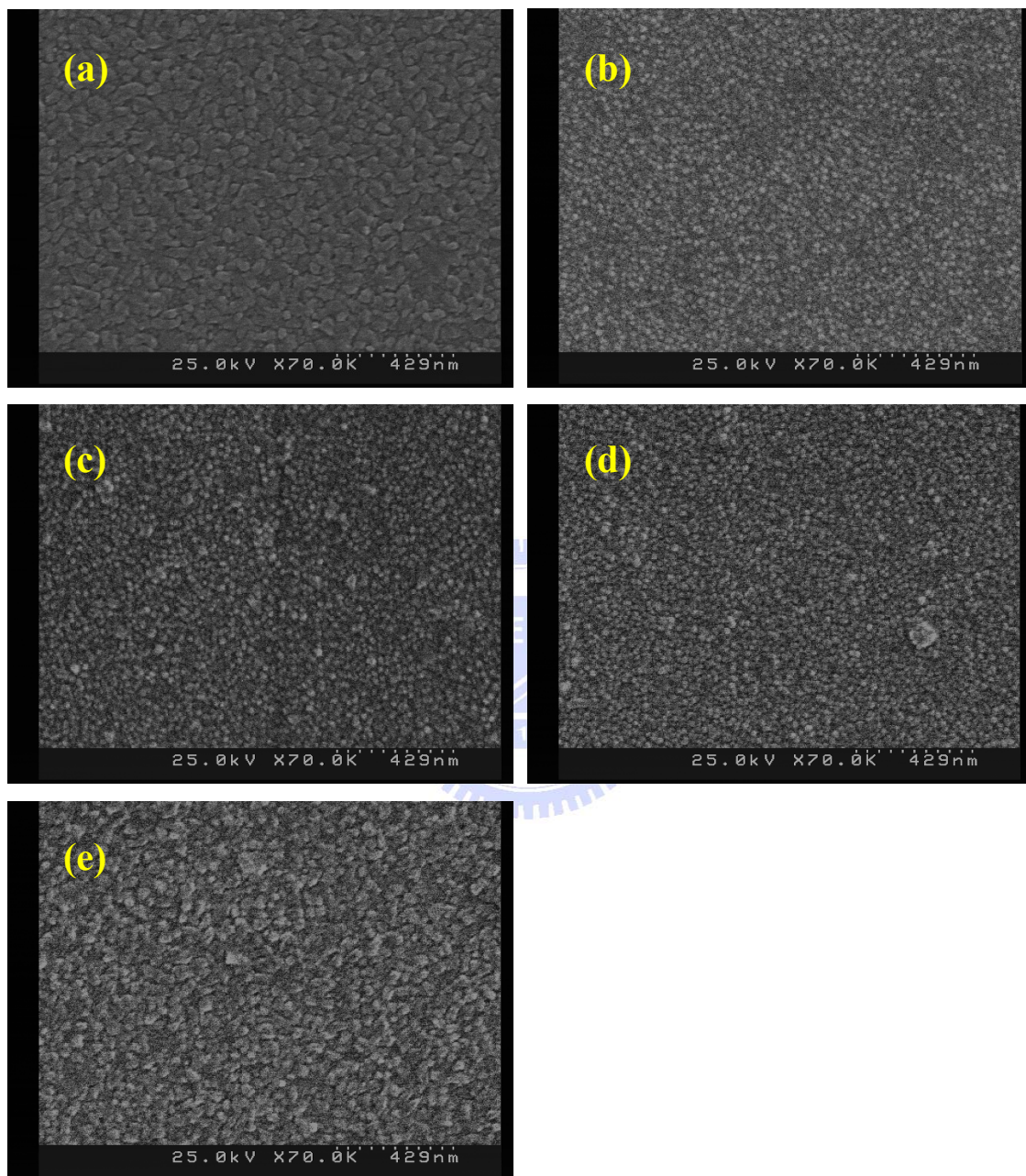


Figure 4.10. SEM image of ZnO thin films for various RF powers - (a) RF 50 W; (b) RF 100 W; (c) RF 200 W; (d) RF 300 W; (e) RF 400 W.

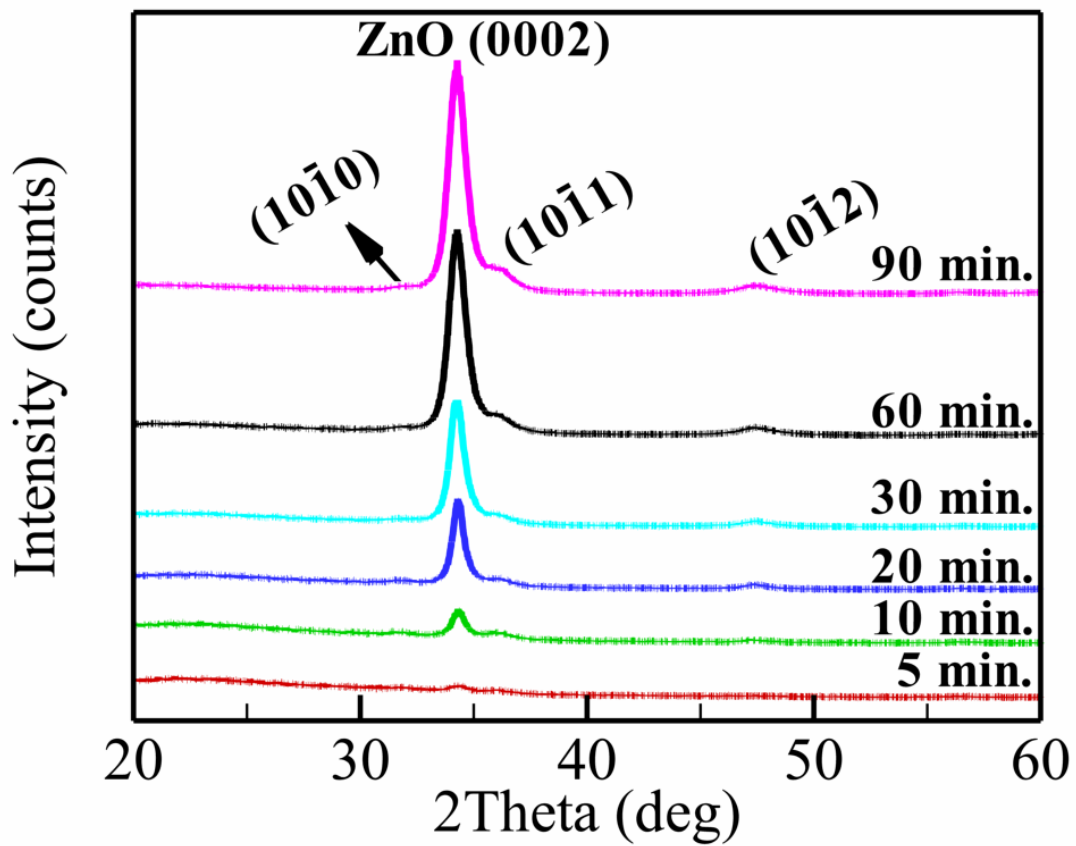


Figure 4.11. XRD patterns of ZnO thin films as a function of deposition time under a constant $O_2/(Ar+O_2)$ ratio of 0.25.

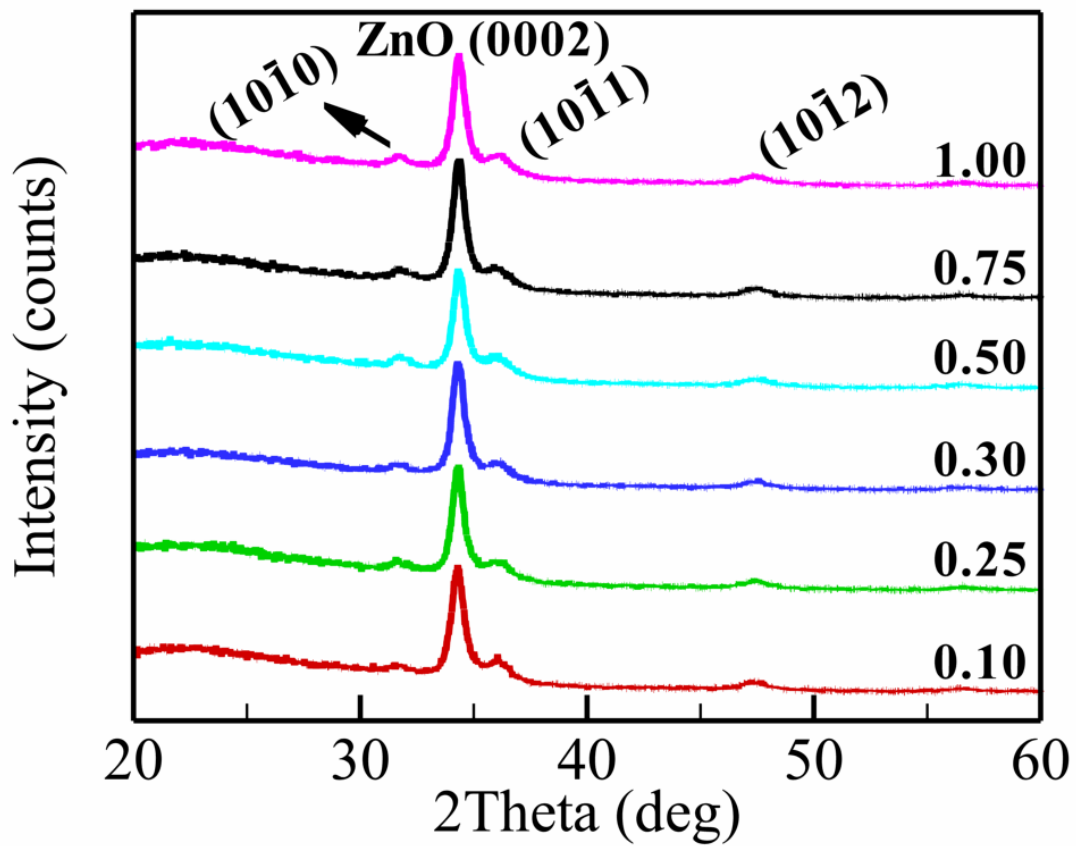


Figure 4.12. XRD patterns of ZnO thin films as a function of $O_2/(Ar+O_2)$ ratio under a constant thickness of 60 nm.

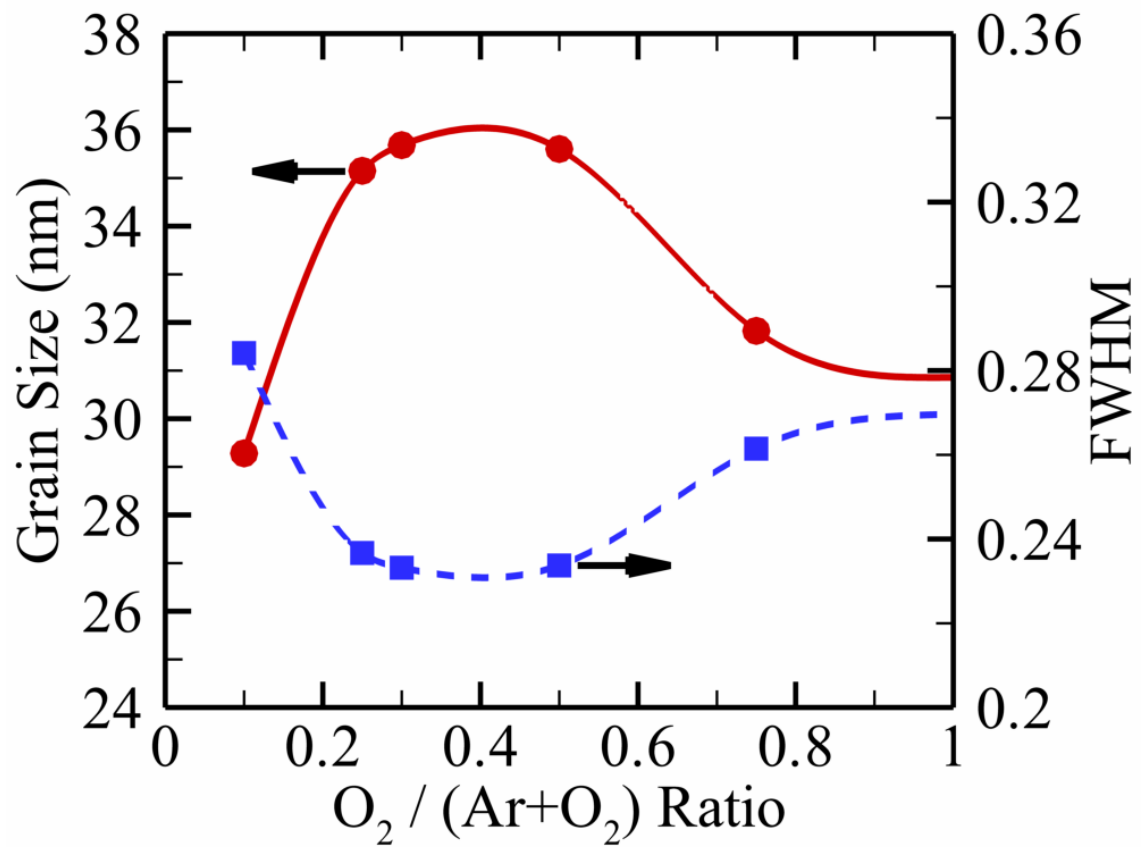


Figure 4.13. Effect of grain size and FWHM of as a function of $O_2/(Ar+O_2)$ ratio at a constant thickness of 60 nm.

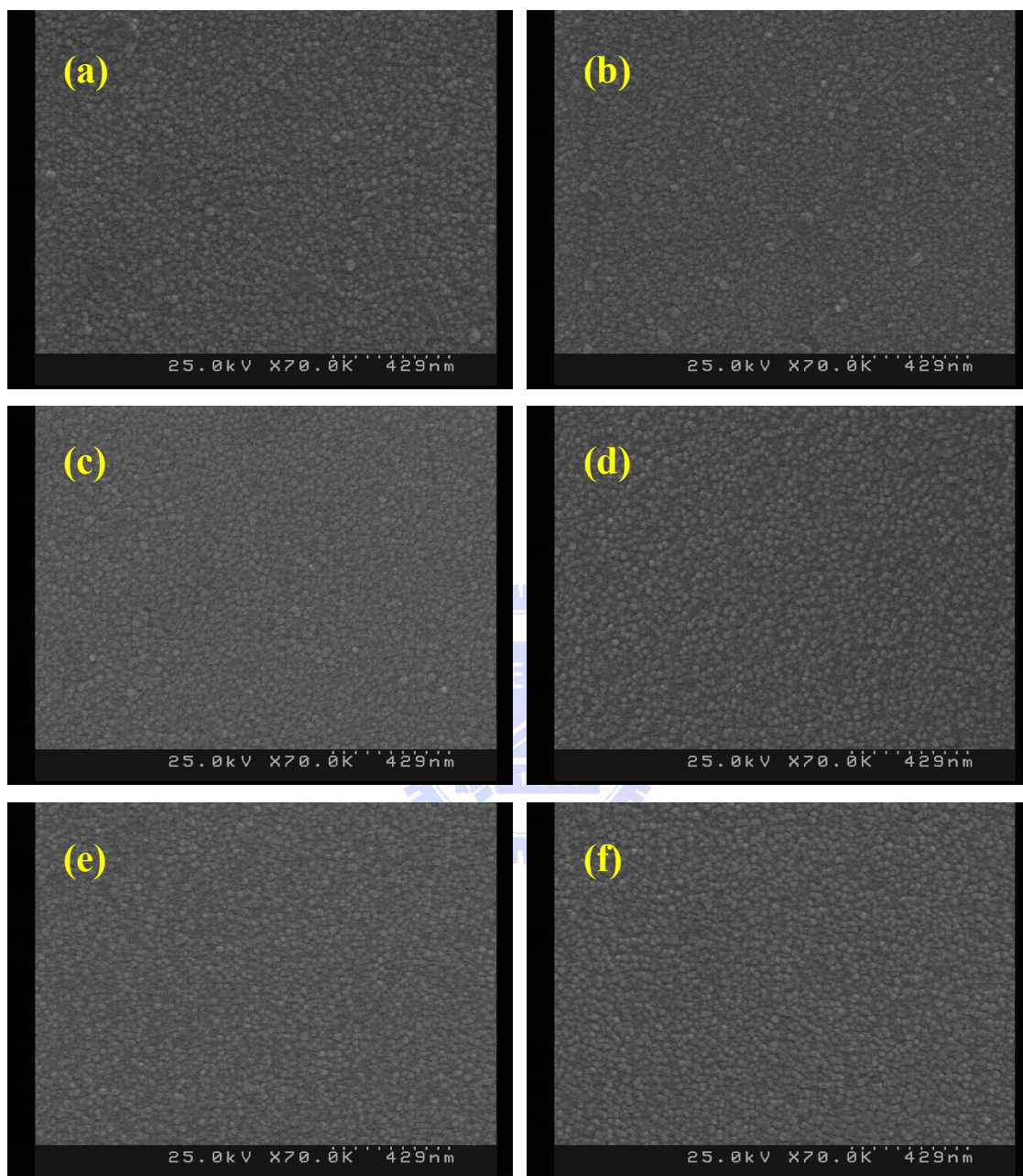


Figure 4.14. SEM image of ZnO thin films for various $O_2/(Ar+O_2)$ ratios - (a) 0.10;

(b) 0.25; (c) 0.30; (d) 0.50; (e) 0.75; (f) 1.00.

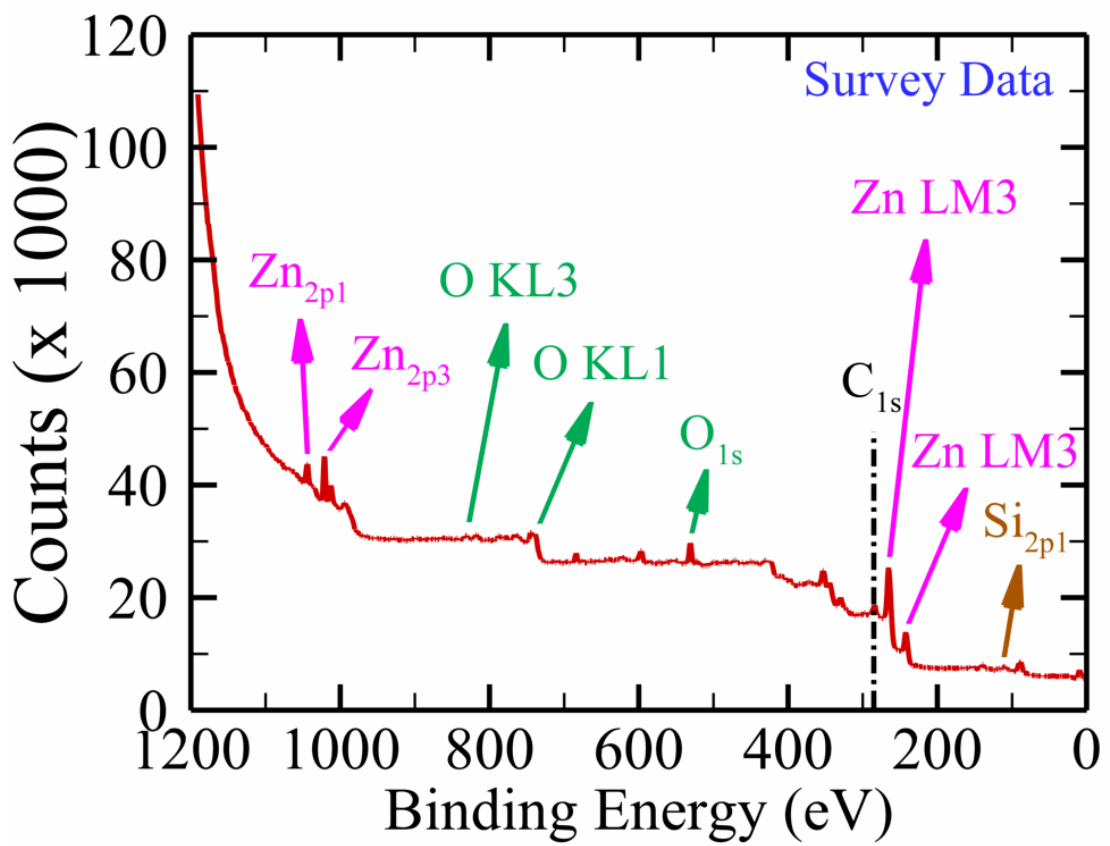


Figure 4.15. XPS survey spectrum of ZnO thin film.

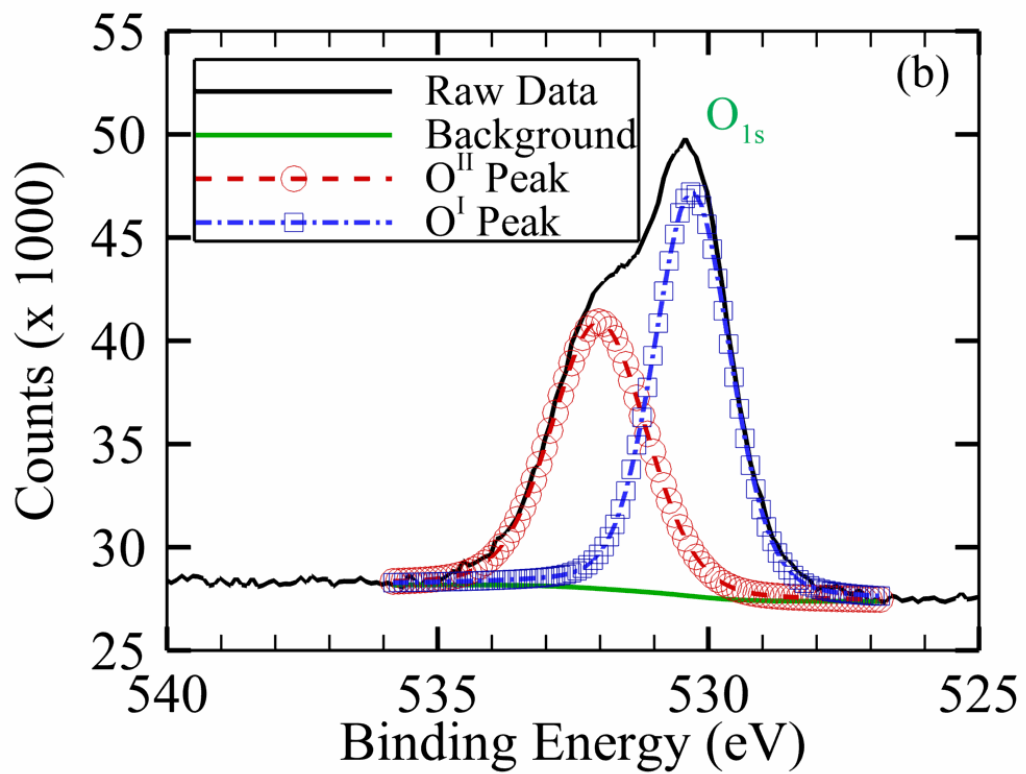
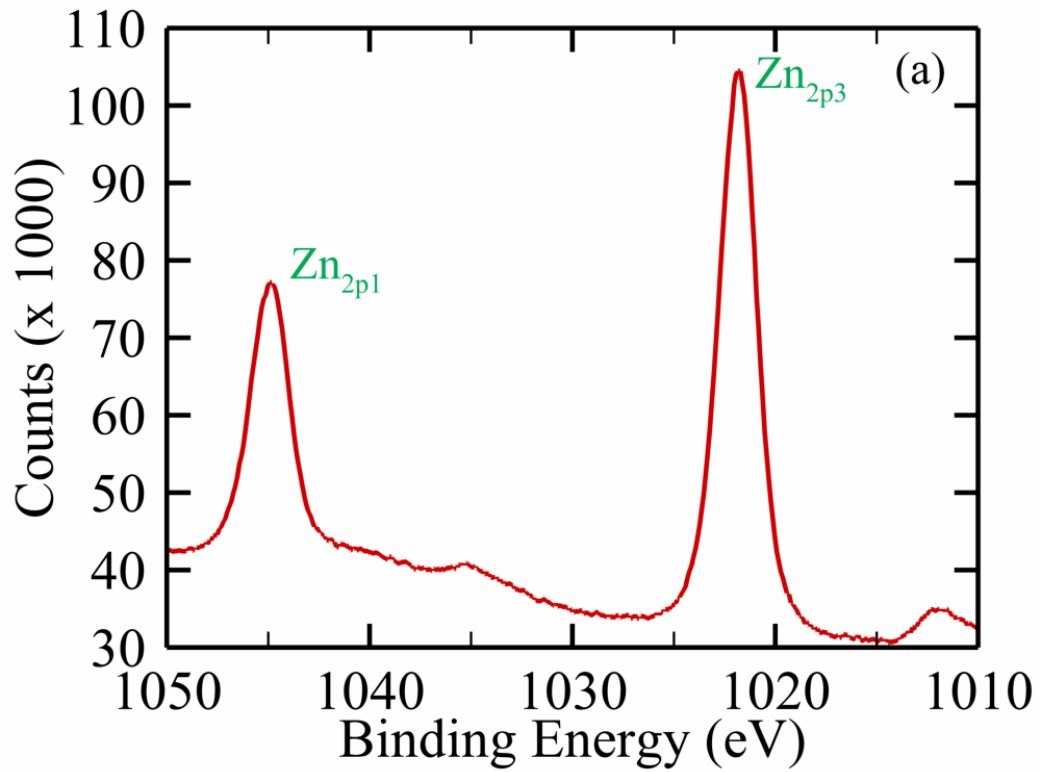


Figure 4.16. The binding energy of (a) Zn $2p$ peak and (b) O $1s$ peak of ZnO thin film from the XPS analysis.

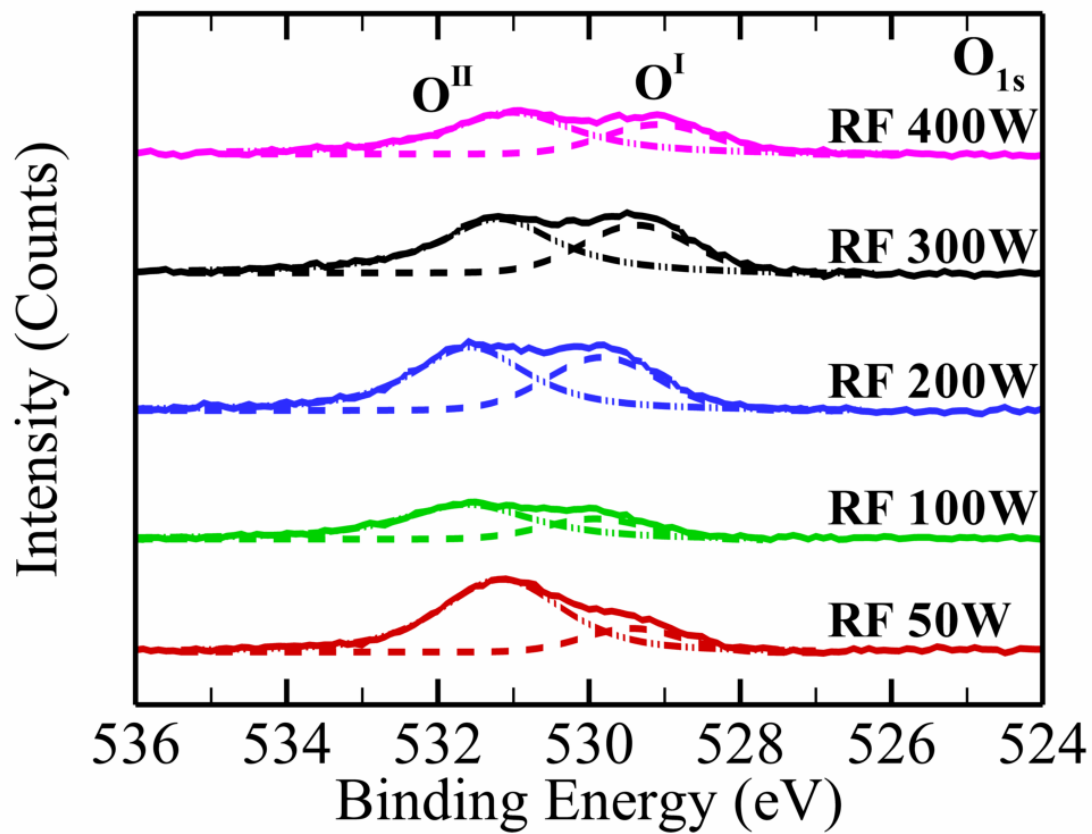


Figure 4.17. The O 1s spectra (solid line), O^I peak (dashed line) and O^{II} peak (dot line) of XPS with various RF powers.

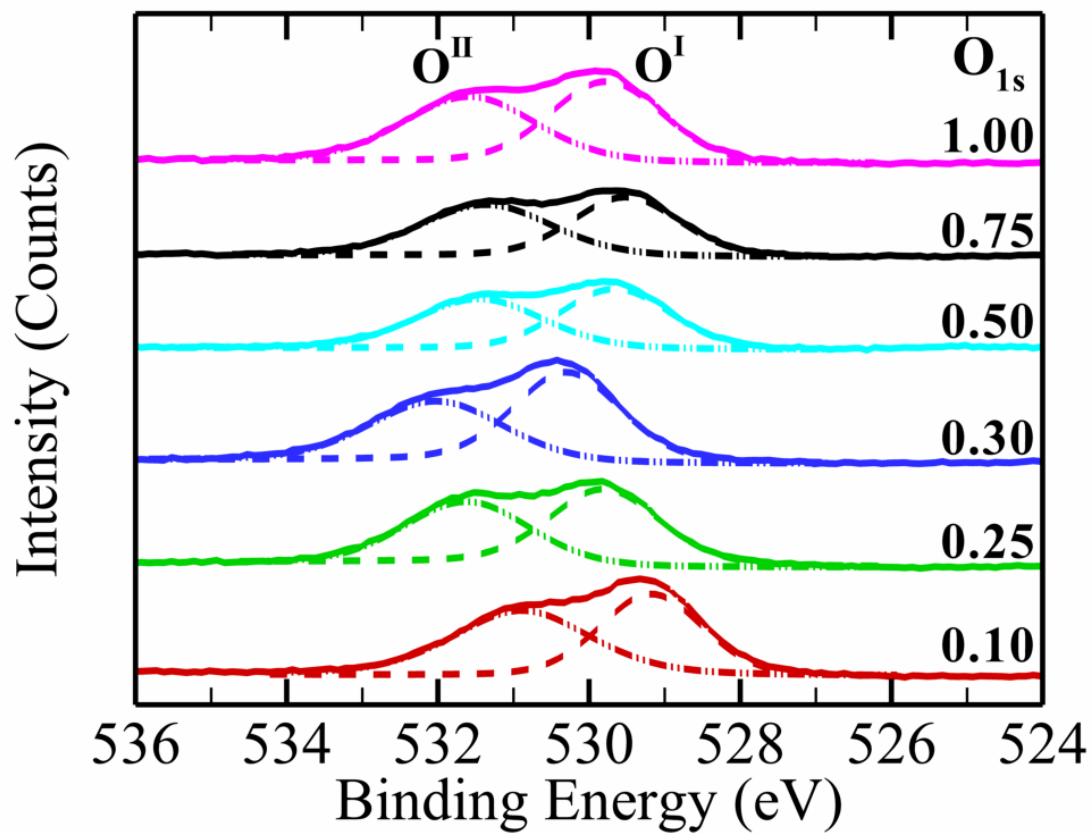


Figure 4.18. The O 1s spectra (solid line), O^I peak (dashed line) and O^{II} peak (dot line) of XPS with various $O_2/(Ar+O_2)$ ratios.

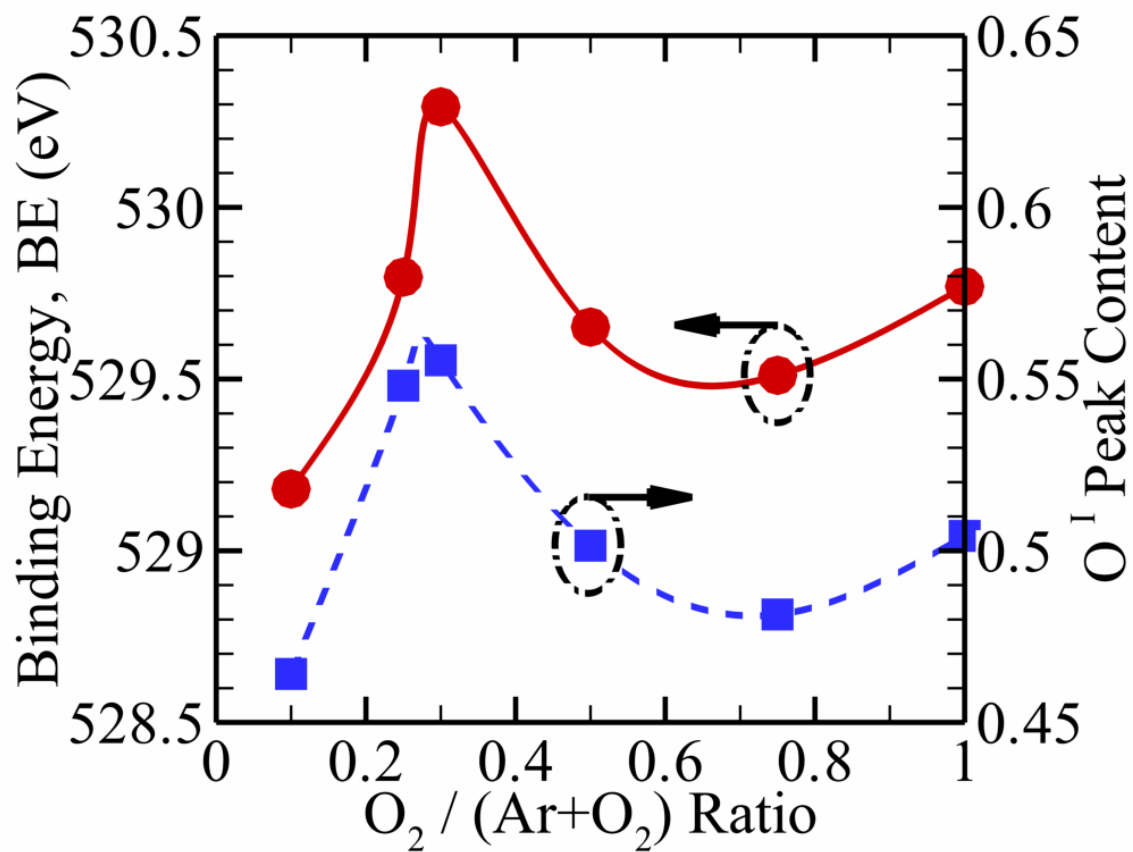


Figure 4.19. The binding energy (●) and the content of O^I peak (■) with various $O_2/(Ar+O_2)$ ratios.

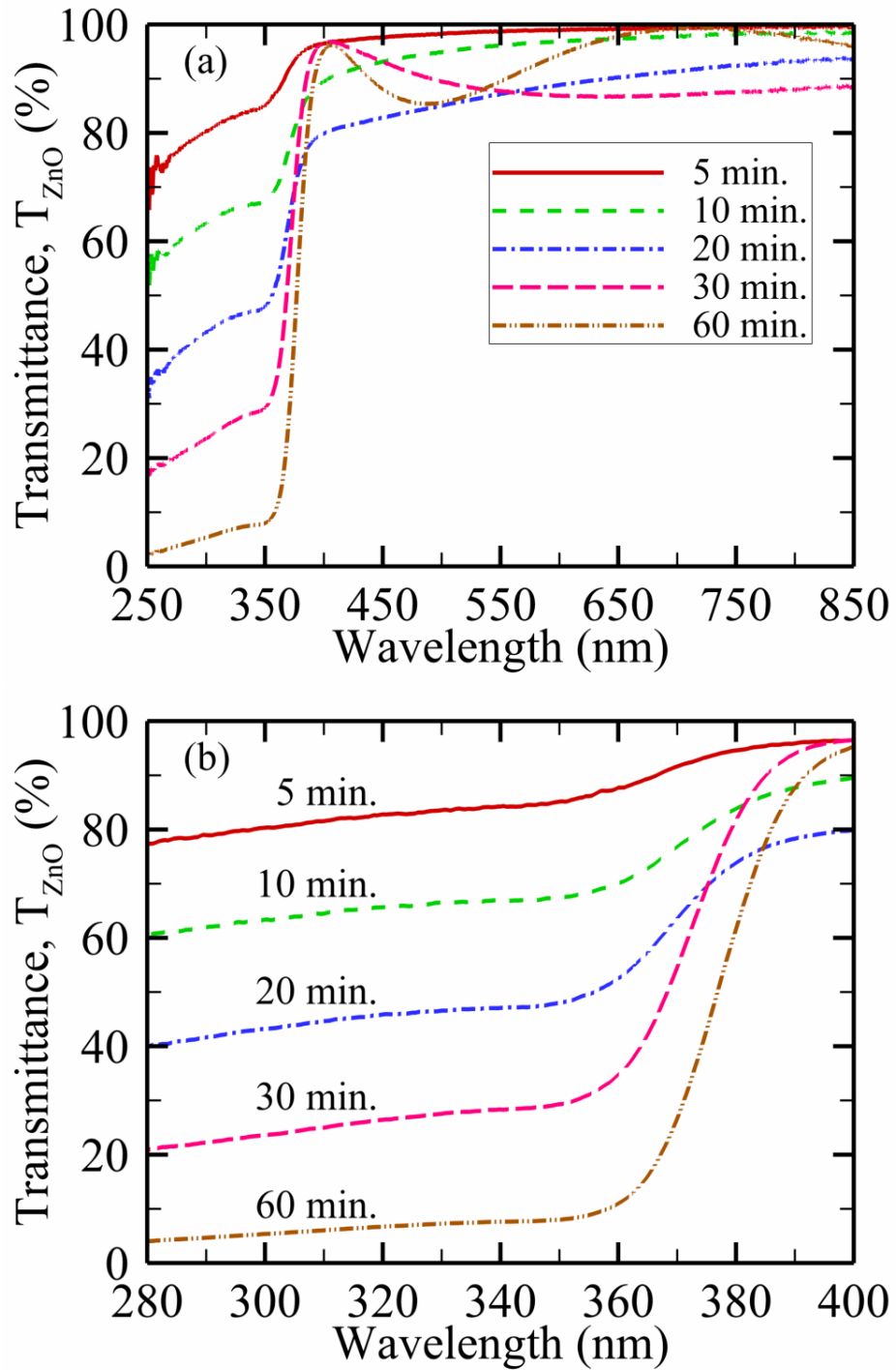


Figure 4.20. Transmittance spectra of pure ZnO thin films as a function of deposition time under a constant RF power of 100 W in (a) overall region and (b) UV region (280-400 nm).

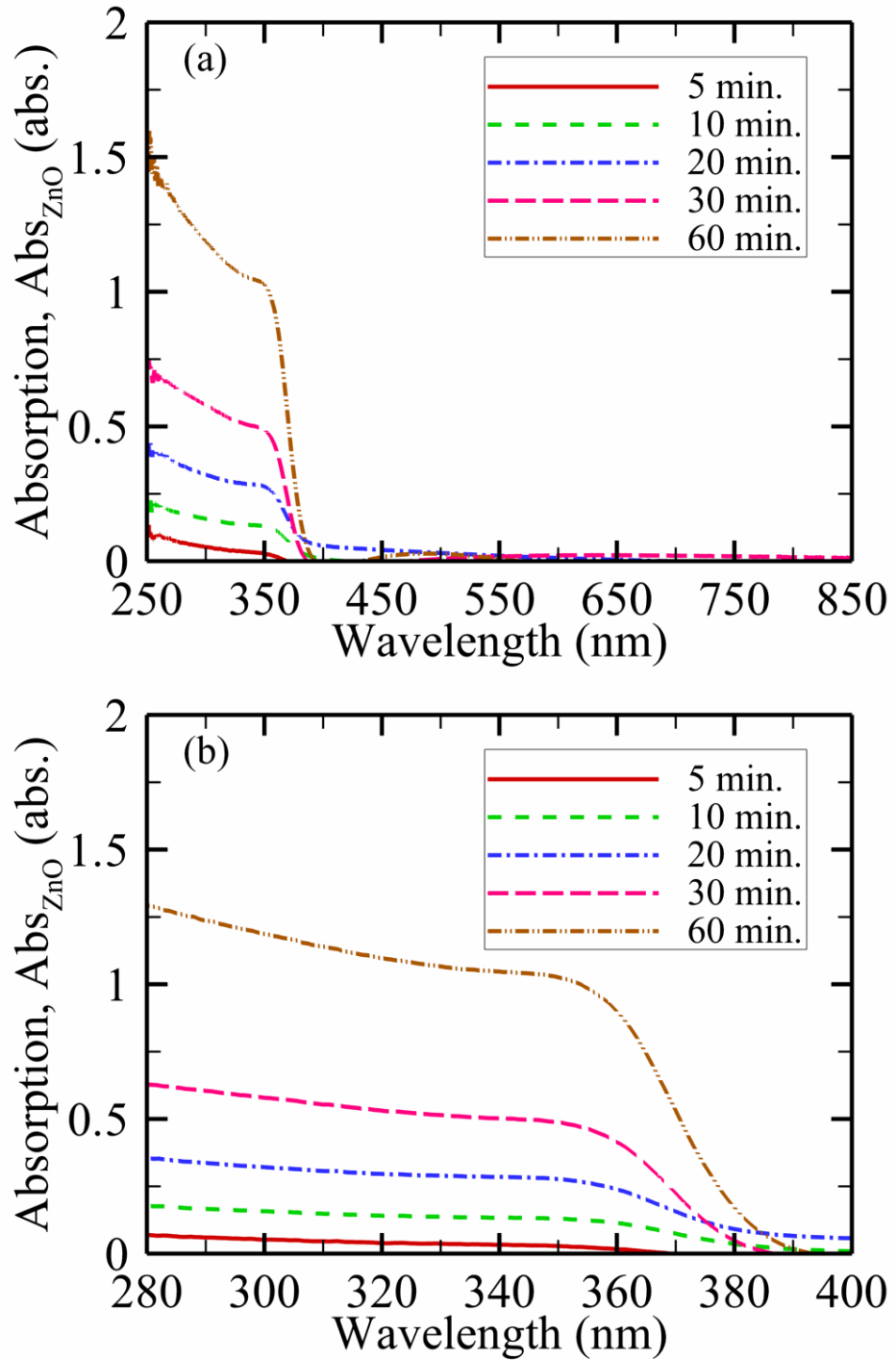


Figure 4.21. Absorption spectra of pure ZnO thin films as a function of deposition time under a constant RF power of 100 W in (a) overall region and (b) UV region (280-400 nm).

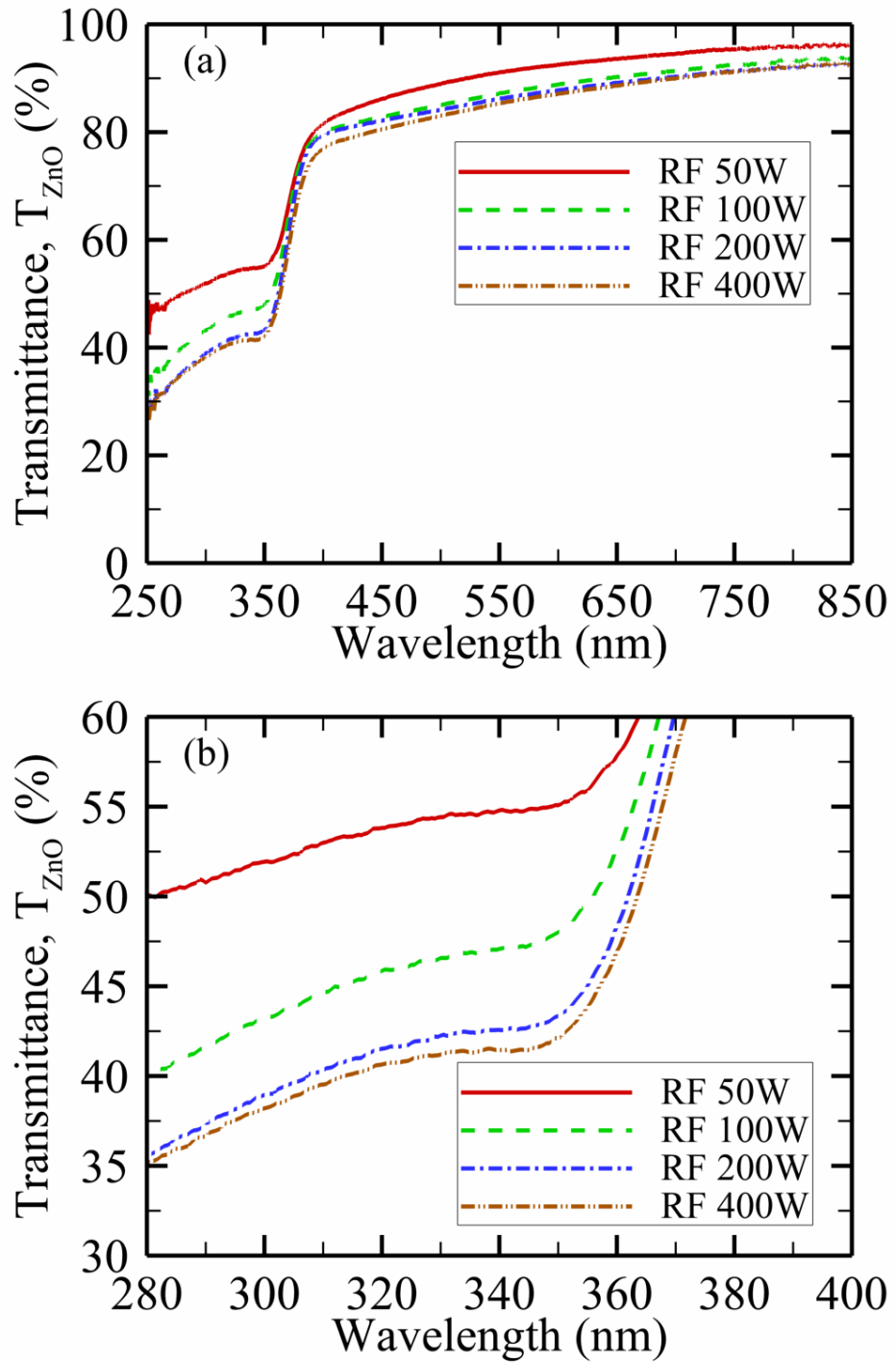


Figure 4.22. Transmittance spectra of pure ZnO thin films as a function of RF power under a constant thickness of 60 nm in (a) overall region and (b) UV region (280-400 nm).

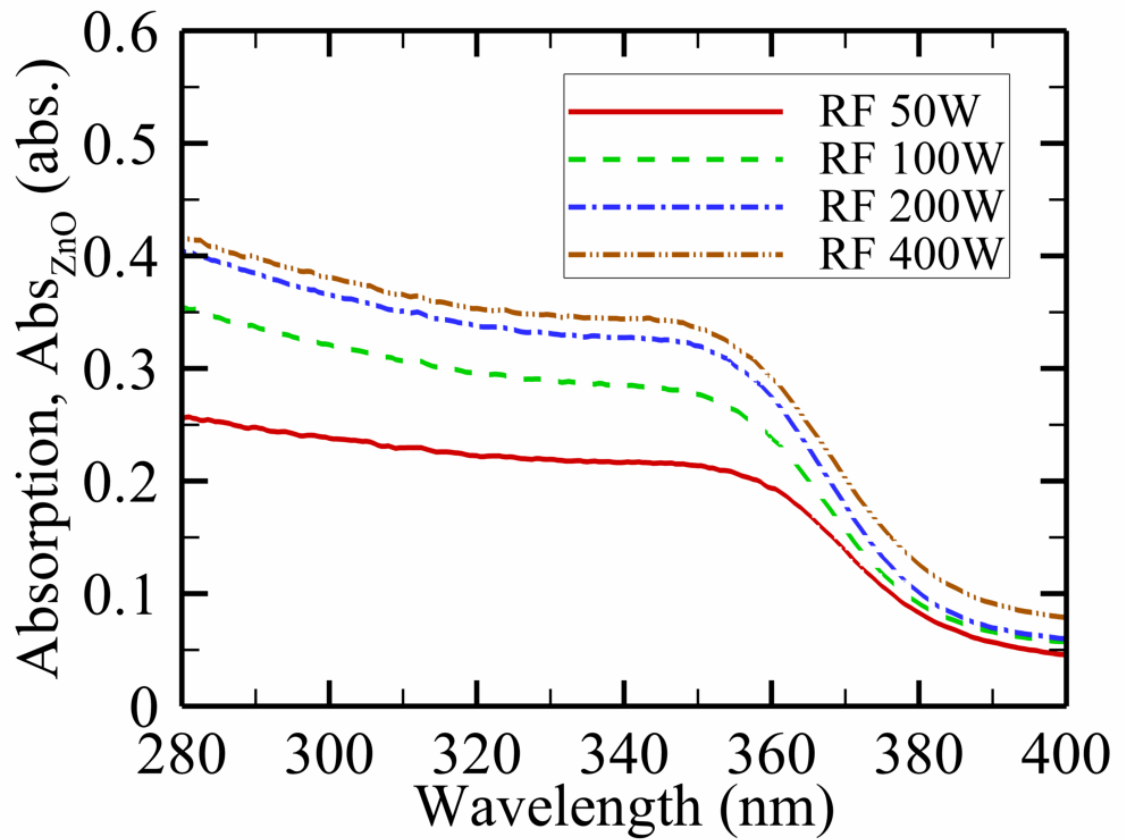


Figure 4.23. Absorption spectra of pure ZnO thin films as a function of RF power under a constant thickness of 60 nm in UV region (280-400 nm).

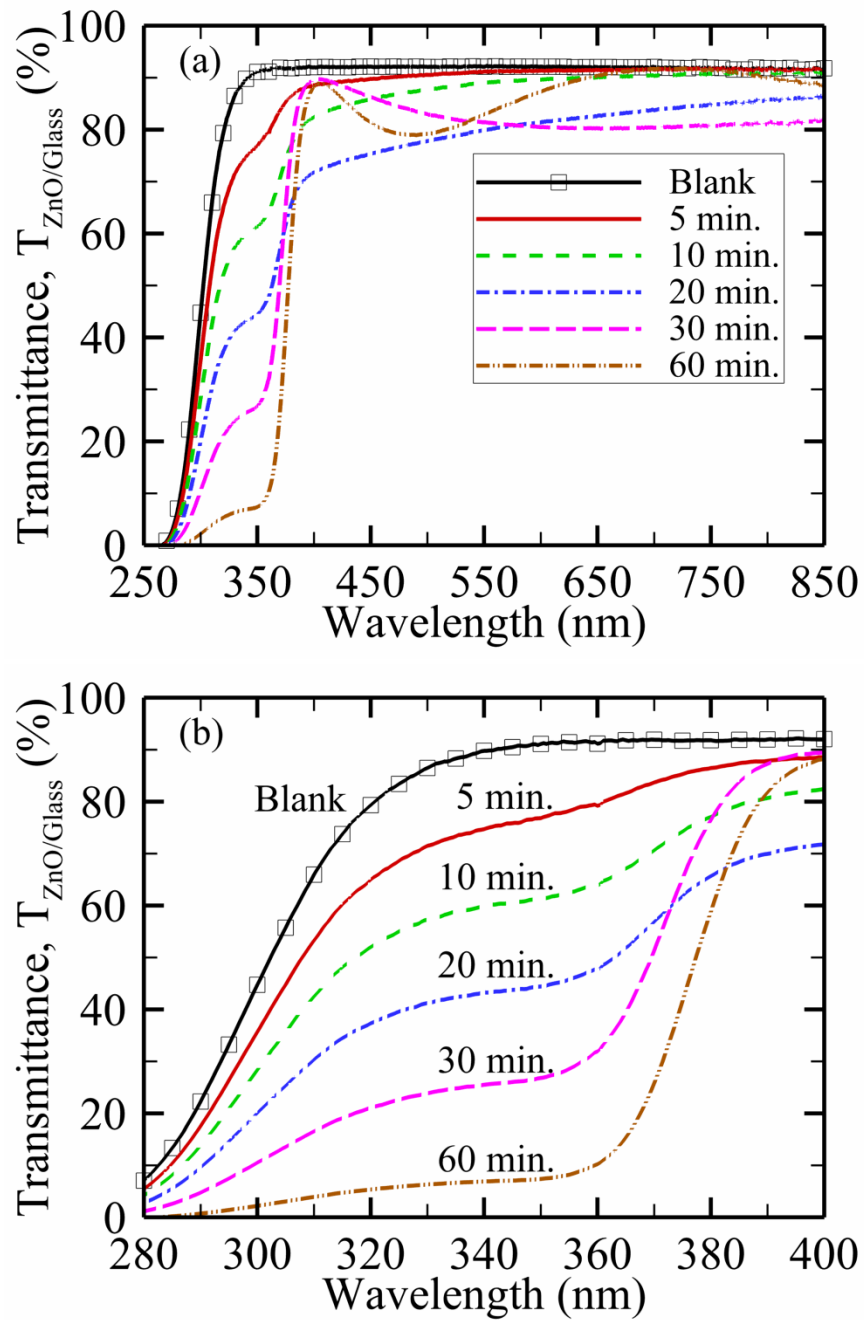


Figure 4.24. Transmittance spectra of ZnO/Glass as a function of deposition time under a constant RF power of 100 W in (a) overall region and (b) UV region (280-400 nm).

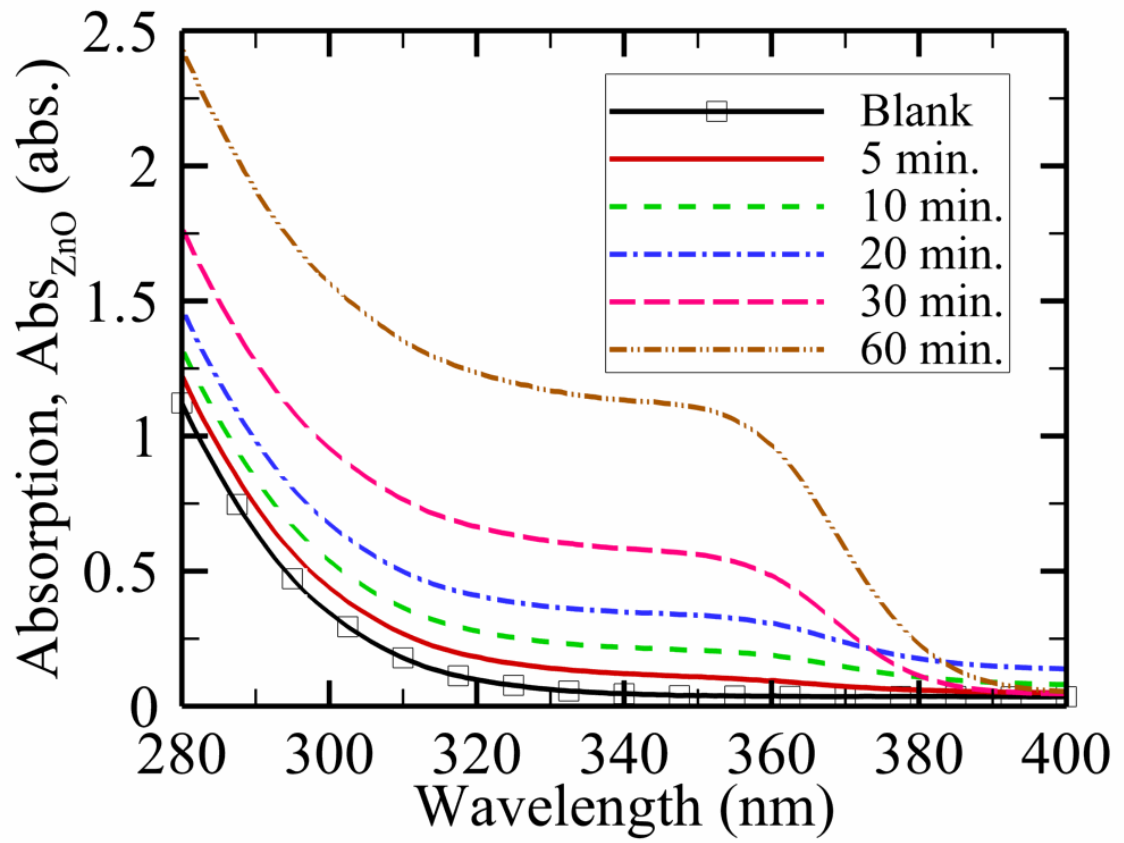


Figure 4.25. Absorption spectra of ZnO/Glass as a function of deposition time under a constant RF power of 100 W in UV region (280-400 nm).

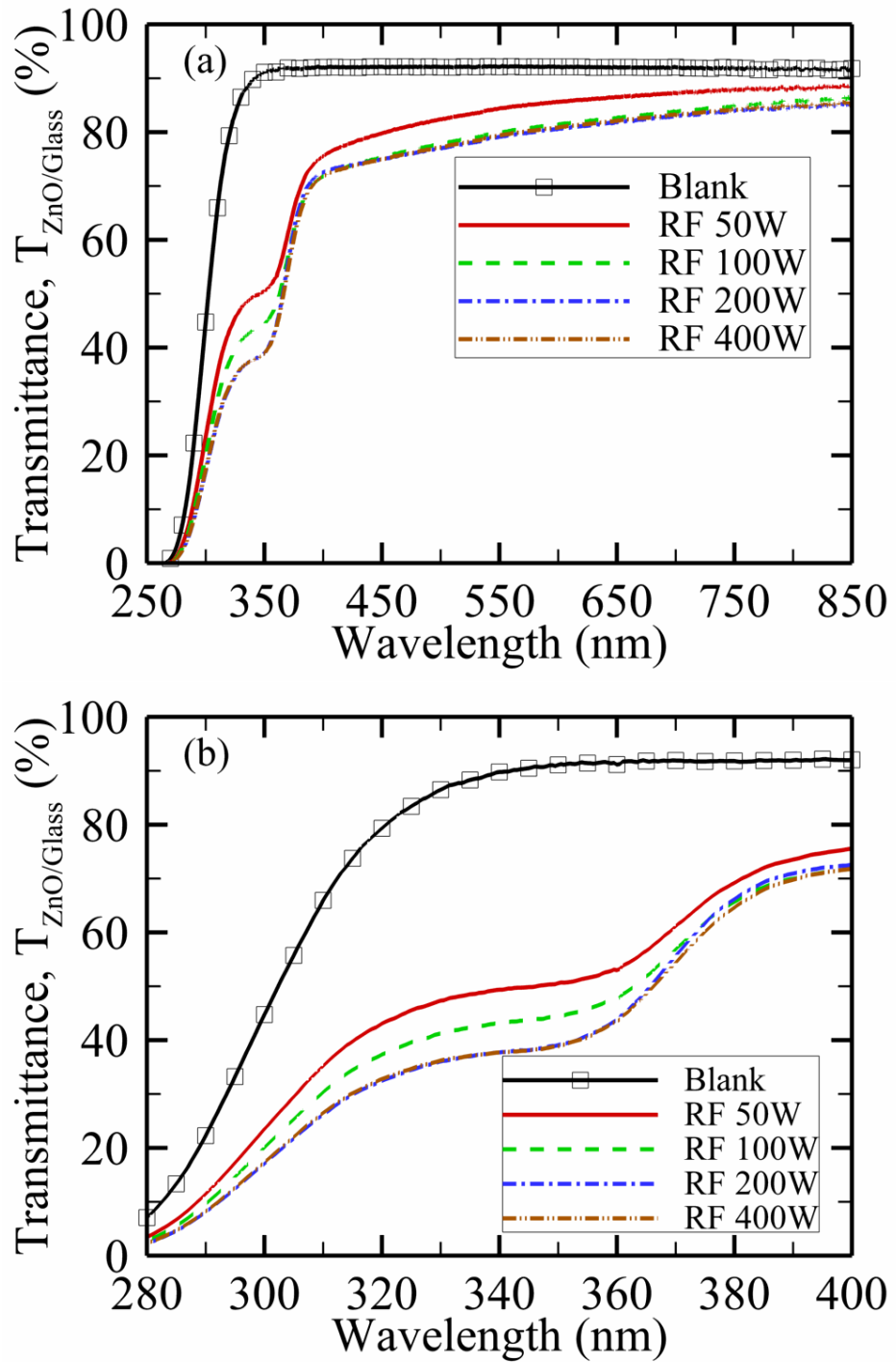


Figure 4.26. Transmittance spectra of ZnO/Glass as a function of RF power under a constant thickness of 60 nm in (a) overall region and (b) UV region (280-400 nm).

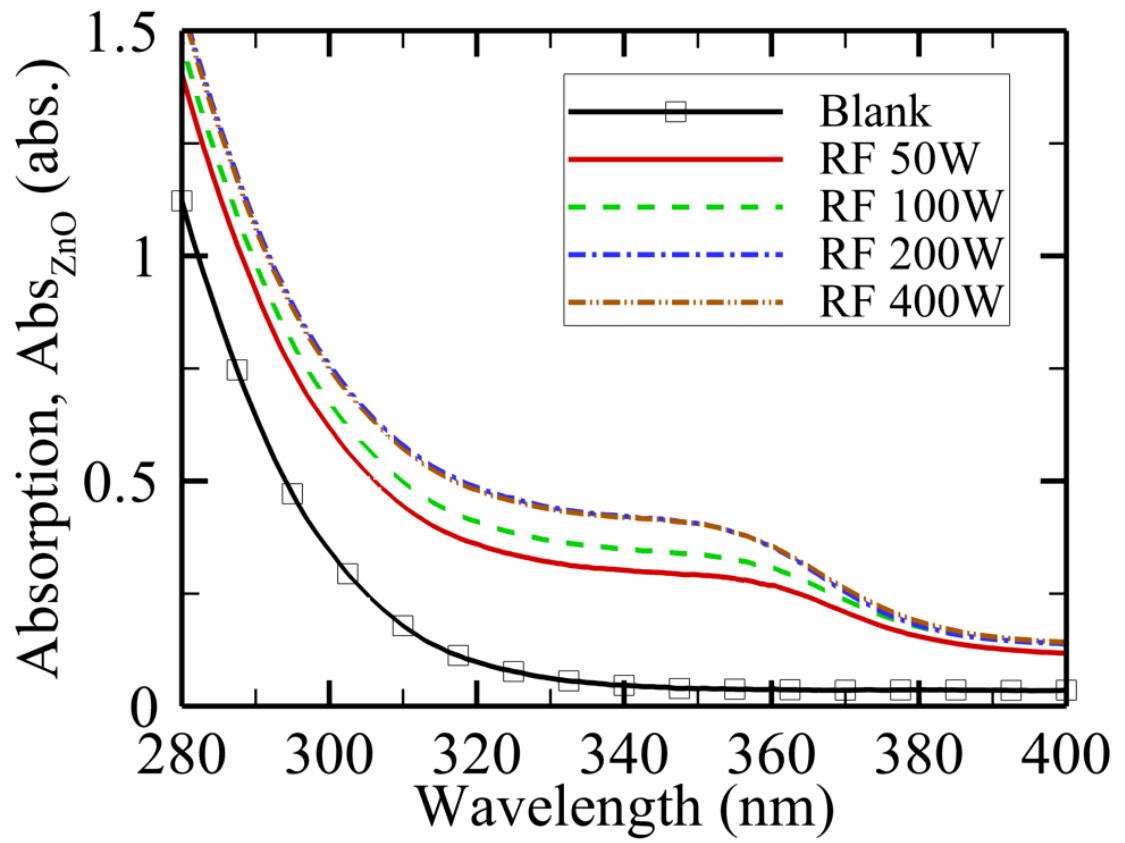


Figure 4.27. Absorption spectra of ZnO/Glass as a function of RF power under a constant thickness of 60 nm in UV region (280-400 nm).

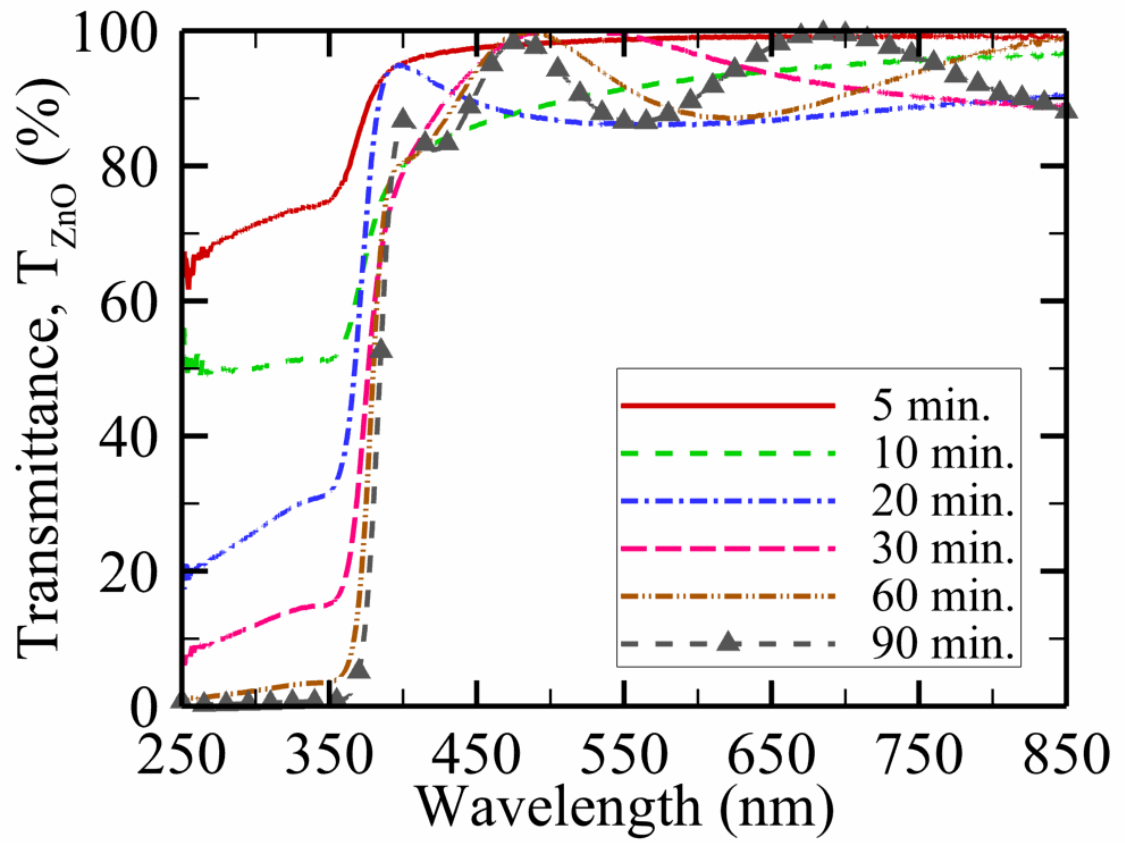


Figure 4.28. Transmittance spectra of pure ZnO thin films as a function of deposition time under a constant $O_2/(Ar+O_2)$ ratio of 0.25.

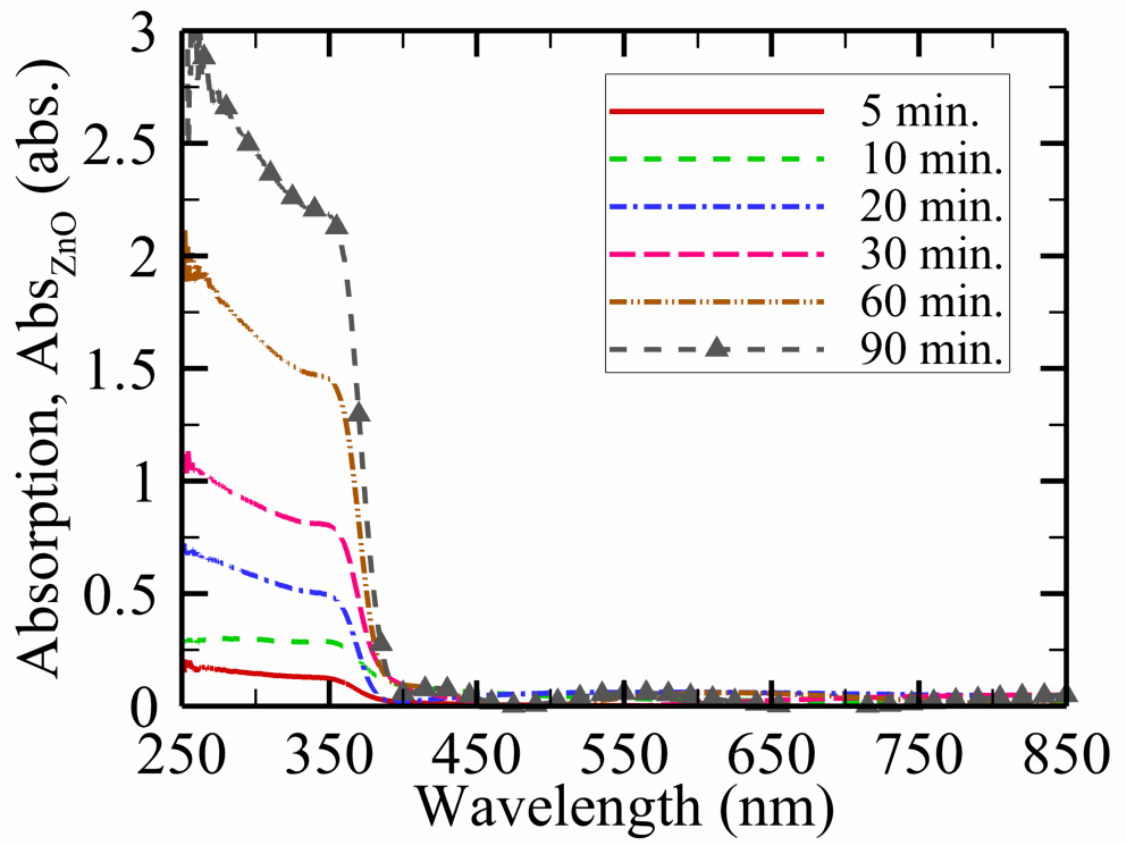


Figure 4.29. Absorption spectra of pure ZnO thin films as a function of deposition time under a constant $O_2/(Ar+O_2)$ ratio of 0.25.

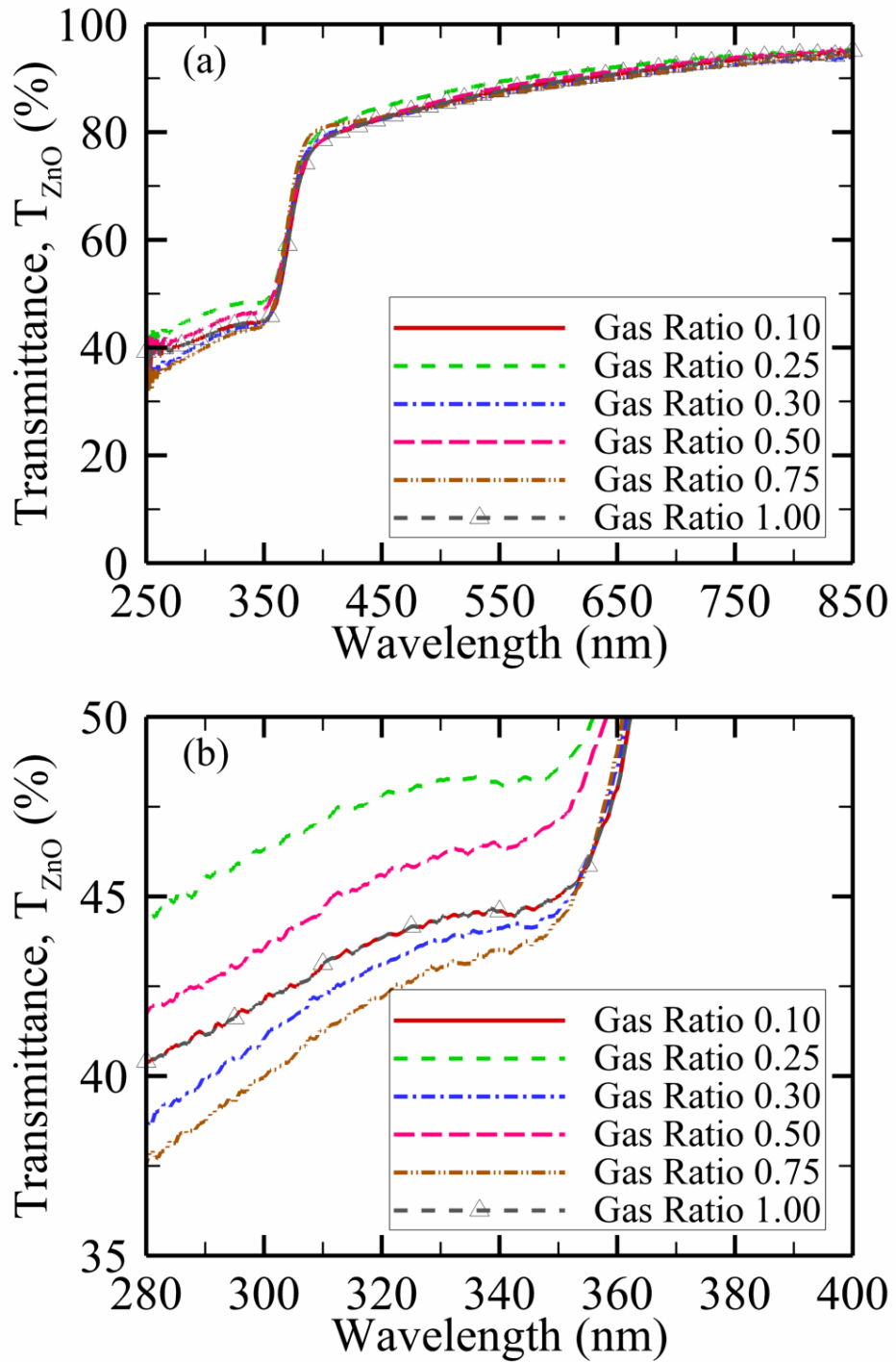


Figure 4.30. Transmittance spectra of pure ZnO thin films as a function of $\text{O}_2/(\text{Ar}+\text{O}_2)$ ratio under a constant thickness of 60 nm in (a) overall region and (b) UV region (280-400 nm).

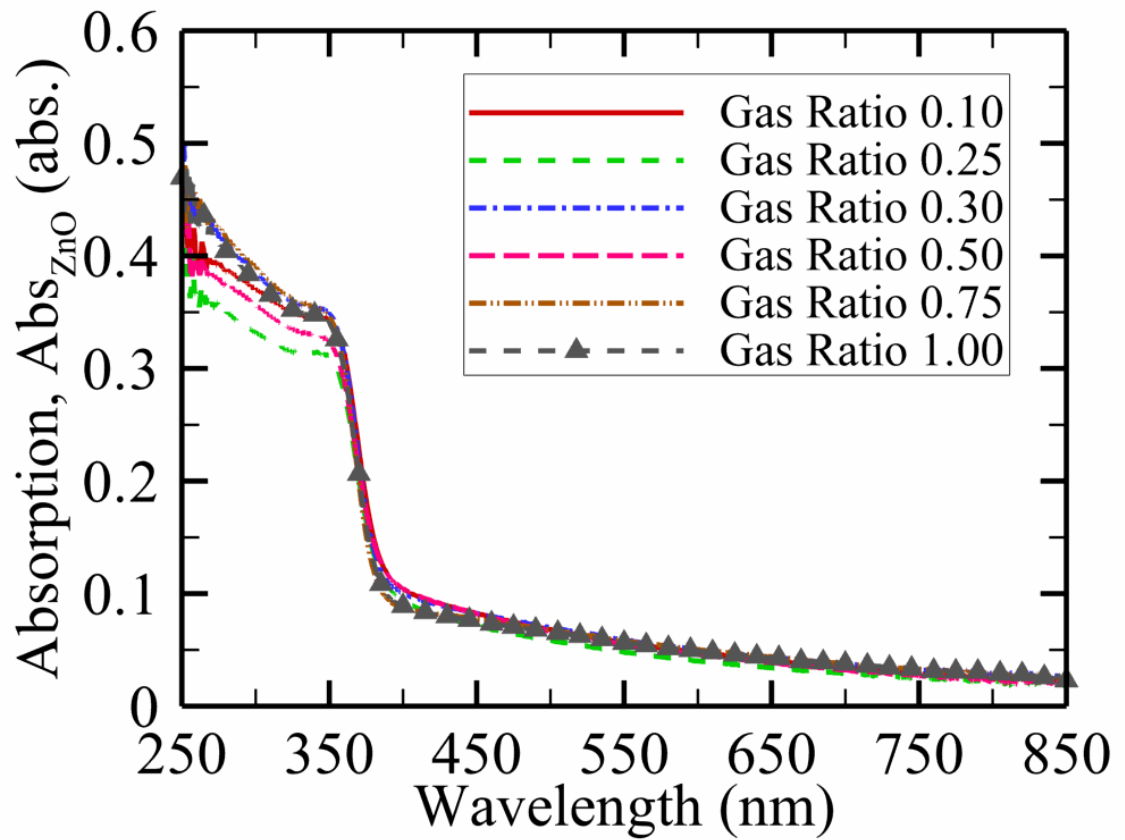


Figure 4.31. Absorption spectra of pure ZnO thin films as a function of $O_2/(Ar+O_2)$

ratio under a constant thickness of 60 nm.

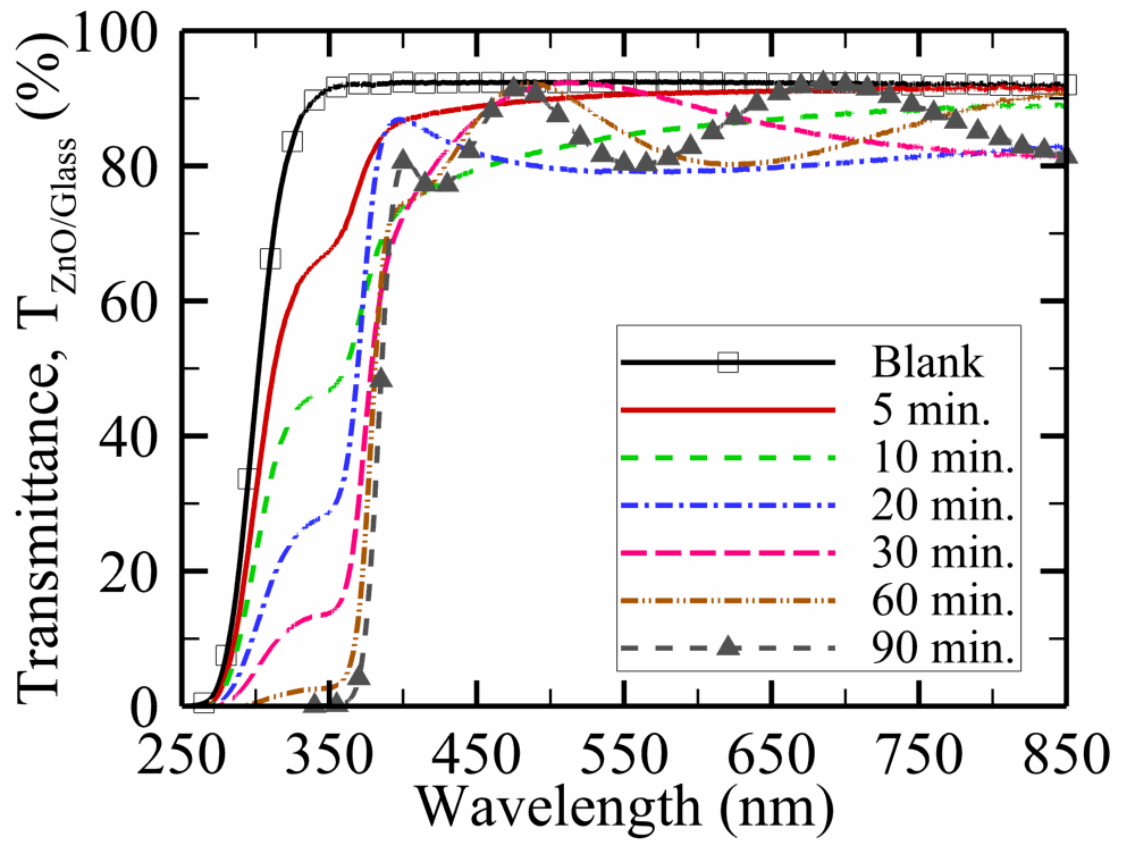


Figure 4.32. Transmittance spectra of ZnO/Glass as a function of deposition time under a constant $O_2/(Ar+O_2)$ ratio of 0.25.

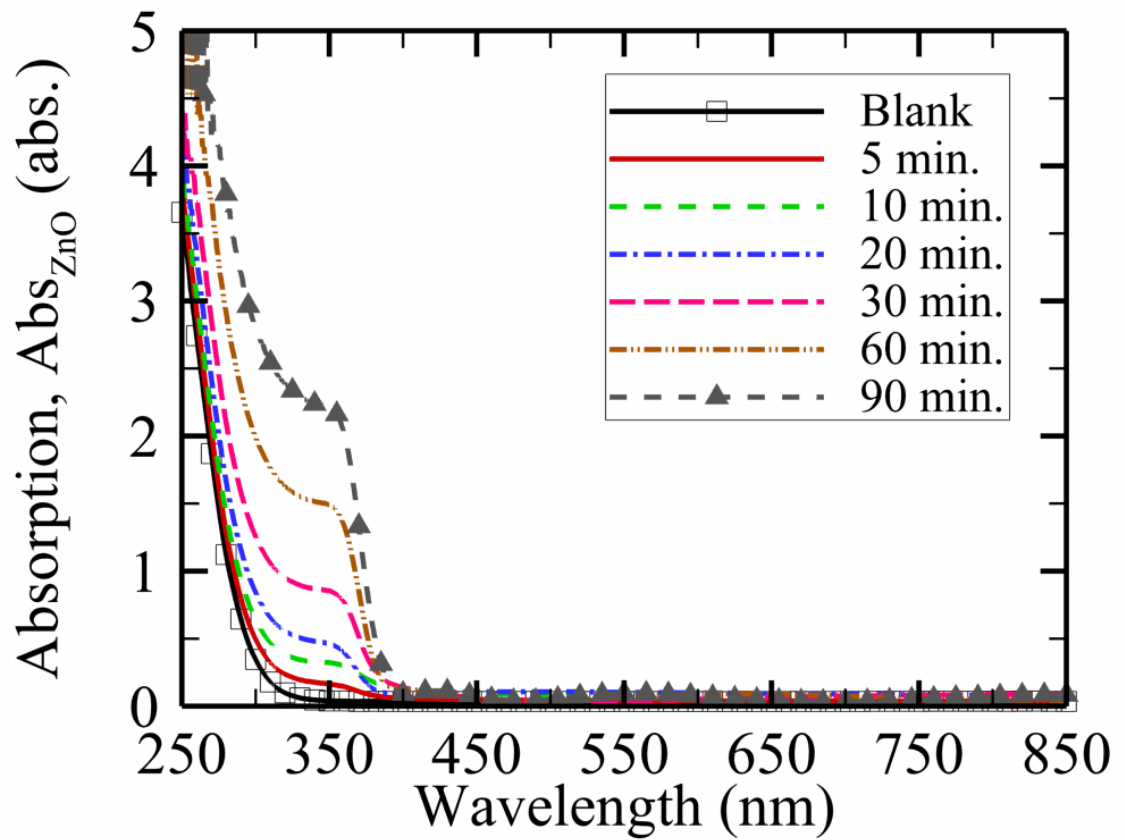


Figure 4.33. Absorption spectra of ZnO/Glass as a function of deposition time under a constant $O_2/(Ar+O_2)$ ratio of 0.25.

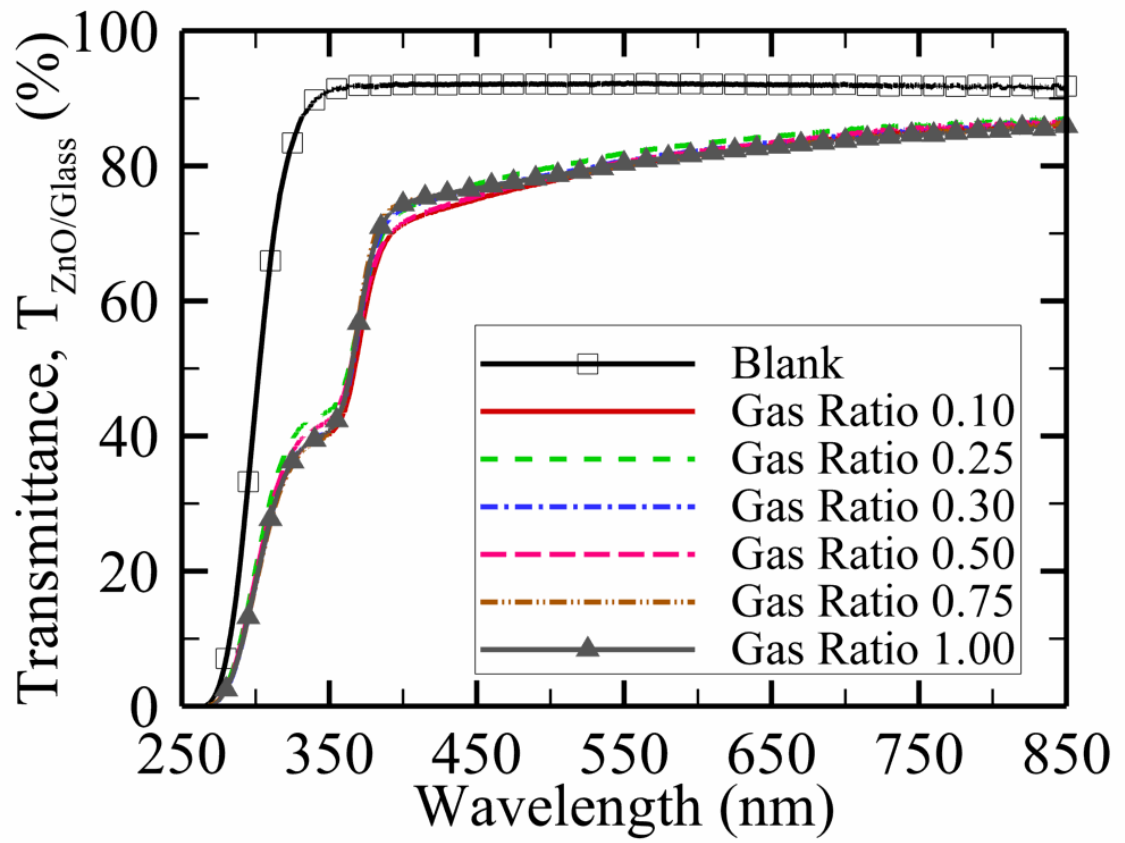


Figure 4.34. Transmittance spectra of ZnO/Glass as a function of $O_2/(Ar+O_2)$ ratio

under a constant thickness of 60 nm.

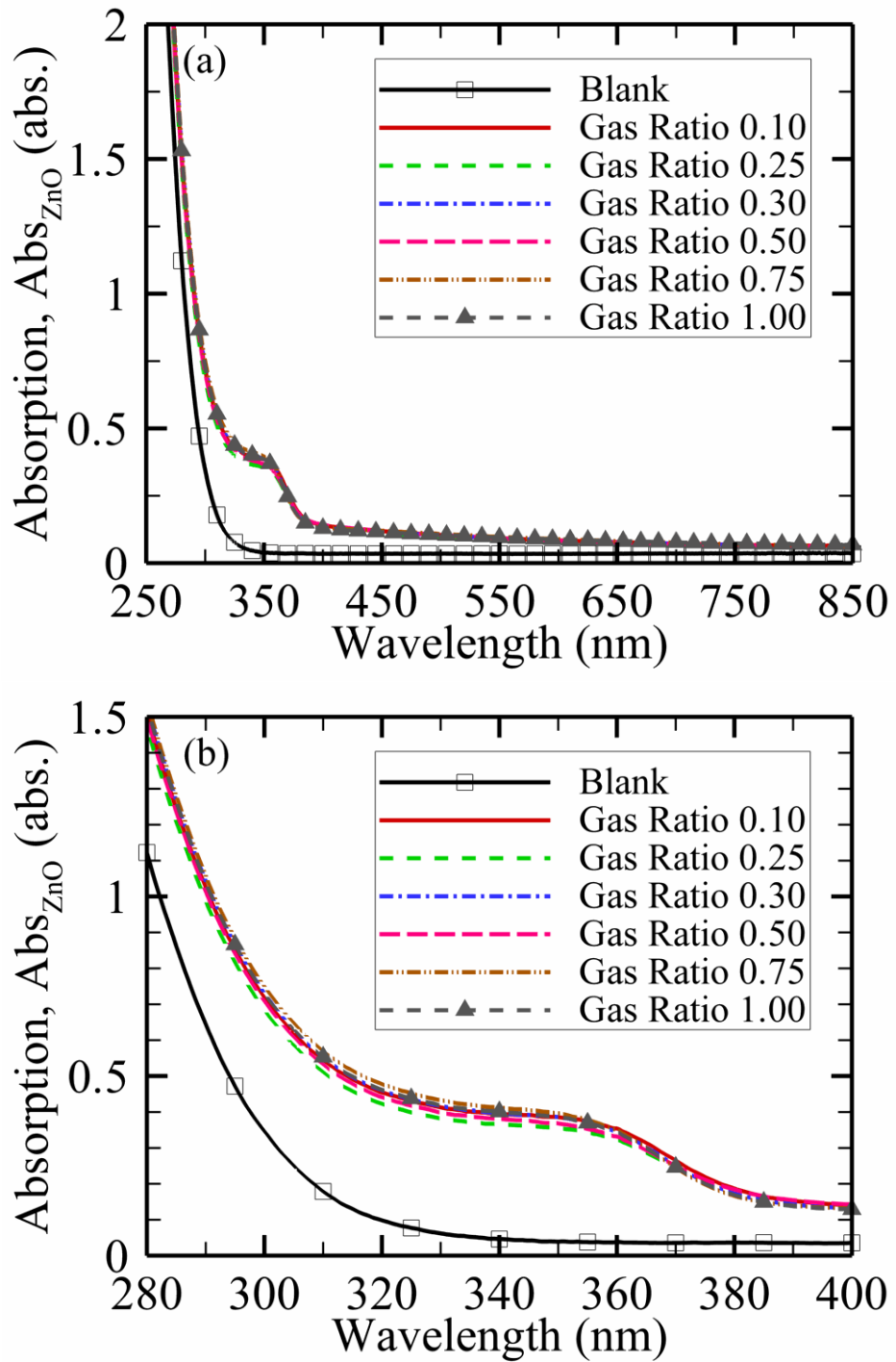


Figure 4.35. Absorption spectra of ZnO/Glass as a function of $O_2/(Ar+O_2)$ ratio under a constant thickness of 60 nm in (a) overall region and (b) UV region (280-400 nm).

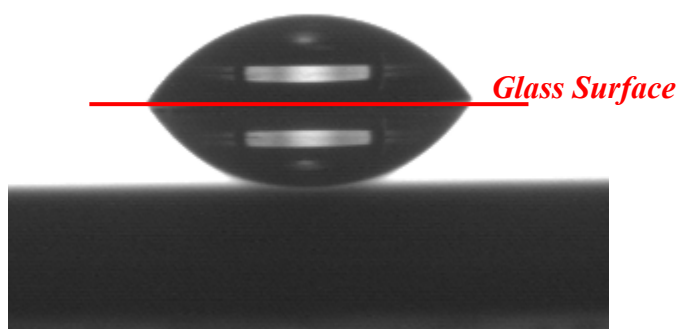


Figure 4.36. Contact angle image of blank glass substrate.



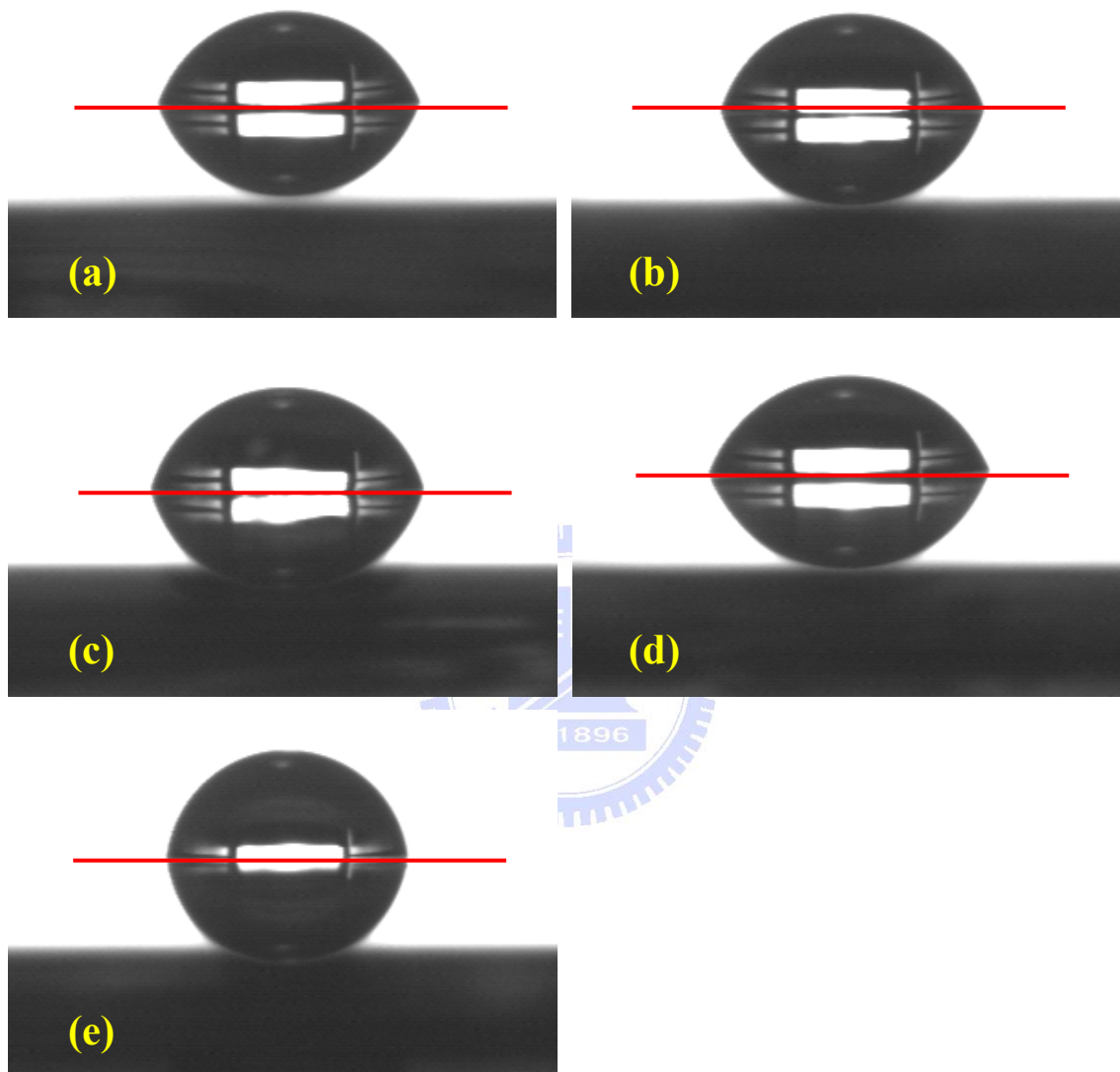


Figure 4.37. Contact angle images of ZnO thin Films under a constant thickness for various RF powers - (a) RF 50 W; (b) RF 100 W; (c) RF 200 W; (d) RF 300 W; (e) RF 400 W.

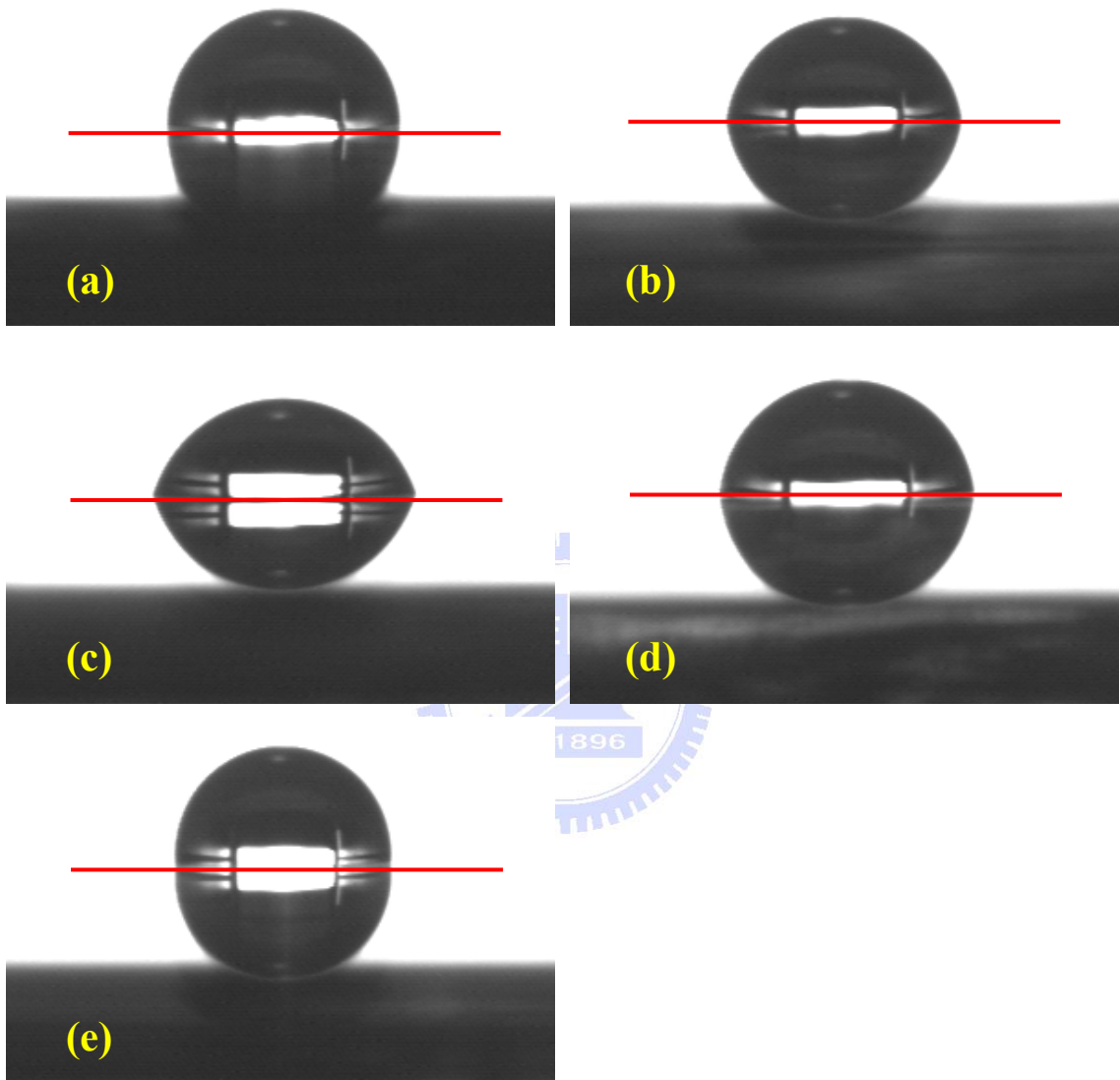


Figure 4.38. Contact angle images of ZnO thin Films under a constant RF power for various deposition time - (a) 5 min.; (b) 10 min.; (c) 20 min.; (d) 30 min.; (e) 60 min.

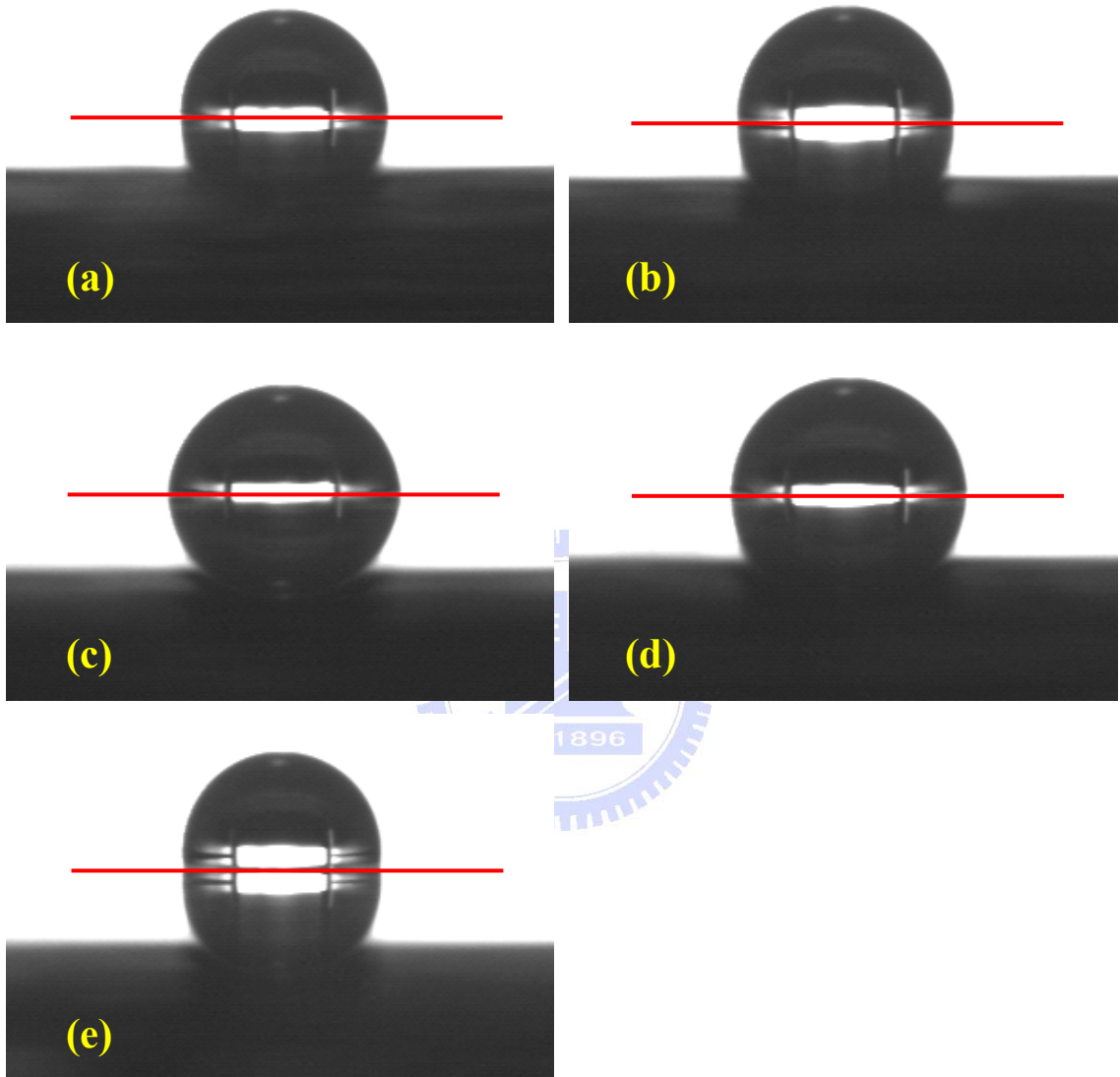


Figure 4.39. Contact angle images of ZnO thin Films under a constant thickness for various $O_2/(Ar+O_2)$ ratio - (a) 0.10; (b) 0.25; (c) 0.50; (d) 0.75; (e) 1.00.

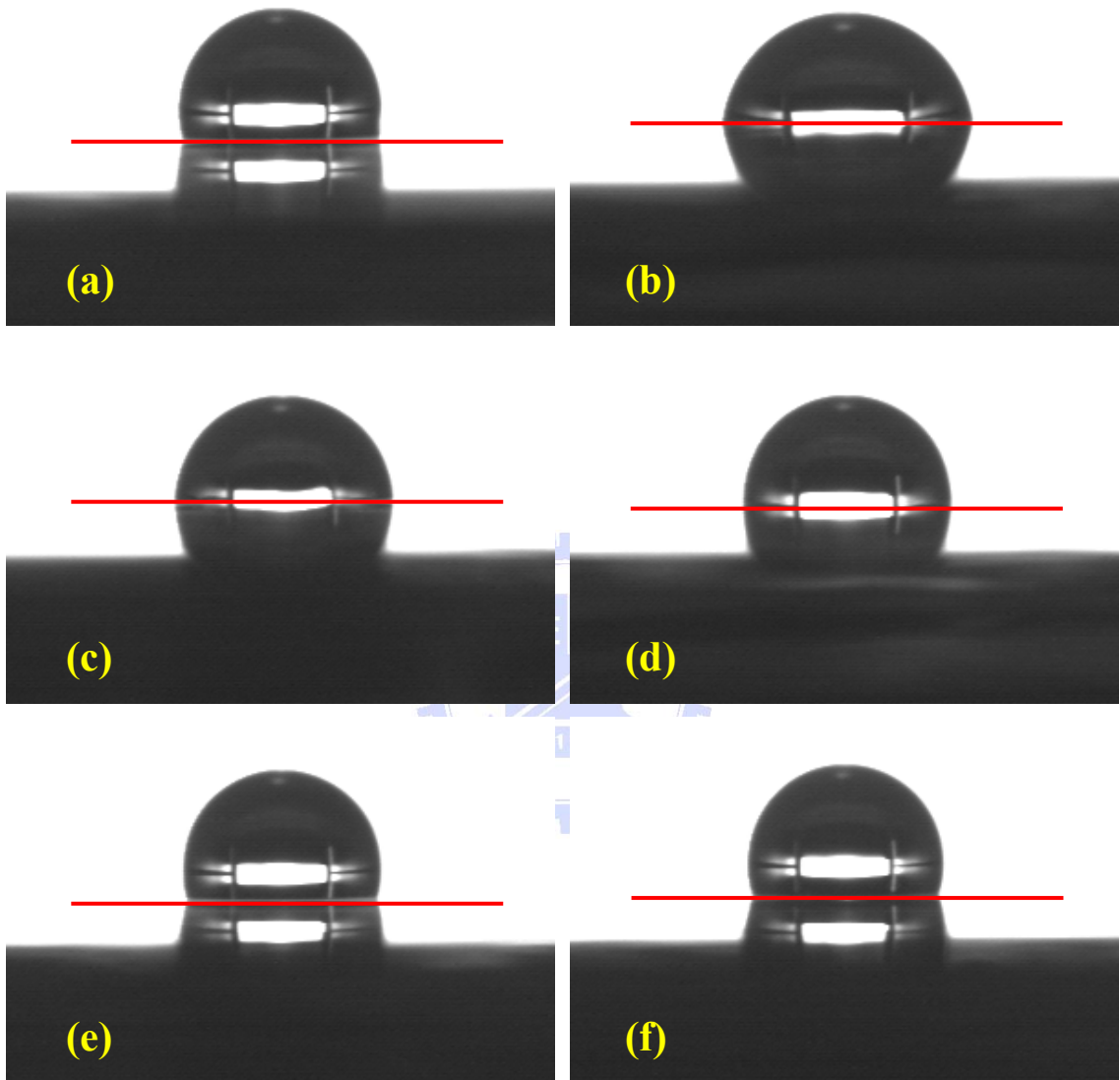


Figure 4.40. Contact angle images of ZnO thin Films under a constant $O_2/(Ar+O_2)$

ratio for various deposition time - (a) 5 min.; (b) 10 min.; (c) 20 min.; (d)

30 min.; (e) 60 min; (f) 90 min.

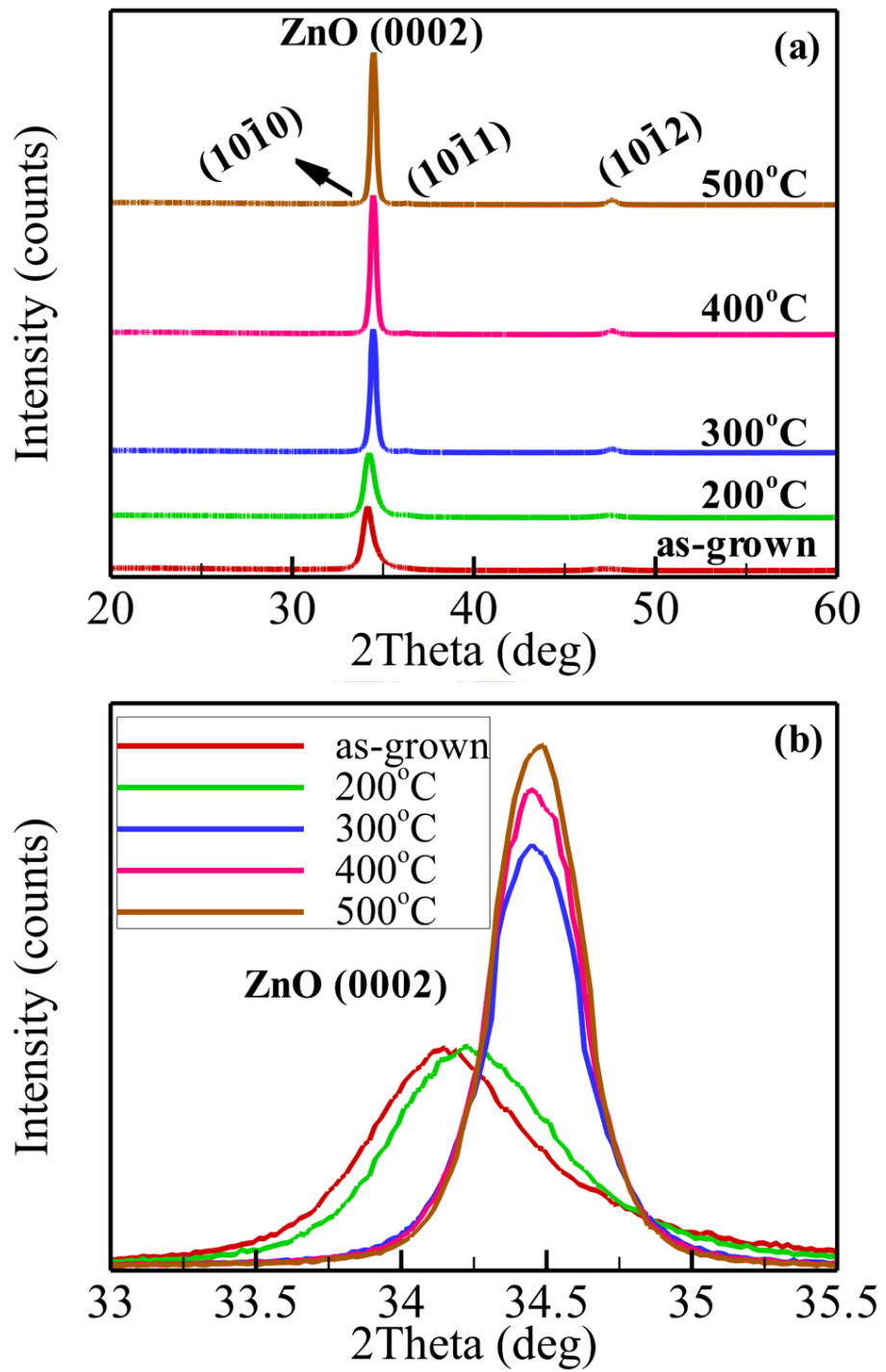


Figure 4.41. XRD patterns of ZnO (0002) orientations as a function of annealing temperature is shown by (a) separation and (b) overlap way.

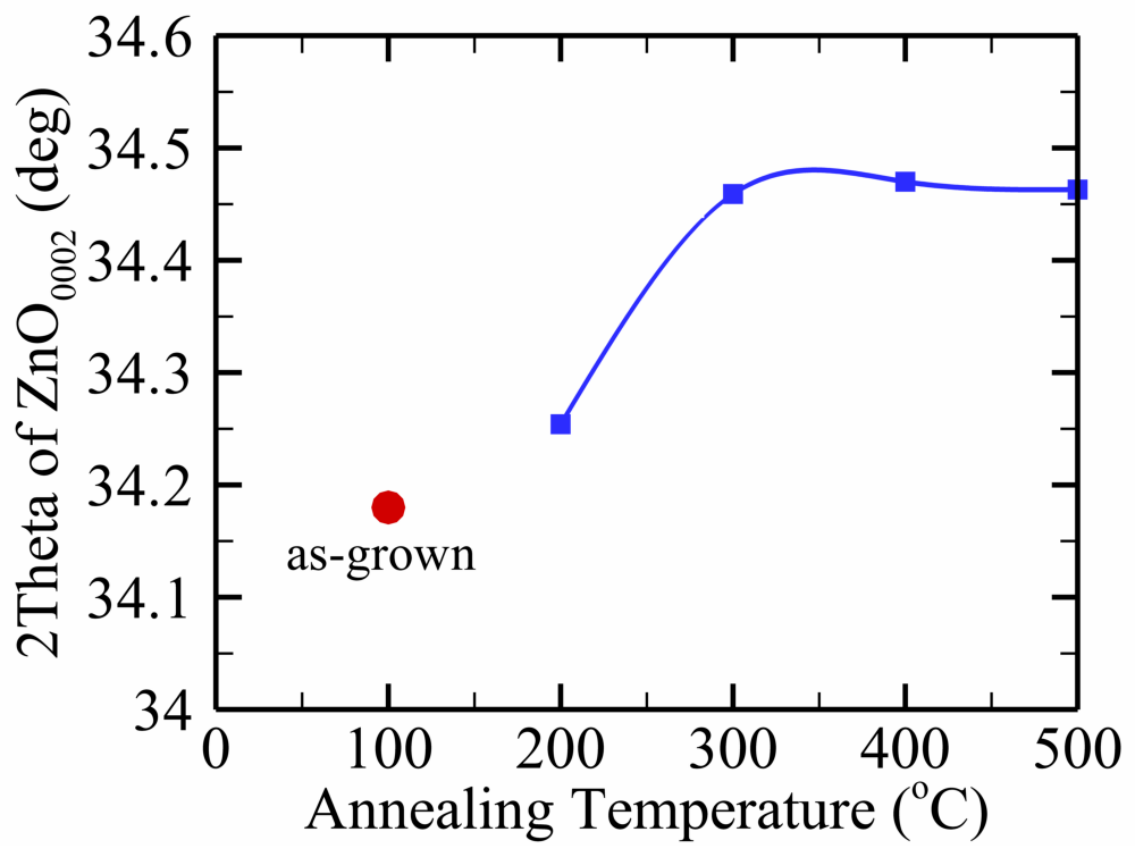


Figure 4.42. The ZnO (0002) diffraction peak shifted as a function of annealing temperature.

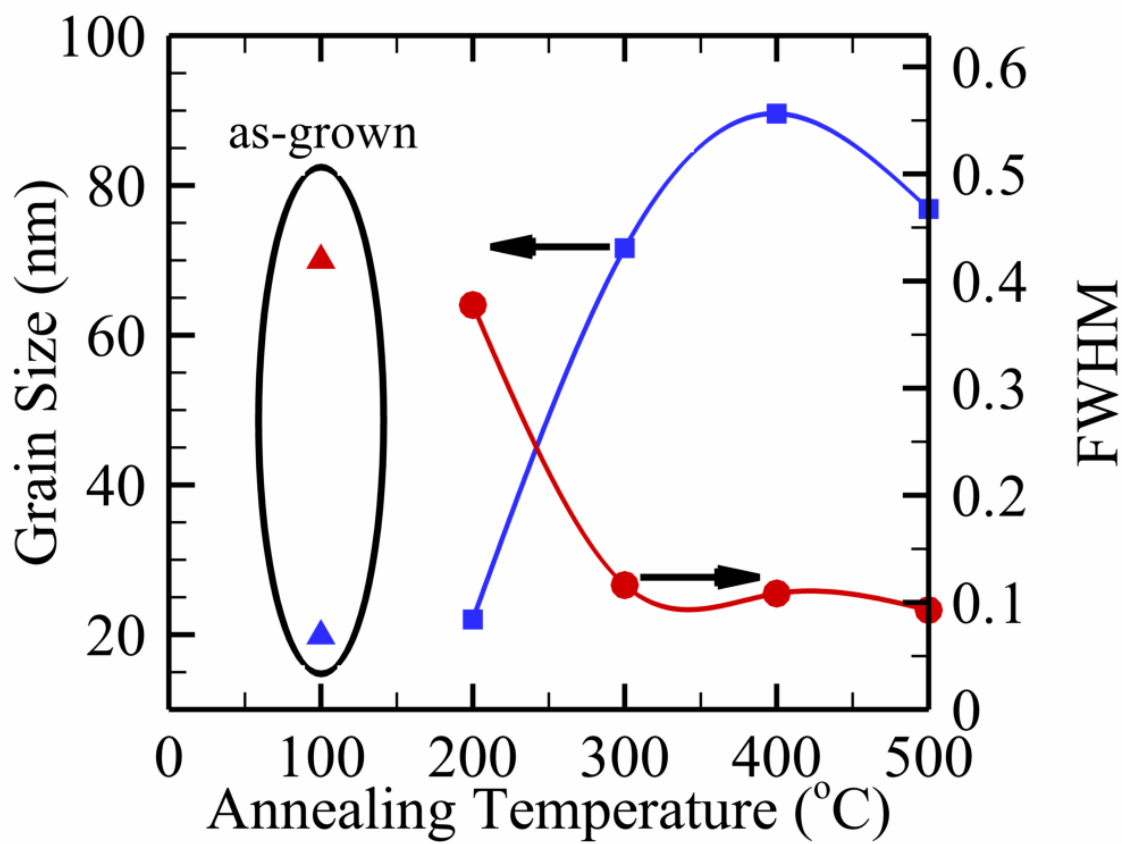


Figure 4.43. Effect of grain size and FWHM as a function of annealing temperature.

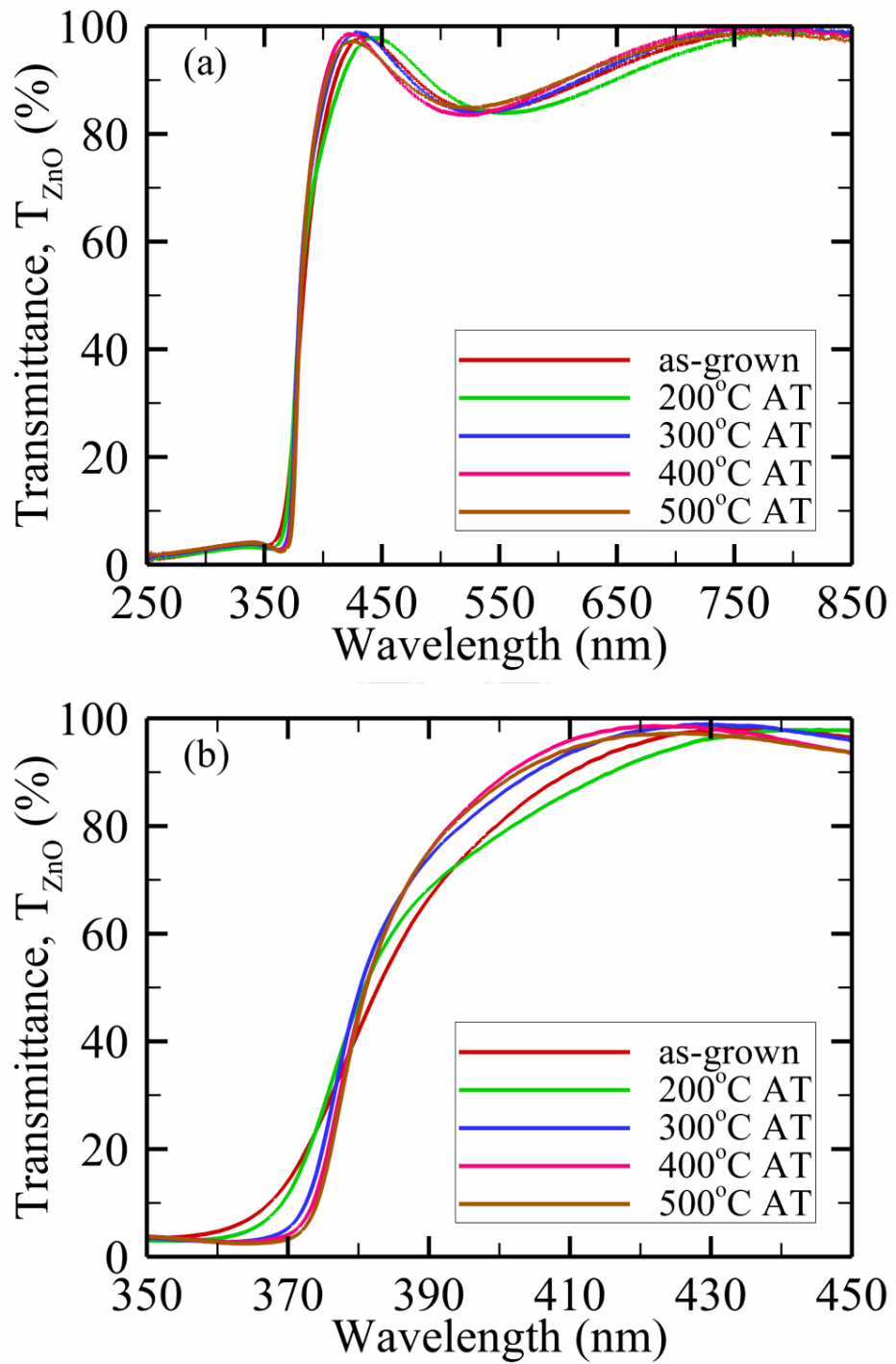


Figure 4.44. Transmittance spectra of pure ZnO thin films as a function of annealing temperature in (a) overall region and (b) near UV edge.

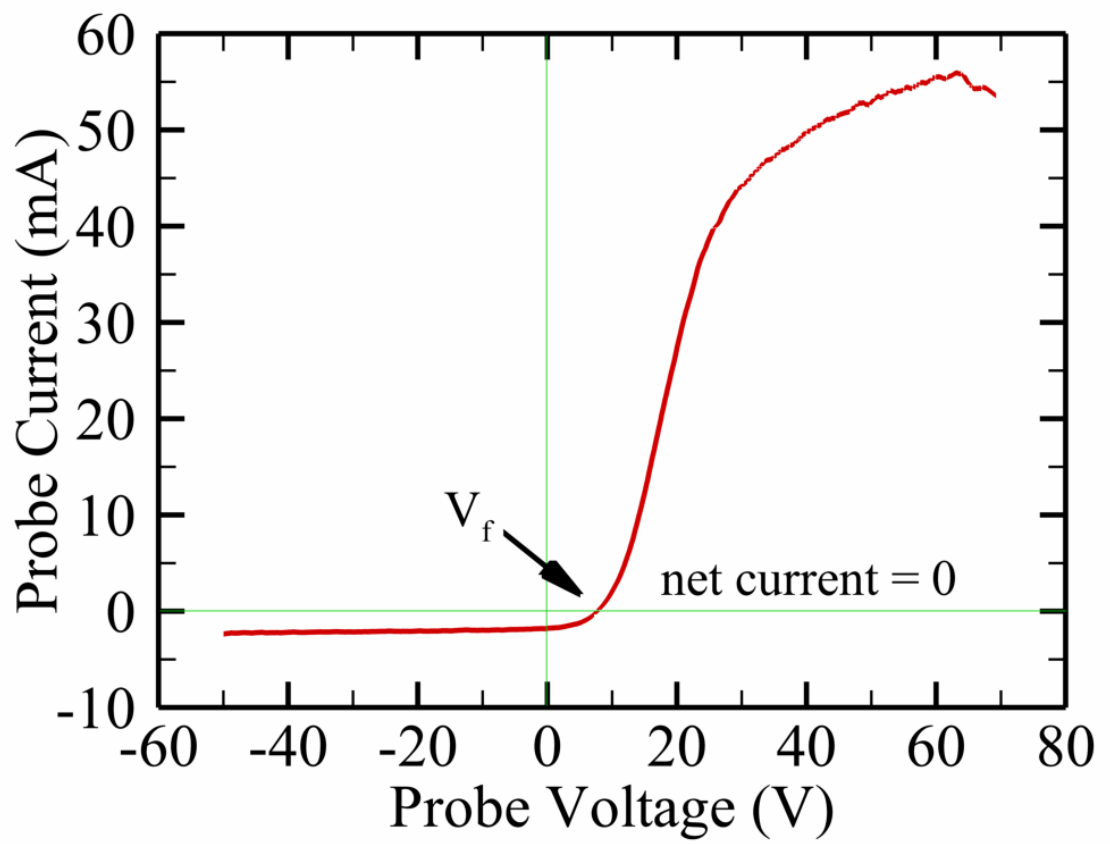


Figure A.1. Step 1 – I - V curve raw data by Langmuir Probe.

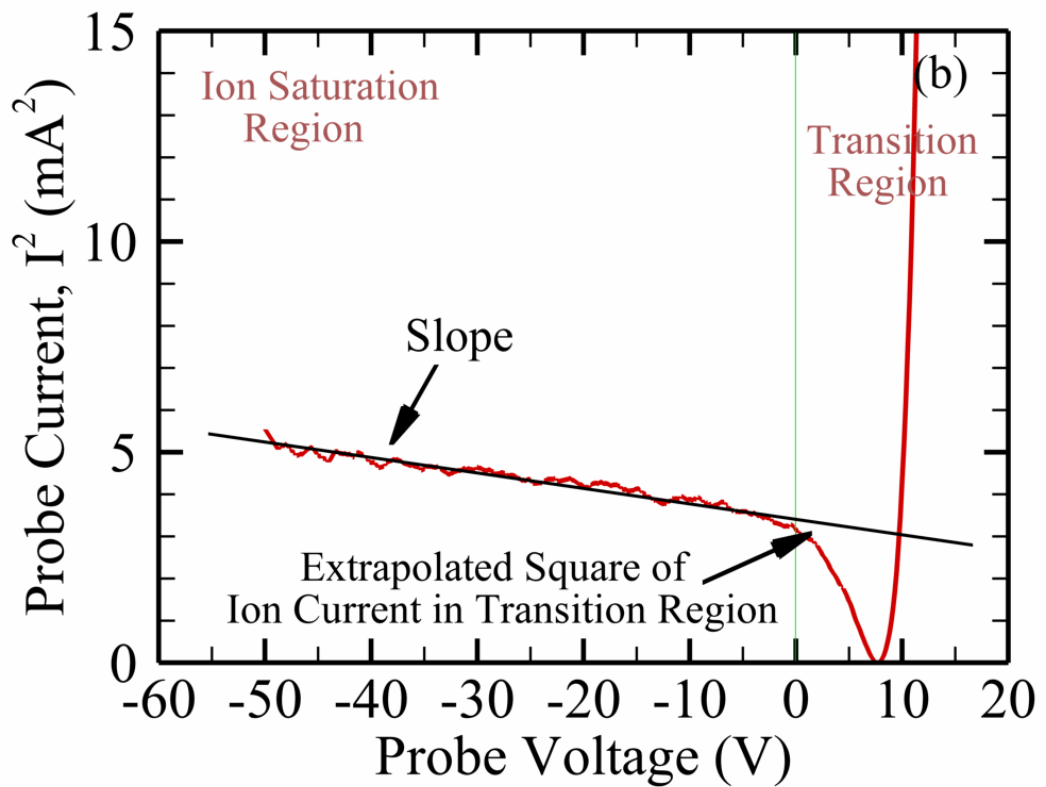
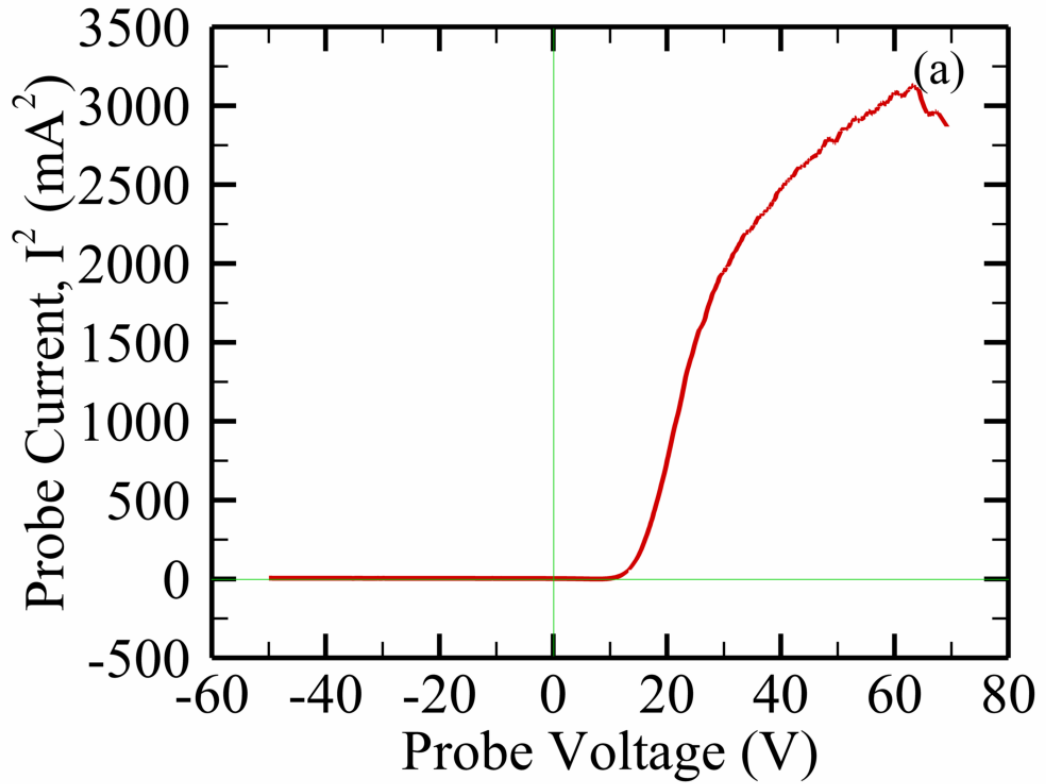


Figure A.2. Step 2 – (a) I^2 - V curve and (b) a ion current linear regression fit is fitted

in the ion saturation.

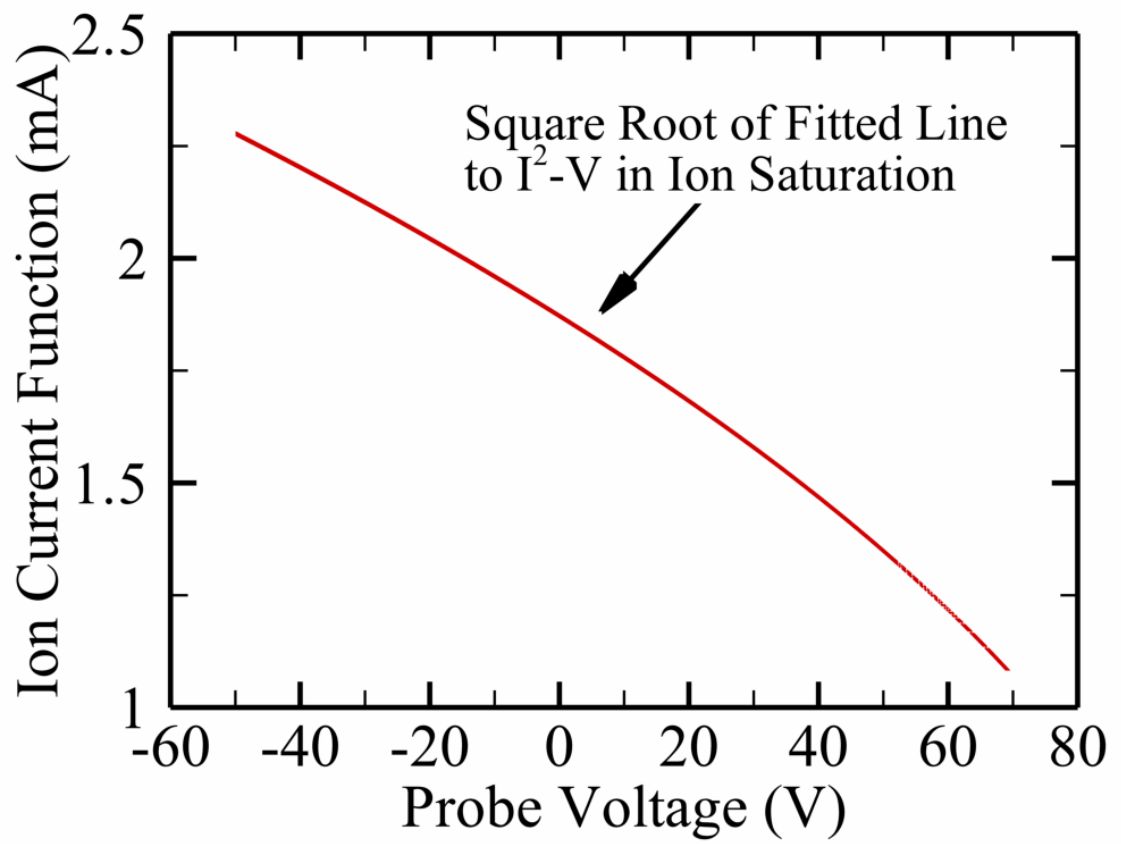


Figure A.3. Step 3 – the square root of fitted line to I^2-V curve in ion saturation.

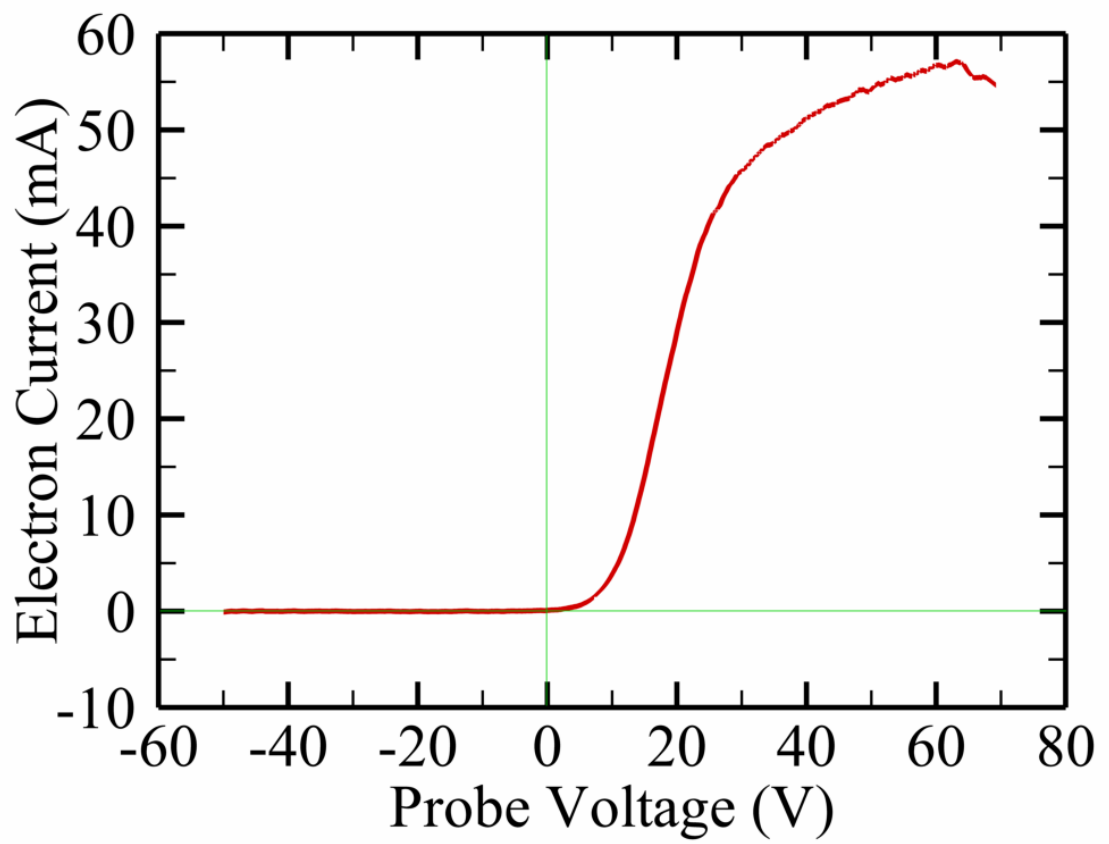


Figure A.4. Step 4 – the electron I - V curve which consists of an electron current component only.

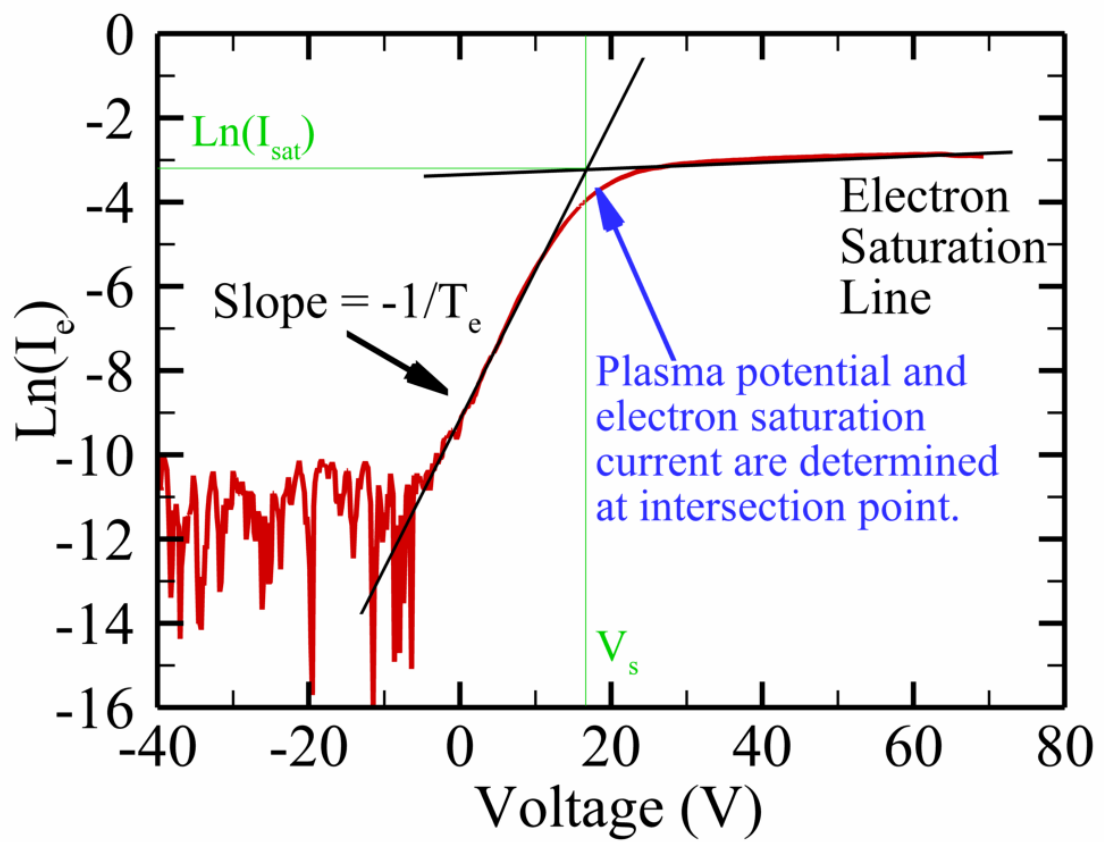


Figure A.5. Step 5 – the natural logarithm of electron current ($\text{Ln}(I_e)$) versus probe potential from the electron I - V curve.

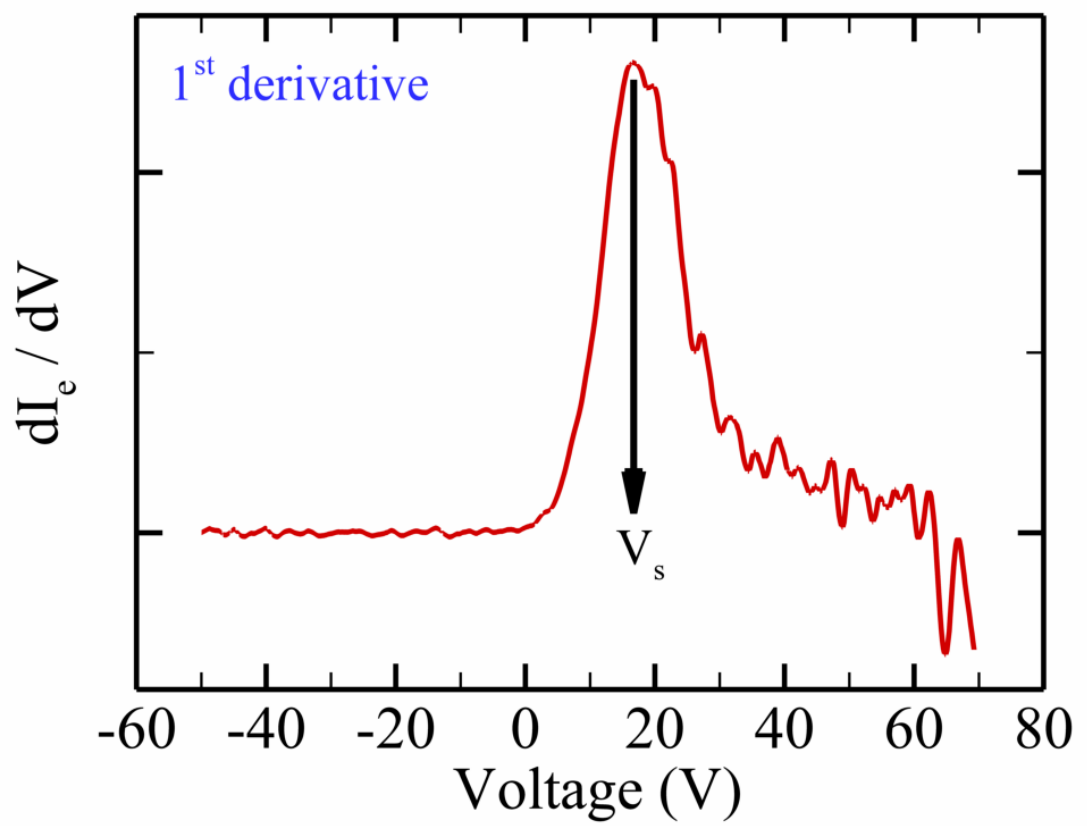


Figure A.6. Step 6 – the 1st derivative of I_e - V curve.

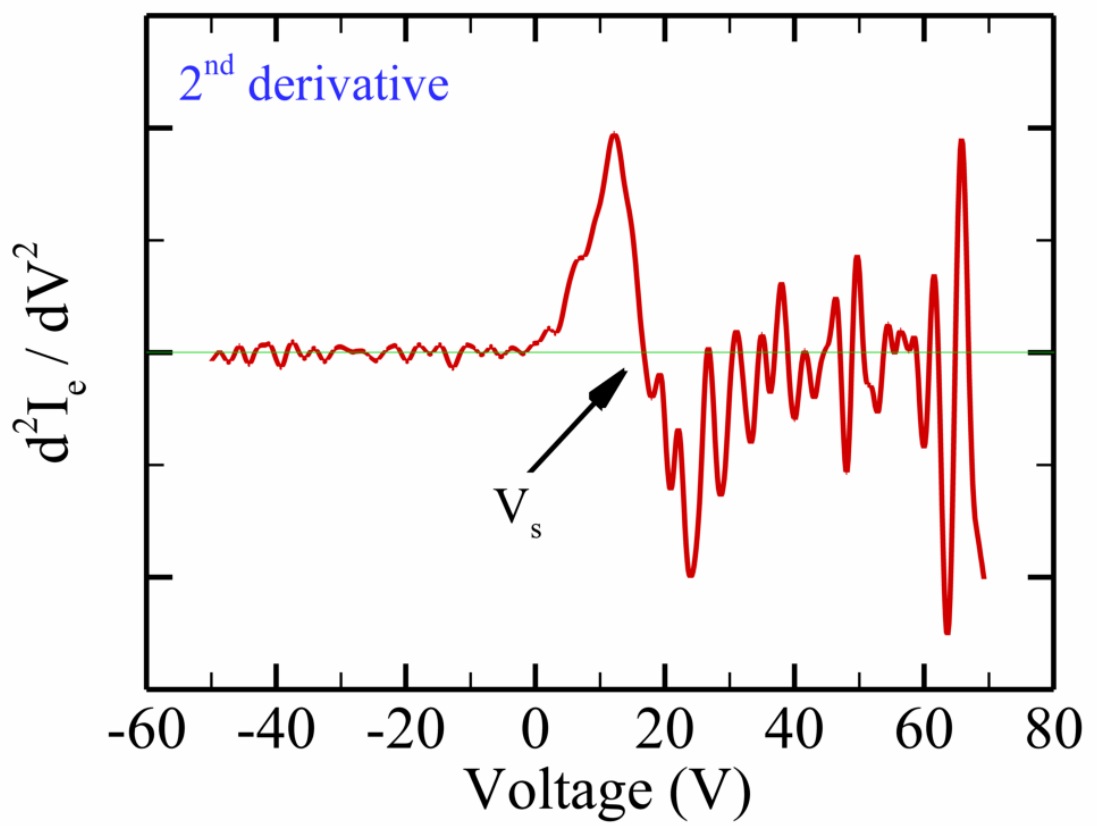


Figure A.7. Step 7 – the 2nd derivative of I_e - V curve.

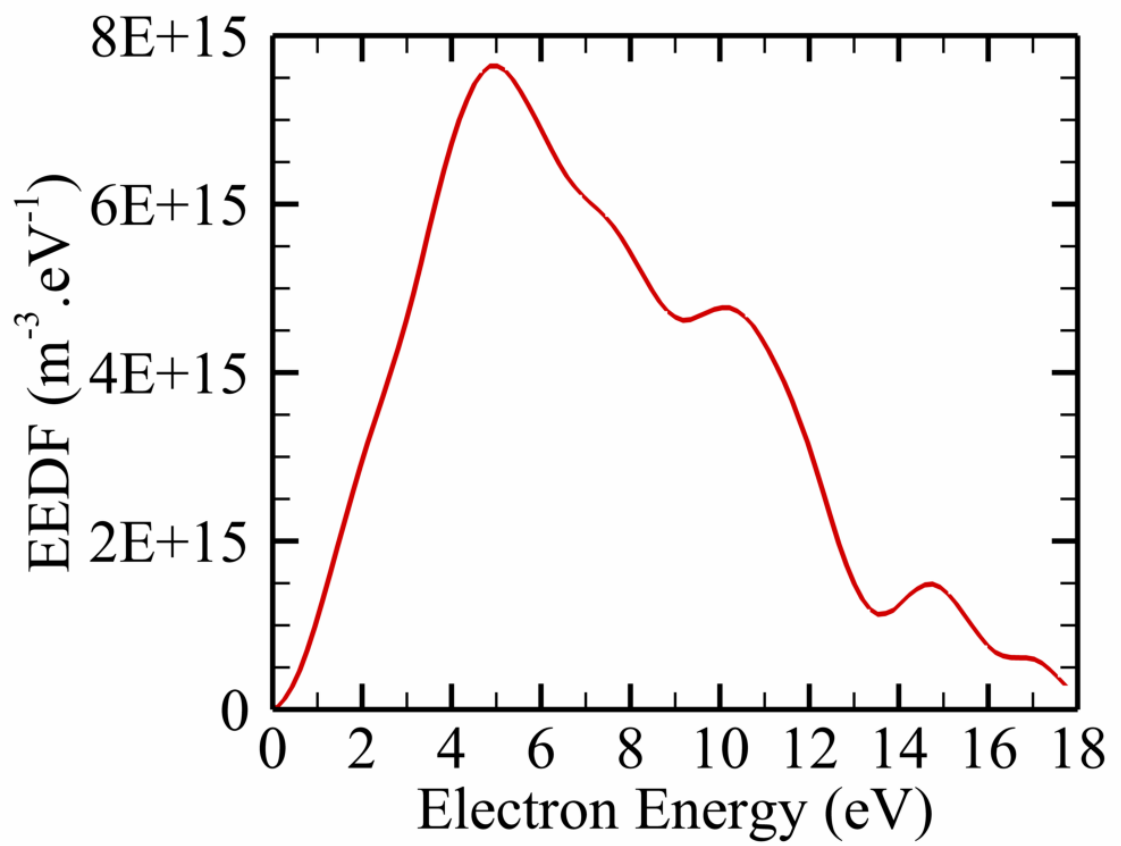


Figure A.8. Step 8 – electron energy distribution function (EEDF).

Publication List of Che-Wei Hsu

Journals:

1. Che-Wei Hsu, Tsung-Chieh Cheng, Wen-Hsien Huang, Jong-Shin Wu*, Cheng-Chih Cheng, Kai-Wen Cheng, and Shih-Chiang Huang, "***Relation between the Plasma Characteristics and Physical Properties of Functional Zinc Oxide Thin Film Prepared by RF Sputtering***," Thin Solid Films 518 (2010) 1953.

Conference Papers:

International

1. Che-Wei Hsu, Tsung-Chieh Cheng, Chun-Hui Yang, Yi-Ling Shen, Jong-Shinn Wu, Sheng-Yao Wu, Wen-Hsien Huang, "***Investigation of Characteristics of Multi-Function ZnO Thin Film Deposited with Various Argon and Oxygen Ratios***," 2009 MRS Spring Meeting, San Francisco, CA, USA, V09-05, April 13-17, 2009. [[Published Online: Mater. Res. Soc. Symp. Proc. Vol. 1174, 1174-V09-05](#)]
2. Che-Wei Hsu, Tsung-Chieh Cheng, Wen-Hsien Huang, Jong-Shinn Wu, and Sheng-Yao Wu, "***Influence of Physical Characteristics of ZnO Thin Film With Various Ratios of Argon and Oxygen Gas***," 2008 International Symposium on Nano Science and Technology (ISNST), Tainan, Taiwan, OS05, pp. 28-29, Nov. 7, 2008. [[Oral Presentation](#)]

3. Tsung-Chieh Cheng, Che-Wei Hsu, Jong-Shinn Wu, Wen-Hsien Huang, Cheng-Chih Cheng, Shih-Chiang Huang, “***Characterization of Anti-ultraviolet Zinc Oxide Thin Film Generated by Radio-Frequency (RF) Reactive Magnetron Sputtering Process***,” 2008 *International Conference on Nanoscience + Technology (ICN+T)*, Colorado, USA, July 20, 2008.

Domestic

1. Che-Wei Hsu, Tsung-Chieh Cheng, Chun-Hui Yang, Yi-Ling Shen, Jong-Shinn Wu and Sheng-Yao Wu, “***A Study of Oxygen Concentration Effect on Zinc Oxide Thin Film Deposition by a RF Magnetron Sputtering Method***,” *Symposium on Nano device Technology (SNDT)*, Hsin-Chu, Taiwan, NM-04, April 29-30, 2009.

[Student Paper Award]

2. Chia-liang Hung, Sheng-Yao Wu, Cheng-Chih Cheng, Che-Wei Hsu, Yun-Long Shao, Jong-Shinn Wu and Tsung-Chieh Cheng, “***Effect of Interlayer for Carbon Nanotubes Grow on Carbon Cloth by Thermal Chemical Vapor Deposition***,” *Symposium on Nano device Technology (SNDT)*, Hsin-Chu, Taiwan, NF-14, April 29-30, 2009.

3. Che-Wei Hsu, Tsung-Chieh Cheng, Sheng-Yao Wu, Wen-Hsien Huang, Jong-Shinn Wu, “*The Influence of Ar/O₂ ratio for Physics Properties of ZnO Thin Film by RF Reactive Magnetron Sputtering*,” 中華民國材料科學學年會暨中國材料科學學會 40 週年 (MRS-T), Taipei, Taiwan, P04-108, Nov. 21-22, 2008.

4. Che-Wei Hsu, Kai-Wen Cheng, Tsung-Chieh Cheng, Wen-Hsien Huang, Jie-Yi Yao, Jiann Hsieh and Jong-Shinn Wu, “*The Influence of Plasma Characteristics between Structural and Optical Properties of Zinc Oxide (ZnO) Thin Films by RF Reactive Magnetron Sputtering*,” *Symposium on Nano device Technology* (SNDT), Hsin-Chu, Taiwan, FM-18, May 15-16, 2008.

5. Kai-Wen Cheng, Che-Wei Hsu, Tsung-Chieh Cheng, Wen-Hsien Huang, Jie-Yi Yao, Jiann Hsieh and Jong-Shinn Wu, “*Influence of RF Power on Plasma, Structural and Optical Properties of ZnO Thin Films by RF Reactive Magnetron Sputtering*,” *Symposium on Nano device Technology* (SNDT), Hsin-Chu, Taiwan, NM-07, May 15-16, 2008.

6. Che-Wei Hsu, Ming-Hung Chiang, Cheng-Chih Cheng, Jong-Shinn Wu and Tsung-Chieh Cheng, “*Preliminary Study of Effect of Plasma Conditions on Aluminium Thin Film Deposition in a RF Magnetron Sputtering Chamber,*” *Symposium on Nano device Technology (SNDT)*, Hsin-Chu, Taiwan, T3-04, May 2007.

7. Jong-Shinn Wu, Che-Wei Hsu, Yun-Long Shao, Po-Cheng Huang, Tsung-Chieh Cheng, “*Design, Manufacture and Performance Analysis for a Spiral Micromixer,*” *Symposium on Nano device Technology (SNDT)*, Hsin-Chu, Taiwan, T5-09, 2006.

